

Analogue VLSI Emulation of the Cochlea

Eric Fragnière

April 18, 1998

To Catherine and Gaspard

Remerciements ¹

Lorsqu'on entreprend un travail de recherche nécessitant des connaissances dans un domaine qui n'est pas de sa spécialisation, tel que la biologie dans cette thèse, il est toujours possible de se référer à des manuels ou des articles spécialisés. Bien qu'y prenant peu à peu connaissance de l'état de l'art, il est difficile de s'éloigner des chemins battus par nos prédécesseurs spécialistes, la confiance nécessaire manquant encore. Ceci est valable pour tout chercheur débutant, spécialisé dans aucun domaine. C'est là qu'intervient un directeur de thèse de la trempe du Professeur Eric Vittoz. Sa profonde connaissance de sa spécialisation est augmentée d'une grande expérience de la recherche en général. Les longues discussions que nous avons eues pendant lesquelles il remettait en question avec le bon sens de l'ingénieur grand nombre de certitudes fraîchement acquises —mais encore faiblement assises, ont grandement contribué à l'aboutissement de ce travail. Elle ont également parfait ma formation d'ingénieur de recherche. Je lui suis infiniment reconnaissant pour tout ce qu'il m'a apporté tant au niveau professionnel qu'humain.

Je remercie également les Professeurs Fred Gardiol, Martin Hasler, Evert Seevinck et le Docteur Marco Pelizzone qui m'ont fait l'honneur d'accepter d'entrer dans la composition de mon jury de thèse.

Bien que formellement membre du Laboratoire d'Electronique Générale (LEG), j'ai été affecté au centre MANTRA du Laboratoire de Micro-informatique (LAMI). Je suis donc particulièrement reconnaissant aux Professeurs Michel Declercq et Jean-Daniel Nicoud, chefs respectifs du LEG et du LAMI, de m'avoir accepté dans leur équipe, ainsi qu'au Professeur Wulfram Gerstner qui dirige le centre MANTRA depuis 1996. Je remercie également l'EPFL et le Fond National Suisse pour la Recherche Scientifique pour le financement de ma recherche ainsi que le professeur Declercq qui m'a accordé une prolongation de mon contrat pour la terminer.

En plus de toute l'infrastructure nécessaire à ma recherche, le centre MANTRA et le LAMI m'ont offert un environnement de travail agréable, pour lequel je remercie tous ses membres. Une attention particulière va à Laurent Tettoni, Yves Cheneval, Yuri Lopez de Meneses et Olivier Car-

¹these acknowledgements are in french, because they are mostly dedicated to french-speaking persons, and also because I feel more comfortable to express sincerely my gratitude using my mother tongue.

mona, vaillants *system managers* qui s'y sont succédés pendant mon séjour et qui ont affronté mes requêtes toujours urgentes, ainsi qu'à leurs homologues au LEG Oscar Buset, François Clément et Raymond Sutter. Merci également à Paolo Ienne dont le support m'a donné le courage d'affronter \LaTeX pour la rédaction de ce mémoire et à Philip Maechler, responsable du parc Macintosh.

Durant les 4 ans de ma recherche, j'ai partagé mon bureau avec André van Schaik, dont l'amitié et la bonne humeur ont rendu notre cellule plus agréable. Son expérience en conception de circuits intégrés ainsi que son esprit d'initiative communicatif ont grandement contribué à ce que je me lance enfin dans la réalisation de mon premier chip, qui en serait peut-être encore à sa n-ième phase de vérification sans lui. Merci André!

Si le lecteur rompu à la langue de Shakespeare aura l'impression que certaines parties de ce rapport sont rédigées dans un meilleur anglais que d'autres, nul doute que celles-ci ont été revues et corrigées par Alix Hermann Scheurer, que je remercie chaleureusement.

Je remercie également tous les collègues du LEG (Dominique Python, Pierre Favrat, Ricardo Lara-Saez, pour ne mentionner que ceux dont j'ai été le plus proche) que j'ai vu moins souvent vu la distance qui séparait le LEG de mon bureau. Cependant, durant les courtes périodes où j'errais dans leurs couloirs entre labo de mesures et salle de CAO, les discussions informelles que j'ai eues avec ces collègues électroniciens ont à chaque fois fait progresser de manière notable mes connaissances pratiques de concepteur de circuits intégrés. Parmi les anciens membres du LEG, je tiens à mentionner Alex Mortara, devenu un ami qui m'a toujours soutenu et redonné confiance dans ma recherche durant les moments de doute.

Un avantage d'être ainsi partagé entre deux laboratoires est de disposer environ du double des services offerts à chacun. Un grand merci aux mamans des grands enfants que sont tous les chercheurs, j'ai nommé nos secrétaires Marie-Jo Pellaud et Monique Dubois pour le LAMI et MANTRA et Danièle Gallay au LEG. Merci également au personnel permanent, toujours prêt (quoiqu'on en dise) à vous rendre le service dont vous avez besoin hier-dernier-délai, nommément André Guignard, Edo Franzi au LAMI, Roland Jaques, Joseph Guzzardi et André Decurnex au LEG, Peter Bruehlmeier et Georges Vaucher à l'ACORT.

Dans le cadre d'application des modèles de cochlée à la reconnaissance automatique de la parole, j'ai eu la chance de profiter des compétences des membres de la Chaire de Circuits et Systèmes (CIRC). Un merci spécial

à Jean Hennebert pour les tests de reconnaissance qu'il a effectué à partir de mes modèles.

Ce travail est en quelque sorte aussi le fruit de mes parents, qui m'ont toujours encouragé et donné les moyens d'entreprendre un cycle d'étude particulièrement long. Je ne les remercierai jamais assez pour tout ce que je leur doit. Un grand merci également à ma famille, belle-famille et amis, qui m'ont supporté, aux deux sens du terme, pendant cette période.

Je terminerai en exprimant tout mon amour et ma gratitude à ma femme Catherine, qui a affronté patiemment cette redoutable rivale qu'est la rédaction d'une thèse, et à mon fiston Gaspard (les cochlées le plus performantes que je n'ai jamais réalisées) dont l'arrivée en a accéléré l'aboutissement.

Abstract

This thesis concerns models of the inner ear's cochlea and their implementation using analogue VLSI circuits. The cochlea is the sensory organ which transduces the incoming acoustical signal into neural pulses on the auditory nerve. As a first step in modeling auditory processing with analogue VLSI, a VLSI cochlea provides the necessary interface with the outside world, in the same way as electronic retinae are used for modeling neural processing in vision. Natural applications of such low-power acoustic sensors include cochlear implants and hearing aids.

An existing model, Lyon & Mead's cochlear filter cascade, is first analysed at a system level. An improved version of this circuit was integrated; it features a novel implementation of a frequency-selective automatic gain control mechanism. This mechanism models the local control of the mechanical properties of the cochlea. Unlike most models of active cochleae in which a saturating feedback creates the required non-linearity of the automatic gain control mechanism, the present version performs this with a feedback gain control from higher levels of neural processing. However, analysis of this circuit, confirmed by chip measurements, shows that despite its potential for large input dynamic range compression, the cascade structure is insufficient to model faithfully the frequency selectivity of the biological cochlea.

A second model is thus proposed, which emulates the hydrodynamics of the cochlea using a dense network of resistors and a bank of resonators. This model performs a computation of the cochlear dynamics in a much more collective fashion than the cascade structure. Characteristics much closer to those measured on live cochleae can be obtained, the most interesting of which is the extremely sharp frequency cutoff (200-300dB/octave).

The implementation envisaged for this model on silicon relies on resistors modeled by single transistors, which work linearly with respect to current and to logarithmically compressed voltage. A novel implementation of a log-domain transcapacitor has been proposed as a building block to design resonators compatible with the log-domain resistive network.

Résumé

Cette thèse traite de la modélisation de la cochlée et de son émulation au moyen de circuits électroniques intégrés VLSI analogiques en technologie CMOS. La cochlée est l'organe de l'oreille interne qui opère la transduction du signal acoustique en impulsions nerveuses sur le nerf auditif. Dans le cadre d'un modèle analogique VLSI du système auditif dans sa totalité, une telle cochlée artificielle procure l'interface nécessaire avec le signal sonore extérieur, similairement aux rétines artificielle utilisées dans les modèles de traitement neuronaux dédiés à la vision. Une des applications les plus naturelles de ce type de capteur bio-inspiré à très basse consommation concerne les prothèses auditives et les implants cochléaires.

Une cascade de filtres cochléaires originellement proposée par Lyon & Mead est d'abord analysée au niveau fonctionnel. Une version améliorée du circuit électronique est proposée, auquel un système de contrôle automatique de gain sélectif en fréquence est rajouté. Ce mécanisme modélise le contrôle local des propriétés mécaniques de la cochlée telle qu'effectuée par son équivalent biologique. A la différence de la plupart des modèles de telles cochlées, dites actives, le mécanisme proposé est basé sur une boucle de contre-réaction incluant des étapes de traitement situées en amont du système auditif, au lieu de simples non linéarités locales aux filtres cochléaires. Cependant, l'analyse du circuit montre, ainsi que l'ont confirmé des mesures sur le circuit intégré, que malgré son potentiel de haute compression de niveau du signal, la structure en cascade est insuffisante pour une modélisation fidèle de la sélectivité fréquentielle telle que mesurée sur la cochlée biologique.

Un second modèle est donc proposé, qui émule la dynamique des fluides de la cochlée à l'aide d'un réseau serré de résistances et de résonateurs électriques. Ce réseau effectue le calcul des équations hydromécaniques dans la cochlée d'une manière plus collective que la cascade de filtres. Des caractéristiques plus proches de celles mesurées dans la cochlée biologique ont pu être obtenues, parmi lesquelles la plus remarquable est la coupure très abrupte (200-300dB/octave) du signal à la fréquence de coupure du filtre ainsi réalisé.

Dans le but d'une réalisation efficace de ce modèle sur silicium, l'utilisation d'un réseau résistif dont chaque résistance est remplacée par un unique transistor est préconisée. Ce réseau reste linéaire par rapport aux courants et à des tensions compressées logarithmiquement. Un nouveau

type de circuit réalisant une transcapacité travaillant linéairement dans le domaine logarithmique est proposé. Ce circuit est assez général pour être utilisé comme élément de base permettant de réaliser des résonateurs compatibles avec le réseau résistif travaillant dans le domaine logarithmique.

Contents

- 1 Introduction** **1**
 - 1.1 General context 2
 - 1.1.1 Auditory perception 2
 - 1.1.2 Pattern recognition 2
 - 1.1.3 Cochlear-like speech processing 4
 - 1.1.4 Analogue VLSI modeling 4
 - 1.2 Presentation of the thesis 5
 - 1.2.1 Background 5
 - 1.2.2 Objectives 6
 - 1.2.3 Contribution 7
 - 1.2.4 Overview 7

- 2 Biological cochlea and models** **9**
 - 2.1 Introduction 10
 - 2.2 Anatomy and physiology 11
 - 2.2.1 Outer and middle ear 11
 - 2.2.2 Anatomy of the cochlea 11
 - 2.2.3 Innervation 14
 - 2.2.4 Hair cell physiology 16
 - 2.2.5 Measurements of basilar membrane vibrations 17
 - 2.3 Mechanisms and models 17
 - 2.3.1 Transduction mechanism 17
 - 2.3.2 Models 21

- 3 VLSI active cochlea** **25**
 - 3.1 Overview 26
 - 3.2 The model 26

3.2.1	Functional model	26
3.2.2	Quality factor modulation	28
3.2.3	Analogue model	28
3.2.4	Level compression	30
3.2.5	Pseudo-resonance	31
3.2.6	Quality factor control loop	34
3.2.7	Closed loop amplitude gain	39
3.2.8	Cochlear filter stability	40
3.3	Time simulations	42
3.3.1	Computer model	42
3.3.2	Level compression and transient enhancement	42
3.3.3	Two-tone suppression	44
3.3.4	Speech cochleogram	44
3.4	VLSI implementation	48
3.4.1	Second-order stage with differentiator	48
3.4.2	Quality factor control	49
3.4.3	IHC rectifier	51
3.4.4	MSR low-pass filter	53
3.4.5	Feedback gain distribution	56
3.4.6	Bias currents generation	57
3.4.7	Effect of internal noise	58
3.4.8	Chip measurement results	63
3.5	Conclusions	66
4	Electrical 2-D cochlear model	69
4.1	Introduction	70
4.2	2-D model of the cochlea	71
4.2.1	3-D hydrodynamics of the cochlea	71
4.2.2	2-D electrical equivalent	74
4.2.3	Micro-mechanics in the organ of Corti	78
4.3	Electrical model	81
4.3.1	Longitudinal symmetry	81
4.3.2	Spatial quantisation	82
4.3.3	Basilar membrane resonator	86
4.3.4	Mechanical to electrical mapping	87
4.4	Electrical simulations	90
4.4.1	Simulated network	90
4.4.2	Simulation results	91

4.4.3	Spatial resolution	93
4.4.4	Spatial resolution vs. frequency selectivity	95
4.4.5	Effect of the shape of the cochlear duct	96
4.4.6	Basilar membrane - liquid mass ratio	98
4.4.7	Parameter values	100
4.5	Summary	103
5	Log-domain VLSI 2-D cochlea	105
5.1	Introduction	106
5.2	Log-domain processing	106
5.2.1	Pseudo-conductance and pseudo-voltage in weak in- version	106
5.2.2	Current to pseudo-voltage conversion	107
5.2.3	Principle of the pseudo-capacitance	110
5.3	Pseudo-transcapacitor circuit	111
5.3.1	Implementation of a pseudo-transcapacitor	111
5.3.2	Range of operation	113
5.3.3	Second-order effects	117
5.3.4	Stability	121
5.3.5	Noise	124
5.3.6	Circuits based on pseudo-transcapacitors	127
5.4	Log-domain cochlea	129
5.4.1	Basilar membrane resonator	129
5.4.2	Parameter mapping	133
5.4.3	Implementation of the log-domain resonator	133
5.4.4	Transient simulation	136
5.4.5	Stability	139
5.4.6	Noise	142
5.4.7	Implementation of the full cochlea	148
5.5	Summary	156
6	Conclusions	159
6.1	Original results	160
6.2	Cochlear models	160
6.2.1	Active cochlea	160
6.2.2	2-D hydrodynamic model	161
6.3	VLSI implementations	162
6.3.1	Filter cascade with automatic gain control	162

6.3.2	Log-domain spatio-temporal processing	163
6.3.3	Analogue VLSI vs. biology	165
6.4	Future work and applications	166
A	Mathematical derivations	171
A.1	Cochlear filter cascade noise	172
A.2	Finite difference approximation	177
A.3	Green's function in a resistive sheet	184
A.4	Resonator noise	188
A.4.1	Integrator	188
A.4.2	Feedback block	191
A.4.3	Full resonator	192
	Biographical data	203

Chapter 1

Introduction

1.1 General context

1.1.1 Auditory perception

Hearing is one of the five senses that link us (and most vertebrates) to our environment. Acoustic information from the outside is processed by the auditory system, together with the information provided by the other senses (vision, smell, taste, and touch), to build an internal representation of the present state of this environment. This *perception* of the environment allows us to interact optimally with it, in order to survive and to procreate.

Since acoustic information is transmitted by pressure variations in the air, hearing could be seen as a specialised subclass of the sense of touch. However, the pressure variations of an acoustical signal are much faster than the mechanical stimuli usually sensed by touch, and they are above all perceived very differently: in addition to its intensity, we are very sensitive to the fine temporal structure of this fast-varying stimulus. An acoustical signal having a regular temporal structure (or more generally, a stationary signal) is perceived as a constant stimulus rather than as a time-varying intensity, and this for stimulus frequencies spanning up to 3 orders of magnitude (20Hz-20kHz for human hearing).

The auditory system, able to extract stationary characteristics of the acoustical signal, is thus similar to a bank of specialised filters, each of which responds best to a specific temporal structure of the sound. In the inner ear, the *cochlea* is the first stage where the physical nature of the sound is transformed. The way the representation of the auditory signal is further transformed into a subtle sensation all along the auditory pathway is still mysterious and subject to intense investigation. Early stages of this processing chain are now fairly well understood, but not so for the higher levels of the auditory pathway.

1.1.2 Pattern recognition

Humans (and more generally animals) recognise and classify external stimuli in ways that rely on signal processing strategies very different from the ones used by engineers. These strategies are much more efficient than any man-made systems dedicated to similar pattern recognition tasks. The “hardware” on which this biological signal processing “runs” is also very

different and its optimal exploitation evolved by the trial-and-error process of natural selection.

In a general approach, artificial pattern recognition systems are based on the extraction of relevant features from the raw stimulus and manipulation of these features as symbols by classification algorithms. If a one-to-one correspondence between features and symbols were available, the problem would be straightforward. However for natural stimuli this one-to-one correspondence cannot be postulated. The reason is that the stimulus corresponding to a given symbol may suffer more variability than stimuli corresponding to different symbols. In other words, as an example from speech recognition, the acoustic stimuli of a given word pronounced by different speakers and/or in different environments may differ more than distinct words pronounced by a unique speaker in identical conditions.

There are two ways to eliminate this ambiguity: extraction of distinguishable features from the raw stimulus, and context-dependent symbol classification. The latter relies on prior knowledge of the meaning of the symbols and their mutual relationship. From a known context (syntax, semantics for speech recognition), the classifier guesses the next most plausible symbol, which is confirmed or discarded by the incoming stimulus. Natural systems do this by learning the required knowledge and logic, resulting in a perception which is, from a somewhat oversimplified point of view, just the confirmation of what is expected to be perceived. The implementation of such technique in artificial pattern recognition system is feasible, but depending on the amount of knowledge required to eliminate all ambiguity in a given context, it can lead to very complex systems, usually based on artificial intelligence techniques.

At the other extreme of the stimulus-to-symbol processing chain, features should be extracted from the raw stimulus that are as relevant as possible for the recognition task. In speech processing, for example, the features necessary to extract invariant symbols among speakers for speech recognition would be almost orthogonal to those required for speaker identification. In biological systems, this seems to be performed by extracting several parallel feature maps among which the appropriate ones are selected by higher processing levels according the recognition task to be performed. A preprocessing stage that extracts similar features from the raw input signal is thus likely to filter out efficiently the undesirable variability degrading the performance of artificial pattern recognition systems.

1.1.3 Cochlear-like speech processing

The stimulus used for speech recognition comprises both an auditory part and a visual part. The visual information of lip movements features relevant clues for speech recognition, but the main information channel is auditory. This auditory portion is exclusively transmitted by the auditory nerve from the cochlea to higher processing levels. It is therefore reasonable to assume that the processing performed by the peripheral auditory system already extracts the adequate features to build the appropriate perceptive maps used for speech recognition, or more generally for sound recognition.

The cochlea is the stage in the peripheral auditory system that performs the most important transformation of the auditory signal. It must be modeled faithfully enough to ensure the appropriate behaviour further in the auditory pathway. This gives at least two reasons for modeling the cochlea: to understand the biological processing performed at this level, and to emulate it efficiently, either in order to provide models of higher level of neural processing with a realistic input signal, or to use as an auditory-like speech processing stage. In the case of preprocessing for an automatic speech recognition system, however, compatibility with what the classifier expects as relevant features is a key issue which is often neglected. On the contrary, speech preprocessing performed by cochlear implants already yields remarkable recognition results despite a rather crude processing of the raw acoustic signal, because it relies on an extremely high performance flexible classifier: the human brain. However if hearing and recognition ability can be recovered by deaf people with hearing aids and cochlear implants in a good acoustical environment, their performance severely degrades in adverse hearing conditions. The same is true in automatic speech recognition. Therefore the field of auditory-like speech processing is still wide open to further research and development.

1.1.4 Analogue VLSI modeling

The auditory system has been shown to be extremely efficient even at its early stages. From an engineering point of view, understanding the processing it performs might be a rich source of original signal processing techniques. Inspiration from biological signal processing is especially expected to be fruitful in the domain of analogue VLSI circuit design because this technology shares with the live substrate the potential to exploit opti-

mally a large number of noisy and imprecise available processing elements: the transistor and the neurone, respectively.

Before the era of powerful digital computers, analogue processing was an interesting alternative for computing large systems of nonlinear differential equations. Several attempts to model the hydrodynamics of the cochlea were based on such a technique. This approach was revived 10 years ago by Carver Mead [1] who suggested using analogue VLSI circuits in MOS technology to model biological systems. Thanks to the rich computational potential of a single MOS transistor [2], this approach can integrate a large amount of processing cells onto a few square millimetres of silicon. This integration is facilitated if their design is based on a cellular architecture where the processing elements are arranged into regular networks performing a collective computation.

However, biological and electronic substrates are still rather different. It would be more appropriate to opportunistically exploit the functions and strategies identified in biological processing than to attempt to replicate the structure of the biological system that performs it. Moreover, an additional distinction must be pointed out concerning the modeling of the mechanical transduction performed in the peripheral auditory system. The first neurones in the auditory pathway are located in the auditory nerve. Up to this point, there is no neural processing to be emulated, but rather a micro-mechanical system. For cochlear modeling, the term “bio-inspired engineering” is therefore preferred to the term “neuro-morphic engineering” often used for this emerging domain. The cochlear models implemented in this thesis are closer to the domain of analogue filters and analogue emulation of hydromechanical systems than to the domain of analogue neural networks. Nevertheless, the advantages of analogue implementations, such as continuous-time collective processing and low power consumption still yield important benefits.

1.2 Presentation of the thesis

1.2.1 Background

An early objective of this research was to connect an existing analogue VLSI model of binaural hearing [3] with a standard speech recognition system in order to evaluate the improvement that auditory-like processing could bring to automatic speech recognition. A cochlear-based interfac-

ing system inspired by auto-regressive filtering techniques used in digital speech processing was proposed [4]. Although the results obtained from this first attempt were encouraging, they were still far from those obtained with state-of-the-art digital speech preprocessors based on more classical signal processing techniques. The conclusion was that in order to exploit the full potential of auditory-like processing, the recognition algorithms had to be adapted consequently [5]. This was beyond the scope of the thesis research, whose principal axis was analogue VLSI speech preprocessing. Another possibility would have been to adapt the auditory-like preprocessing for an optimal compatibility with the classifier, but the biological plausibility would have had to be sacrificed at an early stage of the auditory pathway, which was also the fundamental interest of this research.

The objective of this research was thus restricted to the study and implementation in analogue VLSI of processing performed in the peripheral auditory pathway related to speech feature extraction in adverse conditions. In a parallel thesis [6], some aspects of the neural processing performed in the cochlear nucleus and the inferior colliculus were modeled using analogue VLSI networks of spiking neurones (see also [7]). Since the input of these processing stages originates exclusively from the auditory nerve, an appropriate and compatible analogue VLSI model of the cochlea was necessary, the topic of the present work.

1.2.2 Objectives

Two apparently contradictory objectives are sought in this thesis: a *faithful model* of the cochlea that permits a *simple and efficient implementation* using analogue VLSI techniques.

“Faithfulness” means that the model must capture all the required functionality of the live cochlea, according to its use. Since one of the purposes is to produce an input signal for models of higher levels of auditory processing, potential processing performed at higher levels should not be excluded by the absence of the required functionality at the level of the cochlea.

“Simplicity and efficiency” must permit low-power, low-voltage and real-time operation in a small volume. These requirements are of primordial importance in using the model as a speech processor, either in portable systems or as hearing prostheses. Small integrated area is also required to possibly implement on a single chip a cochlear model together with models

of higher levels of the auditory pathways, avoiding so the need of off-chip communication.

The constant search for an optimal trade-off between faithful modeling and efficient implementation is therefore the guideline of this engineering research thesis.

1.2.3 Contribution

The original contribution of this thesis is summarised in the following points:

- **Active cochlea:** the first analogue VLSI model of an efferent-controlled active cochlea, featuring frequency selective automatic gain control was implemented on silicon. The original contribution of the present work resides in the simple efferent gain control mechanism, which augments an existing analogue VLSI cochlear model.
- **Filtering technique:** the 2-D hydromechanics of the cochlea suggests new temporal filtering techniques based on distributed temporal filters including spatial processing.
- **Pseudo-transcapacitor:** a novel circuit that allows time processing in the log-domain is proposed. It is based on the dynamic translinear principle for CMOS transistors in weak inversion. This pseudo-transcapacitor is general enough to be used as a building block in a collection of reactive components compatible with resistors implemented by a single transistor, bridging the gap between linear spatial processing performed by networks of transistors and linear temporal processing using log-domain filters.
- **Log-domain 2-D cochlea:** the potential of log-domain spatio-temporal processing is exploited in a novel implementation of a 2-D hydrodynamic model of the cochlea, for which the required building blocks are proposed and analysed.

1.2.4 Overview

Chapter 2 summarises the anatomical and physiological properties of the biological cochlea. The basic transduction mechanisms on which most of

the state-of-the-art models rely are explained together with a taxonomy of these models.

Chapter 3 embraces as a whole the design, analysis, and computer simulations of the model of an active cochlea, together with its analogue VLSI implementation from circuit analysis to chip measurements.

In **chapter 4** cochlear modeling is attacked on a different front, which consists of emulating the hydrodynamics equation of the 3-D cochlea as a network of dipoles.

Chapter 5 is split into two main parts. In the first two sections, the basics of linear spatial processing in the log-domain are presented together with a proposal and analysis of a circuit that may be used as a basic block to extend analogue log-domain spatial computation with temporal processing. In a third section, the implementation in the log-domain of the 2-D model of the cochlea is proposed and analysed.

Chapter 6 summarises and discusses the thesis developed in this work. Directions for further research and application in the domains related to this thesis are also proposed.

Chapter 2

The biological cochlea and its models

2.1 Introduction

The cochlea is the organ in the inner ear which transduces the mechanical vibrations induced by the acoustical signal into neural pulses on the auditory nerve. The outer and middle ears transform the raw pressure signal of the outside into a form that can be processed efficiently by the cochlea. The cochlea then transforms the resulting signal into vibrations on an elastic membrane. The transduction gain between input pressure and vibration amplitude at different positions along this membrane depends on different frequency components of the input signal. The resulting mapping from sound frequency to position, called the *tonotopy*, thus originates from the cochlear transduction. Tonotopy is maintained through higher levels of neural processing in the auditory system. This transduction mechanism is still at the heart of current research, because its incredible performance in terms of level sensitivity, dynamic range and frequency selectivity can hardly be explained by simple passive mechanical processes. It is performed by an intricate system that includes the micro-mechanics of a structure much more complicated than a simple elastic membrane. The mechanical properties of the structure are controlled by several layers of feedback loops involving mechanical, chemical and electrical processes. Each section of this structure interacts with the others through a liquid which surround them and whose hydrodynamics play a key role.

Understanding of the cochlear mechanisms is made more difficult because of the role of active processes present only in live cochleae. These make the performance of the cochlea very sensitive to aggressive investigation techniques. Modeling has become a key investigative tool. Research is done in an iterative loop where models are refined as the understanding of the biological system progresses (and as computational resources allow), and the findings obtained using these models suggest new biological experiments. In addition, cochlear models may also be used to generate the appropriate input signals for models of auditory processing at higher levels and for systems that require a cochlear-like preprocessing (e.g. auditory-based automatic speech recognition systems). Finally, cochlear models may find a stand-alone application in cochlear implants or hearing aids.

In section 2.2, the present anatomical and physiological knowledge on the cochlea is summarised, preceded by a brief description of the outer and middle ears. When not cited explicitly, information given in this

section is drawn from [8, 9, 10, 11]. After a description of the transduction mechanisms hypothesised to date, section 2.3 then reviews, discusses and classifies some existing models and their implementations.

2.2 Anatomy and physiology

2.2.1 Outer and middle ear

The outer ear concentrates acoustical pressure on the *tympanic membrane* (eardrum) on which the middle ear's *ossicular chain* is attached. The ossicular chain is made from three ossicles, the *malleus* (hammer), the *incus* (anvil) and the *stapes* (stirrup). Transduction performed by the cochlea relies on a pressure difference between its two openings. The purpose of the ossicular chain is to generate this pressure difference: it performs an acoustic impedance adaptation which increases the pressure to one cochlear opening, the *oval window*, whereas the second one, the *round window* opens directly to the atmospheric pressure through the *eustachian tube* (see figure 2.1a). This impedance adaptation is performed by the system of levers formed by the ossicles. The amplitude of the input pressure at the oval window is also increased by the large area ratio between the tympanic membrane and the oval window.

Except for the slow active control performed by contracting the ligaments attaching the stapes to protect the ear at very high sound levels, the transduction chain from outside pressure to oval window pressure is mainly passive and linear. Its gain is frequency-dependent, with a broad peak at 30 dB around 1 kHz. Direction-sensitive filtering performed by the *pinna* (visible part of the ear), might be used as a cue for sound localisation.

2.2.2 Anatomy of the cochlea

The cochlea is a coiled bony duct filled with a liquid. Its length is about 30 mm, coiled in 3.5 turns (figure 2.1a,b). It is divided into three chambers, the *scala vestibuli*, the *scala media* and the *scala tympani*. These chambers run along the cochlea (x-axis in figure 2.1c) from its *base* (entrance of the coil) to its *apex* (dead end of the coil). The *scala media*, as its name suggests, is located between the two other *scalae*. It is separated from the *scala vestibuli* by the *Reissner's membrane* and from the *scala tympani* by the *cochlear partition*. The *scala vestibuli* communicates with the *scala*

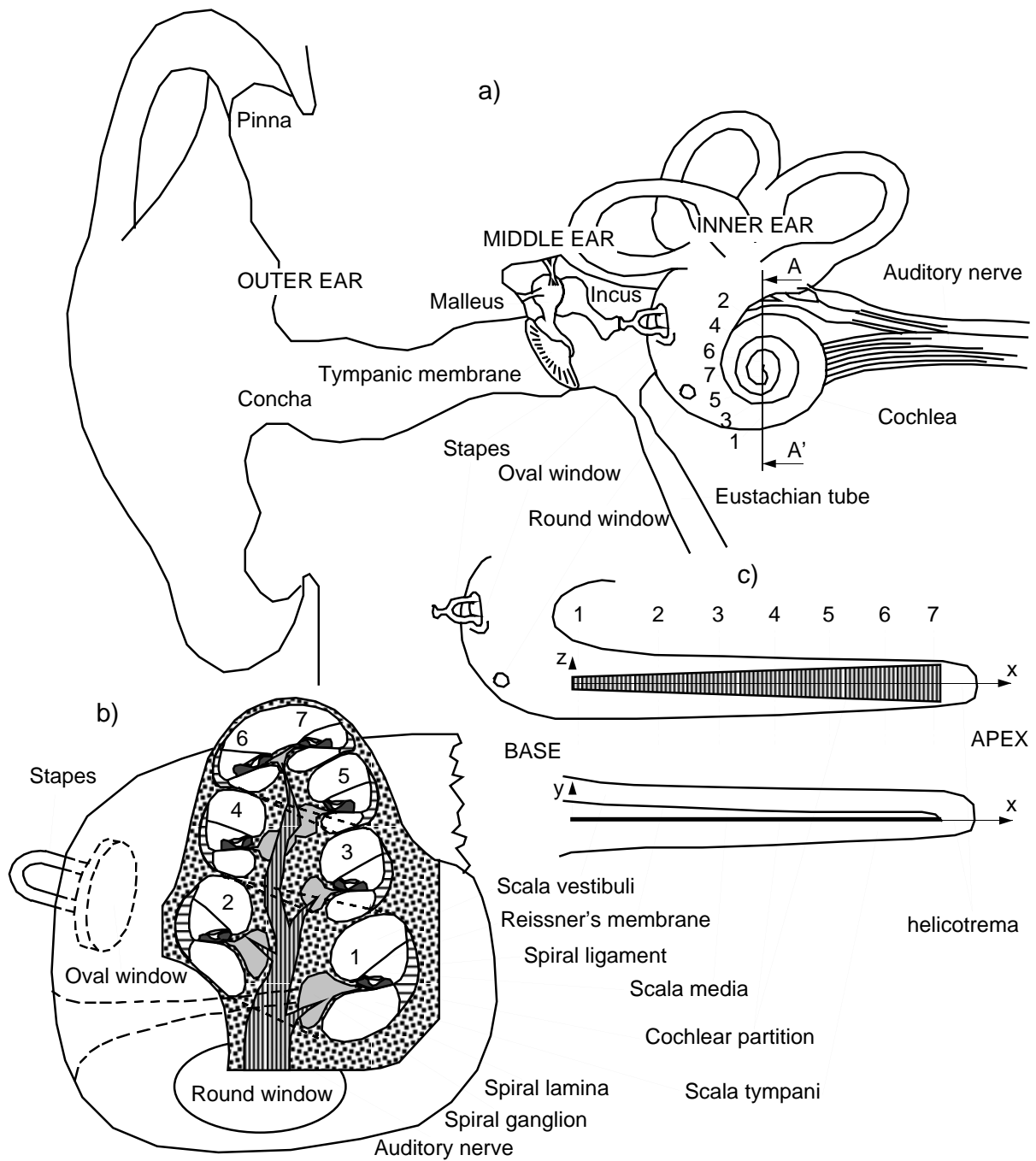


Figure 2.1: a) Anatomy of the peripheral auditory system; b) cross-section A-A' of the cochlea in a); c) schematic views of an uncoiled cochlea.

tympani through an opening in the cochlear partition at the apex of the cochlea, the *helicotrema*. Its purpose is to equalise the static pressure between the two chambers. The oval window is located 1-2 mm before the base on the outer wall of the scala vestibuli; the round window opens

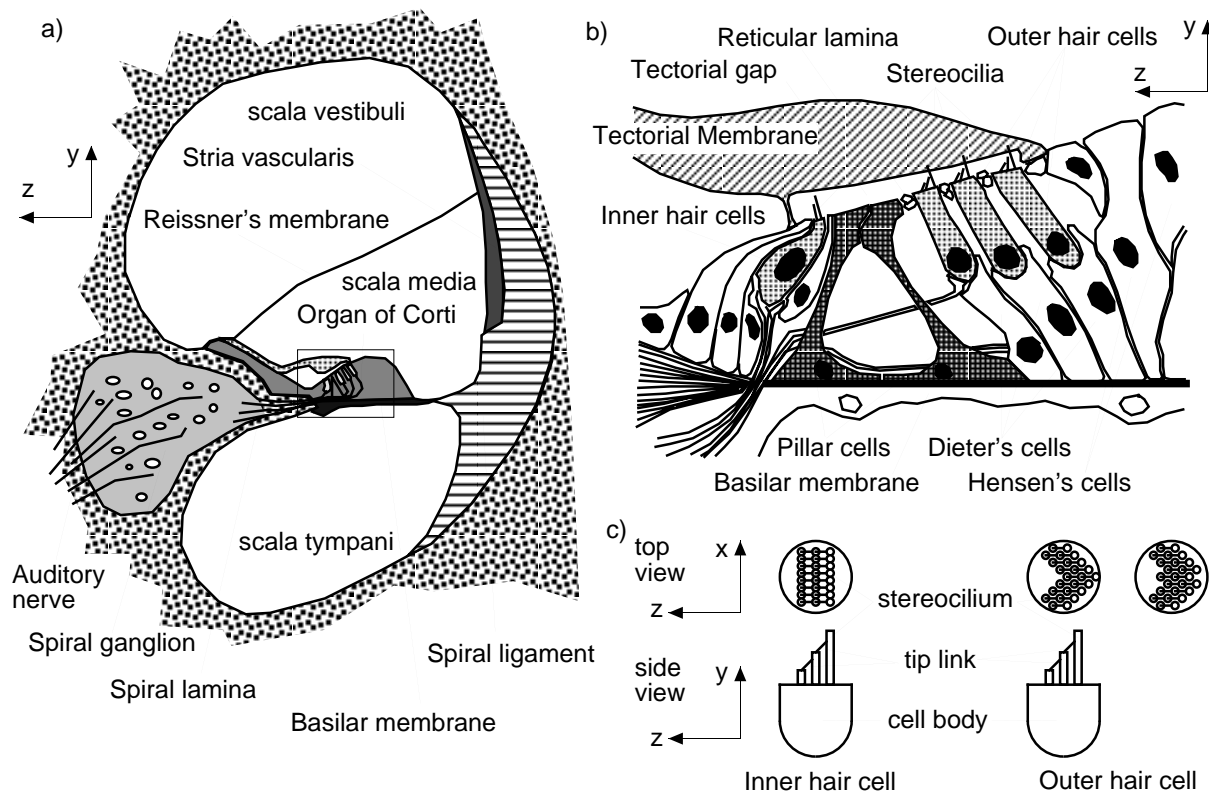


Figure 2.2: a) Cross-section of the cochlear duct; b) detail of the organ of Corti; c) schematic view of the hair cells

through a compliant membrane to the middle ear cavity on the basal-most 5%-10% of the outer wall of the scala tympani.

The *scala vestibuli* and *tympani* are both filled with the same fluid, the *perilymph*, whereas the *scala media* is filled with a different one, the *endolymph*. The electrical potential in the endolymph (*endocochlear potential*) is 90 mV higher than in the perilymph. This electrical potential difference is supplied by ionic pumps located in the *stria vascularis* covering the outer wall of the *scala media*. The Reissner's membrane has a negligible influence on the hydromechanics of the cochlea. All the mechanical properties on which the cochlear transduction rely are concentrated in the cochlear partition, which is made of the elastic *basilar membrane* on which sits the *organ of Corti* (figure 2.2a).

The inner edge of the basilar membrane is attached to a helicoidal bony shelf, the *spiral lamina*, whereas its outer edge is attached to the bony wall of the cochlea by mean of the *spiral ligament* which is a specialised tissue able to maintain the basilar membrane under radial tension (*z*-axis). This

radial tension is such that the stiffness of the basilar membrane decreases approximately exponentially from the base to the apex. Basilar membrane stiffness is the dominant parameter determining the position dependent *characteristic frequency* at which the cochlea vibrates best. The width (z-axis) of the basilar membrane increases almost linearly from $100\mu\text{m}$ at the base to $400\mu\text{m}$ at the apex. The organ of Corti is built around a rigid framework made from two rows of *pillar cells*, whose feet are anchored on the basilar membrane and whose tops support a plate like structure, the *reticular lamina*. This framework is arranged so that when the inner side of the basilar membrane pivots around its attachment to the spiral lamina, the reticular lamina follows this rotational movement. The basilar membrane movement is detected and amplified by the *hair cells* embedded in the reticular lamina (figure 2.2b).

On the inner side of the reticular lamina (relative to its attachment to the pillar cells), a single row of *inner hair cells* runs along the cochlea, whereas the *outer hair cells* are arranged into three parallel rows on the outer side of the reticular lamina. The hairs, or *stereocilia*, of the hair cells protrude from the reticular lamina. The stereocilia of a single hair cell are arranged in parallel rows (V- or W-shaped for the outer hair cells, see top view of figure 2.2c), following the longitudinal dimension of the cochlea (x-axis). The stereocilia in each row are of the same height. This height increases from row to row in the radial direction (z-axis) toward the outer wall of the cochlea. The top of each stereocilium (except in the tallest row) is attached to its neighbouring stereocilium in the next taller row by a *tip link* which is stretched when the hair bundle bends toward the outer wall of the cochlea (side view of figure 2.2c). The stereocilia of the inner hair cells float in the endolymph, whereas the tallest stereocilia of each outer hair cell is attached to the *tectorial membrane*, a gelatinous structure covering the reticular lamina all along the length of the cochlea. The narrow space left between the reticular lamina and the tectorial membrane is called the *tectorial gap*.

2.2.3 Innervation

All the nervous connexion of the cochlea are bundled together in the auditory nerve. About 95% of the afferences (toward the brain) innervate the inner hair cells. They are made from type-I neurones whose large cell bodies are located in the *spiral ganglion* and that synapse onto the inner

hair cell bodies. Each hair cell is innervated by 10-30 such afferent fibres, each of which originates from a single type I neurone. The remaining 5% of the afferences innervate the outer hair cells via type II neurones having a smaller cell body than type I neurones. Each outer hair cell is connected to about 5-15 afferent fibres, which implies considerable branching. The outer hair cell innervation path is different from that of the inner hair cells: the latter project radially directly to the inner hair cell bodies, while the former turns basally after a similar radial projection and follows the cochlear spiral for about 0.6 mm before synapsing on the outer hair cells. At the output of the cochlea, afferences from inner hair cells are thus topologically paired with afferences from outer hair cells sensitive to a higher characteristic frequency (see figure 2.3).

As for the efferences (from the brain), the organ of Corti receives an innervation from the superior olivary complex. The *lateral olivocochlear system* innervates the afferent fibres of the inner hair cells and the *medial olivocochlear system* projects to the outer hair cells. Very little is known about the inner hair cells' efferences, whereas the efferences of the outer hair cells are believed to control the transduction mechanism of the

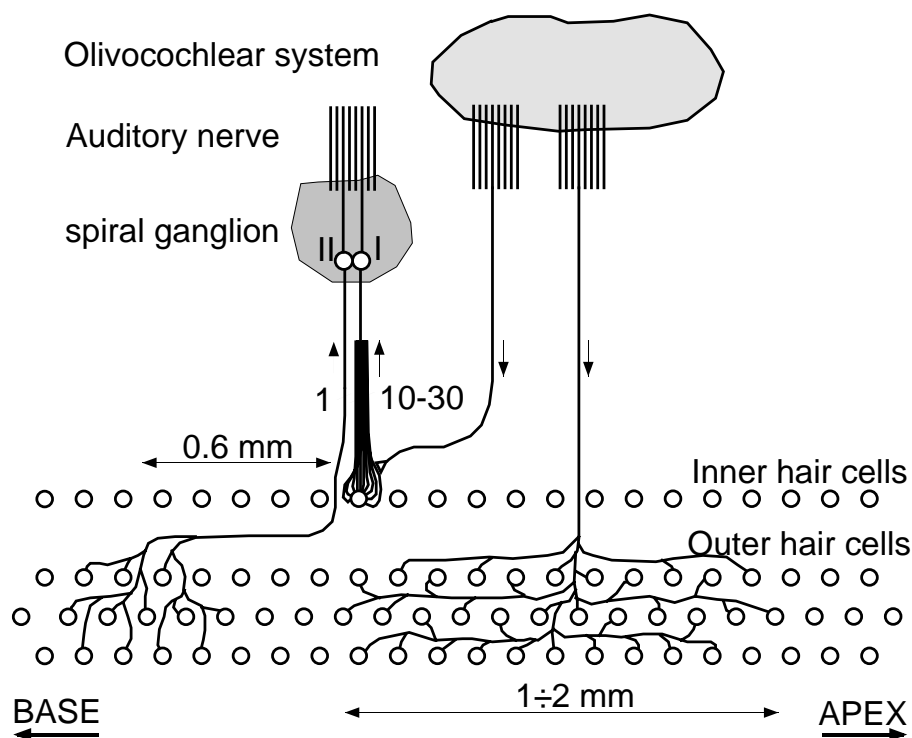


Figure 2.3: Innervation of the cochlea's hair cells

cochlea by means of the motile properties of the outer hair cells (see paragraph 2.2.4). The medial olivocochlear fibres branch to innervate outer hair cells spanning 1-2 mm along the cochlea.

2.2.4 Hair cell physiology

As mentioned in paragraph 2.2.2, the hair cells are embedded in the reticular lamina, with their bodies on the basilar membrane side of the reticular lamina and their stereocilia emerging in the tectorial gap. Because the basilar membrane is quite permeable to ions whereas the reticular lamina is not, the hair cell's body is in the perilymph-like medium and its stereocilia in an endolymph-like liquid having a 90mV higher electrical potential. As a consequence, ionic current can penetrate the body of the hair cells through ionic channels situated on the hair cell's surface in contact with the endolymph. The conductance of these channels is controlled by the bending of the stereocilia and the subsequent tension in their tip links (paragraph 2.2.2). The accumulation of ions in the cell body increases its intracellular potential. Due to the asymmetric structure of the hair bundle, the transfer function between hair bundle deflection and intracellular potential is asymmetric.

In turn, the hair cell intracellular potential controls the spike generation of the auditory nerve neurones through the synaptic connection which links them. When the hair cell's intracellular potential increases, its membrane depolarises and neurotransmitters are released in these synapses. This process is based on several pools where vesicles are filled with neurotransmitter, stored and transmitted to the afferent neurone.

In addition to the stereocilia-driven ionic channels, the inside of the hair cell's body is connected to its surrounding medium by voltage-driven conductances and chemically driven conductances (called "ligand-gated conductances"). The latter are present only in outer hair cells and are associated with their efferent synapses. The variation speed of the hair cell's intracellular potential depends on the dynamics of its ionic channels. The efferent-controlled variations of the intracellular potential are quite slow (100 ms time constant), whereas the stereocilia-controlled variations are usually assumed to be limited by the membrane capacitance of the cell, according to a first-order low-pass filtering having a cutoff frequency at about 1kHz.

In addition, the outer hair cells possess electro-motile properties. When

a cell's membrane potential increases, its body shortens. The length can change by up to $2\mu\text{m}$ for a membrane potential varying over 200mV. This motility was shown to be fast enough to vibrate at frequencies up to 25kHz [12].

2.2.5 Measurements of basilar membrane vibrations

The transduction performed by the basilar membrane has been shown only recently to feature almost all the characteristics measured at the level of the auditory nerve. This performance can be observed only in live and healthy cochleae. It is measured on animals under anaesthesia, usually in the basal region of the cochlear duct, which is the most accessible. Figure 2.4a shows the rms velocity in the y-direction of the basilar membrane for different input sound levels (in dB SPL, i.e. referred to $20\mu\text{Pa}$) measured on a live chinchilla (an exceptionally sensitive one, according to the author [13]). At low input pressure levels the transduction gain is very large and highly frequency-selective. As the input level increases, this gain diminishes and its frequency selectivity broadens around a peak at a slightly lower frequency (figure 2.4b). This proves that a frequency-selective level compression —from an 80dB input dynamic range into an output dynamic range down to 20dB (figure 2.4c)— is already performed at the level of the cochlear mechanics. This compressive non-linearity, as well as the high sensitivity and selectivity, are shown to be very physiologically vulnerable. When the responsiveness of the outer hair cells is inhibited (by poisoning or electrical dc stimulation), the transduction gain is brought back to the linear, much less selective and sensitive one measured in dead cochleae. Together with other experimental evidence, such as acoustic emissions by the cochlea [14], motility of the outer hair cells [15], electrically induced basilar membrane movement [16] or two-tone suppression measured on the basilar membrane [17], this suggests strongly an active non-linear process performed by the outer hair cells [18].

2.3 Mechanisms and models

2.3.1 Transduction mechanism

Both perilymph and endolymph are usually assumed incompressible. The pressure variations induced by the stapes' movement are thus applied al-

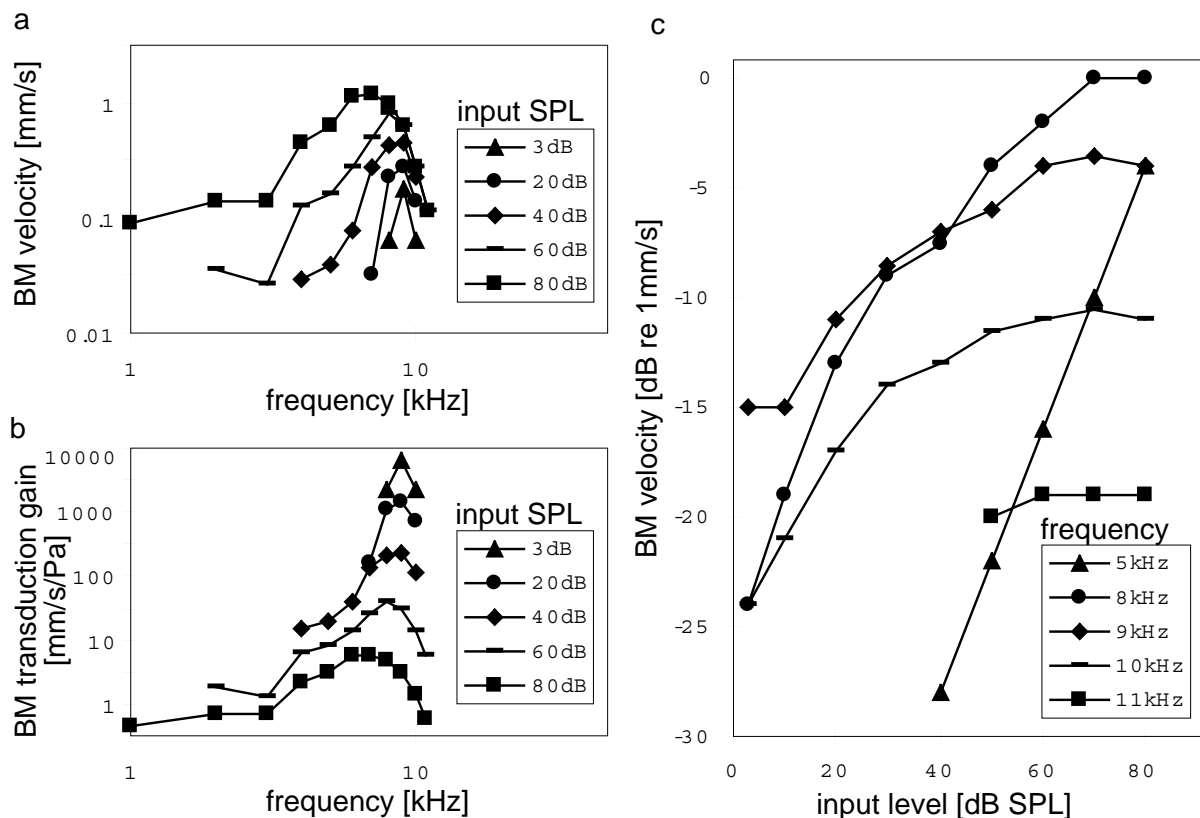


Figure 2.4: Measurement results (redrawn from [13]) of basilar membrane velocity for different input pressure level (a), resulting transduction gain (b) and frequency-dependent compressive input-output transfer function (c).

most instantaneously across the cochlear partition along its full length. The mechanical properties of the cochlear partition, together with the interaction with the liquid, yield a wave of vertical displacement of the partition that travels from the base to the apex. This *travelling wave* would exist even if each segment of cochlear partition was separated from the next (like piano strings), as is often assumed to simplify the models, because the energy is transmitted between segments through the liquid. The propagation of this wave is mainly governed by the compliance of the cochlear partition and the mass of the liquid (while the mass and the viscosity of the partition has an effect on the finer detail of this propagation).

At each position, the volume velocity of the liquid is determined by the local acoustic impedance, which makes it proportional to pressure gradient. The perpendicular and longitudinal impedances define the components of the volume velocities perpendicular (y -axis) and parallel (x -axis),

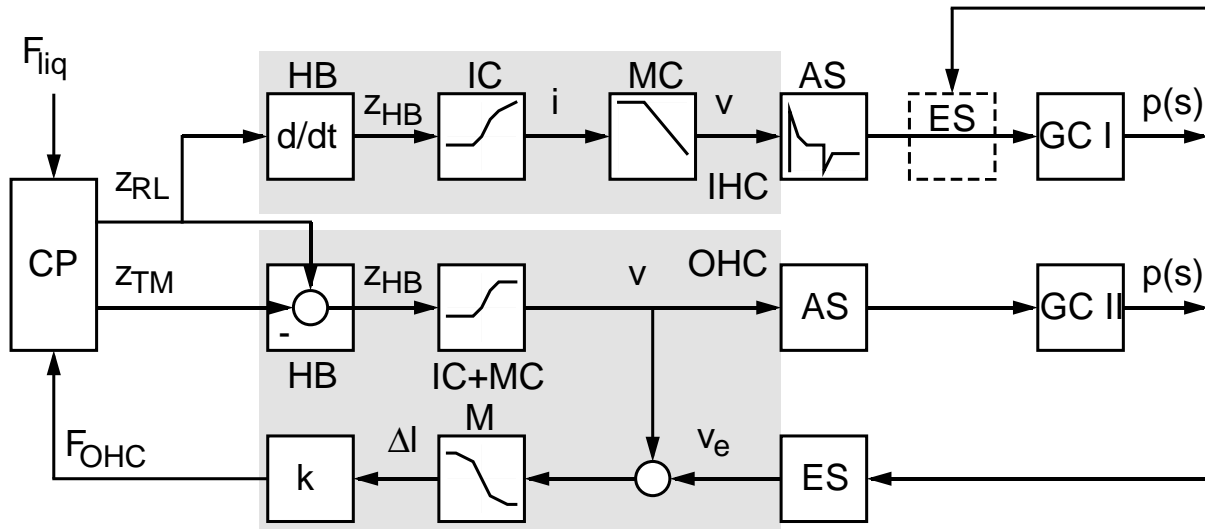


Figure 2.5: Transduction chain from cochlear liquid force to auditory nerve spikes.

respectively, to the cochlear partition. This directional impedance is also frequency-dependent. At a given frequency, the perpendicular impedance has a minimal value which corresponds to the resonance of the cochlear partition. It is dominated by the partition stiffness basally from the resonant position and by the partition mass and the vertical liquid load apically. In the longitudinal direction, however, the impedance is only mass-dominated by the longitudinal liquid load. If the perpendicular impedance were perfectly resonant, it would act as a hole in the partition at its resonance frequency: all the liquid flow would virtually cross it at this position, leaving the liquid immobile apically. Since in reality the partition is damped, a fraction of the longitudinal velocity survives after the resonant point, where the perpendicular impedance is mass-dominated. The cutoff of the travelling wave is therefore determined by the ratio of the cochlear partition's mass and the liquid load at this position. The volume velocity perpendicular to the cochlear partition corresponds to its vertical movement (y -axis), induced by the pressure difference across the partition. This movement is sensed and amplified by the hair cells, as depicted schematically in figure 2.5.

The force F_{liq} resulting from the pressure difference across the cochlear partition (CP) produces the up-and-down movement of the basilar membrane which is transmitted to the reticular lamina by the rigid pillar cell. The bodies of the hair cells, embedded in the reticular lamina, thus move

laterally. This lateral movement z_{RL} induces the bending z_{HB} of the inner hair cells' stereocilia, dragged by the reticular lamina in the liquid in which they float. The displacement of the hair bundle (HB) is thus proportional to the velocity of the reticular lamina. The tip links joining neighbouring stereocilia are stretched and released according to the movement of the hair bundle, opening and closing ionic channels (IC) of the cells. The resulting modulation of the ionic current i penetrating the cell body causes its intracellular potential v to follow the movement of their hair bundle, with a time constant that depends on the membrane capacitance (MC) of the cell. Due to the asymmetric mechano-electrical transfer function of the hair cells [19], the intracellular potential is roughly proportional to the half-wave rectified hair bundle displacement at low frequency. Finally, the dynamics of the vesicle pools in the afferent synapses (AS) of the hair cells result in a spiking probability $p(s)$ of the afferent ganglion cells (GC) that is proportional to the intracellular potential of the hair cell. In addition, the dynamics of the synaptic transduction yield an adaptation mechanism which enhances the auditory nerve response at the onset of an excitation [20]. The efferent synapses (ES) on the inner hair cells are represented in figure 2.5, but their function has not yet been identified to date.

The transduction chain for the outer hair cells is roughly similar. In addition two fundamental features are responsible for the active control of the cochlear mechanics: the motile properties of the outer hair cell body and the attachment of its tallest stereocilia to the tectorial membrane. The former allows the outer hair cell to feed energy back to the mechanical structure through the latter. The outer hair cells shorten under the influence of an internal force $F_{OHC} = k\Delta l$ when their intracellular potential v increases [15]. This force F_{OHC} is therefore caused by the displacement of the cell's hair bundle (HB), which corresponds to the relative displacement $Z_{RL} - Z_{TM}$ between the reticular lamina and the tectorial membrane, where the cell's tallest stereocilia are attached. The force F_{OHC} is thus applied within the cochlear partition, whose articulated framework's structure transforms it into an internal rotational force which adds to the force F_{liq} induced by liquid pressure. This feedback loop is not yet fully understood because it involves the dynamics of the entire microstructure of the cochlear partition (CP) together with that of the outer hair cell's motile transduction (M, k). The effect of the outer hair cell's force F_{OHC} on the partition's mechanical properties depends on its phase relation with the liquid force F_{liq} . It is usually assumed that the coupling

of partition's resonant structures by outer hair cells applying their force with the appropriate delays yields an undamping of the cochlear partition [21, 15, 22, 23, 24].

It is hypothesised that the efferences of the outer hair cells control this undamping using the non-linearity of the transduction M from intracellular potential v to hair cell's length variations Δl [15]. A dc, or slowly varying, intracellular potential offset might be adjusted by the outer hair cell's efference through its synapses (ES). This dc intracellular potential v_e determines the operating point on the non-linear transduction curve M , so controlling the linear motility gain for small ac signals [18]. *In vitro* measurements of guinea-pig outer hair cells showed that their motility is fast enough theoretically to amplify ac signals up to 25kHz [12], confirming the plausibility for the outer hair cells to act as a "cochlear amplifier".

2.3.2 Models

There are two major goals in modeling the biological cochlea: understanding it and emulating it. The former requires *structural models* that capture and explain the functions performed by the real structure of the biological cochlea, whereas the latter only needs *functional models* that are able to perform these functions efficiently. Structural models rely on the biological knowledge provided by anatomical dissections and physiological experiments of every constituting part of the cochlea, whereas functional models are intended to replicate the behaviour of the cochlea. The purpose of emulating the cochlea is to replace it in larger systems where real-time is often required. As a consequence, structural models are much more complicated than functional models. Of course, a structural model becomes more convenient when simplifying assumptions make it work faster enough, and a functional model will better reproduce the required behaviour if it is based on the real structure of the cochlea. The border between structural and functional models is thus not well defined.

Structural models

Structural models implement the cochlear mechanisms as described in paragraph 2.3.1, in which several unknowns still remain. The hydrodynamics in the 3-D structure of the cochlea can be simplified into 1-D or 2-D descriptions. As suggested by the description of the hydrodynamics using longitudinal and perpendicular acoustic impedance, a 2-D model

seems most appropriate. The calculation of the 3-D hydrodynamics is too difficult to implement efficiently when compared with the refinement it adds to the models. 1-D hydrodynamical models follow the longitudinal (x-) axis of the cochlea; they do not take into account the vertical liquid movement near the resonant position of the cochlear partition, which is very relevant for the shape of the frequency response in its peak and cutoff slope [25]. Alternatively, geometry-dependent parameters of the 3-D hydrodynamics can be estimated separately and lumped into a kernel depending only on the longitudinal dimension [24].

The continuous hydrodynamics of the cochlea are advantageously described by a spatially quantised network of acoustical impedance, which can be solved numerically [26] or emulated using analogue electrical dipoles [27]. In such *macro-mechanical models*, the cochlear partition is described by a parallel bank of impedances. As the understanding of the micro-mechanics of the organ of Corti progresses, the principal effort focuses on *micro-mechanical models* of the cochlear partition impedance, which has been shown to be active and nonlinear and which is now accepted to explain much of the performance of cochlear transduction.

As presented in paragraph 2.3.1, the framework of the cochlear partition mechanisms is understood, but several unknowns remain in the micro-mechanics as well as in the dynamics of the motile outer hair cell's feedback loop. In macro-mechanical model, the cochlear partition is simply described by a serial mass-dashpot-spring system (L-R-C in its electrical analogue), whose damping can be non-linear, active (negative damping), and/or controlled by higher level of neural processing. On the contrary, micro-mechanical models attempt to describe the dynamics of the micro-structure of the organ of Corti with various levels of refinements (see [9] for a review).

Functional models

Functional models (called “signal processing models” in [9]) lump all the parameters of the structural models into a transfer function between the input pressure signal and the cochlear output required by the use of the model. In some cases, internal variables in the implementation of the transfer function can be identified as internal variables of the structural model [28], which illustrates the fuzziness of the limit between functional and structural modeling. Some other models, like the widely used “gam-

matone filter”, are derived from the impulse response measured on the auditory nerve fibres [29, 30].

Functional models can roughly be split into *parallel* and *cascade* structures, with an intermediate class of cascade-parallel structure. A parallel structure consists of a bank of filters having a common input and several output channels with frequency responses that reproduce those measured in the cochlea [30] or obtained from psychoacoustic experiments [31]. The propagation of the travelling wave is mimicked by a growing time constant in a bank of filters having characteristic frequencies that decrease in the direction of the propagation. It might be thought that a cascade structure would better reproduce this propagation, but in this case the propagation delay would depend on the spatial resolution of the cascade [32]. In the cascade-parallel structure, the wave propagation is supported by a filter cascade whereas the fine detail of the frequency responses is adjusted by a parallel bank of filters whose inputs are picked along the cascade [33].

Implementation

With the computational power available nowadays, most of the models are implemented on computers, digital signal processors or dedicated digital filter circuits which permit fast design and flexible use by a large community of researcher. However, analogue emulation of cochlear dynamics is also investigated on alternative media, including electronic VLSI circuits (with which the present work deals) [34, 35, 27, 33, 36, 37, 38] or even micro-machined electro-mechanical systems [39]. The expected advantage of the analogue VLSI approach is the possibility of emulating cochlear functions in real-time on a tiny device with low power consumption, for applications where these issues are of highest priority such as portable auditory-like speech processors [40], hearing aids or cochlear implants.

Chapter 3

Analogue VLSI model of the active cochlea

3.1 Overview

An analogue VLSI model of an active cochlea is proposed, whose key feature is a frequency selective automatic gain control mechanism. This model is based on Lyon and Mead's cochlear filter cascade structure [34] and its most recent improvement [37]. In section 3.2, the model is carefully analysed. After a brief description of the functions required to model a single section of the cochlea, its analogue VLSI implementation is outlined in order to estimate its crucial parameters. This analysis shows that an individual cochlear filter could not support the quality factor required to match the physiological data measured on biological cochleae. The pseudo-resonance, which yields frequency selective high gains despite limited quality factors in the individual stages is then presented and analysed in order to design an appropriate pseudo-resonant gain control loop. In section 3.3, experiments performed by a computer model of the entire cochlea on synthetic and natural speech signal demonstrate the validity of the concept. Section 3.4 proposes the analogue building blocks required for a VLSI implementation of the model, while the effect of the major technological limitations of a standard CMOS process are discussed together with chip measurements results. The fundamental advantages and drawbacks of the filter cascade structure are finally discussed in section 3.5.

3.2 The model

3.2.1 Functional model

The cochlea is modeled by a cascade structure where each stage emulates the wave propagation along the basilar membrane in a section of the cochlea [41]. As a functional model, the transfer function of each stage k can be emulated by a second-order low-pass filter

$$H_k(s) = \frac{1}{s^2\tau_k^2 + s\tau_k/Q_k + 1}, \quad (3.1)$$

where the characteristic frequency and the resonant property of the cochlea at the corresponding position are characterised by the filter's cutoff frequency $f_{ck} = 1/2\pi\tau_k$ and quality factor Q_k , respectively [34, 35, 37].

As a structural model, each stage can be interpreted as a section of the cochlea as shown in figure 3.1. The second-order low-pass filter models the

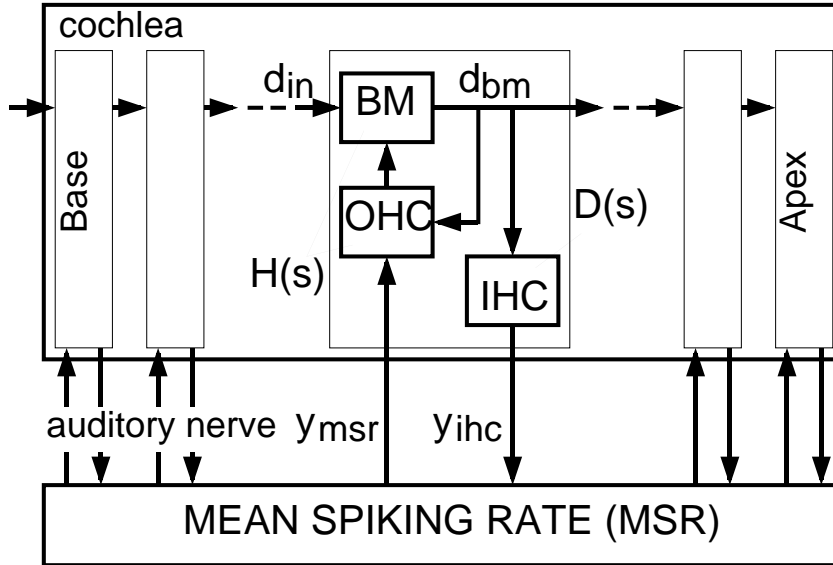


Figure 3.1: Active cochlear filter cascade, with functional block diagram detailed for one stage.

basilar membrane (BM) whose damping is actively controlled by the outer hair cells' motile properties (OHC). The input and output signal of the filter models the local basilar membrane displacement d_{bm} that propagates from the base (first stage) toward the apex (last stage) of the cascade.

Because the inner hair cells' stereocilia are in a viscous medium, they detect the velocity of the basilar membrane movement relative to its supporting structure. The inner hair cell model (IHC) thus includes a scaled differentiator

$$D_k(s) = s\tau_k \quad (3.2)$$

that converts the basilar membrane displacement d_{bm} into basilar membrane velocity v_{bm} [35, 37]. In addition, the transmitter release in the inner hair cells' afferent synapses happens only when its stereocilia bend in one direction. The inner hair cells perform therefore to a first approximation a half-wave rectification of the basilar membrane velocity signal v_{bm} , yielding the inner hair cell output y_{ihc} . In this first approach, the temporal adaptation of the transmitter release [20] was neglected, assuming for simplicity the effect of the outer hair cells' active process to be dominant for temporal adaptation and transient enhancement.

It is reasonable to assume that, in the auditory pathway, the mean value of the basilar membrane velocity V_{bm} can be estimated at a higher level as a *mean spiking rate* (MSR) on the afferent nerve fibres projected

from the inner hair cells at the corresponding basilar membrane position. As the dynamics of transmitter release has been neglected, the instantaneous spiking rate (or spiking probability) is roughly proportional to the inner hair cell output y_{ihc} , thus a measure of the mean basilar membrane velocity $y_{msr} \propto V_{bm}$ may be available at the outer hair cells' efferent nerve fibres [42].

The adaptive loop is closed by controlling the quality factor of the basilar membrane, assumed to be the action of the outer hair cells (OHC), using an appropriate quality factor modulation by this measure y_{msr} of the mean basilar membrane velocity.

3.2.2 Quality factor modulation

The effect of the outer hair cells is modeled by controlling the quality factor Q_k of each stage $H_k(s)$. On a single stage $H(s)D(s)$, a sine wave input signal at frequency f and with a peak amplitude X produces an output signal having a peak amplitude $Y = \|H(f)D(f)\|X$. At a frequency f close to the characteristic frequency of the stage, the amplitude gain $\|H(f)D(f)\| \approx Q$, thus the output signal has a peak amplitude $Y \approx QX$. Modulating the quality factor with a power λ of the peak output amplitude Y ,

$$Q \propto Y^\lambda, \quad (3.3)$$

yields

$$Y \propto X^{\frac{1}{1-\lambda}}, \quad (3.4)$$

where $\lambda < 0$ produces the desired compressive input-output function.

3.2.3 Analogue model

The analogue VLSI implementation of the active cochlea is depicted in figure 3.2. In the analogue model proposed in [34, 35, 37], the cutoff frequency $f_{ck} = 1/2\pi\tau_k$ of a second-order stage H_k is determined by $\tau_k = C_\tau/g_{m\tau k}$. The capacitances C_τ of the BM block are identical for every stage and the transconductances $g_{m\tau k}$ of its operational transconductance amplifiers (OTAs) are controlled by the bias currents $I_{\tau k}$. The quality factor Q_k of any stage k is controlled by the ratio between the transconductances g_{mQk} and $g_{m\tau k}$ of its OHC OTA and its BM OTAs, respectively. As the

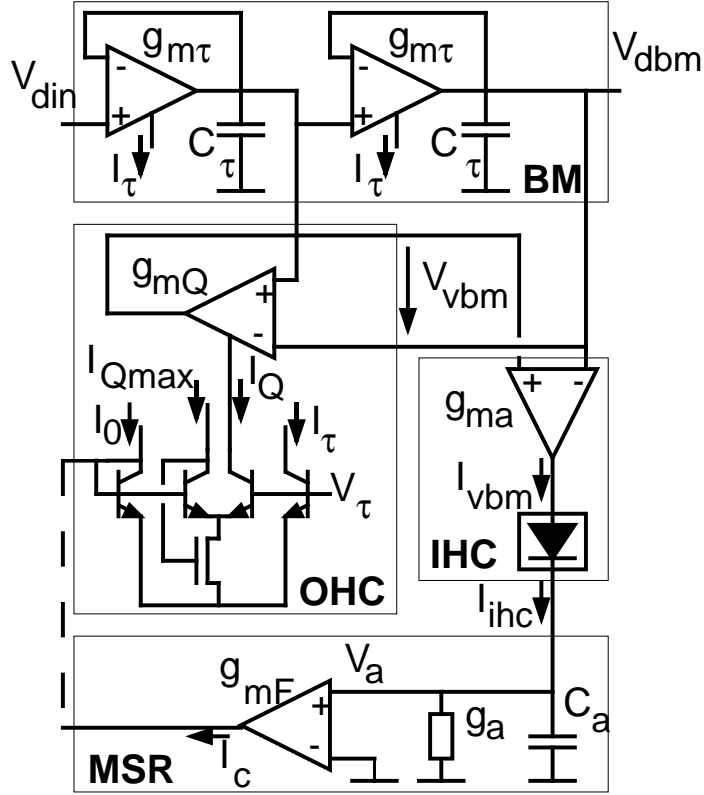


Figure 3.2: Analogue model of one stage of the active cochlear filter cascade.

differential pair of all OTAs operates in weak inversion, their transconductance $g_{m\tau,Q}$ is proportional to their bias current $I_{\tau,Q}$. The quality factor is given by

$$Q = \frac{1}{2(1 - \alpha \frac{I_Q}{I_\tau})}, \quad (3.5)$$

where

$$\alpha = \frac{g_{mQ}}{2I_Q} \frac{I_\tau}{g_{m\tau}} \quad (3.6)$$

is a constant.

A quality factor varying between Q_{min} and Q_{max} can thus be controlled by means of a translinear loop which imposes

$$\frac{I_Q}{I_\tau} = \frac{I_{Qmax}}{I_c + I_0}. \quad (3.7)$$

Using normalised currents $i_c = I_c/I_0$ and $i_{Qmax} = I_{Qmax}/I_0$, equa-

tion (3.5) can be expressed as

$$Q = \frac{1}{2} \left[1 + \frac{2Q_{max} - 1}{2Q_{max}i_c + 1} \right], \quad (3.8)$$

where

$$Q_{max} = \frac{1}{2(1 - \alpha i_{Q_{max}})} \quad (3.9)$$

is obtained for $i_c = 0$ and Q_{min} depends on the maximal available value of i_c .

The *quality factor control signal* i_c is made proportional to the peak amplitude \hat{V}_{vbm} of the basilar membrane velocity analogue signal,

$$i_c = F\hat{V}_{vbm}, \quad (3.10)$$

by the *feedback gain*

$$F = \frac{g_{ma}A_r g_{mF}}{g_a I_0}, \quad (3.11)$$

which takes into account the transconductance g_{ma} of the IHC OTA, the IHC rectifier gain A_r between the dc component of the rectified basilar membrane velocity signal and its peak amplitude \hat{V}_{vbm} , the dc gain g_{mF}/g_a of the MSR low-pass filter which extracts this dc component and the normalising current I_0 .

The peak basilar membrane velocity \hat{V}_{vbm} is given by the amplitude gain of the BM stage $\|H(f)\|$ and its differentiator $\|D(f)\|$, for an input signal at frequency f having a peak amplitude \hat{V}_{din} :

$$\hat{V}_{vbm} = \|H(f)D(f)\|\hat{V}_{din}. \quad (3.12)$$

The differentiation $D(s) = s\tau$ is simply performed by taking the difference between the output voltages of the two BM OTAs [37], which yields a second-order band-pass transfer function

$$H(s)D(s) = \frac{s\tau}{s^2\tau^2 + s\tau/Q + 1}. \quad (3.13)$$

3.2.4 Level compression

Except for the shift of variable limiting the quality factor between Q_{min} and Q_{max} , with i_c proportional to the peak amplitude \hat{V}_{vbm} of the output

signal after stage $H(s)D(s)$, equation (3.8) respects the form of equation (3.3) with $\lambda = -1$. The required compressive input-output relation expressed by equation (3.4) is thus obtained and the output peak amplitude \hat{V}_{vbm} is proportional to the square root of the input peak amplitude \hat{V}_{din} .

The limited quality factor range implies that the square root compression is performed only on a limited input dynamic range. Under the same assumption as in section 3.2.2, equations (3.8), (3.10), and (3.12) yield

$$Y = \frac{X - 1 + \sqrt{(1 - X)^2 + 8Q_{max}X}}{4}, \quad (3.14)$$

where $X = Q_{max}F\hat{V}_{din}$ and $Y = Q_{max}F\hat{V}_{vbm}$. This function has an asymptote $\lim_{X \rightarrow \infty} Y = X/2$ and a slope Q_{max} at the origin $X = 0$. The square root compression is thus active between the corresponding gains $Y/X = 1/2$ and $Y/X = Q_{max}$. According to physiological data [43], an input sound level of 60 dB SPL corresponds to 1 nm basilar membrane displacement at frequencies below the characteristic frequency of the measured basilar membrane position, thus where $\|H_k\| \approx 1$ according to the model. On the other hand, at frequencies close to the characteristic frequency, the amplitude of the basilar membrane displacement divided by the filter's time constant equals the amplitude of the basilar membrane velocity since $\|D_k\| \approx 1$. A good correspondence between the physiological data [43] and equation (3.14) can be obtained for a peak basilar membrane displacement lower than 10 nm (figure 3.3). At higher intensity values, a saturation that does not stem from the quality factor control loop appears. This saturation will correspond to the saturation of the physical devices used for the VLSI implementation of the model. At lower intensities, the model fits the physiological data with a maximal quality factor $Q_{max} \approx 180$, allowing an amplitude gain up to 45dB at characteristic frequency for low input level.

3.2.5 Pseudo-resonance

The quality factor required to match physiological data cannot be safely implemented on a single analogue second-order filter, because the mismatch of its internal components are likely to drive it into instability. Nevertheless, amplitude gains corresponding to such a high quality factor

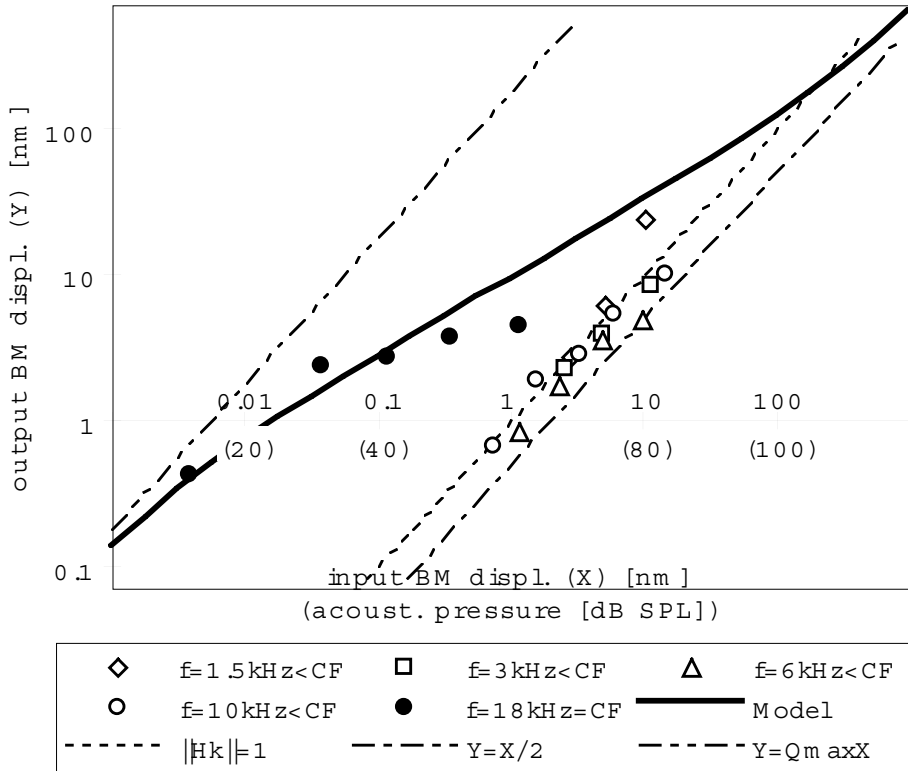


Figure 3.3: Compression curves; the boldface curve plots equation (3.14) for a quality factor $Q = 180$; physiological data [43] are given as function of input acoustic pressure relative to $20 \mu\text{Pa}$ (dB SPL).

can be achieved using the *pseudo-resonance* of the cochlear filter cascade. The control is made locally at every cascade stage in a narrow range of quality factors (between $1/\sqrt{2}$ and 2), but the accumulation of these effects along the cascade can yield gains up to 45dB for low intensity input levels. The compression of an 80dB input dynamic range into the 40dB output dynamic range corresponding to the physiological data of figure 3.3 is thus possible with reasonable individual quality factors. The frequency selectivity, however, cannot be as sharp as measured on biological cochleae, since it is determined by the quality factor of a single stage.

The pseudo-resonance results from the accumulation of the individual second-order low-pass filter gains $H_k(s)$ all along the cascade [34]. If their characteristic frequencies are close enough to each other to allow their resonant bumps to overlap, their multiplicative effect can lead to high overall

gains at frequencies close to the *pseudo-resonant frequency* f_{PR} . Since the cascade consists of filters with decreasing characteristic frequency, this cumulative effect occurs only on a limited number of filters, for which the individual gain is substantially greater than unity. Stages with a characteristic frequency much higher than the signal frequency have no effect on this signal (gain close to unity), whereas the stages with a characteristic frequency lower than the signal frequency rapidly attenuate the signal since their individual gain drops by 12dB per octave. The pseudo-resonance therefore

- strongly amplifies frequencies $f \approx f_{PR}$,
- sharply attenuate frequencies $f > f_{PR}$, and
- has no effect on frequencies $f < f_{PR}$.

The cutoff frequency of each stage in the cascade models the corresponding characteristic frequency of the cochlea. It is set to decrease exponentially along the cascade by one octave every b stages from f_{c0} at stage 0, which is expressed by

$$f_{ck} = f_{c0} 2^{-k/b}. \quad (3.15)$$

The transfer function between the input vibration at stage 0 and the basilar membrane displacement at the output of stage k is given by the product of the transfer function of all individual stages between the cascade input to the output of stage k .

These transfer functions are advantageously expressed as functions of frequency normalised to the characteristic frequency of stage k . Using equations (3.1) and (3.15), the transfer function between the input of the first stage in the cascade and the output of stage k is thus expressed by

$$G_k(\Omega) = \prod_{l=0}^k H_l(\Omega) = \prod_{l=0}^k \frac{1}{1 - \Omega^2 2^{\frac{2(l-k)}{b}} + j \frac{\Omega}{Q_l} 2^{\frac{l-k}{b}}}, \quad (3.16)$$

where $\Omega = f/f_{ck}$ is the frequency normalised to the characteristic frequency of stage k .

The normalised pseudo-resonant frequency Ω_{PR} at the output of stage k can be estimated by finding the maximum $G_{PR} = \|G_k(\Omega_{PR})\|$ of the amplitude gain function $\|G_k(\Omega)\|$. The pseudo-resonance involves a limited number L of basal stages, since all stages $l < k - L$ have a gain $H_l(\Omega)$

close to unity. Therefore the product in equation (3.16) can start with the index $l = k - L$ if $k \geq L$ and 0 otherwise.

By a simple change of variable, the transfer function $G_{k+d}(\Omega)$ after stage $k + d$ can be expressed by $G_k(\Omega 2^{d/b})$ using equation (3.16) in which the quality factors Q_l must be shifted to Q_{l+d} and the product must start with the index $l = -d$ instead of 0. Hence, provided that the stage k (or $k + d$ if $d < 0$) is far enough from the base to allow full pseudo-resonance to build up, and with the same quality factor for all stages participating to pseudo-resonance, $G(x) = G_k(\Omega = 2^x)$ expresses either the pseudo-resonant gain at stage k , at a frequency x octaves away from its characteristic frequency, or the pseudo-resonant gain at stage $k + bx$, at the characteristic frequency of stage k .

Figure 3.4 shows the accumulation of the individual amplitude gains $\|H_l(\Omega)\|$ on a growing number of basal stages and the accumulated gain $\|G_k(\Omega)\|$ for several cases of resolution b and quality factors Q . An important point to notice is that for $4 < b < 10$ and for any resonant Q , the normalised pseudo-resonant frequency Ω_{PR} is about 0.4 octaves higher than the normalised peak frequency Ω_p of the stage k alone. Since $G_k(\Omega)$ also measures the gain of the stage $k + b \log_2 \Omega$ at the characteristic frequency of stage k , this implies that the stage $k + d_{PR}$ with highest amplitude gain at the characteristic frequency of stage k is located d_{PR} stages toward the apex from stage k , where

$$d_{PR} = b \left(0.4 + \log_2 \sqrt{1 - 1/2Q^2} \right) \quad (3.17)$$

is the *pseudo-resonant distance*. For an individual quality factor Q between 1.5 and 2, the pseudo-resonant distance lies between $0.22b$ and $0.30b$, while the pseudo-resonant gain G_{PR} easily reaches the 45dB required to match physiological data as shown in section 3.2.4.

3.2.6 Quality factor control loop

In order to locally control the pseudo-resonant gain $G_k(\Omega)$ at the output of stage k , only the quality factors of the stages participating to the pseudo-resonance have to be controlled. A natural way of doing this, is to distribute the signal controlling the quality factor over this range.

The spatial distribution of the quality factors $Q(d) = Q_{k+d}$ on the pseudo-resonant region around stage k depends on the distribution of the control signals $i_c(d)$, in response to the distribution $\hat{V}_{vbm}(d)$ of the peak

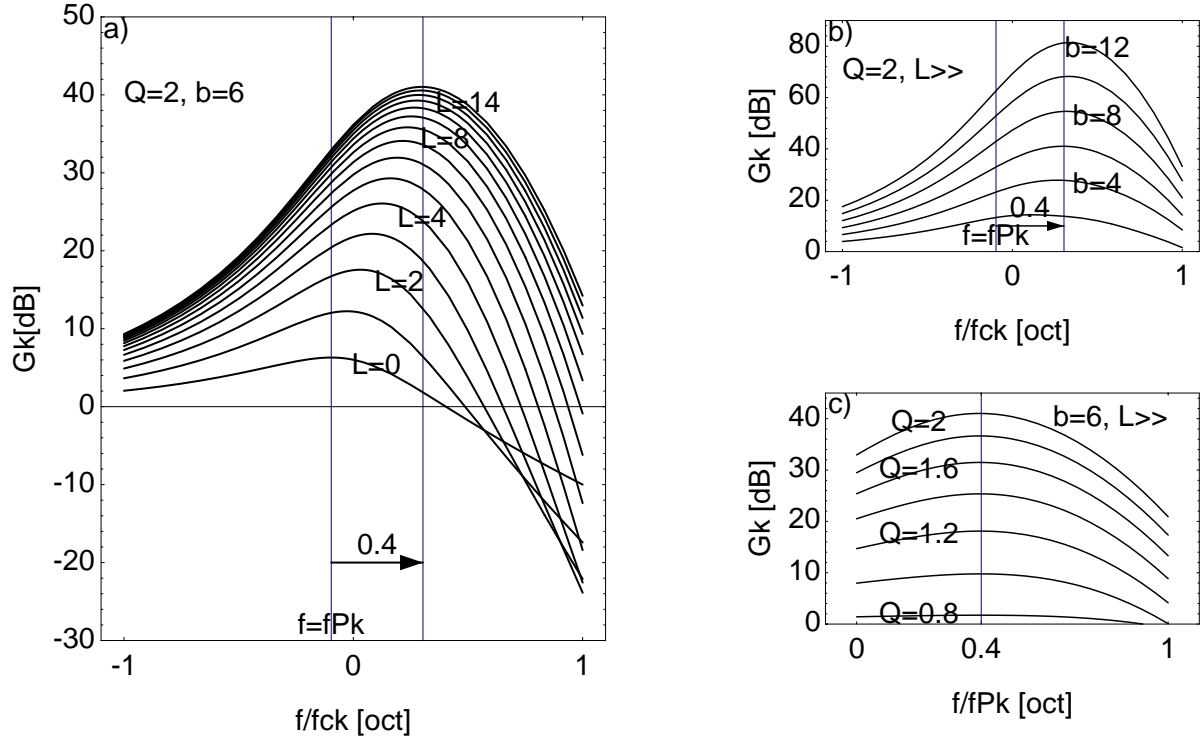


Figure 3.4: Pseudo-resonance; a) accumulation of amplitude gain of L individual stages toward the base from stage k ($G_k = \prod_{l=k-L}^k H_l$), as a function of normalised frequency $\Omega = f/f_{ck}$; resulting amplitude gains for several b) resolutions (stages per octave b) and c) quality factors (as a function of frequency f normalised to peak frequency f_{Pk} of individual stage k).

basilar membrane velocity signals at the output of stages $k + d$. Similarly to the single stage presented in section (3.2.3), the control signals $i_c(d)$ are made proportional to the peak amplitude $\hat{V}_{vbm}(d)$ of the differentiator outputs, but they can interact between stages, which is expressed by the spatial convolution product

$$i_c(d) = \sum_{d'=-\infty}^{\infty} F(d-d') \hat{V}_{vbm}(d'), \quad (3.18)$$

where $F(d)$ represents the spatial distribution of the feedback gains around any stage k in the cascade. In the single stage control loop of section 3.2.3, $F(0) = F$ and $F(d \neq 0) = 0$.

As mentioned in paragraph 3.2.5, the spatial distribution around stage k of the cascade's output responses at the characteristic frequency of stage k can be expressed using the gain function of equation (3.16) in which Q_{l+d}

must be used instead of Q_l . Since the equivalence between stage index shift d and relative frequency Ω applies also to the differentiators, the spatial distribution $\hat{V}_{vbm}(d)$ around stage k can be expressed by

$$\hat{V}_{vbm}(d) = \|G_D(d, \Omega)\| \hat{V}_{din0}, \quad (3.19)$$

where

$$\|G_D(d, \Omega)\| = \|G_k(\Omega 2^{d/b})\| \Omega 2^{d/b} \quad (3.20)$$

is the amplitude gain of the cascade after stage $k + d$, including the differentiator D_{k+d} , at frequency Ωf_{ck} , while \hat{V}_{din0} is the peak amplitude of the cascade input signal.

Hence, using equations (3.8), (3.18), and (3.19), the distribution of the quality factor $Q(d)$ on stages $k + d$ can be calculated by

$$Q(d) = \frac{1}{2} \left[1 + \frac{2Q_{max} - 1}{2Q_{max} \hat{V}_{din0} G_{OL}(d) + 1} \right], \quad (3.21)$$

where

$$G_{OL}(d) = \sum_{d'=-\infty}^{\infty} F(d - d') \|G_D(d', \Omega)\| \quad (3.22)$$

is the open loop gain distribution resulting from the spatial convolution of the feedback gain distribution $F(d)$ with the distribution $\|G_D(d, \Omega)\|$ of the amplitude gains in the cascade.

Since $\|G_D(d)\|$ —and, thus, $G_{OL}(d)$ —depends on the quality factors distribution $Q(d)$, equation (3.21) has the form of a nonlinear system of equations

$$Q(d) = Q(d, \hat{V}_{din0}, Q(-L), \dots, Q(M)). \quad (3.23)$$

The size of the system to solve is given by the range $-L \geq d \geq M$ for which $\hat{V}_{din0} G_{OL}(d)$ substantially modulates the quality factors $Q(d)$.

The amplitude gains distribution $\|G_D(d)\|$ with identical quality factors $Q(d) = Q$ all along the cascade can be approximated using a normalised gain

$$g_D(d) \approx Q^{-p_G} \|G_D(d + d_{PR})\| \quad (3.24)$$

which has its maximum at $d = 0$ (figure 3.5a). The modulation of the quality factors by control signals $i_c(d)$ having the same distribution as the normalised gain $g_D(d)$ and amplitudes varying on the expected 40dB output dynamic range (figure 3.5b) yields its maximal effect at a *quality*

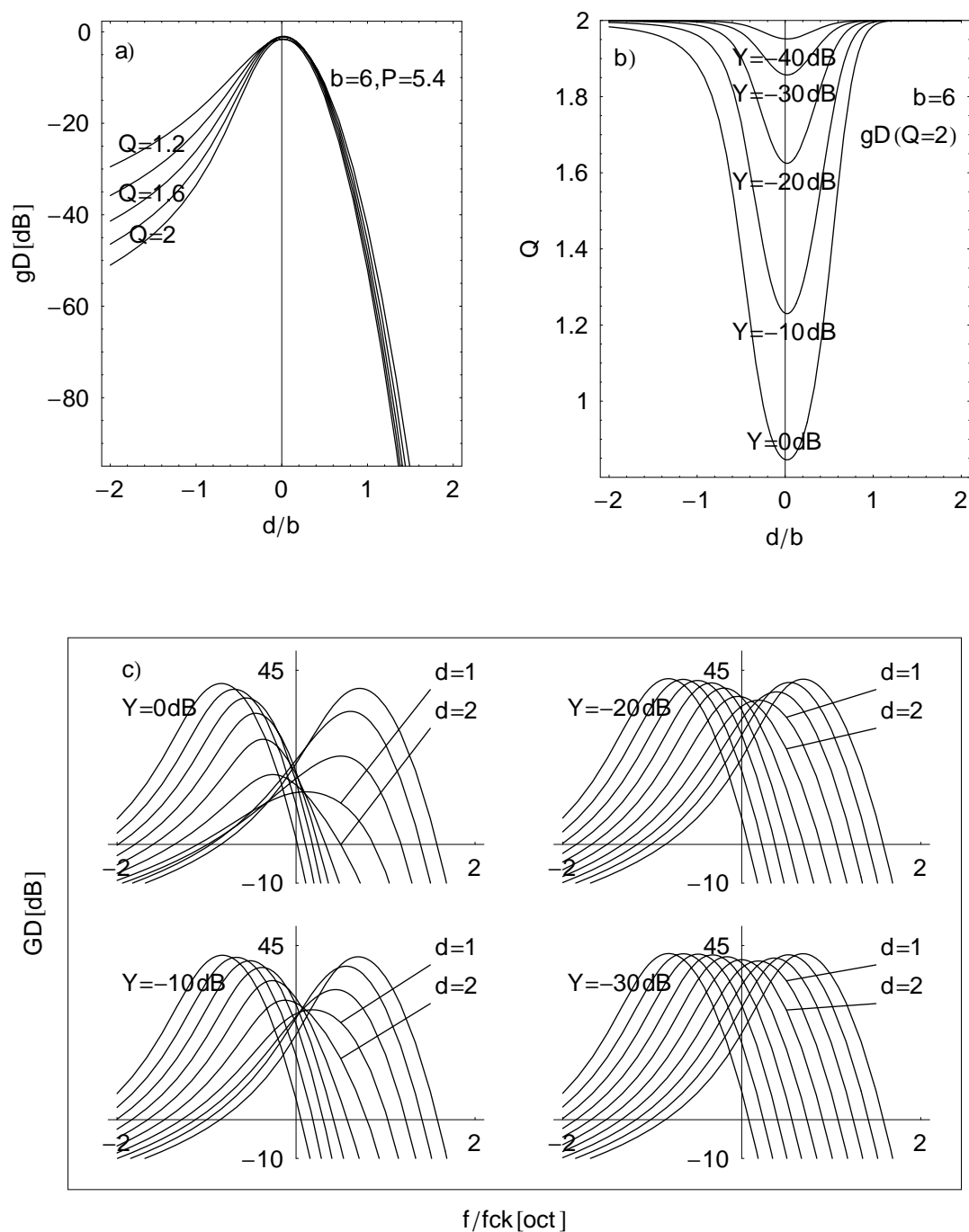


Figure 3.5: Most sensitive stage to quality factor modulation; a) normalised gains g_D at the characteristic frequency of stage k for several quality factors and b) resulting quality factors for several IHC output level Y , at normalised position d/b around stage k ; c) gains G_D after stages $k+d$ for several IHC output levels Y as a function of normalised frequency $\Omega = f/f_{ck}$.

factor modulation distance d_{QM} close to the pseudo-resonance distance d_{PR} . Figure 3.5c shows that on a $b = 6$ stages per octave cascade, the amplitude gains of the stages $k + 1$ and $k + 2$ are most attenuated. This quality factor best modulation distance d_{QM} between 1 and 2 is similar to the pseudo-resonance distance d_{PR} lying in this case between $0.22b = 1.32$ and $0.30b = 1.8$.

This means that the stage $k + d_{PR}$ has the best response $\hat{V}_{vbm}(d_{PR})$ to an input signal at the characteristic frequency of stage k , whereas *the same stage* $k + d_{QM}$ is the most sensitive to a control signals $i_c(d)$ having the same distribution as the peak basilar membrane velocity signals $\hat{V}_{vbm}(d)$, but shifted by $-d_{PR}$ in order to have its maximum $i_c(0)$ at stage k . Since the most efficient quality factor adaptation is performed for the highest open loop gain, the feedback gain's spatial distribution $F(d)$ should have its maximum at $d = -d_{QM}$. In conclusion, *the output of any stage in the cascade must control the quality factor of a stage located at a basal distance $-d_{QM}$, corresponding to an increase of characteristic frequency between one sixth to one third octave* (Figure 3.6).

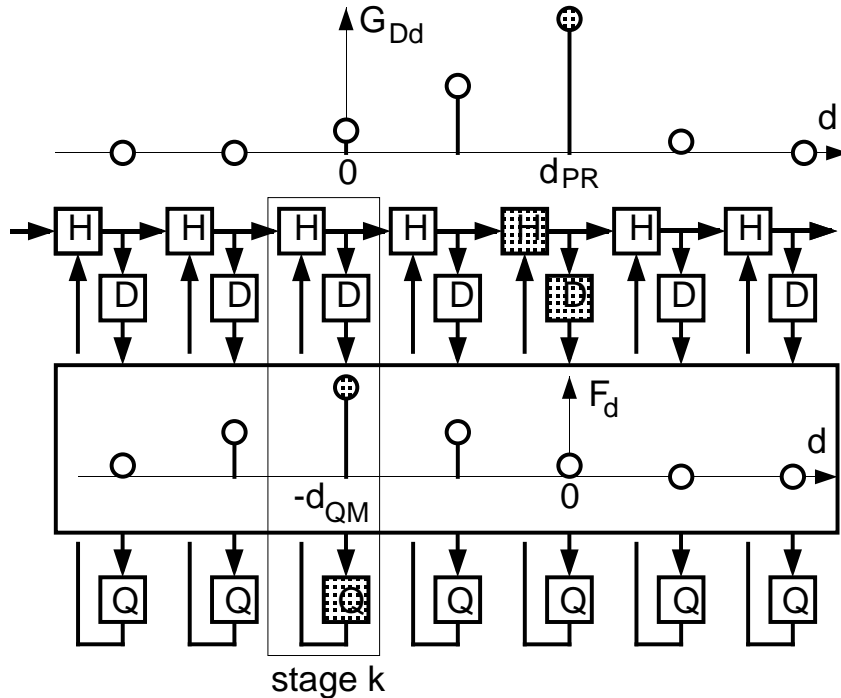


Figure 3.6: Cascade quality factor control loop; the feedback gain distribution $F(d)$ shifts toward the base at a distance $d_{QM} \approx d_{PR}$ the output signal with highest peak amplitude occurring at stage $k + d_{PR}$.

As mentioned in section 3.2.3, the feedback gain distribution $F(d)$ models the IHCs and the MSR blocks. The distribution of $F(d)$ can thus model interactions between stages that may occur at higher levels of auditory processing, such as lateral inhibition, diffusion and nonlinear spatial filtering. As for the basal shift $-d_{QM}$, its biological counterpart is plausible, since afferent fibres of the inner hair cells are paired with the afferent fibres of the outer hair cells located where the characteristic frequency is one seventh to one third octave higher [18]. The operating point of the outer hair cells is likely to provide the auditory brainstem with information relative to the signal level, which has been lost by the gain adaptation.

3.2.7 Closed loop amplitude gain

The closed loop analysis of the Q -control scheme consists of solving the system (3.23). In this analysis, the simplest feedback gain distribution is imposed, i.e. $F(-d_F) = F$ and $F(d \neq -d_F) = 0$, where d_F is an integer such that $1/6 \leq d_F/b \leq 1/3$, according to the conclusion about the best quality factor modulation distance d_{QM} (paragraph 3.2.6). The term $G_{OL}(d)$ in equation (3.21) equals in this case $F\|G_D(d + d_F, \Omega)\|$ and it depends on the quality factor distribution $Q(d)$, since $\|G_D(d + d_F, \Omega)\|$ is the product of amplitude gain functions of stages with the quality factors that follow the distribution $Q(d)$. An iterative loop must estimate the distribution $Q(d)$ on a range of stages for which $Q(d)$ is substantially modulated by the feedback loop.

This iterative loop can advantageously be driven by the averaging performed in the MSR blocks. The MSR is estimated by averaging the IHC output V_{ihc} of every stage in the cascade according to a first order low-pass filtering $1/(s\tau_a + 1)$. Using equation (3.18), the quality factor control signal $i_c(d)$ can be described in the time domain identically for each stage by

$$\tau_a \frac{\partial i_c(d, t)}{\partial t} = F\hat{V}_{vbm}(d + d_F, t) - i_c(d, t), \quad (3.25)$$

where the distribution $\hat{V}_{vbm}(d, t)$ of the differentiator outputs is controlled in time by the input peak amplitude $\hat{V}_{din0}(t)$ and in space and time by the distribution at time t of the amplitude gain $\|G_D(d, \Omega, t)\|$ of the cascade, according to equation (3.19).

Figure 3.7 shows the simulation result of such a closed loop analysis, performed on a $b = 6$ stages per octave cascade with a quality factor

limited at $Q_{max} = 1.8$. In figure 3.7a, the amplitude gain after stage $k + d$ at the characteristic frequency of stage k is represented as a function of the stage shift d relative to stage k . The index d equivalently represents the frequency in b -th of an octave relative to the characteristic frequency of stage k . The peak amplitude gain adapts from 40dB at -80dB input level to nearly -10dB at 0dB input signal, yielding the 50dB dynamic compression also measured on biological cochleae. The shift of the peak frequency Ω_{PR} from 1/3 octave to -1/2 octave relative to the characteristic frequency as well as the frequency selectivity decrease for an increasing input level are also in accordance with physiological data. Figure 3.7b, in addition to the level adaptation, shows the level transition enhancement which might improve the detection of relevant features in the speech signal and help its segmentation into phonemes.

3.2.8 Cochlear filter stability

Instability can occur locally in a single stage k if $\alpha i_{Q_{max}} > 1$ in equation (3.9) leads to a negative value of Q_{max} . In this case, according to equation (3.8), the quality factor Q of this stage becomes negative with $i_c = 0$, that is, in absence of any input signal. As a result, the real part of the poles of the transfer function $H_k(\Omega)$ becomes positive. Any perturbation would cause its output signal V_{dbm} to oscillate with an amplitude growing exponentially. Thanks to the quality factor control loop, as the amplitude of V_{dbm} grows, the control signal i_c grows proportionally until it yields a quality factor $Q = -\infty$ for which V_{dbm} stabilises to a peak amplitude \hat{V}_{osc} . This amplitude is directly related to the control signal $i_{c_{osc}} = -1/2Q_{max}$ yielding $Q = -\infty$. The resulting output oscillation at the output of the second-order stage H_{k+d_F} has therefore a peak amplitude

$$\hat{V}_{osc} = \frac{\alpha i_{Q_{max}} - 1}{F}. \quad (3.26)$$

This oscillation does however not propagate apically in the cascade. Since its frequency equals the characteristic frequency of the oscillating stage, it is rapidly attenuated by the sharp cutoff at the following stages.

This sustained oscillation caused by a malfunction of the outer hair cells was observed in the biological cochlea as an otoacoustic emission, which strongly suggested that an active process performs the automatic gain control in the cochlea.

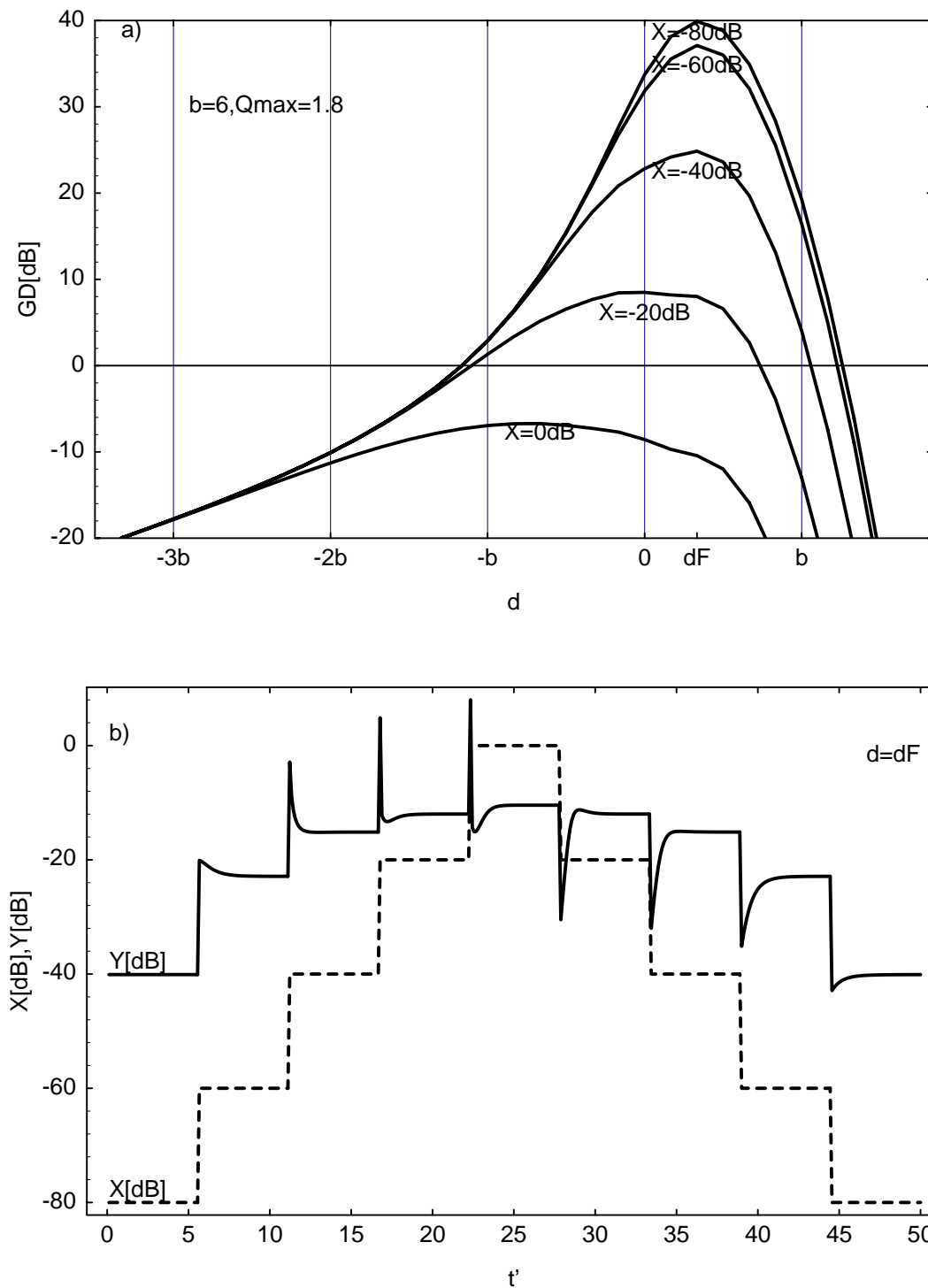


Figure 3.7: Closed loop analysis; a) amplitude gains G_D after stages $k + d$ for an input signal at the characteristic frequency of stage k with input levels X between -80 dB and 0 dB; b) time evolution of the output level Y for an input level X increasing then decreasing by steps between -80 dB and 0 dB (time t' normalised to the time constant τ_a of the MSR low-pass filter).

3.3 Time simulations

3.3.1 Computer model

In order to verify the behaviour of the model in the time domain and by this the stability of the Q -control loop (not taken into account by the frequency description of paragraph 3.2.7), a computer implementation of the model was written in C. The computer model features for each stage the digital implementation of the linear second-order band-pass filter $H(s)D(s)$ of equation (3.13), the full wave rectification of its output and then its averaging with a digital implementation of a first order low-pass filter $F/(s\tau_a + 1)$, yielding the Q -control signal i_c . The Q -control loop is closed by adjusting continuously the quality factor Q of the band-pass filter located d_F stages toward the base using equation (3.8).

All the results below were produced using a filter cascade set with a characteristic frequency decreasing by one octave every $b = 6$ stages. The Q -factor of each stage was controlled between 0.5 and $Q_{max} = 2$ by the MSR output of the stage located $d_F = 2$ stages toward the apex. The feedback gain was set to $F = 1$ and the MSR time constant to $\tau_a = 16\text{ms}$ (10Hz cutoff frequency).

3.3.2 Level compression and transient enhancement

In order to illustrate the level compression and the frequency selective transient enhancement performed by the Q -control in the entire cascade, the computer model was excited with a 1kHz tone having step-varying levels. Figure 3.8a shows that an 80dB input dynamic range is compressed into a 30dB output dynamic range thanks to a pseudo-resonant gain varying between 40dB and -10dB. The frequency selectivity of this gain is shown in figure 3.8c, where the stage index axis equivalently represents the frequency of an input tone (numbered in sixth of an octave decreasing from the characteristic frequency of the first stage); this plot represents thus also the frequency response of the most sensitive stage (marked by the vertical line). Figure 3.8a and c, obtained from the time simulation, are in quite good accordance with figure 3.7a and b, respectively, obtained with the frequency model of paragraph 3.2.7. Since the gain is adjusted with the large time constant of the MSR block, abrupt level changes in the input signal result in strong over- and undershoots of the basilar membrane velocity, as detailed in figure 3.8b. The delay between the input level

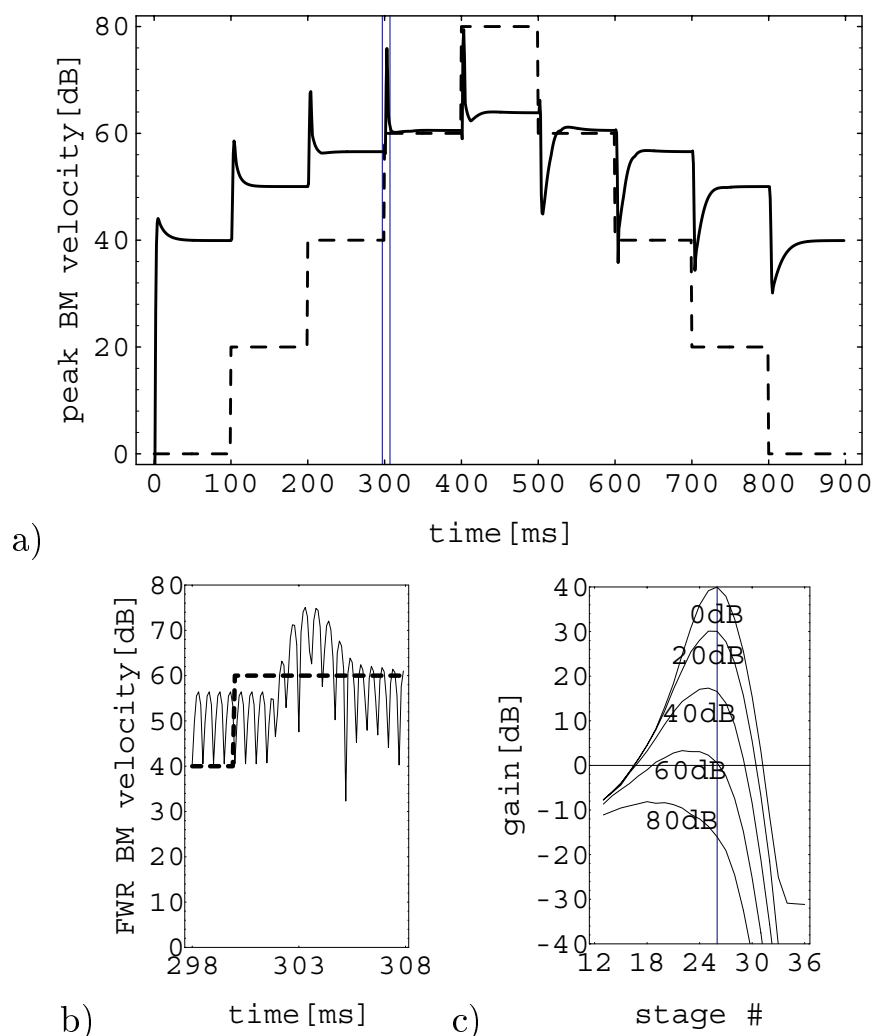


Figure 3.8: Time simulation results: a) peak basilar membrane velocity (solid line) of the best responding stage to an input basilar membrane peak displacement (dashed line); b) full wave rectified basilar membrane velocity (IHC output) for the transient marked in a); c) amplitude gains between input basilar membrane displacement and stationary basilar membrane velocities at each stage for several input levels.

transition and the reaction of the output is due to the accumulation of the individual stage's delays all along the cascade, not taken into account by the frequency model.

Moreover, the Q -control loop was verified to keep the entire system stable even without MSR low-pass filter.

3.3.3 Two-tone suppression

The frequency selective automatic gain control is well illustrated by the *two-tone suppression* effect which was also shown in live cochleae [13]. The response to a probe tone is reduced when a suppressor tone is simultaneously presented. This reduction depends on both suppressor level and frequency. The two-tone suppression curve, as well as the closely related *tuning curve*, are usually drawn from the neural response measured on the auditory nerve. They represent the input tone level needed, as function of its frequency, to obtain a given output level.

Figure 3.9a shows the tuning curve at the output of the stage which best responds to a 1kHz reference tone at a level of 0dB (according to the experiment of section 3.3.2). Each curve follows an isoamplitude of basilar membrane velocity in the plane of the input tone's level and frequency. Figure 3.9b shows the two-tone suppression curve, which is the tuning curve of the basilar membrane velocity component at the frequency of the probe tone in the plane of the suppressor tone's levels and frequencies. The isoamplitudes are given as percentages of the basilar membrane velocity in response to the probe presented alone. The probe tone had the same level and frequency as the reference tone of the tuning curve 3.9a. The increasing levels needed for the suppressor to notably suppress the probe when the suppressor frequency moves away from the probe frequency demonstrate that the suppression performed by the frequency selective automatic gain control is active in a limited frequency range.

3.3.4 Speech cochleogram

One of the ultimate goal of a cochlear model is to preprocess efficiently speech signal for recognition by man (cochlear implants and hearing aid) or by machine (automatic speech recognition system). The potential efficiency of the processing performed by the active cochlear filter cascade model must therefore be evaluated on such natural signals. In automatic speech recognition, in order to be insensitive to the speaker-related pitch, the effect of the glottal pulses remaining in the band-pass filtered envelopes of the speech signal at the IHC output of the cochlea has to be removed. This can be done by low-pass filtering these envelopes. Such filtering must have a cutoff frequency below the pitch frequency, but the large integration time constant of such a filter would also remove the transients occurring at the plosives, which contain relevant speech information. The automatic

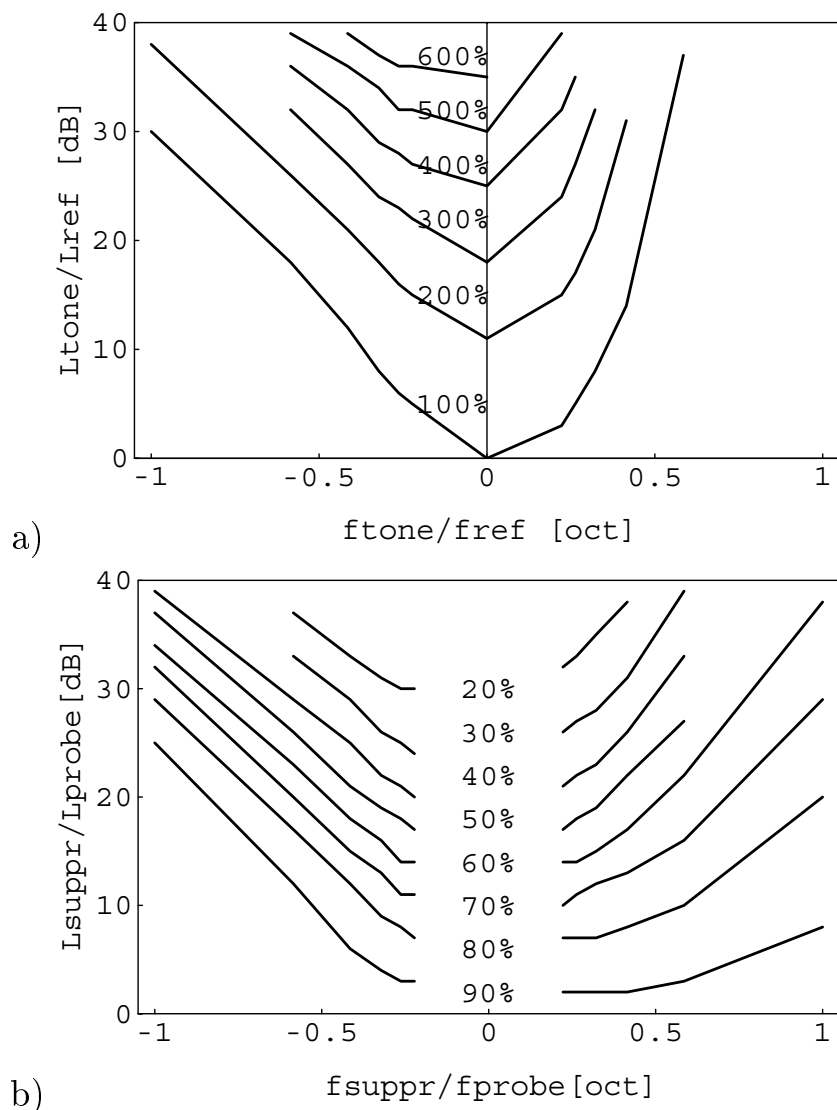


Figure 3.9: a) Tuning curves: loci of the isoamplitude of the basilar membrane velocity (relative to its value in response to a reference input tone) in the plane of the input tone’s level and frequency; b) two-tone suppression curve: loci of the isoamplitude of the basilar membrane velocity component at the frequency of the probe tone (relative to its value in response to the probe tone presented alone) in the plane of the suppressor tone’s level and frequency.

gain control solves this problem by enhancing the transients that appear once in a while in the envelopes of the speech signal, whereas the regular pitch pulses are filtered out by the MSR estimator.

The utterance “print preview” pronounced by a female speaker across a telephone line was given as an input to a 42 stages cascade. The level

compression performed by the Q -control is illustrated in figure 3.10, where the MSR output of stage 30 (having a characteristic frequency $CF=425\text{Hz}$) is compared to two cases with constant quality factors. The Q -control also reduces the level difference between the transients (“p”, “t”) and the slowly varying parts of the signal (“i”, “e”, “iew”), by about 20dB for this utterance. Transients are thus enhanced relatively to the average level of the signal. In utterances where the transients were better pronounced, they even rose to levels exceeding by far the level of the stationary parts of the signal. Such high level transients would however be truncated by the saturations of the VLSI implementation.

Figure 3.11 shows *cochleograms* for the same utterance, which consist of the MSR outputs of stages 13 to stage 42, spanning characteristic frequencies from $CF=3400\text{Hz}$ to $CF=106\text{Hz}$. The first 12 stages have characteristic frequencies above the telephone band, but they are needed to accumulate the individual stage’s gains. In the cochleogram 3.11a, the Q -factor is controlled between 0.5 and 2.0, whereas in the cochleograms 3.11b and c the Q -control was disabled, with a Q -factor fixed at $Q = 0.8$ and $Q = 2$, respectively. This illustrates how the transients without Q -control would appear only weakly on a cochleogram, which can be considered as the visual equivalent of the perceived speech. In addition to the transient enhancement, figure 3.11 clearly shows that the Q -control also reveal more structure in the cochleogram.

Although suppression of the pitch pulses might improve speaker in-

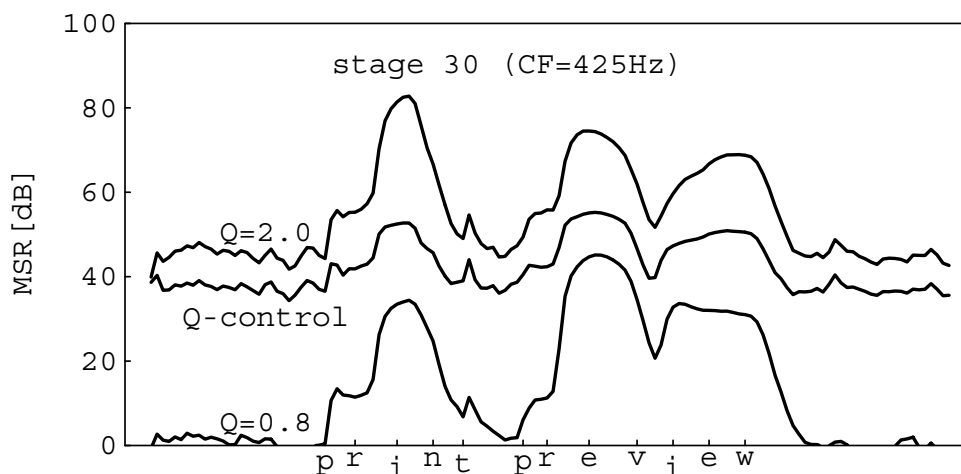


Figure 3.10: MSR output of stage 30 for the utterance “print preview” pronounced by a female speaker across a telephone line.

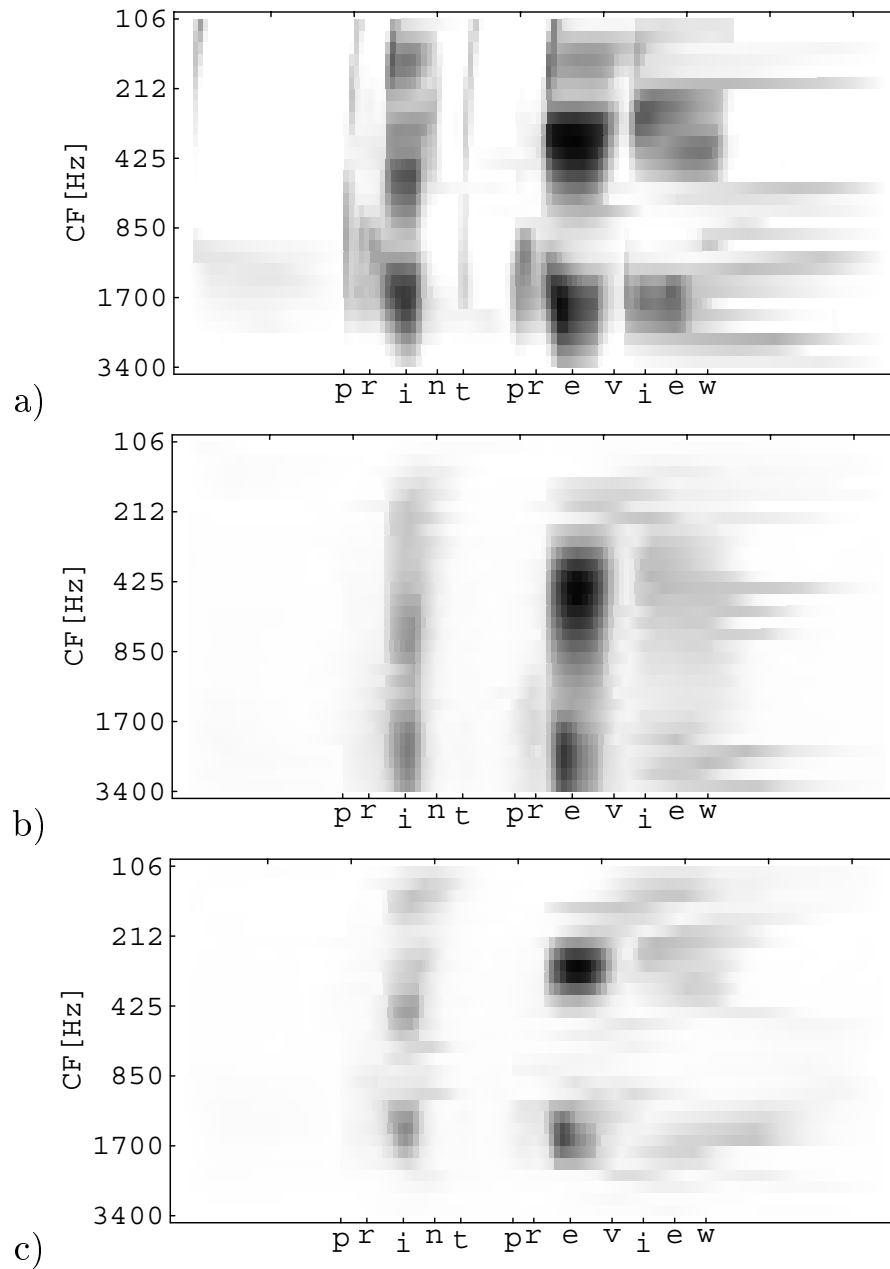


Figure 3.11: MSR cochleogram for the utterance “print preview” pronounced by a female speaker across a telephone line a) with Q -control; b) with a constant quality factor $Q = 0.8$ and c) $Q = 2.0$.

dependence for automatic speech recognition, it would also suppress a relevant cue that helps source separation in the well known “cocktail party” problem. Nevertheless, pitch pulses are suppressed at the level of the MSR output, but they are still present at the inner hair cell output of the cochlea projecting on the auditory nerve. Different higher-level processing

stages parallel to the MRS block may still use this pitch signature of an individual speaker to help focusing on its speech stream.

3.4 VLSI implementation

3.4.1 Second-order stage with differentiator

The second-order stage cascade modeling the basilar membrane displacement as well as the differentiators converting its outputs into the basilar membrane velocity all along the cascade are the same as described in [35, 37]: the mirrors copying the currents of the OTA's differential pair to its output node in the first BM OTA and in the OHC OTA are merged, and the scaled differentiation $s\tau$ is performed by taking as an output the voltage difference between the outputs of the first and the second BM OTA. However, in order to minimise the systematic dc offset of the filter due to the output conductance of the transistors in the OTAs' mirrors and differential pair, large output range OTAs with cascoded output were preferred (figure 3.12). The cascode transistors reduce the output conductance of the OTA's output mirrors whereas the structure of the wide output range OTA symmetrizes the drain voltage of the differential pair transistors and, thus, their output conductance, reducing the systematic dc offset voltage of the follower-connected OTAs. Systematic dc offset accumulates along the cascade and might bring the operating point of the apical stages out of their operational domain; reducing it allows thus to implement longer cascades.

Because of the limited slew-rate of the BM OTAs due to their load capacitance C_τ , a limit-cycle oscillation may occur when the OTA's outputs saturate to their bias current. According to the analysis shown in [1], this large signal oscillation occurs if $I_Q/I_\tau > (1 + \sqrt{5})/2 = 1.618$. Using the definition of α in equation (3.5), the second-order stage prevents this oscillation if $g_{mQ}/2g_{m\tau} < 1.618\alpha$. On the other hand, small signal stability is ensured if $g_{mQ}/2g_{m\tau} < 1$. Therefore, with $1.618\alpha > 1$, the limit-cycle oscillation is prevented as long as the small signal stability is ensured. This condition is imposed by degenerating the differential pair of the BM OTAs using diode connected transistors, yielding for these OTAs a linear input voltage range $(n + 1)$ times larger than the OHC OTA, and thus

$$\alpha = \frac{n + 1}{2}, \quad (3.27)$$

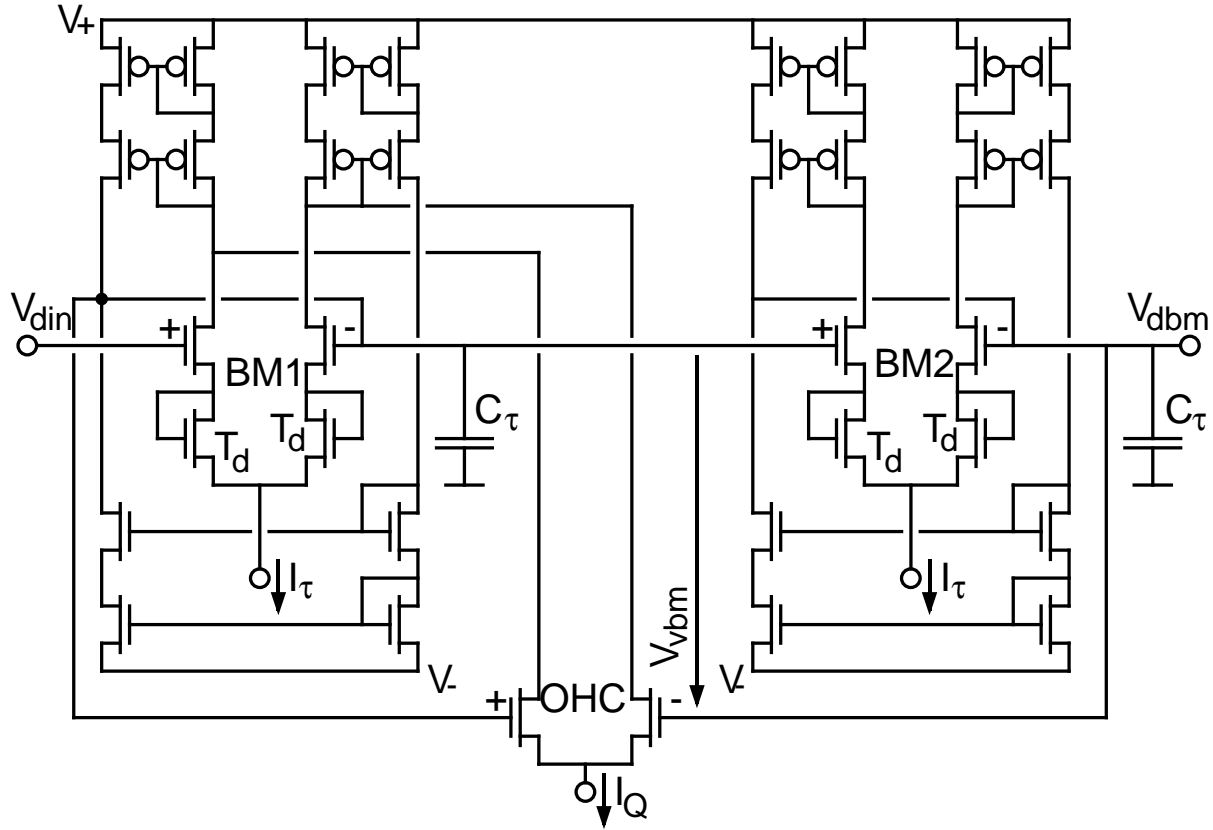


Figure 3.12: Second-order low-pass filter; the differential pair of the BM OTAs are degenerated by the transistors T_d ; the current mirrors copying the OTA's differential pair currents to its output node are shared between the OTAs BM1 and OHC.

where n is the slope factor of the diode-connected transistors T_d [35, 37]. The slope factor n is always greater than unity, which implies that the small signal instability occurring when I_Q reaches $2I_\tau/(n+1)$, and which is limited to this value by the quality factor feedback loop, never allows a large signal oscillation to persist.

3.4.2 Quality factor control

A remarkable improvement in the regularity of the frequency characteristics along the cascade can be obtained using *compatible lateral bipolar transistors* (CLBTs) [44, 45] to impose the bias currents I_τ decreasing exponentially along the cascade, while ensuring a constant I_τ/I_Q [37]. Using this technique, the ratio I_Q/I_τ modulating the quality factor independently for any stage can be controlled by a translinear loop including

these CLBTs. The circuit proposed in figure 3.13 generates I_Q and I_τ from the currents I_{Qmax} , $I_c + I_0$ and I_τ according to equation (3.7). The currents I_{Qmax} and $I_c + I_0$ are imposed at the collectors of the CLBTs T_{qm} and T_c , respectively, whereas I_τ is imposed by the voltage V_τ at the base of T_t , tapped on the resistive line controlling the exponential decrease of the characteristic frequency along the cascade. The common voltage V_Q at the emitters of the CLBTs T_q and T_{qm} is controlled by the MOS transistor T_e which sinks these emitters with a current that allows their respective collectors to sink the required currents I_Q and I_{Qmax} .

The output conductance of each CLBT is reduced by cascoding it using a MOS transistor. A compact layout can be obtained by sharing the base of the CLBT with the bulk of this cascode transistor. The cascode transistor is biased using an additional cascoded CLBT, as shown in the base and apex bias generation circuit of figure 3.13 [45].

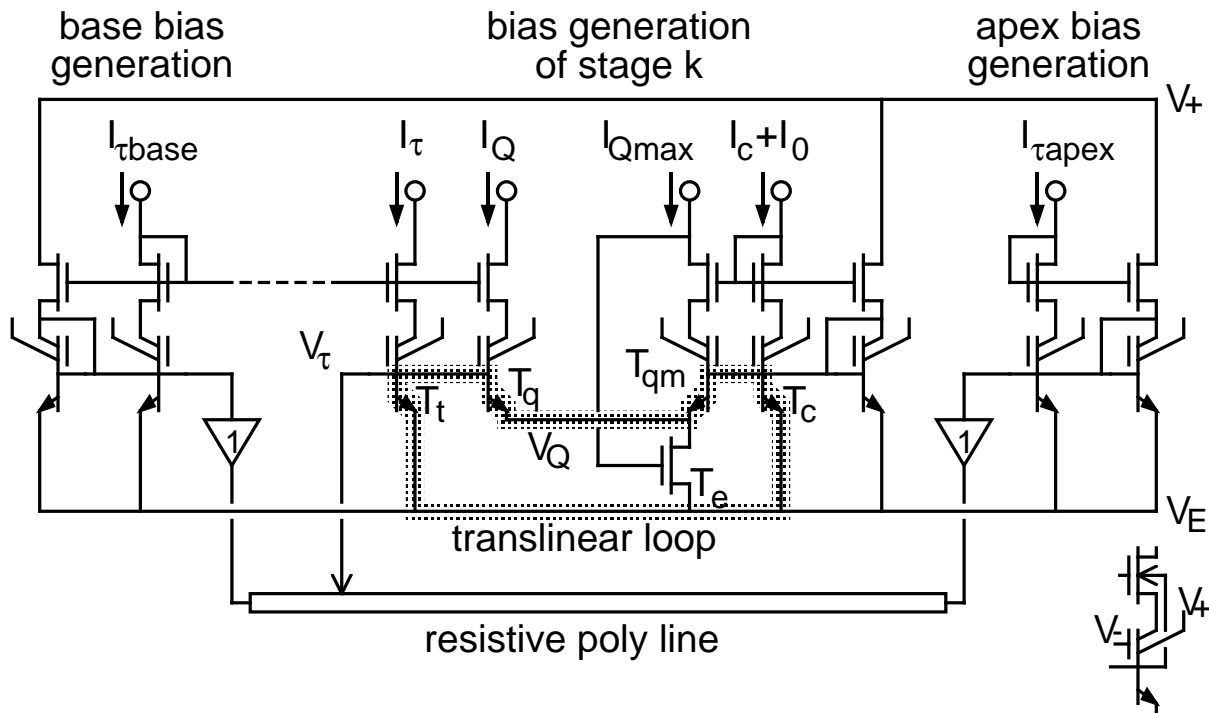


Figure 3.13: Translinear loop; the emitter current of transistors T_q and T_{qm} is sunk by the transistor T_e ; inset: in each cascoded CLBT, the bulk of the cascode MOS transistor corresponds to the base of the CLBT, and the emitter of the parasitic vertical transistor is connected to substrate (V_+); the gate of the MOS transistor implementing the CLBT is connected to the lowest voltage (V_-) to set it in the accumulation regime.

An important point to analyse is the effect on the quality factor of the dispersion of the translinear loop input currents. According to equation (3.9), for a maximal quality factor $Q_{max} > 0$ at every stage, the condition $\alpha i_{Q_{max}} < 1$ must be respected for every stage. Allowing variations of $\alpha' = \alpha i_{Q_{max}}$ within the range $\pm \varepsilon_{\alpha_{max}} \alpha'$ leads to a nominal maximal quality factor

$$Q_{max} = \frac{1 + \varepsilon_{\alpha_{max}}}{2\varepsilon_{\alpha_{max}}}, \quad (3.28)$$

so that $\varepsilon_{\alpha} \leq \varepsilon_{\alpha_{max}}$ ensures $Q_{max}(\alpha' + \varepsilon_{\alpha} \alpha') > 0$. However a negative variation within the same range can be shown to reduce Q_{max} by up to a factor two: $Q_{max}(\alpha' - \varepsilon_{\alpha_{max}} \alpha') = Q_{max}(\alpha')/2$.

The variations ε_{α} of α' depend on the matching of n , $I_{Q_{max}}$ and I_0 all along the cascade, which may result in important variations of α' . Equation (3.28) shows that a 33% variation of α' allows a nominal $Q_{max} = 2$, with a worst case $Q_{max} = 1$ while ensuring $Q_{max} > 0$ in any case.

3.4.3 IHC rectifier

The function of the rectifier is to generate a dc component from the basilar membrane velocity signal. The basilar membrane velocity is available at the level of the BM second-order filter as the voltage difference V_{vbm} . Therefore an OTA suffices to generate a current $I_{vbm} = g_{ma} V_{vbm}$. This current can be half-wave rectified using a single diode at the output of this IHC OTA, but in order to limit the large voltage swing at the output of the IHC OTA resulting from its large load resistance when the diode is blocked, the current wave blocked by the diode is sunked through a second diode. Full-wave rectification can be performed by mirroring this negative current wave to the output of the rectifier (figure 3.14a).

The delicate points to master in this circuit are related to its need to rectify a very small current varying at frequencies up to the highest characteristic frequency of the cascade (at least up to 5kHz, for speech signal processing). The rectified current must be as small as possible because it will determine the large time constant τ_a of the MSR low-pass filter together with its capacitance C_a , which must in turn be small enough not to waste chip area.

The time to switch from a negative current $-I_{vbm}$ to a positive one I_{vbm} depends on the charge accumulated on the parasitic capacitance C_m

leakage current I_{p0} is determined by the voltage difference $V_n - V_p$. The rectifier output voltage V_p may be assumed almost constant if the large capacitor C_a of the MSR low-pass filter loads directly the output of the IHC rectifier, shorting so the ac component of the rectified current I_{ihc} . As for the voltage V_n , it is imposed independently from I_n by the current conveyor T_1 - T_2 . The value of V_n is advantageously imposed by the required leakage current I_{p0} using an identical current conveyor (T_5 - T_6) and a current mirror (T_7 - T_8).

Imposing a leakage current I_{p0} less than 1% of the amplitude of I_{vbm} and a switching time shorter than a quarter of a period at a characteristic frequency of 5kHz and assuming a capacitance $C_m = 0.1$ pF, the amplitude of the IHC OTA output current I_{vbm} must be larger than 0.5 nA.

3.4.4 MSR low-pass filter

In order to estimate the mean value of the basilar membrane velocity, the MSR low pass filter separates the dc component \bar{I}_{ihc} from the harmonics generated by the rectification of the basilar membrane velocity signal $I_{vbm} = g_{ma}V_{vbm}$.

The Q -control loop has been shown by time simulations to maintain the system stable even without filtering the ac components of the IHC output block. However, it reinjects the harmonics generated by the IHC rectifier into the BM block. These harmonics do not propagate apically in the cascade thanks to the sharp pseudo-resonant cutoff, but they still affect locally the signal to be processed. Moreover, in order to enhance the transients in the band-pass filtered envelopes of the speech signal, the automatic gain control loop must react more slowly than the temporal evolution of these envelopes. Since these envelopes vary with a time constant of several milliseconds, the MSR block controlling the reaction time of the Q -control loop must have a maximal cutoff frequency at a few hundreds hertz. This low-pass filtering is also intended to remove the periodic pitch pulses remaining in the band-pass filtered envelopes of the speech signal, whose frequency can descend down to 100 Hz for some speakers.

The MSR low-pass filtering is implemented by injecting the rectifier output current I_{ihc} into a capacitance C_a in parallel with a conductance g_a . The voltage V_a across g_a or the current I_a flowing through it is proportional to the mean basilar membrane velocity signal (see figure 3.2). It will thus be used to generate the current I_c to be injected into the translinear loop

controlling the quality factor as described in paragraph 3.4.2.

The conductance g_a can be implemented by a single MOS transistor (figure 3.15a) or by an OTA (figure 3.15b). In both cases, the value of the linearised conductance g_a is determined by the dc current I_a flowing through it, thus in weak inversion

$$g_a(I_a) = \begin{cases} \frac{I_a}{nU_T} & \text{single transistor} \\ \frac{I_B}{2nU_T} \left(1 - \frac{I_a^2}{I_B^2}\right) & \text{OTA,} \end{cases} \quad (3.31)$$

where I_B is the bias current of the MSR OTA g_a and the dc current I_a corresponds to the mean rectifier output current \bar{I}_{ihc} , which is proportional to the mean basilar membrane velocity. The MSR time constant $\tau_a = C_a/g_a$ will thus depend on the mean basilar membrane velocity.

It can be shown that the OTA implementation reduces by almost a factor two the variations of this time constant with the dc current level, within the operation range of the model; moreover, since the OTA transconductance is halved compared to a single MOS transistor biased with the same dc current, the large time constants can be implemented on a half-sized capacitor, saving area if the capacitor is much larger than the OTAs.

The degeneration of the OTA's differential pair by diode-connected transistors decreases once more the transconductance g_{ma} , —and thus decreases the required capacitor area for the same time constant, by a factor $n+1$ at the price of four additional transistors (since in this case the differential pair of the feedback OTA g_{mF} must be degenerated similarly to

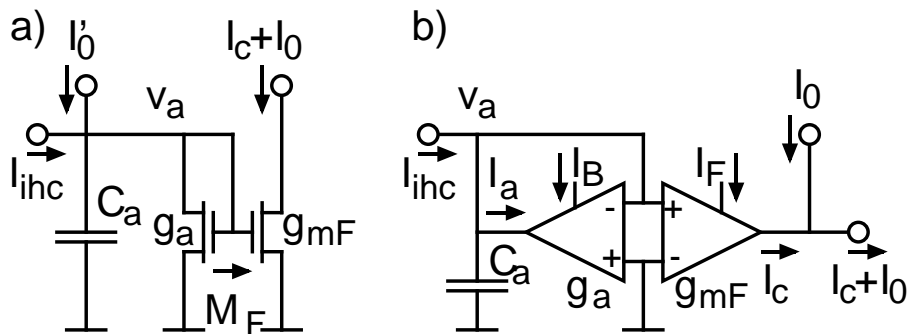


Figure 3.15: MSR low-pass filter; implementation using a single MOS transistor (a) and an OTA (b) for the conductance g_a .

keep the transconductance ratio g_{mF}/g_a independent of the mean basilar membrane velocity).

Using degenerated OTAs with a capacitance $C_a = 10\text{pF}$, a 200Hz cut-off frequency can be obtained with a bias current $I_B = 1.76\text{ nA}$. With a maximal mean rectifier output current $\bar{I}_{ihcmax} = 0.53I_B$ (which corresponds to a MSR OTA output current $I_a(V_a)$ 10% lower than its value $g_a V_a$ with a transconductance g_a linearised around $I_a = 0$), the expected 40dB dynamic range of the basilar membrane velocity permits to estimate a minimal mean current $\bar{I}_{ihcmin} = 9\text{ pA}$ at the output of the rectifier, which reaches the limits of the leakage current of MOS transistors.

Since the input current I_{ihc} of the MSR block is directly produced by the rectification of the IHC OTA output current I_{vbm} , the minimal peak value \hat{I}_{vbmmin} of the IHC OTA output current, assumed here to be a sine wave, amounts to $A_r \bar{I}_{ihcmin}$, where A_r is the ratio between the dc component of a full-wave-rectified sine wave and its peak amplitude, thus $A_r = \pi/2$ and $\hat{I}_{vbmmin} = 15\text{pA}$. In section 3.4.3 it has been shown that the current I_{vbm} must equal 0.5nA to rectify signals at 5kHz. The leakage current I_{p0} was set 100 times smaller, thus only 3 times smaller than the minimal peak IHC OTA output currents $\hat{I}_{vbmmin} = 15\text{pA}$. With this minimal value, equations (3.29) and (3.30) give a switching time that properly rectifies a signal at a maximal frequency of 630Hz in the same conditions. Such a maximal frequency is too low at the basal stages of the cascade where the characteristic frequency is higher.

The IHC OTA has its minimal output current imposed by the high frequency limit of the rectifier given by the highest characteristic frequency in the cascade. On the other hand, the maximal mean rectifier output current is imposed by the minimal MSR time constant required to average signals having a frequency corresponding to the lowest characteristic frequency in the cascade. This situation may be exploited by grading the currents biasing the IHC and MSR OTAs along the cascade similarly to the bias current I_τ defining the characteristic frequency of the BM second-order stage (see paragraph 3.4.6). Doing so, high frequency are rectified properly and averaged with a higher cutoff frequency, whereas low frequency components can be averaged with a larger time constant since slower switching can be tolerated for their rectification.

Exploiting further the structure of the filter cascade, an additional solution is implemented to better remove the ac oscillation of the rectified basilar membrane velocity signal. Since the BM sections are modeled by

second-order stages, the basilar membrane velocities measured at adjacent stages have a phase difference close to $\pi/2$ near their characteristic frequencies, for which they also have the largest amplitude. Summing the output currents of full-wave-rectified sine waves shifted by a quarter of a period yields a signal whose first ac component has a frequency four times higher than the one of the input sine wave: a twofold attenuation can be obtained with the same first-order MSR low-pass filter. This “double-wave rectification” increases thus the ratio between the dc components of the mean basilar membrane velocity and its ac components. This additional attenuation reduces the ac components reinjected into the filter cascade through the Q -control loop, but it does not increase the MSR time constant. Assuming the MSR filtering to be linear, this summing of MSR inputs of adjacent stages is equivalently performed on their outputs, where the current levels are more important. Doing so, this interaction between stages is performed together with the feedback of the MSR output of a stage k to the Q -control block of the basal stage $k - d_F$, as it will be described in paragraph 3.4.5.

3.4.5 Feedback gain distribution

According to equation (3.18), the current I_c at the output of the MSR of the stage k must control the quality factor of the cascade through the distributed feedback gain $F(d)$ having its maximal value at $d = -d_F$. The simplest distribution $F(-d_F) = F$ and $F(d \neq -d_F) = 0$ is implemented by connecting the output node sourcing I_c in the MSR block of stage k , to the collector of the CLBT transistor T_c in the translinear loop of stage $k - d_F$.

The disadvantage of this fixed connection is its limited flexibility, since d_F has been shown in section 3.2.6 to lie between $b/6$ and $b/3$ for the most efficient quality factor control loop. The number of stages per octave b can be adjusted by the characteristic frequencies of the first and the last cascade stage through the resistive line [37], but it should therefore not extend too far outside the limits $3d_F$ and $6d_F$.

Figure 3.16 shows the implementation of such Q -control loop at a feedback distance $d_F = 2$. It includes the summing of adjacent stage’s MSR output reducing the remaining ac oscillations of the Q -control signal i_c (see paragraph 3.4.4).

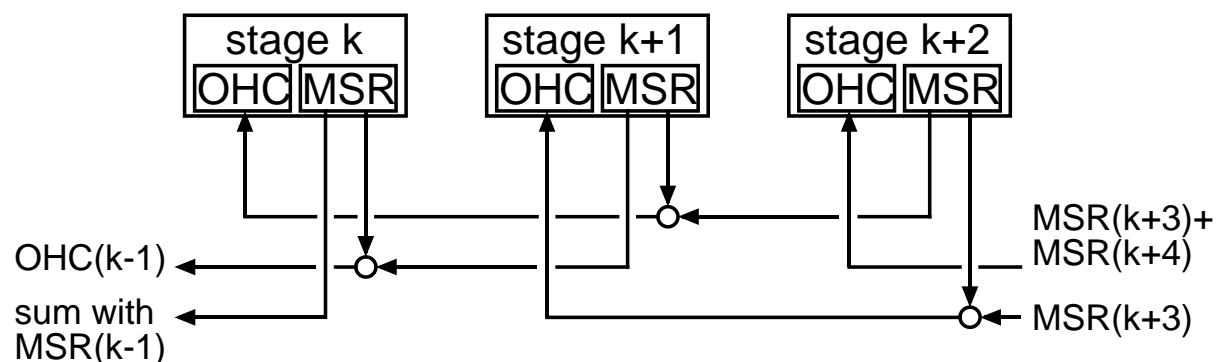


Figure 3.16: Implementation of the Q -control loop at a feedback distance $d_F = 2$, including the summing of adjacent stages' MSR output current reducing the remaining ac oscillations in the Q -control signal.

3.4.6 Bias currents generation

Figure 3.17 shows the generation of the different bias currents within a stage k and at the level of the full circuit. The bias currents I_B of the IHC and MSR OTAs g_{ma} and g_a are identical since the output current of the latter is the mean rectified output current of the former. According

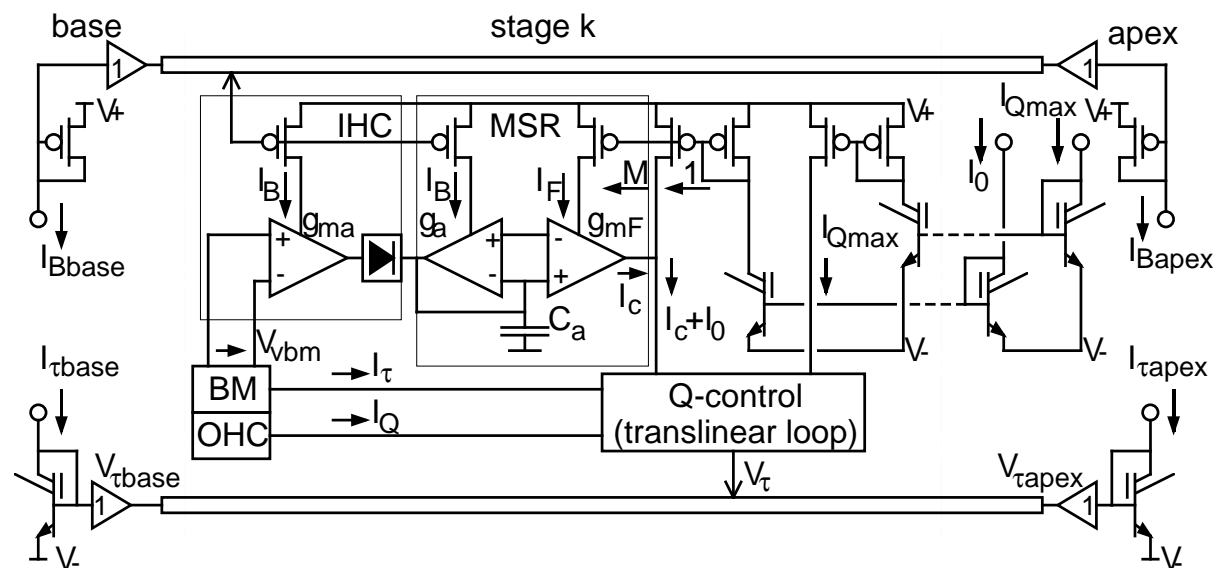


Figure 3.17: Implementation of bias currents for one stage of the cascade; for illustration clarity, in this diagram the MSR output of stage k controls the OHC of the same stage k (feedback distance $d_F = 0$); for the same reason CLBTs are not shown cascaded.

to the conclusion of paragraph 3.4.4, the value of I_B is scaled with the characteristic frequencies of the BM filters using an additional resistive line.

The bias current I_F controlling the transconductance g_{mF} of the feedback OTA is scaled with the normalising current I_0 in order to have a controlling variable $i_c = I_c/I_0$ independent of I_0 . The control variable i_c saturates thus at a value M corresponding to the gain of the mirror generating I_F from I_0 .

Finally, in order to minimise the dispersion of the maximal quality factors Q_{max} along the cascade, the bias currents I_0 and I_{Qmax} are distributed among stages using CLBTs. The dispersion of the current in identical MOS transistors set in weak inversion and having the same gate voltage depends exponentially on the dispersion of their threshold voltage, which can have important gradient on the chip surface. The long distance distribution of I_0 and I_{Qmax} along the cascade is thus performed by CLBTs, whose current is independent from this threshold voltage thanks to their bipolar mode of operation. In most CMOS technologies, only one type of CLBT can be implemented. MOS mirrors cannot be avoided to give the currents I_0 and I_{Qmax} the appropriate polarity. However, these mirrors are local and the mismatch of their threshold voltage is expected to be less important on this short distance; moreover, its effect can be reduced by layout techniques that cancel locally the threshold voltage gradients (common centroid geometries [52]). Note that the CLBTs implementing this long distance current distribution are cascoded and biased as in figure 3.13 (not shown in figure 3.17 for clarity).

3.4.7 Effect of internal noise

The automatic gain control can theoretically compress a 80 dB input dynamic range into a 30dB output dynamic range, but this input dynamic range is limited between the internal noise generated by the circuit and the saturation of its elements. The BM OTAs saturate at voltages above $V_{dbm} \approx 75\text{mV}$ (which corresponds to a 10% deviation from the linear transconductance $g_{m\tau}$). Since in this case the cascade gain is lower than unity, this value defines the maximal input level. At a given output of the cascade, the minimal input level must produce a power equal to that resulting from internal noise. The noise V_{vbmN} at the basilar membrane velocity outputs when no input is present must therefore be estimated.

This estimation will be performed with the Q -control loop disabled. Since this estimation is done for low level signals, its value will be almost identical as the one resulting from the Q -controlled cascade.

The major contribution of this noise results from the accumulation along the cascade of the internal noise generated by each stage. The input-referred noise of each OTA of the second-order filter is represented by its noise resistance R_N which generates a voltage noise v_N having a power spectral density $s_N = 4k_B T R_N$, where k_B is the Boltzmann constant and T the temperature in Kelvin. This input noise resistance is split into two components, $R_N = R_T + R_F$, where R_T produces the thermal contribution of the noise and R_F its flicker contribution. The thermal resistance depends on the OTA transconductance, $R_T = \gamma_T / g_m$. For the BM OTAs, it can be expressed in terms of filter's time constant and capacitance,

$$R_{T\tau} = \gamma_{T\tau} \frac{\tau}{C_\tau}, \quad (3.32)$$

whereas for the OHC OTA it also depends on the quality factor,

$$R_{Tq} = \frac{\gamma_{Tq}}{2 - 1/Q} \frac{\tau}{C_\tau}. \quad (3.33)$$

The flicker resistance is frequency dependent,

$$R_F = \frac{\gamma_F}{C_F 2\pi f}, \quad (3.34)$$

where C_F has the dimension of a capacitance. The noise factors $\gamma_{T\tau,q}$ and $\gamma_{F\tau,q}$ of the OTAs, as well as the *flicker capacitance* C_F are constants which depend only on the design of the OTAs and technological parameters.

The thermal and flicker noise power contribution $V_{T,F}^2(n, d)$ of the second-order filter of the stage $n - d$ at the differentiated output of stage n is calculated by integrating over frequencies the sum of the noise power spectral density generated by each noise resistance in the stage $n - d$ multiplied by the squared transfer function between the noise resistance and the differentiated output of stage n . The small signal analysis of the noisy cascade in figure 3.18 yields (see details in appendix A.1):

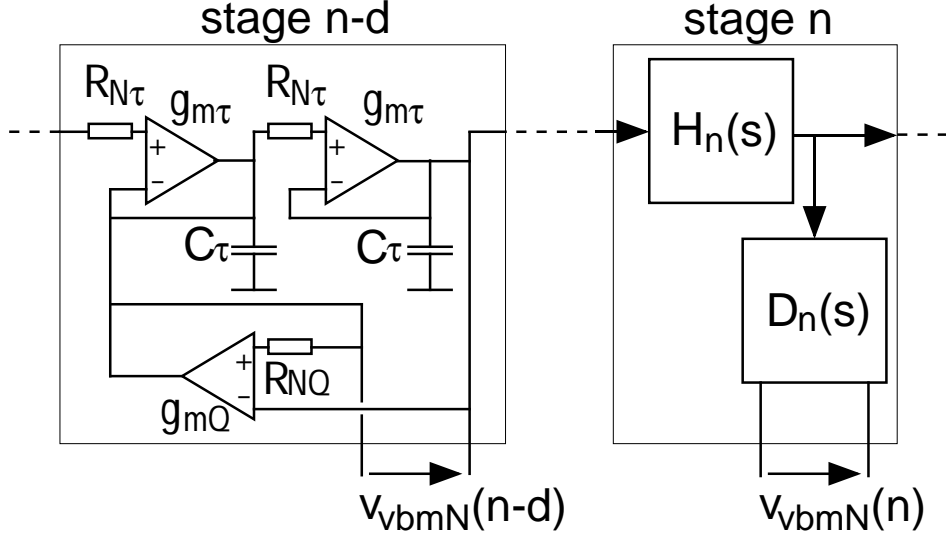


Figure 3.18: Noisy cochlear filter cascade

$$\begin{aligned} \frac{V_T^2(n, d)}{k_B T / C_\tau} &= 2^{-d/b} \Gamma_T(Q) \frac{2}{\pi} \int_0^\infty \Omega^2 G_{n,d}^2(\Omega) d\Omega \\ &+ 2^{-3d/b} \gamma_{T\tau} \frac{2}{\pi} \int_0^\infty \Omega^4 G_{n,d}^2(\Omega) d\Omega, \end{aligned} \quad (3.35)$$

$$\begin{aligned} \frac{V_F^2(n, d)}{k_B T / C_F} &= \Gamma_F(Q) \frac{2}{\pi} \int_0^\infty \Omega G_{n,d}^2(\Omega) d\Omega \\ &+ 2^{-2d/b} \gamma_{F\tau} \frac{2}{\pi} \int_0^\infty \Omega^3 G_{n,d}^2(\Omega) d\Omega, \end{aligned} \quad (3.36)$$

where

$$G_{n,d}(\Omega) = \prod_{l=n-d}^n \|H_l(s = j\Omega/\tau_n)\| \quad (3.37)$$

expresses the gain accumulated on a b stages per octave cascade from the stage $n - d$ to the stage n , as a function of frequency normalised to the characteristic frequency of the stage n . All integrals converge, included for the flicker noise since its $1/f$ dependency yields an output power spectral density proportional to f thanks to the differentiation performed in the stage n . The factors $\Gamma_{T,F}(Q)$ include the noise factor of both BM and OHC OTAs and depend on the quality factor:

$$\Gamma_T(Q) = \gamma_{T\tau} \left[1 + (1 - 1/Q)^2 \right]$$

$$+ \gamma_{Tq} (2 - 1/Q) \quad (3.38)$$

$$\begin{aligned} \Gamma_F(Q) &= \gamma_{F\tau} \left[1 + (1 - 1/Q)^2 \right] \\ &+ \gamma_{Fq} (2 - 1/Q)^2. \end{aligned} \quad (3.39)$$

Equations (3.35) and (3.36) do not apply for $d = 0$ because the noise contributions $V_{T,FD}^2 = V_{T,F}^2(n, 0)$ of the stage n itself is different (see appendix A.1):

$$\begin{aligned} \frac{V_{TD}^2}{k_B T / C_\tau} &= \Gamma_{TD1}(Q) \frac{2}{\pi} \int_0^\infty \|H(\Omega)\|^2 d\Omega \\ &+ \Gamma_{TD2}(Q) \frac{2}{\pi} \int_0^\infty \Omega^2 \|H(\Omega)\|^2 d\Omega, \end{aligned} \quad (3.40)$$

$$\begin{aligned} \frac{V_{FD}^2}{k_B T / C_F} &= \Gamma_{FD1}(Q) \frac{2}{\pi} \int_{\Omega_0}^\infty \frac{\|H(\Omega)\|^2}{\Omega} d\Omega \\ &+ \Gamma_{FD2}(Q) \frac{2}{\pi} \int_0^\infty \Omega \|H(\Omega)\|^2 d\Omega, \end{aligned} \quad (3.41)$$

where

$$\begin{aligned} \Gamma_{TD1}(Q) &= \gamma_{T\tau} \left[2 + (1/Q - 1)^2 + (1/Q - 2)^2 \right] \\ &+ 2\gamma_{TQ} (2 - 1/Q), \end{aligned} \quad (3.42)$$

$$\Gamma_{TD2}(Q) = 2\gamma_{T\tau} + \gamma_{TQ} (2 - 1/Q), \quad (3.43)$$

$$\begin{aligned} \Gamma_{FD1}(Q) &= \gamma_{T\tau} \left[2 + (1/Q - 1)^2 + (1/Q - 2)^2 \right] \\ &+ 2\gamma_{TQ} (2 - 1/Q)^2, \end{aligned} \quad (3.44)$$

$$\Gamma_{FD2}(Q) = 2\gamma_{T\tau} + \gamma_{TQ} (2 - 1/Q)^2. \quad (3.45)$$

Note that the first integral of equation (3.41) has its lower limit set to Ω_0 instead of 0 in order to make it converge. It is the only contribution where the $1/f$ dependency of the flicker noise is not compensated by the differentiation $D(s)$ performed by the IHC. The value of the lower limit Ω_0 is practically determined by the observation time window used for measuring the noise.

The internal noise power $V_{vbmN}^2(n)$ generated by the entire cascade at the basilar membrane velocity output of the stage n is given by summing

the noise power contributions of every stage,

$$V_{vbmN}^2(n) = V_{TD}^2 + V_{FD}^2 + \sum_{d=1}^n [V_T^2(n, d) + V_F^2(n, d)]. \quad (3.46)$$

Equation (3.35) shows that the thermal contribution decreases exponentially with d . Since the accumulated gain $G_{n,d}(\Omega)$ also reaches a value that does not anymore depend on d for large enough d , the thermal noise at the stage n will reach a constant value, even for n growing to infinity. This is explained by the fact that the thermal noise power generated by each filter $H(s)$ is the same $(Q(\Gamma_T(Q) + \gamma_{T\tau})k_B T/C_\tau)$, and since the bandwidth of the filter increases exponentially toward the base, the thermal noise power spectral density decreases at the same rate. The power spectral density of each filter having to be integrated within the bandwidth of the cascade after stage n , which is narrower than the one of the basal stages $n - d$, the thermal noise contribution of basal stages will decrease exponentially, resulting in a thermal noise power independent of the length of the cascade. The situation is different for the flicker noise. The first term in the right hand-side of equation (3.36) does not decrease exponentially with d . The reason is that each stage generates a flicker noise with the same power spectral density, since R_F depends only on fixed layout parameters (the area of the transistors). After the build up of the cascade gain, the flicker noise at the output of the stage n increases linearly with n .

Figure 3.19 shows the dynamic range of an input tone at the frequency at which a stage n best responds, yielding a basilar membrane velocity lying between the saturation of the second-order filter's OTAs and the rms noise at this stage. It was computed for a $b = 6$ stages per octave cascade with realistic design and technological parameters ($\gamma_{T\tau} = 2.55$, $\gamma_{Tq} = 3$, $\gamma_{F\tau} = 19$, $\gamma_{FTq} = 4$, $C_\tau = 10$ pF, $C_F = 1$ pF). The effect of the Q -factor on the dynamic range becomes negligible when it reaches $Q = 2$. In this case, the build-up of the cascade gain together with the accumulation of the noise along the cascade yields a peak dynamic range of 52dB after the first b stages. The input dynamic range then decreases linearly (logarithmically on the dB scale) due to the growing effect of the flicker noise. In a cascade having characteristic frequencies spanning 6 octaves, an operational input dynamic range of nearly 50dB is possible, which is however smaller than the 80dB on which the automatic gain control is effective in a linear and noiseless cascade.

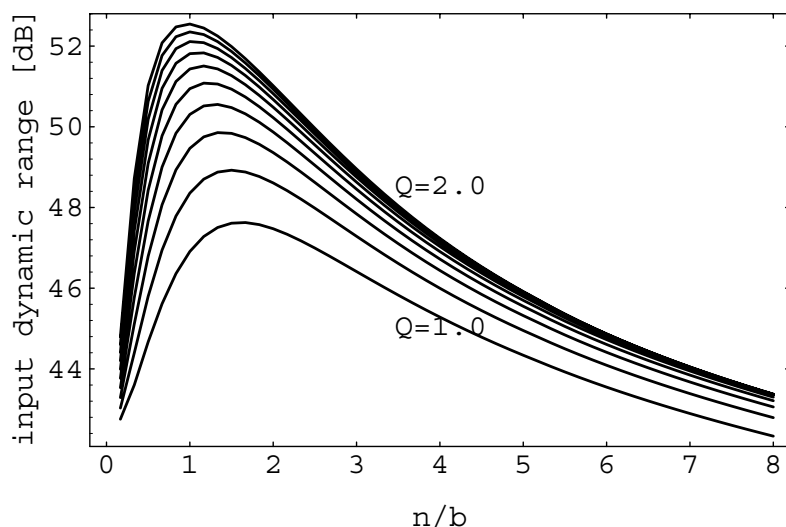


Figure 3.19: Input dynamic range yielding a response between the internal noise and the saturation at the output of stage n , for a cascade set to $b = 6$ stages per octave of characteristic frequency.

3.4.8 Chip measurement results

The circuit was designed for a standard CMOS process (ES2 0.7μ). Since it is a N-well process, only PNP-type CLBTs are available. As a consequence, the translinear loop, the second-order filters, the IHC and MSR OTAs as well as the biasing transistors are the complementary version of the diagram shown in figures 3.13, 3.12 and 3.17, respectively. For the same reason, the inputs of the feedback OTA g_{mF} in figure 3.15 are reversed.

A 36 stages cascade, 7 additional test stages and circuitry for scanning the cascade outputs on a single pin was integrated on a 4mm^2 chip (2.2mm^2 for the cascade alone, where more than half the area is used by MSR and BM capacitors).

The measurements made on chip confirmed the critical points identified during the design, namely the dispersion of the individual stages' quality factors and the effect of the internal noise. As for the MSR time constant, it was impossible to set it large enough to noticeably enhance transients without degrading the performance of the IHC rectifier, due to the too small currents required at its output.

The effect of the dispersion of the quality factors is illustrated in figure 3.20, which shows the maximal cascade open loop gains that could be obtained. The dispersion of the individual quality factor, and to a

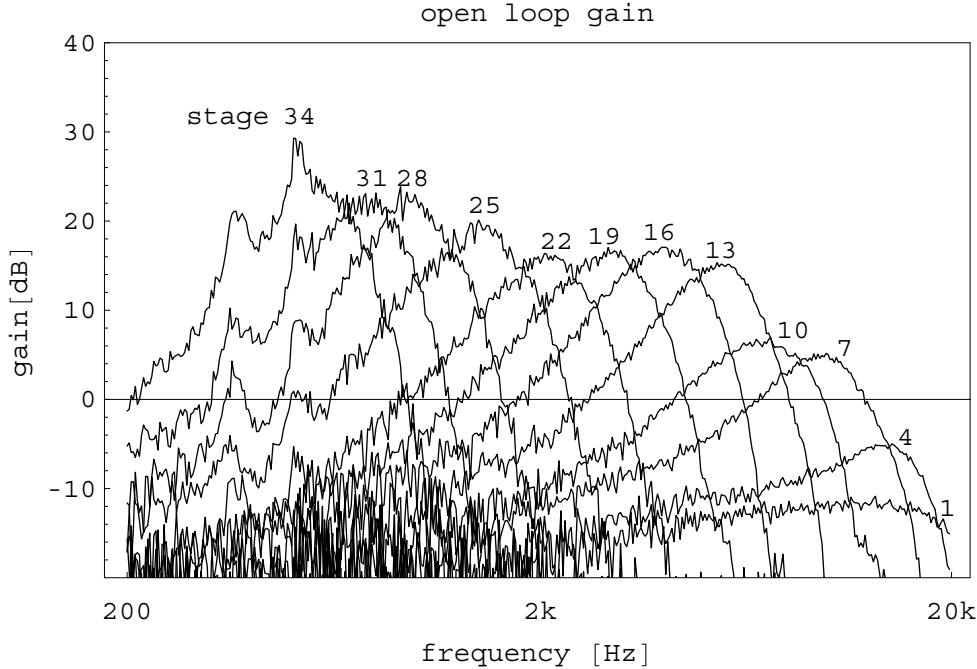


Figure 3.20: Open loop gain measured every 3 stages along the 36 stages cascade chip (Q -control loop disabled).

lesser extent its influence on the regularity of the exponential decrease of the characteristic frequencies, is more important than in the VLSI cochlea [37], where the bias currents I_q was controlled by a common voltage on the emitter of every corresponding CLBTs. In the active cochlea presented here, however, this current depends locally on the currents $I_{Q_{max}}$ and I_0 , which are locally copied by MOS current mirrors, much more sensitive to mismatch than CLBTs (paragraph 3.4.6). As a consequence, the peak gain between the basilar membrane displacement at the input of the cascade and the basilar membrane velocities along the cascade is limited by the maximal individual quality factor, which has to be set to a value smaller than the theoretical $Q_{max} = 2$ in order to ensure the stability of the most sensitive stage (around stage 34 for the measured chip). Instead of the expected 45dB, a peak gain larger than 20dB is hardly obtained from the chip.

This reduced open loop gain, together with the internal noise accumulated along the cascade limits also the input dynamic range effectively compressed by the automatic gain control, as illustrated in figure 3.21. Even for very low input level, the closed loop gain saturates to a value

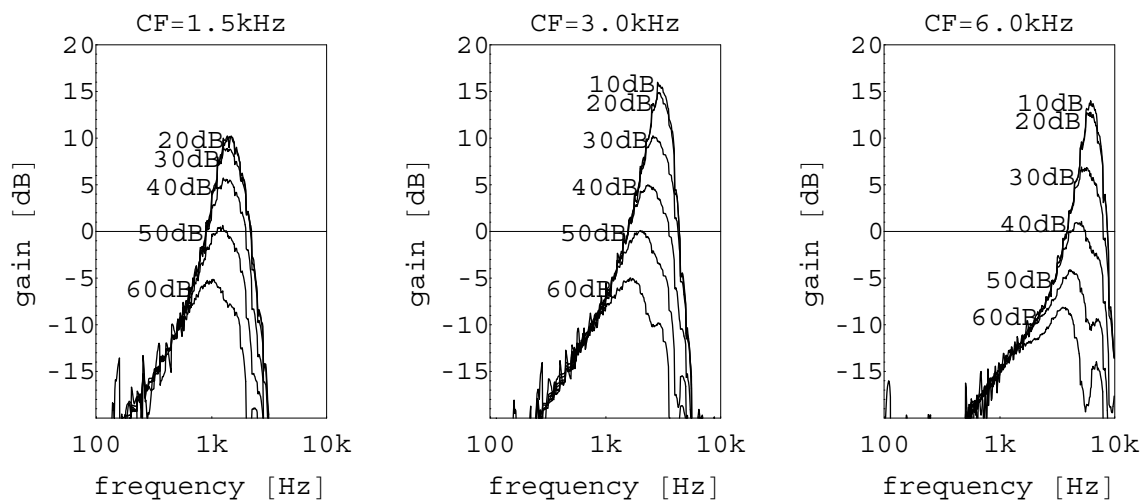


Figure 3.21: Closed loop gain measured at three different position on the 36 stage chip (Q -control enabled), for different input levels (in dB relative to $100\mu\text{V}$).

lower than the 20dB open loop gain, because the internal noise generated by the cascade yields a mean basilar membrane velocity large enough to reduce the quality factor, and thus the closed loop gain. At high characteristic frequency ($CF=6\text{kHz}$), the open loop gain has not yet accumulated to its nominal value, and at lower characteristic frequency ($CF=1.5\text{kHz}$) the accumulated noise has become too important. The maximal closed loop gain was obtained at medium characteristic frequency ($CF=3\text{kHz}$), but instead of compressing the 80dB input dynamic range into a 30dB output dynamic range, only a 40dB to 20dB dynamic range compression could be obtained. This 40dB input dynamic range over which the level compression is active is within the order of magnitude of the maximal input dynamic range estimated to 50dB in paragraph 3.4.7.

Although not as efficiently as in its computer model, the 4mm^2 low-power analogue VLSI chip was shown to implement in real-time a 36 stages cochlear filter cascade featuring a frequency selective automatic gain control.

3.5 Conclusions

The model of the active cochlea proposed in this chapter relies on the assumption that the gain between the vibrations of the basilar membrane at the base of the cochlea and its vibrations at each position along the cochlea is modulated by a local measure of the amplitude of these vibrations. This modulation is performed by controlling locally the damping of the basilar membrane such that at positions where the amplitude of the vibrations is small, the basilar membrane resonates with a high quality factor and inversely. Thanks to the tonotopy of the cochlea, this local modulation of the quality factor results in a frequency selective automatic gain control.

This gain control can be obtained with the simplest feedback loop, i.e. a single connection from the averaged IHC output at each position of the cochlea to the OHC's Q -control input at a slightly more basal position. Since the averaging (MSR) and feedback connection is assumed to model higher level of neural processing, more complicated spatio-temporal processing can be envisaged in the MSR block.

This feedback loop is implemented on a cochlea modeled by a cascade of filters, which permits to obtain large open loop gain with small individual quality factors. Level compression from 80dB input dynamic range into 30dB output dynamic range could be obtained on a computer model, thanks to an accumulated gain varying from -10dB to about 40dB.

This model was integrated on a 4mm² low power analogue VLSI chip, and performed successfully the expected frequency selective automatic gain control. However, due to internal noise and technological parameters variations, the VLSI implementation could not reach the performance of the computer model. If the automatic gain control scheme has proven to bring a valuable improvement in analogue VLSI cochlear modeling, the filter cascade structure limiting its performance must be questioned.

The inherent properties of such *serial* structure is the accumulation of the characteristics of its individual components:

- the reduced gains of relatively low quality-factor filters multiply, yielding accumulated gains that could theoretically reach very high values.
- the internal noise generated by individual elements accumulates along the cascade.
- the delays introduced by individual stages add.

As a consequence, the structure is very sensitive to the performance of its individual components. A malfunction of one of them has a dramatic effect on all further components in the cascade.

In the particular case of the cochlear filter cascade, the key characteristics of its stages vary exponentially. The accumulation of exponentially decreasing characteristics are bounded, even for an infinite-length cascade. For this reason, the pseudo-resonant gain involves a limited number of low-pass filters having decreasing cutoff frequencies. Its limit peak value depends on the decrease rate of the cutoff frequencies. The same applies for the accumulated thermal noise, which depends on the same decrease rate. This implies that the input dynamic range over which the pseudo-resonant gain is modulated by the Q -control loop cannot be increased by introducing more filters to span a given range of characteristic frequency.

At the other extreme, the gain of the individual filters cannot be increased using higher individual quality factor, because this would also sharpen their frequency response, making more difficult the setting of a cutoff frequency decrease rate that ensures the appropriate overlapping of individual frequency response necessary to build a regular pseudo-resonant frequency response. Another reason for a limited quality factor is the sensitivity to the mismatch of the components in a VLSI implementation. The consequence of this relatively low individual quality factor is that despite a theoretically large pseudo-resonant gain, the pseudo-resonant frequency selectivity corresponds to the one of an individual stage, which is much smaller than the one measured in live cochleae for low sound level. Nevertheless, the high frequency side of the frequency response has a much steeper slope than the 12dB per octave of an individual second-order low-pass filter.

Since the cutoff frequency of the filters decreases exponentially, their time constant increases at the same rate. Each second-order low-pass filter in the cascade, loaded by the infinite input impedance of the next stage, adds a phase lag of $\pi/2$ at its cutoff frequency. Imposing more filters to span a given range of cutoff frequencies would increase the delay accumulated along the cascade, which depends therefore on its spatial (and, thus, frequency) resolution. In a cascade model of the cochlea, each stage should therefore not be seen as a structural model of a the cochlear duct section, but as an emulation of the propagation of the basilar membrane displacement along this section [32]. Although, such description assumes a wave propagation without reflections, it does not model properly

the coupling between sections.

The filter cascade models thus *sequentially* the propagation of the basilar membrane vibration along the cochlea. The interaction between stages consists only of the transmission from a stage to the next of the result of the *local* emulation of this propagation in a section of the cochlea. In reality any segment of the cochlear partition is connected to any other segment through the cochlear liquid, which transmits almost instantaneously the acoustical input signal all along the cochlea.

A parallel bank of filters having a common input would therefore better model the cochlea. However such purely parallel model does not take into account the interaction between neighbouring stage through the liquid. The propagation of pressure waves induced by the stapes, *as well as by the cochlear partition itself* must be included in the model, which is the case of the 2-D model presented in the next chapter.

Chapter 4

Electrical emulation a 2-D cochlear model

4.1 Introduction

In the previous chapter we concluded that a filter cascade model of the cochlea suffers from several drawbacks, all of them related to its purely serial structure. In this chapter, a quantised 2-D model of the cochlea is proposed, derived from on the hydrodynamics of its continuous 3-D description. The two dimensions taken into account are the longitudinal axis which runs along the basilar membrane from the base to the apex, and a vertical axis perpendicular to the basilar membrane surface.

The practical advantage of the 2-D model is that it may be emulated by a dense network of linear dipoles which performs the analogue computation of the cochlear hydrodynamics in real-time. Moreover, the equivalent cross-section of the cochlea can be mapped onto a network having the same shape, which is hard to achieve using numerical computation.

As opposed to the cascade model, the cochlear partition is modeled by a parallel structure since it is implemented by a bank of resonators. However, these resonators are connected together by the network modeling the liquid and since they are not high input impedance stages, they interact with each other. The strength of these interactions depends on the proximity of the interacting resonators and the ratio between their impedance and the local impedance of the network.

Compared to 1-D hydrodynamic models, which considers only the longitudinal axis, the 2-D model additionally takes into account the liquid movements perpendicular to the basilar membrane. These vertical movements are necessary to describe the different regimes of wave propagation along the cochlea (long-wave far before, short-wave around and cutoff after the best responding position [34, 27]), and they are important to faithfully model the sharp cutoff observed in live cochlea [9].

In section 4.2 the 3-D model of the cochlea is simplified into a 2-D continuous electrical equivalent, whose quantisation into a network of dipole is analysed in section 4.3. This network is simulated in section 4.4, resulting in the determination of the relevant parameters for faithfully modeling the 3-D hydrodynamics of the cochlea, summarised and discussed in section 4.5.

4.2 2-D model of the cochlea

4.2.1 3-D hydrodynamics of the cochlea

In a liquid of density ρ assumed to be non-viscous, neglecting gravitational forces, the motion of each element of liquid is given by the *Euler equation*:

$$-\mathbf{grad} p(x, y, z) = \rho \mathbf{a}(x, y, z) \quad (4.1)$$

where $\mathbf{a}(x, y, z)$ and $p(x, y, z)$ are the acceleration field and the pressure in the liquid, respectively, described in the rectangular coordinates x , y and z as shown in figure 4.1.

Moreover, if the liquid is incompressible, time differentiation of the *continuity equation* $\text{div} \cdot \mathbf{v}(x, y, z) + \partial\rho/\partial t = 0$ imposes

$$\text{div} \cdot \mathbf{a}(x, y, z) = 0. \quad (4.2)$$

Equations (4.1) and (4.2) mean that the acceleration potential $p(x, y, z)/\rho$ in the liquid satisfies the *Laplace equation*

$$\Delta \frac{p(x, y, z)}{\rho} = \text{div} \cdot \mathbf{grad} \frac{p(x, y, z)}{\rho} = 0 \quad (4.3)$$

with the boundary conditions $\mathbf{a}(x, y, z)_b$ or $p(x, y, z)_b$ imposed at the coordinate $(x, y, z)_b$ of the surface enclosing the liquid. In the cochlea these

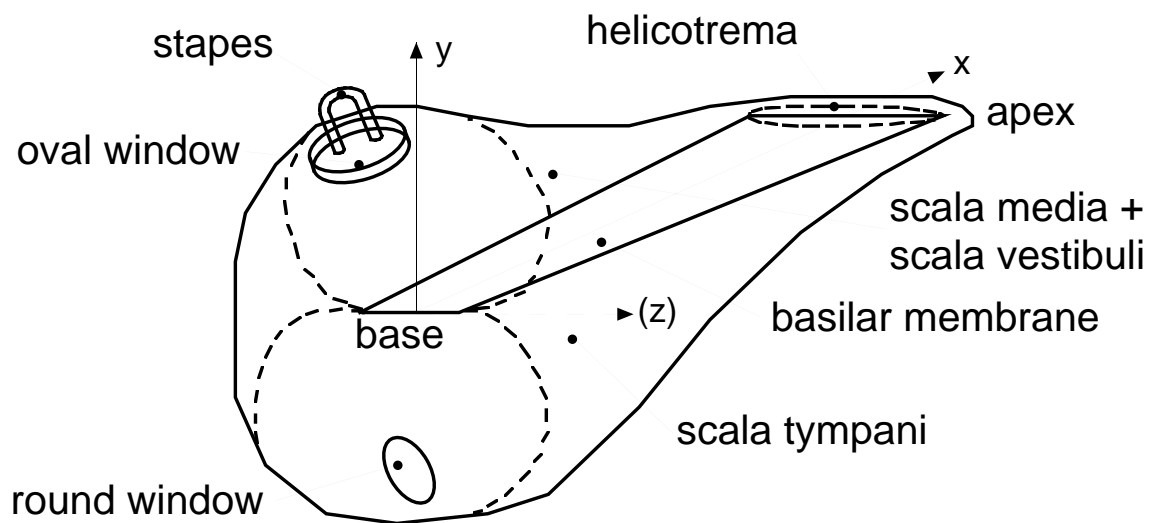


Figure 4.1: 3-D uncoiled cochlea.

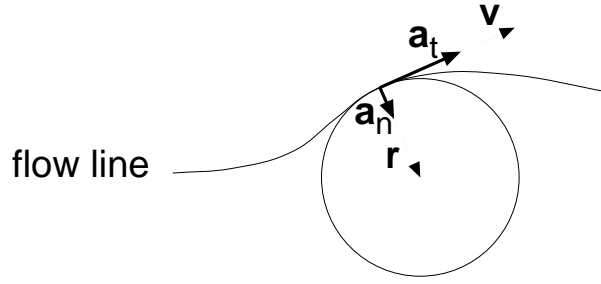


Figure 4.2: Acceleration vectors along a flow line in the cochlear liquid.

boundaries consist of the bony shell, the oval and round windows and the basilar membrane. Due to the negligible mechanical influence of the Reissner's membrane, the scala media and vestibuli are merged in this analysis.

At each position (x, y, z) the acceleration vector \mathbf{a} is the sum of a component $\mathbf{a}_t = \partial \mathbf{v} / \partial t$ tangential to the flow line, where \mathbf{v} is the local liquid velocity vector, and a component $\mathbf{a}_n = \|\mathbf{v}\|^2 \mathbf{r} / \|\mathbf{r}\|^2$ normal to the flow line, where \mathbf{r} is its local curvature radius vector (which points from the flow line to its centre of curvature, see figure 4.2). Each frequency component of the normal acceleration $\mathbf{a}_n(\omega) = \omega^2 \|\mathbf{d}(\omega)\|^2 \mathbf{r} / \|\mathbf{r}\|^2$ may be neglected with respect to those of the tangential acceleration $\mathbf{a}_t(\omega) = \omega^2 \mathbf{d}(\omega)$ if the local curvature radius $\|\mathbf{r}\|$ is much larger than the amplitude $\|\mathbf{d}(\omega)\|$ of the local liquid displacement along the stream line.

Liquid displacement perpendicular to the inflexible wall of the bony shell surface is impossible, thus the flow lines are tangential to the bony shell boundary. Since we can reasonably assume that the curvature radius at any position on the bony shell boundary is much larger than any liquid displacement along this boundary, the acceleration component normal to the bony shell boundary can be neglected, yielding for the bony shell boundary condition of equation (4.3):

$$\mathbf{a}_n(x, y, z)_{BS} = 0. \quad (4.4)$$

Note that this assumption may appear not to be valid at the helicotrema, where the curvature radius of the flow lines is shorter due to their U-turn from the scala vestibuli into the scala tympani. Moreover, the liquid displacements are more important there because the flow lines compress in crossing the opening of the helicotrema. Nevertheless, at this position of the cochlea no filtering is performed; the validity of this assumption is

likely to have little effect on the effective cochlear processing.

In absence of any displacement imposed by the stapes on the oval and round windows or by the basilar membrane reaction, the assumption 4.4 applies to these boundaries as well. This means that the only acceleration component normal to the oval window is imposed by the input acceleration a_S of the stapes, resulting in the oval window boundary condition of equation (4.3):

$$\mathbf{a}_n(x, y, z)_{OW} = a_S \mathbf{e}_n(x, y, z)_{OW} \quad (4.5)$$

where $\mathbf{e}_n(x, y, z)_b$ is the unit vector normal to the considered boundary at its position $(x, y, z)_b$, defined positively when pointing inside the volume enclosed by this boundary.

Similarly, the acceleration component normal to the basilar membrane surface is due only to its reaction to the difference of pressure between its two faces. Since the basilar membrane is incompressible, the acceleration component normal to its surface on the scala media side is opposite to the acceleration component normal to its surface on the scala tympani side. The boundary conditions of equation (4.3) at the basilar membrane surface facing the scala media $(x, y, z)_{SM}$ and the scala tympani $(x, y, z)_{ST}$ are thus imposed by the basilar membrane acceleration $a_{BM}(x, y, z)_{BM}$, defined positively from scala media toward scala tympani,

$$\begin{aligned} \mathbf{a}_n(x, y, z)_{SM} &= -a_{BM}(x, y, z)_{BM} \mathbf{e}_n(x, y, z)_{SM} \\ \mathbf{a}_n(x, y, z)_{ST} &= a_{BM}(x, y, z)_{BM} \mathbf{e}_n(x, y, z)_{ST} \end{aligned} \quad (4.6)$$

where $(x, y, z)_{SM} = (x, y, z)_{ST} = (x, y, z)_{BM}$ if the basilar membrane is assumed to have no thickness.

Finally the acceleration component normal to the round window, which opens to the pressure of the outside, is determined by integrating equation (4.2) on the whole boundary. Since the acceleration components normal to basilar membrane boundary facing the scala media and the scala tympani cancel and the acceleration component normal to the bony shell boundary is negligible, the round window boundary condition of equation (4.3) becomes:

$$\mathbf{a}_n(x, y, z)_{RW} = -\frac{S_{OW}}{S_{RW}} a_S \mathbf{e}_n(x, y, z)_{RW} \quad (4.7)$$

where S_{OW} and S_{RW} are the areas of the oval and round windows, respectively.

Hence, the boundary conditions are entirely determined by the stapes acceleration a_S , which is given as an input signal to the cochlea, and the acceleration $a_{BM}(x, y, z)_{BM}$ normal to the basilar membrane, which responds to the forces applied by the liquid onto it.

The local acceleration $a_{BM}(x, y, z)_{BM}$ of the basilar membrane depends on the pressure difference between the scala media and the scala tympani, just above and below the basilar membrane:

$$Z'_{(x,y,z)_{BM}} \{a_{BM}(x, y, z)_{BM}\} = p_{SM}(x, y, z)_{BM} - p_{ST}(x, y, z)_{BM} \quad (4.8)$$

where $Z'_{(x,y,z)_{BM}} \{\cdot\}$ is the impedance function per unit area expressing the local mechanical properties of the basilar membrane.

The pressures $p_{SM}(x, y, z)_{BM}$ and $p_{ST}(x, y, z)_{BM}$ are determined by solving the Laplace equation (4.3) and its boundary conditions (4.4), (4.5), (4.6) and (4.7), but the boundary condition (4.6) depends in turn on the pressure through equation (4.8). The problem can be solved using a Green's function computed from the geometry of the cochlea which links the force at any position on the boundary with the acceleration at any other position on the boundary [24] (see also appendix A.3). Alternatively, a numerical solution of the problem can be obtained using a finite difference approximation of the Laplace equation and its boundary conditions [26].

This calculation may be emulated in real-time in an electrical equivalent, as proposed in [27]. In order to calculate the acceleration field efficiently, the 3-D model is reduced to a 2-D model without sacrificing the important characteristics of the cochlear hydrodynamics.

4.2.2 2-D electrical equivalent

The 2-D model shown in figure 4.3a consists of a longitudinal cross-section along the basilar membrane of the uncoiled cochlea shown in figure 4.1. The x -axis runs along the basilar membrane, which is assumed to have no thickness, whereas the y -axis is normal to the basilar membrane surface. The width of the basilar membrane (in the dimension ignored by the 2-D model) is given by $w(x)$, as shown in figure 4.3b. The 3-D model is reduced to a 2-D approximation by assuming that each cross-section perpendicular to the longitudinal x -axis is a rectangle having the same width as the basilar membrane, $w(x)$, and whose height is given by the longitudinal

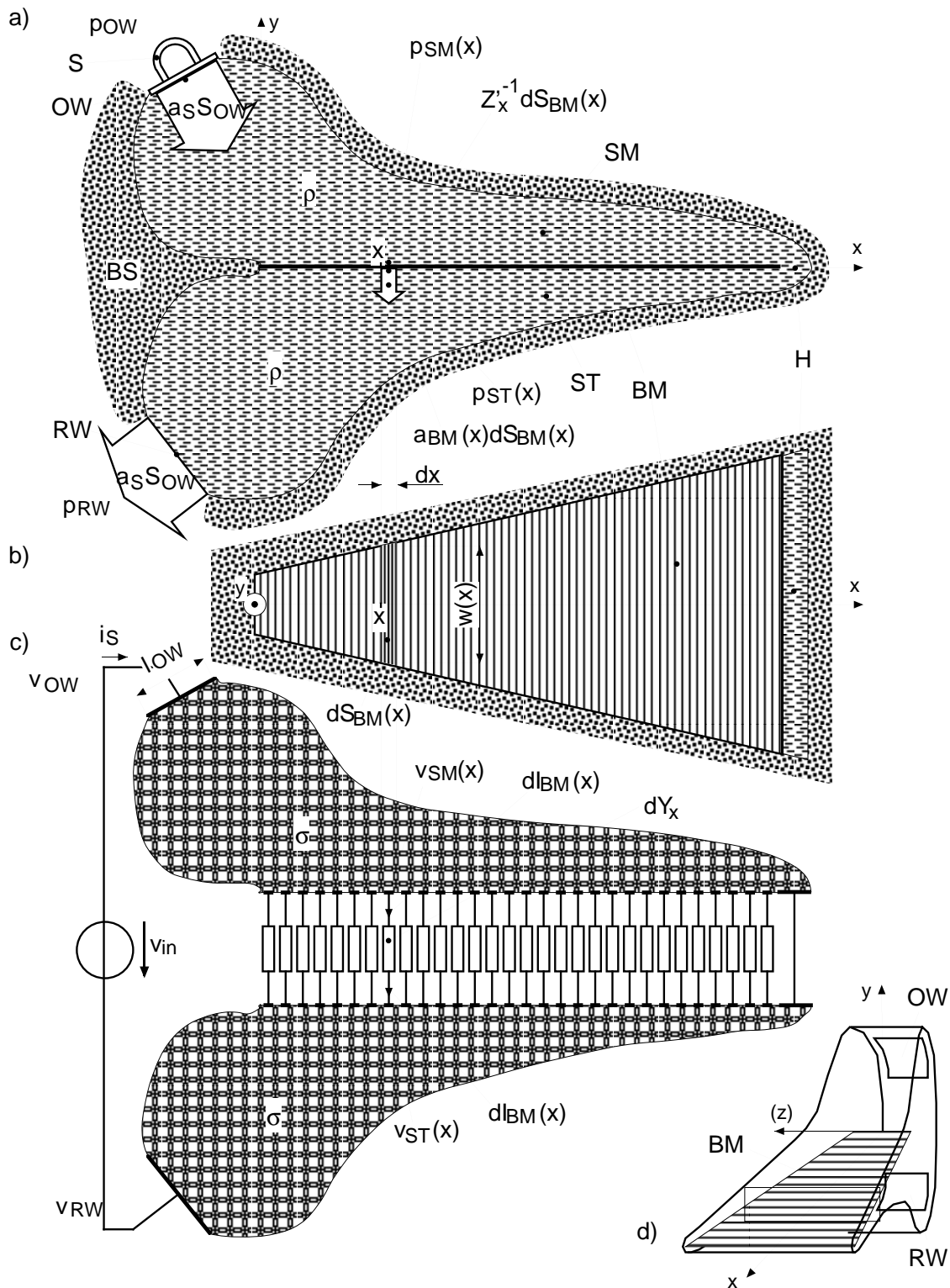


Figure 4.3: a) Longitudinal cross-section of the uncoiled cochlea; b) shape of the basilar membrane; c) equivalent electrical circuit, d) simplified 3-D cochlea used for 2-D reduction.

cross-section of the cochlea (figure 4.3d). This means that only the mass of the liquid above and below the basilar membrane is taken into account. Moreover the pressure and the acceleration field in the liquid are assumed constant along the width of the membrane, i.e., along the z -axis dropped in the dimension reduction, as well as the mechanical properties of the basilar membrane.

Doing so, the liquid density ρ in the 3-D model becomes a surface density $\rho w(x)$, which is scaled in the x -direction by the width $w(x)$ of the basilar membrane. Similarly, the pressure $p(x, y, z)$ becomes a force per unit length $p(x, y)w(x)$. According to equations (4.5) and (4.7), the acceleration flow entering the cochlea through the oval window and escaping the cochlea through the round window is given by $a_S l_{OW}$, where $l_{OW} = S_{OW}/w_{OW}$ is the 2-D equivalent of the oval window area S_{OW} . Similarly, the acceleration flow of a basilar membrane segment of length dx is given, using equation (4.8) by

$$a_{BM}(x)dx = Z'_x{}^{-1} \{ [p_{SM}(x, 0) - p_{ST}(x, 0)] w(x) \} dx, \quad (4.9)$$

where $Z'_x \{ \cdot \}$ is the impedance function per unit length of the basilar membrane at position x .

The electrical analogy shown in figure 4.3c is now straightforward. The liquid is modeled by a resistive sheet having a sheet resistivity $1/\sigma(x)$ (in $[\Omega] = [VA^{-1}]$) proportional to the surface density $\rho w(x)$. The relationship between the sheet current density \mathbf{J} (in $[Am^{-1}]$) and the electric field \mathbf{E} (in $[Vm^{-1}]$) in a resistive sheet obeys the conduction equation

$$\mathbf{J}(x, y) = \sigma(x, y)\mathbf{E}(x, y), \quad (4.10)$$

where the electric field $\mathbf{E}(x, y)$ derives from the potential $V(x, y)$:

$$\mathbf{E}(x, y) = -\mathbf{grad} V(x, y). \quad (4.11)$$

The continuity equation applies also for sheet current densities,

$$\text{div} \cdot \mathbf{J}(x, y) = 0, \quad (4.12)$$

resulting in the Laplace equation

$$\sigma(x, y)\Delta V(x, y) = 0, \quad (4.13)$$

with the boundary condition $\mathbf{J}(x_b, y_b)$ or $V(x_b, y_b)$ imposed at the edge (x_b, y_b) of the resistive sheet.

According to the 3-D hydrodynamics described in paragraph 4.2.1, the stapes acceleration a_S imposing the oval window boundary condition 4.5 should be implemented by injecting a constant surface current density J_S along the edge of the resistive sheet corresponding to the oval window. In many computer models, the stapes' acceleration a_S is also given as an input because it simplifies the calculation of the solution. However, the input of the auditory pathway is the acoustical pressure. The stapes' acceleration is determined from this input through the equivalent impedance of the outer and middle ear together with the impedance of the cochlea. Assuming a constant pressure p_{OW} at the oval window, an alternative solution easier to implement in an electrical model consists of imposing an input voltage V_{OW} proportional to the force per unit length $p_{OW}w_{OW}$ at the oval window. This can be obtained using a metallic contact all along the corresponding edge l_{OW} . At the round window, which opens onto atmospheric pressure, a similar contact allows the circuit to be closed with a voltage source V_{in} between the oval and round window contacts.

Finally the mechanics of the basilar membrane reaction is modeled by a bank of infinitesimal dipoles connecting the scala media and the scala tympani. Each dipole is crossed by an infinitesimal current $dI_{BM}(x) = J_{BM}(x)dx$ imposed by the voltage difference $V_{SM}(x) - V_{ST}(x)$ between their two poles:

$$dI_{BM}(x) = dY_x \{V_{SM}(x) - V_{ST}(x)\} \quad (4.14)$$

where $dY_x \{\cdot\}$ is the admittance function of the infinitesimal dipoles at position x .

Comparing equations (4.3) and its boundary conditions, (4.2) and (4.9) with equations (4.13) and its boundary conditions, (4.12) and (4.14), respectively leads to the correspondences listed in table 4.1.

The hydrodynamic quantities and the electrical quantities are related to each other by scaling factors. The force per unit length pw is related to the voltage V by the *voltage scaling factor* $F_v = V/pw$ (in $[Vs^2kg^{-1}]$) and the acceleration \mathbf{a} is related to the sheet current density \mathbf{J} by the *current scaling factor* $F_j = \mathbf{J}/\mathbf{a}$ (in $[As^2m^{-2}]$). As a result, the sheet conductivity above and below the basilar membrane is given by

$$\sigma(x) = \frac{F_j}{F_v} \frac{1}{\rho w(x)}, \quad (4.15)$$

Hydrodynamics quantities	Electrical quantities
ρw [kgm ⁻¹ s ⁻²][m]	V [V]
\mathbf{a} [ms ⁻²]	\mathbf{J} [Am ⁻¹]
ρw [kgm ⁻³][m]	$1/\sigma$ [VA ⁻¹]
$a_{BM}(x)dx$ [ms ⁻²][m]	$dI_{BM}(x)$ [A]
$Z'_x{}^{-1}\{\cdot\}dx$	$dY_x\{\cdot\} = Y'_x\{\cdot\}dx$

Table 4.1: Analogy between the hydrodynamic equations of the cochlea and its 2-D electrical equivalent.

and the basilar membrane admittance function per unit length becomes

$$Y'_x\{V\} = F_j Z'_x{}^{-1} \left\{ \frac{Vw(x)}{F_v} \right\}. \quad (4.16)$$

4.2.3 Micro-mechanics in the organ of Corti

Neglecting any interactions between them (such as shearing resistance and longitudinal stiffness), each section of the cochlear partition (basilar membrane and organ of Corti) reacts to the force $dF(x)$ applied onto it with a displacement $y(x)$ in the direction of the force according to

$$dF(x) = \frac{\partial^2 y(x)}{\partial t^2} m'(x) dx + \frac{\partial y(x)}{\partial t} h'(x) dx + y(x) k'(x) dx \quad (4.17)$$

where $m'(x)$, $h'(x)$ and $k'(x)$ are the mass, viscosity, and stiffness by unit length of the basilar membrane and its overlying organ of Corti. The viscosity term may appear to be in contradiction with the assumption of negligible viscosity stated in writing equation (4.1). It turns out that, the viscosity cannot be neglected in the complicated micro-structure of the organ of Corti, where the up-down displacement of the basilar membrane is transformed into a lateral displacement of the reticular lamina relative the tectorial membrane (figure 4.4). The viscosity of the endolymph in the narrow space between these two surfaces causes energy losses which damp the basilar membrane movement. The force term $dF(x)$ (defined as positive in the direction of positive y) is the sum of the forces $dF_{BM}(x) = -[p_{SM}(x, 0) - p_{ST}(x, 0)]w(x)dx$ due to the pressure difference between the scala media and tympani, and a force $dF_{OHC}(x)$ caused by the *active reaction of the outer hair cells*.

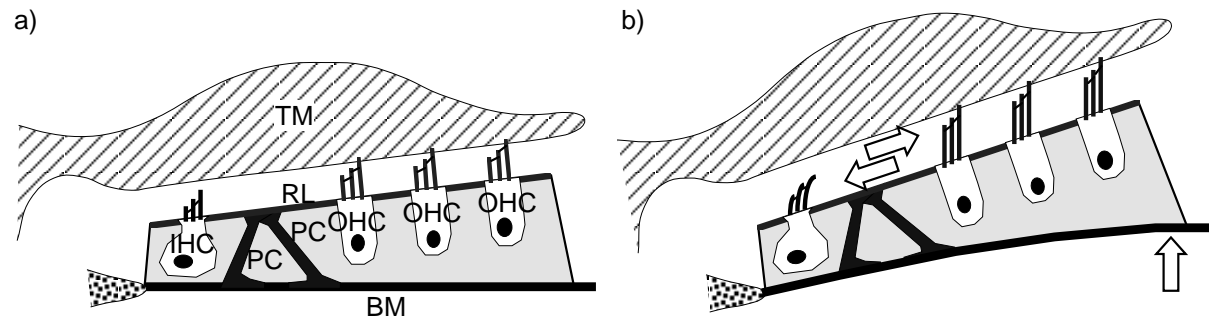


Figure 4.4: Cross-section of the cochlear partition showing the conversion of the vertical basilar membrane movement into a shearing movement between tectorial membrane (TM) and reticular lamina (RL).

The outer hair cells have motile properties which are believed to be responsible for a positive feedback of the force applied on the basilar membrane through the following mechanism, depicted in figure 4.5:

1. The basilar membrane is pushed (pulled) toward the scala media (tympani) by the force $(-)\,dF_{BM}$.
2. The organ of Corti follows the vertical displacement y of the basilar membrane. Due to the rigid framework of the pillar cells and the reticular lamina and since the ends of the tallest stereocilia of the outer hair cells are firmly anchored in the tectorial membrane, this vertical movement would be transformed into a lateral movement d of the attachment point of the stereocilia on the tectorial membrane, if the stereocilia were infinitely stiff.
3. Due to the flexion stiffness of the stereocilia, the radial compression stiffness and the mass of the tectorial membrane, as well as the resistances of the stereocilia in the endolymph, the movement d induces a flexion of the stereocilia characterised by the displacement δ of its attachment point on the tectorial membrane.
4. The flexion of the outer hair cells' stereocilia opens (closes) transducer channels allowing a potassium current to depolarise (hyperpolarise) the cell by increasing (decreasing) its intracellular potential v .

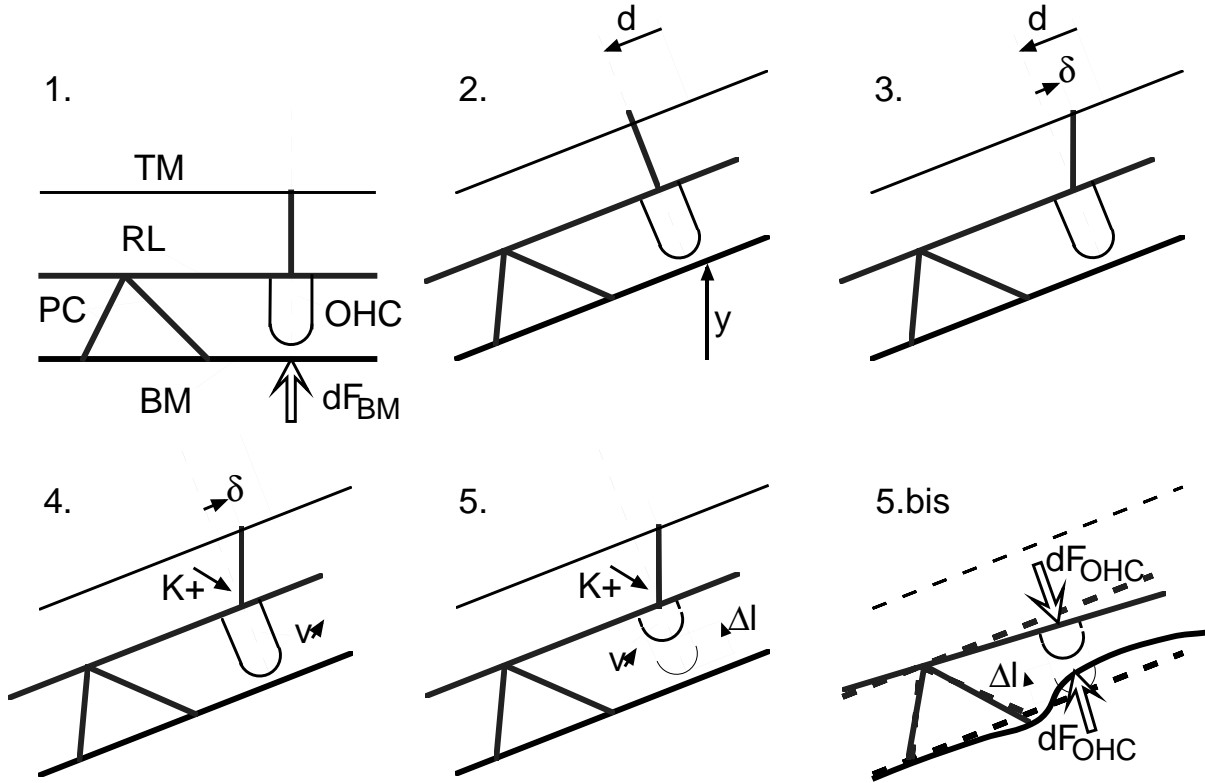


Figure 4.5: Outer hair cell feedback mechanism.

5. The body of the outer hair cell shortens (elongates) as the intracellular potential increases (decreases), resulting in the force F_{OHC} pulling (pushing) the basilar membrane further up (down). The length variation Δl has been shown to be a saturating function of the intracellular potential v [15].

The detailed mechanisms of this feedback loop have been investigated ([21], [18], [25], [15], [22], [46], [24], [47]) but too many unknowns remain in these mechanisms and in the order of magnitude of their parameters (often measured on animals of different species). Although these analyses are sometimes based on quite different assumptions, they all conclude that this feedback would result in an *undamping* term h'_u imposing:

$$dF_{OHC}(x) = \frac{\partial y(x)}{\partial t} h'_u(x) dx. \quad (4.18)$$

This term permits to reproduce closely the frequency characteristics measured on live cochleae. It is beyond the scope of this work to investigate

further the mechanisms of the outer hair cell's feedback loop, and this model is based on the commonly accepted undamping paradigm (4.18).

Equation (4.17) thus yields in the Laplace domain:

$$\frac{1}{y(x)} \frac{dF_{BM}(x)}{dx} = s^2 m'(x) + sh'(x)(1-u) + k'(x) \quad (4.19)$$

where the undamping ratio $u = h'_u(x)/h'(x)$ is hypothesised to be slowly controlled by the efferent innervation of the outer hair cells which would bias the operating point of the saturating transfer function $\Delta l(v)$ of the feedback stage 5 [18]. This bias would modify the motility gain $d\Delta l/dv$ with which the cell length changes in response to small intracellular potential variations, controlling in this way the undamping factor $h'_u(x)$.

Since the acceleration $a_{BM}(x)$ of the basilar membrane (defined positively from scala media toward scala tympani in section 4.2.1) is expressed by $-s^2 y(x)$ in the Laplace domain, and recalling that $dF_{BM}(x) = -[p_{SM}(x) - p_{ST}(x)]w(x)dx$, equation (4.19) can be rewritten

$$\begin{aligned} [p_{SM}(x) - p_{ST}(x)]w(x) = \\ \frac{s^2 m'(x) + sh'(x)(1-u) + k'(x)}{s^2} a_{BM}(x) \end{aligned} \quad (4.20)$$

Comparing equation (4.20) and (4.9), the impedance function per unit length $Z'_x\{\cdot\}$ becomes a linear impedance per unit length

$$Z'(x) = m'(x) + \frac{h'(x)(1-u)}{s} + \frac{k'(x)}{s^2}, \quad (4.21)$$

which imposes

$$[p_{SM}(x) - p_{ST}(x)]w(x) = Z'_x\{a_{BM}(x)\} = Z'(x)a_{BM}(x), \quad (4.22)$$

Its electrical equivalent thus becomes, using equation (4.16), a linear admittance per unit length

$$Y'(x) = \frac{F_j}{F_v} \frac{1}{Z'(x)}. \quad (4.23)$$

4.3 Electrical model

4.3.1 Longitudinal symmetry

Figure 4.3 shows that the 2-D equivalent of the cochlea is almost symmetric about the x -axis. Imposing a perfect symmetry of both scalae

and splitting the basilar membrane admittances $dY(x)$ into two identical serial admittances $2dY(x)$, the equivalent admittance between any point (x, y) in the scala vestibuli and any resulting splitting node $(x', 0)$ is the same as the admittance between a symmetrical point $(x, -y)$ in the scala tympani and the same splitting node. With a current flowing from one scala to the other through the basilar membrane admittances (and the helicotrema, which can be considered as a degenerate basilar membrane admittance), the voltage drop between any points (x, y) and any splitting nodes $(x', 0)$ is equal with opposite sign to the voltage drop between any symmetrical point $(x, -y)$ and the same splitting node $(x', 0)$ (both voltage being defined positive from scalae to basilar membrane). This applies for the input voltage at the oval and round windows, thus $v_{OW} - v(x', 0) = -v_{RW} + v(x', 0)$, where $v(x', 0)$ is the voltage on any splitting node $(x', 0)$, which equals thus $(v_{OW} + v_{RW})/2$ for all x' . Splitting the input voltage $v_{in} = v_{OW} - v_{RW}$ into two identical sources $v_{in}/2$, one between v_{OW} and a reference V_0 and the other between v_{RW} and V_0 , imposes thus $v(x', 0) = V_0$ on all the splitting nodes $(x', 0)$. The entire cochlea can therefore be modeled using the scala vestibuli alone with the admittances $dY(x)$ doubled and the input voltage divided by two, all of them (including the helicotrema) being grounded at a the reference voltage V_0 . Note that equivalently, the input voltage and the basilar membrane admittances can be kept at their original value, but in this case the sheet conductivity must be halved, in which case equation (4.15) is rewritten.

$$\sigma(x) = \frac{F_j}{F_v} \frac{1}{2\rho w(x)}, \quad (4.24)$$

Such a perfect symmetry is of course not achieved in the real cochlea, and this assumption will affect the tonotopical mapping of the cochlea. Nevertheless, since the tonotopy is mainly determined by the basilar membrane stiffness which is not affected by the symmetry assumption, this is an acceptable price to pay for decreasing by a factor two the large number of resistors required to model the liquid.

4.3.2 Spatial quantisation

The resistive sheet could be implemented directly as a resistive layer available in some VLSI analogue processes. However such layers are not available in all processes and their sheet conductivity, imposed by the technol-

ogy, cannot be adjusted. Moreover a continuous model of the basilar membrane admittance per unit length would require a continuous medium to implement the continuous admittance per unit length modeling the graded mass, viscosity and stiffness per unit length, which is unfeasible using the available VLSI processes.

Therefore, a solution consists of spatially quantising the continuous electrical model using a network of dipoles. This network is designed such that it implements exactly the finite difference approximation of the differential equations governing the continuous electrical model, i.e. the Laplace equation (4.13) and its boundary conditions, in particular the basilar membrane's admittance per unit length, described by equation (4.23).

Appendix A.2 shows how the finite difference approximation of the Laplace equation performed on a rectangular grid,

$$\begin{aligned} \Delta V(i\Delta_x, j\Delta_y) & \quad (4.25) \\ \approx \frac{V_{i-1,j} + V_{i+1,j} - 2V_{i,j}}{\Delta_x^2} + \frac{V_{i,j-1} + V_{i,j+1} - 2V_{i,j}}{\Delta_y^2} & = 0 \end{aligned}$$

where Δ_x and Δ_y are the grid spacing in the x - and y -direction, respectively, can be modeled by a rectangular network of resistors. Each node (i, j) of the network is mapped onto the coordinates $(x = i\Delta_x, y = j\Delta_y)$ of the resistive sheet. Each node pair $(i, j) - (i - 1, j)$ is connected together by an horizontal resistor $R_x(i, j)$ and each node pair $(i, j) - (i, j - 1)$ by a vertical resistor $R_y(i, j)$. The current flowing in these resistors corresponds to the current density in the resistive sheet. This current density being a vector field, its components in the x - and y -directions at coordinate $(i\Delta_x, j\Delta_y)$ are given by the average current flowing in the resistors $R_x(i, j)$ and $R_x(i + 1, j)$, and the average current in $R_y(i, j)$ and $R_y(i, j + 1)$, respectively. Since the conduction equation derived from equations (4.10) and (4.11) imposes

$$-\sigma(x, y)\mathbf{grad} V(x, y) = \mathbf{J}(x, y) \quad (4.26)$$

the value of the resistors $R_x(i, j)$ and $R_y(i, j)$ is mapped onto the local conductivity $\sigma(x = [i - \frac{1}{2}]\Delta_x, y = j\Delta_y)$ and $\sigma(x = i\Delta_x, y = [j - \frac{1}{2}]\Delta_y)$ midway between the coordinates corresponding to the nodes connected by the resistors. In addition, the resistance R_x and R_y must be scaled by the aspect ratio of the grid Δ_x/Δ_y and Δ_y/Δ_x , respectively, thus:

$$R_x(i, j) = \frac{1}{\sigma([i - \frac{1}{2}]\Delta_x, j\Delta_y)} \frac{\Delta_x}{\Delta_y} \quad (4.27)$$

$$R_y(i, j) = \frac{1}{\sigma(i\Delta_x, [j - \frac{1}{2}]\Delta_y)} \frac{\Delta_y}{\Delta_x} \quad (4.28)$$

The boundary conditions imposed as a voltage are simply implemented by applying the required voltage at the nodes sampled on the corresponding boundary. The value of the resistors connecting two successive nodes on such boundary is irrelevant. In the particular case of constant voltage applied on the boundary these resistors are shorted by the voltage source.

Alternatively, the boundary conditions which consist of a current density $J_n(x_b, y_b)$ normal to the boundary are imposed by injecting currents into the network. The currents $I(i_{bx}, j_{bx})$ and $I(i_{by}, j_{by})$ at network boundaries following the x -axis and y -axis, respectively, are related to the corresponding current densities $J_y(x_{bx}, y_{bx})$ and $J_x(x_{by}, y_{by})$ by

$$I(i_{bx}, j_{bx}) = J_y(i_{bx}\Delta_x, j_{bx}\Delta_y)\Delta_x \quad (4.29)$$

$$I(i_{by}, j_{by}) = J_x(i_{by}\Delta_x, j_{by}\Delta_y)\Delta_y. \quad (4.30)$$

The resistors connecting nodes on such a boundary are twice as large as if these resistors were inside the network. This is because the resistive path which spread symmetrically around the line joining two nodes within the network cannot spread outside the boundary when the two nodes lie on it (see in figure 4.6a).

Finally the basilar membrane boundary is similar to a current density boundary, since the current density is imposed by the grounded admittance per unit length $Y'(x)$ which constitutes the boundary $(x, 0)$, as shown in paragraph 4.3.1. This admittance per unit length $Y'(i\Delta_x)$ is quantised by an bank of admittances $Y(i)$ which connect the boundary nodes $(i, 0)$ to ground. The value of the admittances $Y(i)$ is given by

$$Y(i) = Y'(x\Delta_x)\Delta_x \quad (4.31)$$

The resistances $R_x(i, 0)$ following this boundary are also doubled, since in the admittance per unit length $Y'(x)$ no current density can flow in the x -direction.

The spatial quantisation of a rectangular resistive sheet into a network of dipoles is illustrated in figure 4.6. In this example, the resistive sheet has a constant voltage imposed by a metallic contact at its left boundary, current densities imposed at its top and right boundaries and a grounded admittance per unit length at its bottom boundary. The value of the dipoles are summarised in table 4.2.

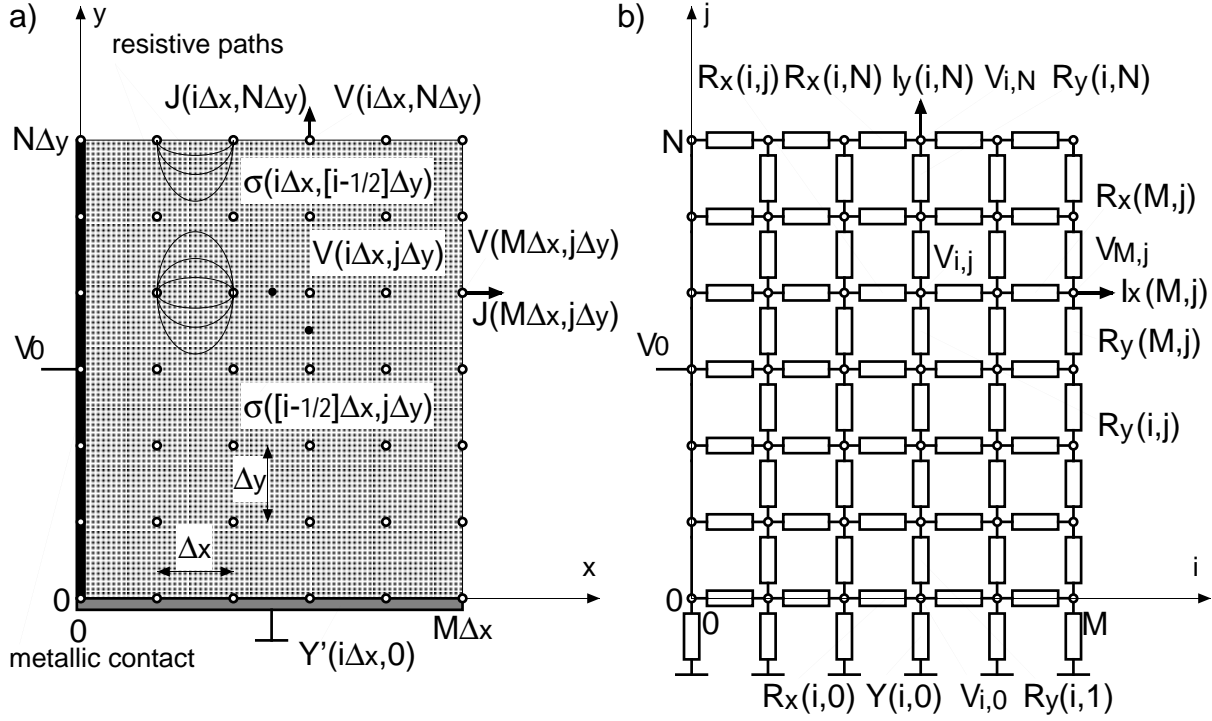


Figure 4.6: Quantisation of a resistive sheet (a) into a resistive network (b).

The error caused by this spatial quantisation of the resistive sheet must be evaluated in order to limit the amount of resistors, which will approximate the resistive sheet with the loosest acceptable grid. The quantisation of the resistive sheet into a network of resistors corresponds to a spatial sampling of the potential $V(x, y)$ at the positions corresponding to the nodes (i, j) of the network, with a linear interpolation in the resistors between these nodes. The sampled potential $V(i, j) = V(x = i\Delta x, y = j\Delta y)$ thus depends on the grid spacing Δx and Δy of the network. The two-dimensional spatial Fourier transform of $V(i, j)$ results in the repetition of the two-dimensional spatial Fourier transform of $V(x, y)$ with a spacing $1/\Delta x$ and $1/\Delta y$ in the x - and y -directions of the spatial frequency plane (f_x, f_y) . These repeated spatial spectra are filtered out by the spatial Fourier transform of the linear interpolation, which has a spectrum of the form $\sin^2(f_x \Delta x) \sin^2(f_y \Delta y) / (f_x^2 f_y^2)$. If the grid spacing Δx or Δy is too large, aliasing can result from the overlapping of the original spatial spectrum with its frequency-shifted copies. In order to prevent such aliasing, the frequency spacing $1/\Delta x$ and $1/\Delta y$ must be at least twice as large as the highest spatial frequency f_x and f_y , respectively, of the voltage $V(x, y)$.

$R_x(i, j) = \frac{1}{\sigma([i - \frac{1}{2}]\Delta_x, j\Delta_y)} \frac{\Delta_x}{\Delta_y}$
$R_y(i, j) = \frac{1}{\sigma(i\Delta_x, [j - \frac{1}{2}]\Delta_y)} \frac{\Delta_y}{\Delta_x}$
$R_x(M, j) = \frac{1}{\sigma([M - \frac{1}{2}]\Delta_x, j\Delta_y)} \frac{\Delta_x}{\Delta_y}$
$R_y(M, j) = \frac{1}{\sigma(M\Delta_x, [j - \frac{1}{2}]\Delta_y)} \frac{\Delta_y}{\Delta_x}$
$R_x(i, N) = \frac{1}{\sigma([i - \frac{1}{2}]\Delta_x, N\Delta_y)} \frac{\Delta_x}{\Delta_y}$
$R_y(i, N) = \frac{1}{\sigma(i\Delta_x, [N - \frac{1}{2}]\Delta_y)} \frac{\Delta_y}{\Delta_x}$
$R_x(i, 0) = \frac{1}{\sigma([i - \frac{1}{2}]\Delta_x, 0)} \frac{\Delta_x}{\Delta_y}$
$R_y(i, 1) = \frac{1}{\sigma(i\Delta_x, \frac{1}{2}\Delta_y)} \frac{\Delta_y}{\Delta_x}$
$Y(i, 0) = \Delta_x Y'(i\Delta_x, 0)$

Table 4.2: Correspondences between resistive sheet parameters and resistive network parameters.

The spatial Fourier transform of the potential $V(x, y)$ should thus be estimated to determine the grid spacing $\Delta_{x,y}$, which would require knowing $V(x, y)$. But since no analytical expression of $V(x, y)$ accurate enough to take into account all the peculiarities of the cochlear hydrodynamics is available, we must rely on numerical computations, themselves based on a spatial quantisation of the variable onto a grid. This point will be further discussed when analysing the simulation results in paragraph 4.4.3.

4.3.3 Basilar membrane resonator

The basilar membrane is quantised by a bank of resonators. Using equations (4.21), (4.23) and (4.31), each basilar membrane resonator has an impedance

$$Z(i) = \frac{1}{Y(i)} = \frac{1}{G_{BM}(i)} + \frac{1}{sC_{BM}(i)} + \frac{1}{s^2S_{BM}(i)} \quad (4.32)$$

whose equivalent electrical circuit consists of a branch formed by three serial dipoles, namely a resistor

$$G_{BM}(i) = \frac{F_j}{F_v} \frac{\Delta_x}{m'(i\Delta_x)}, \quad (4.33)$$

a capacitor

$$C_{BM}(i) = \frac{F_j}{F_v} \frac{\Delta_x}{h'(i\Delta_x)} \frac{1}{1-u}, \quad (4.34)$$

and a *super-capacitor*

$$S_{BM}(i) = \frac{F_j}{F_v} \frac{\Delta_x}{k'(i\Delta_x)} \quad (4.35)$$

which is defined as a dipole whose voltage is proportional to the double temporal integration of its current (see inset of figure 4.7).

The resonator has thus a second-order high-pass admittance

$$Y(i) = G_{BM}(i) \frac{s^2\tau^2(i)}{s^2\tau^2(i) + s\tau(i)/Q(i) + 1} \quad (4.36)$$

having a cutoff frequency $1/2\pi\tau(i)$ defined by the time constant

$$\tau(i) = \sqrt{\frac{S_{BM}(i)}{G_{BM}(i)}} = \sqrt{\frac{m'(i\Delta)}{k'(i\Delta)}} \quad (4.37)$$

and a quality factor

$$Q(i) = \frac{C_{BM}(i)}{\sqrt{G_{BM}(i)S_{BM}(i)}} = \frac{\sqrt{k'(i\Delta)m'(i\Delta)}}{h'(i\Delta)(1-u)} \quad (4.38)$$

4.3.4 Mechanical to electrical mapping

The schematic of the 2-D electrical model is now determined, as shown in figure 4.7. The remaining task is to map the mechanical quantities of the biological cochlea onto the electrical quantities of its analogue model.

According to the physiological data used in [24], the mechanical parameters having important variation along the longitudinal axis are the stiffness of the basilar membrane and the cross-section area of the cochlea. The basilar membrane stiffness decreases exponentially from the base to

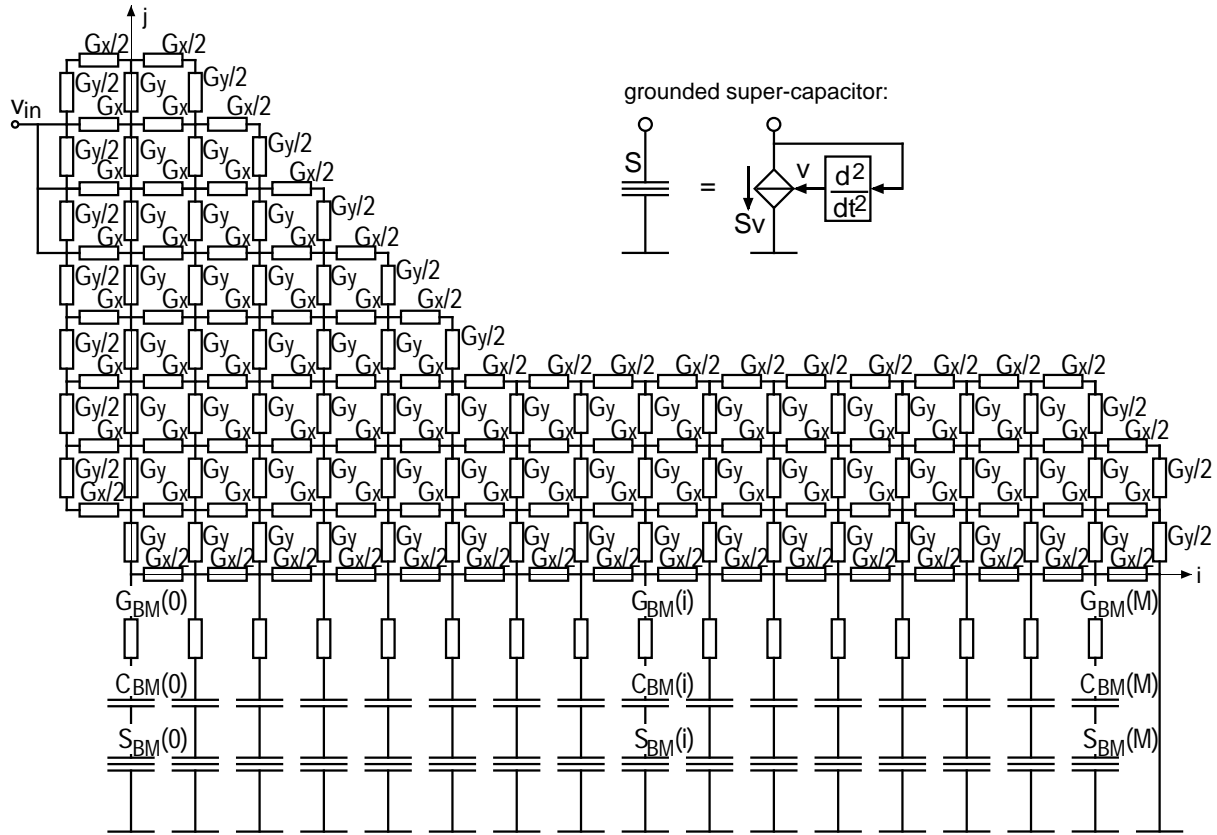


Figure 4.7: Schematic of the 2-D electrical model of the cochlea.

the apex. The exponential decrease of the characteristic frequencies along the cochlea is thus mostly due to this parameter. The cross-section of the cochlea decreases quite abruptly shortly after the base, such that half of the volume of the cochlea (and thus the mass of liquid it contains) is located in the basal quarter of its length.

The basilar membrane width increases by a factor 4 from the base to the apex, but it varies by a factor less than 2 from 10% to 90% of its length. The mass of the basilar membrane together with that of the organ of Corti vary to a lesser extent, since the width of the organ of Corti, which is the major mass contribution, is only slightly scaled on the width of the organ of Corti. The viscosity term was shown to decrease almost linearly by a factor 2 from the base to the apex [24].

Using equations (4.33), (4.34) and (4.35), the electrical quantities G_{BM} , C_{BM} and S_{BM} could be mapped exactly to their mechanical and geometrical equivalents, provided these biological data are known exactly. However, in order to simplify the design of the electronic circuit by using similar

mechanical quantity	electrical element
liquid density	$G_x(i) = \frac{F_j}{F_v} \frac{1}{2\rho w} \frac{\Delta_y}{\Delta_x}$
	$G_y(i) = \frac{F_j}{F_v} \frac{1}{2\rho w} \frac{\Delta_x}{\Delta_y}$
BM mass	$G_{BM}(i) = \frac{F_j}{F_v} \frac{\Delta_x}{m'}$
BM eff. viscosity	$C_{BM}(i) = \frac{F_j}{F_v} \frac{\Delta_x}{h'} \frac{1}{1-u}$
BM stiffness	$S_{BM}(i) = \frac{F_j}{F_v} \frac{\Delta_x}{k'(0)} 2^{i/b}$

Table 4.3: Position dependence of the elements of the basilar membrane resonator.

cells for each section of the cochlea, a constant basilar membrane width $w(x) = w$, mass per unit length $m'(x) = m'$ and viscosity $h'(x) = h'$ are assumed. The variation of the basilar membrane stiffness per unit length is set to be purely exponential by imposing $k'(x) = k'(0)2^{-x/b\Delta_x}$. As a result, the cutoff frequency of the basilar membrane resonators will decrease exponentially at a rate of one octave every $2b$ stages:

$$f_c(i) = \frac{1}{2\pi\tau(i)} = \frac{1}{2\pi} \sqrt{\frac{k'(0)}{m'}} 2^{-i/2b}. \quad (4.39)$$

The quality factor of the resonators

$$Q(i) = \frac{\sqrt{k'(0)m'}}{h'(1-u)} 2^{-i/2b} \quad (4.40)$$

also decreases exponentially along the cascade. The resulting decreasing relative frequency selectivity towards low characteristic frequencies has been observed on the tuning curves measured on the auditory nerve [48]. The equivalence between the mechanical quantities and their electrical model is summarised in table 4.3.

The values of G_{BM} , C_{BM} and S_{BM} , as well as the values of the conductances $G_{x,y} = 1/R_{x,y}$ modeling the liquid are estimated either by matching the behaviour of the resulting model with the observed biological behaviour or by matching them directly with the corresponding quantities

measured in the cochlea. However, this cannot be done simply by matching the characteristic frequencies and filter shapes of the biological cochlea with the cutoff frequencies and quality factor of the basilar membrane resonator, because the processing performed by the cochlea depends largely on the hydrodynamics of the liquid.

4.4 Electrical simulations

4.4.1 Simulated network

In order to estimate the values of the model's parameters yielding transfer functions that correspond to those measured in live cochleae, the 2-D electrical model is simulated using an electrical simulator (Anacad ELDO). Because the electrical model implements the finite difference approximation [26] exactly, the same parameter values are used as reference. These reference values are a constant basilar membrane mass m'' , viscosity h'' per unit area and an exponentially decreasing stiffness $k''(x) = k''(0) \exp(x/d_k)$ per unit area. The mass m' , viscosity h' and stiffness k' per unit length used in table 4.3 are obtained by multiplying m'' , h'' and k'' by the basilar membrane width w , which can be lumped into the scaling factor F_j/F_v since it scales similarly the liquid density ρ . The reference values for the simulation are summarised in table 4.4. Introducing these reference values in equations (4.39) and (4.40) results in a cutoff frequency of 13kHz and a quality factor without undamping ($u = 0$) of 60 in the basal-most basilar membrane resonator. Implementing such quality factor on the VLSI circuit appears to be somewhat challenging.

In [26], the shape of the cochlear duct is approximated by a rectangle for computational reasons. In order to investigate the effect of the real duct shape, the radius of the cochlear duct given in [24] and [47] (figure 4.8a) is used as the height $H(x)$ of the the scalae media and vestibuli merged together. The resulting surface delimited by $y = 0$ and $y = H(x)$ along the y -axis and between $x = 0$ (base) and $x = L$ (apex) along the x -axis is then quantised to a grid imposing M points on the length L of the cochlea and N_{min} points on the smallest height $H_{min} = H(L)$, at the apex (figure 4.8b), defining so the grid size $\Delta_{x,y}$ as given in table 4.4.

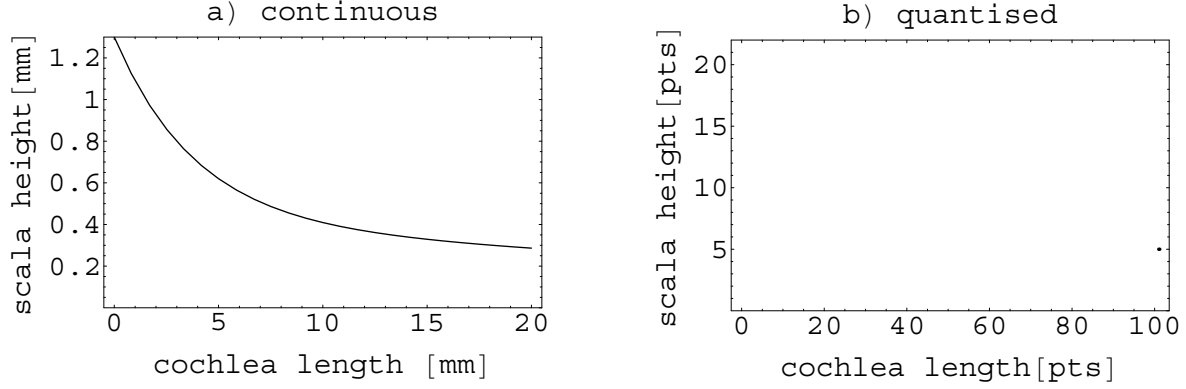


Figure 4.8: a) Continuous shape of the cochlea; b) quantised shape to $M = 100$ points in length and $N_{min} = 5$ points in minimal height.

parameter	reference value
$2\rho w$	$w[\text{m}] \cdot 2 \cdot 10^3 \text{ kg m}^{-3}$
m'	$w[\text{m}] \cdot 1.5 \text{ kg m}^{-2}$
h'	$w[\text{m}] \cdot 2 \cdot 10^3 \text{ kg m}^{-2} \text{ s}^{-1}$
$k'(0)$	$w[\text{m}] \cdot 10 \cdot 10^9 \text{ kg m}^{-2} \text{ s}^{-2}$
b	$\frac{d_k}{\Delta_x} \ln 2 = \frac{0.005 \text{ m}}{\Delta_x[\text{m}]} \ln 2$
Δ_x	L/M
Δ_y	H_{min}/N_{min}

Table 4.4: Reference parameter values for simulation.

4.4.2 Simulation results

An AC simulation of a 20 mm long cochlea quantised to $M = 100$ points in length and $N_{min} = 5$ points in a minimal height of 0.37 mm was performed. Figure 4.9 shows the frequency response of the voltage $V_c(i)$ measured on the capacitors $C_{BM}(i)$ at different positions along the cochlea. This voltage is proportional to the basilar membrane velocity $v_{BM}(i)$, since the capacitor performs the temporal integration of the resonator current $I(i) = J(i, 0)\Delta_x$ which represents the basilar membrane acceleration $a_{BM}(i) =$

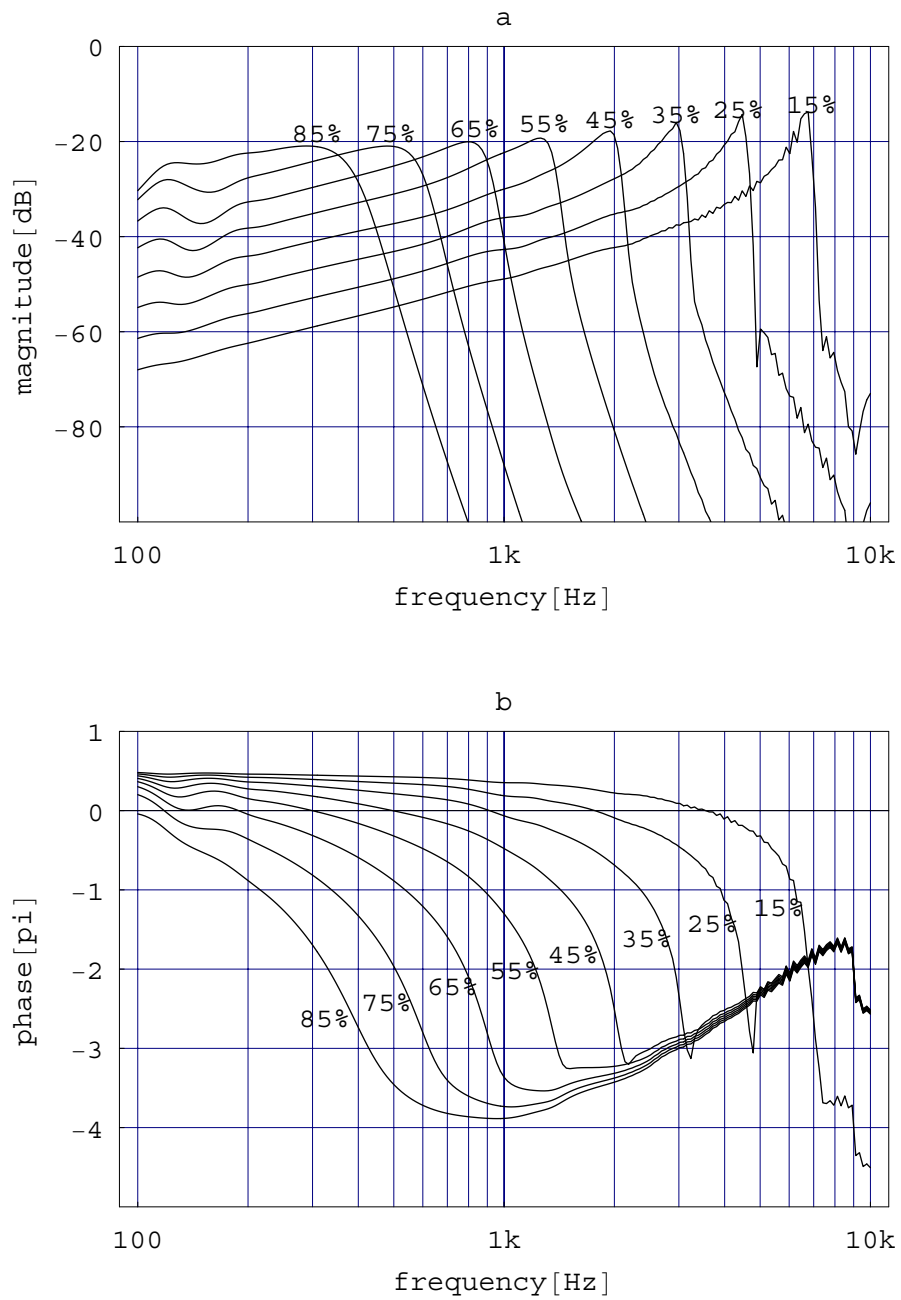


Figure 4.9: a) Magnitude and b) phase of the gain between the input voltage V_{in} at the stapes and the voltage $V_c(i)$ on the capacitor $C_{bm}(i)$ as function of frequency, at different positions $i\Delta_x$ along the cochlea (indicated in % of cochlea length).

$J(i, 0)/F_j$:

$$V_c(i) = \frac{F_j \Delta_x}{C_{BM}(i)} \int_{-\infty}^t a_{BM}(i, t') dt' = \frac{F_j \Delta_y}{C_{BM}(i)} v_{BM}(i, t) \quad (4.41)$$

Using equation (4.34) with the undamping control term u set to zero, the local basilar membrane velocity is thus given by:

$$v_{BM}(i) = \frac{1}{F_v h'} V_c(i) = \frac{1}{F_v h'' w} V_c(i) \quad (4.42)$$

Expressing the input voltage V_{in} by the pressure $p_{in} = V_{in}/(wF_v)$ it models, the curve 4.9a shifted by $-20 \log(h'') = -66\text{dB}$ represents the acoustical transadmittance (in dB relative to $1 \text{ ms}^{-1}/\text{Pa}$) between the input pressure and the local basilar membrane velocity. In other words, with a stapes pressure $p_{in} = 2 \cdot 10^{-5} \text{Pa}$ used as reference to express pressure in “dB SPL” (*Sound Pressure Level*), the vertical axis represents the local basilar membrane velocity in dB referred to 10 nm/s at 0dB SPL on the stapes (about 30 dB SPL on the eardrum for frequencies around 1 kHz , see paragraph 2.2.1, p. 11).

The sharp cutoff of about 300dB/octave measured in live cochleae as well as the corresponding fast phase shift is obtained at high characteristic frequencies. At lower characteristic frequencies the cutoff becomes less sharp as the quality factor of the basilar membrane resonators decreases due to the constant mass and viscosity scaling. On the phase curve, the apparent additional phase shift of 2π after the cutoff measured at 15% of cochlear length seems to be an artifact due to the extension of the phase scale given between $-\pi$ and $+\pi$ by the electrical simulator. The oscillations visible on the transfer function at low frequencies are due to reflections at the helicotrema, whose impedance is not adapted to the local impedance of the cochlea. In the simulation presented here, the amplitude of these oscillations was minimised by replacing the short of the helicotrema to ground by a capacitance equal to the viscous parameter C_{BM} of the resonators, which emulated so the resistance to liquid flow when crossing the small hole of the helicotrema.

4.4.3 Spatial resolution

The effect of the quantisation is shown in figure 4.10. Quantising the x -axis too loosely with respect to the decrease of the resonator characteristic

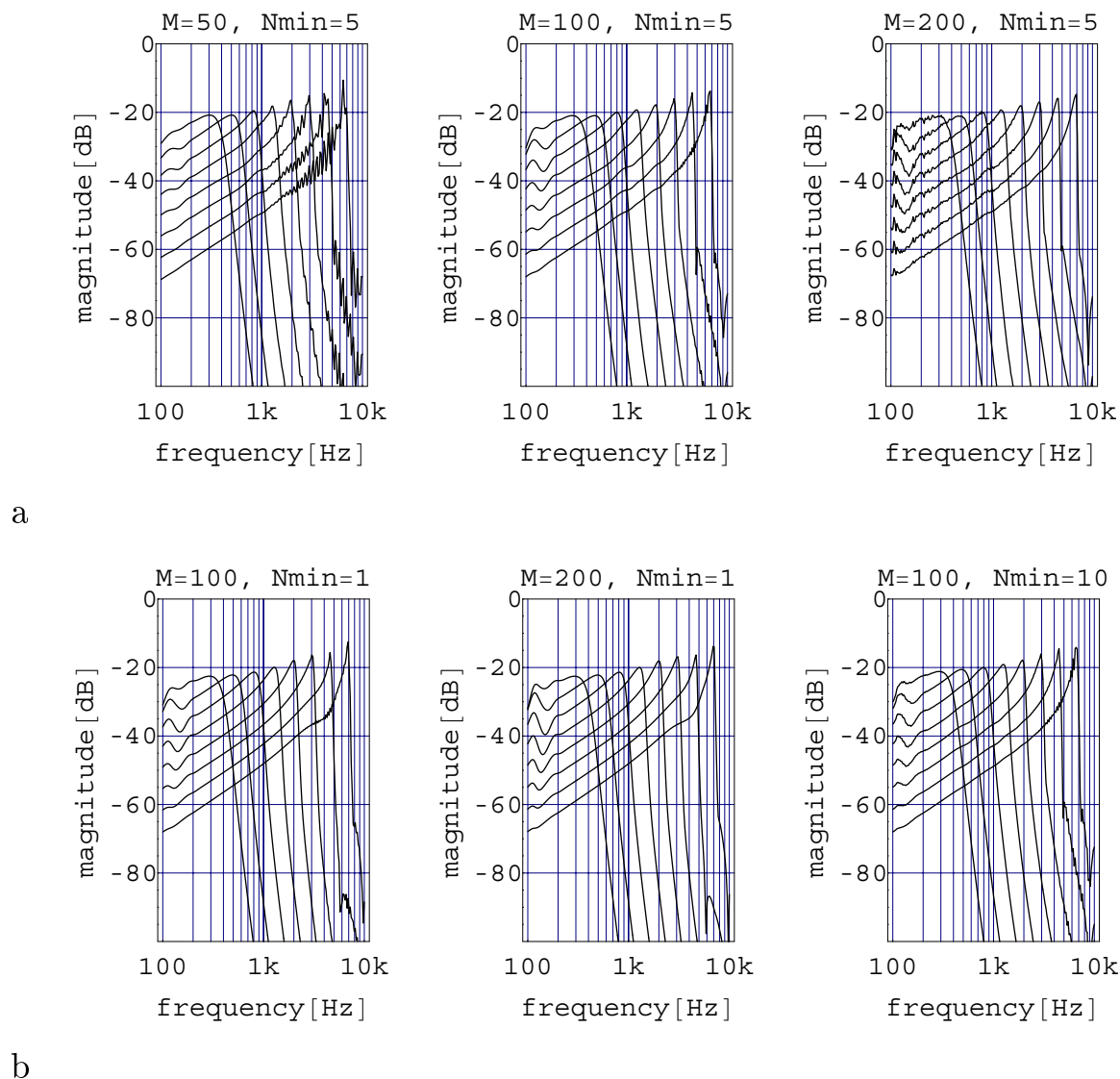


Figure 4.10: a) Quantisation of the x axis with $M = 50, 100,$ and 200 points, keeping $N_{min} = 5$ points at the smallest height of the cochlear duct; b) quantisation of the y axis with $N_{min} = 1$ and 10 points, keeping $M = 100$ (200) points.

frequencies causes oscillations in the frequency response. These appear at higher frequencies, for which the characteristic frequencies of two neighbouring best-responding resonators are too far away from each other. This effect is analysed more thoroughly in paragraph 4.4.4.

The longitudinal quantisation also has an effect on the low-frequency reflection at the apex of the cochlea: the amplitude of the oscillations in

the frequency response at low frequencies increases with the resolution. Since the helicotrema is quantised to a single dipole, the effect of the impedance adaptation it performs becomes negligible when the resolution increases. The helicotrema should therefore be modeled on a fixed length of the cochlea apex rather than by the last resonator of the bank only.

As for the quantisation of the y -axis, figure 4.9b shows that it almost does not affect the magnitude of the frequency response, even with $N_{min} = 1$ which corresponds to only two rows of resistors at the smallest height of the cochlear duct. The most noticeable effect is that the curves corresponding to high characteristic frequencies feature a slight notch before the low-frequency side steepens toward the peak frequency. Surprisingly, this effect occurs only at higher characteristic frequencies, where the cochlear duct is higher and thus quantised with more points. No explanation could be found for this marginal effect.

While keeping the cochlear duct quantised to $N_{min} = 1$ points, the longitudinal quantisation was increased to $M = 200$ points in order to check whether the effect of the minimal y -resolution had an influence on the x -resolution, which would be the case if the cochlear duct were modeled by a single row of resistors. The middle plot of figure 4.9b confirms the independence of the x - and y -resolutions, even when the latter is minimal.

4.4.4 Spatial resolution vs. frequency selectivity

A sharp frequency cutoff at a given stage corresponds to a sharp spatial edge in the responses of the resonators at a given frequency. If these spatial edges are sampled too loosely by a reduced number of resonators, spatial aliasing will cause oscillations in the spatial response and thus in the frequency response (see paragraph 4.3.2). With $M = 50$, these oscillations appear at 2 kHz, which corresponds to the best frequency of the resonator located at 55% of the cochlea length. At this position the difference of the characteristic frequency of two neighbouring resonators is estimated to about 170 Hz, which corresponds to the frequency difference between two peaks of these oscillations around 2 kHz. The grid spacing $\Delta_x = L/M$ must therefore be chosen such that the most selective frequency peaks of two neighbouring resonators sufficiently overlap to yield a single peak. The bandwidth $B(i)$ of the most frequency-selective output i must be larger than the difference $\Delta f(i) = f_p(i) - f_p(i + 1)$ of the peak frequencies f_p of two neighbouring outputs at position i . With the peak frequencies

decreasing at a local rate of 1 octave over a distance $x_b(i) = b(i)\Delta_x$ along the cochlea, the following condition can be stated to ensure $B(i) > \Delta f(i)$:

$$M > M_{min} = \frac{L}{x_b(i)} \frac{-1}{\log_2(1 - 1/Q(i))} \quad (4.43)$$

where the inverse of the local quality factor $1/Q(i) = B(i)/f_p(i)$ expresses the relative bandwidth and L is the length of the cochlea. It is important to note that the terms $b(i) = x_b(i)/\Delta_x$ and $Q(i)$ are *not* the cutoff frequency rate of decrease and the resonator quality factor as given by equations (4.39) and (4.40), respectively, but those taking into account the effect of the resistive network modeling the liquid. As an example, the curves in figure 4.9a shows that over 70% of the cochlea length the peak frequencies span from 300 Hz to 7 kHz, yielding an average $L/\bar{x}_b = 6.5$. The relative bandwidth for 6 dB attenuation estimated at the output located at 15% of the cochlea length is about $1/Q = 1/10$, resulting in $M_{min} = 42$, which seems underestimated.

This particular case shows that equation (4.43) should be used carefully, because the minimal value of M is very sensitive to the definition of the relative bandwidth $1/Q$. Actually, the interaction between two neighbouring resonators is not simply multiplicative as in the cascade of filter described in chapter 3. On the contrary, it is governed by the complicated interaction of oscillators coupled by a liquid. Equation (4.43) therefore simply illustrates the qualitative relationship between the frequency-selectivity of the basilar membrane resonators and the longitudinal resolution required to avoid local reflections in the model.

4.4.5 Effect of the shape of the cochlear duct

In order to estimate the effect of the shape of the cochlear duct, the frequency responses resulting from the trumpet-like shape of figure 4.8 are compared in figure 4.11 to the frequency responses obtained with two rectangular shapes, one wide and one narrow, having a constant height H corresponding to the height at the base ($H = H(0)$) and at the apex ($H = H(L)$) of the trumpet-like cochlea, respectively. Each of these shapes are quantised with $M = 100$ point and $N_{min} = 5$ points.

The effect of the shape on the magnitude of the transfer function is visible in the cutoff region, as shown in figure 4.11a: the sharp cutoff of the wide cochlea is followed by a notch, which increases the cutoff slope over

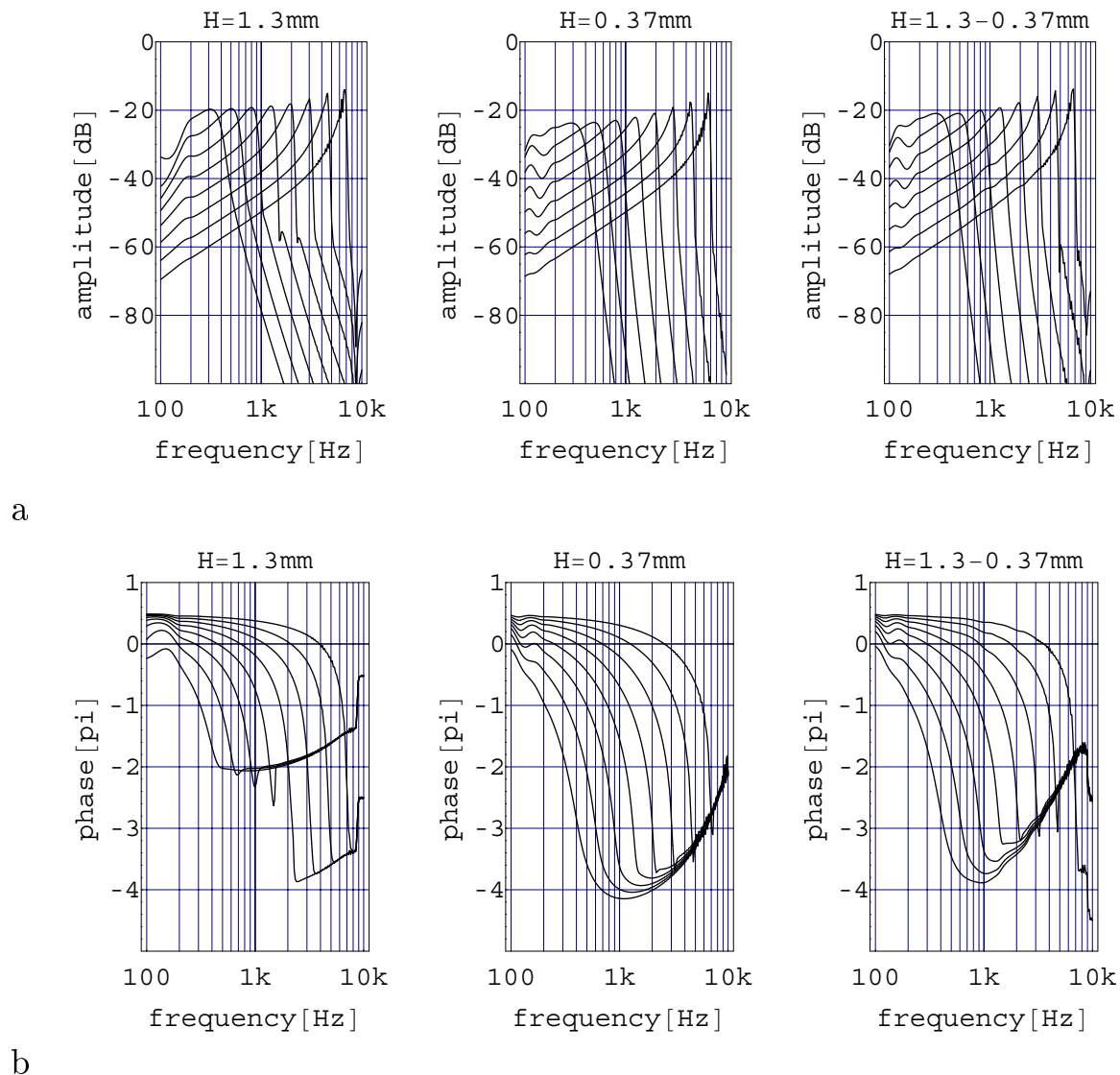


Figure 4.11: a) Magnitude and b) phase of the transfer function at different output of the cochlea for three different shapes of cochlear duct: a wide rectangular duct (left), a narrow rectangular duct (centre) and the trumpet-like duct (right).

about 40dB. Right after this notch, however, the transfer function exhibits a much gentler slope. This notch is also present at the high characteristic frequency outputs of the trumpet-like cochlea, whose cochlear duct has the same height than the wide cochlea. In contrast, in the narrow cochlea the cutoff slope is almost regular over 80dB.

This effect is more visible in the corresponding phase curves (figure

4.11b). The phase of the wide cochlea and at the basal outputs of the trumpet-like cochlea hardly turns more than 2π , whereas the one of the narrow cochlea turns up to 4π at the cutoff. The additional phase shift of 2π in the high characteristic frequency output of the wide and trumpet-like cochleae is an artifact due to the abrupt phase lead after the notch and should be disregarded.

Another effect of the wide cochlea is to reduce the low-frequency reflections due to the poor impedance adaptation of the helicotrema. This effect is not present in the trumpet-like cochlea because at the apex, where these reflections occur, the cochlear duct is narrow.

4.4.6 Basilar membrane - liquid mass ratio

Given the geometry of the cochlear duct and independently from the resolution of its spatial quantisation, the shape of the frequency response of the cochlea depends on four parameters: the liquid density, and the basilar membrane mass, viscosity and stiffness per unit length.

Keeping the three other parameters constant, stiffness variations result in shifts in the peak frequencies and modulation of the sharpness of these peaks, but have no noticeable effect on the cutoff slopes. Similarly varying the viscosity alone will affect only the sharpness of the peaks.

As shown in figure 4.12, the general aspect of the transfer function is controlled by the ratio between the mass of the basilar membrane (modeled by G_{BM}), and the mass of the liquid in movement (modeled by $G_{x,y}$). In this simulation, the reference value $1/G_{BM}$ was modulated by a factor r varying from 0.01 to 100. The shape resulting from the parameter used in [26] is an optimum between the following two extreme cases:

- The basilar membrane mass is negligible compared to the liquid mass: in this case the peak frequency is given by the ratio of the basilar membrane stiffness and the liquid mass in movement at a given position along the cochlea. Similarly the quality factor is given by the product of these parameter values divided by the basilar membrane viscosity. Since these three parameters are kept constant, the shape of the transfer function tends to be independent from the basilar membrane mass, as shown in figure 4.12 for $r \leq 0.01$
- The basilar membrane mass increases such that the liquid mass becomes comparatively negligible: in this case the basilar membrane

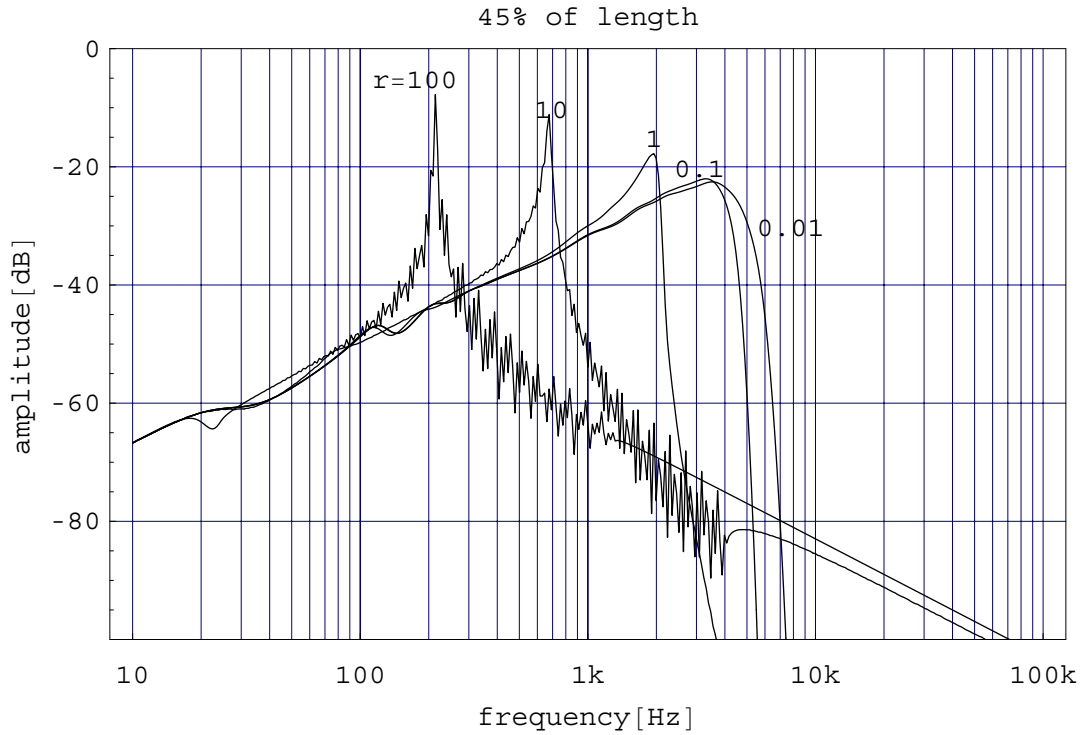


Figure 4.12: Magnitude of the transfer function at 45% of cochlea length with the resistance modeling the basilar membrane mass varying from $r = 0.01$ to 100 times its reference value $1/G_{BM}$.

resonators are no longer coupled together by the liquid. The transfer function at a given position along the cochlea corresponds to the transfer function of the resonator alone. Since the resonator's mass increases, its peak frequency and quality factors tend to vary according to equations (4.37) and (4.38), as shown in figure 4.12 for $r \geq 100$

The optimal transfer functions at $r = 1$ are obtained using the parameters given in [26], i.e. a basilar membrane mass per unit area $m'' = 1.5\text{kg/m}^2$ and a liquid density $\rho = 10^3\text{kg/m}^3$, independently from vertical and horizontal resolutions. This means that the hydrodynamics of the basilar membrane – liquid system depends on the ratio

$$H_c(i) = \frac{m''(i)}{2\rho} = \frac{m'(i)\Delta_x}{2\rho w(i)\Delta_x} \quad (4.44)$$

which is the ratio of the mass of a basilar membrane segment to the mass per unit cochlear duct height of the liquid over this basilar membrane seg-

ment. This ratio has thus the dimension of a distance, the *characteristic height* which expresses the height the cochlear duct should have at position $i\Delta_x$ such that the local mass of the basilar membrane equals the local mass of the liquid above and below it in the duct. With the parameters [26] the characteristic height is 0.75 mm all along the cochlea.

Using the correspondences listed in table 4.3, the characteristic height can be expressed as a function of the resistances $R_{BM}(i) = 1/G_{BM}(i)$ and $R_y(i) = 1/G_y(i)$ modeling the basilar membrane mass and the liquid moving in the y -direction, respectively:

$$H_c(i) = \frac{R_{BM}(i)}{R_y(i)/\Delta_y} \quad (4.45)$$

Expressing the vertical grid spacing Δ_y by the ratio $H(i)/N(i)$ of the height of the cochlear duct to the number of vertical resistors modeling the liquid at position $x = i\Delta_x$ gives thus

$$\frac{R_{BM}(i)}{N(i)R_y(i)} = \frac{m'(i)\Delta_x}{2\rho w(i)\Delta_x H(i)} \quad (4.46)$$

which means, as expected, that at any position i , the sum of the vertical resistances $N(i)R_y(i)$ models the liquid mass over a basilar membrane segment of length Δ_x while the resistance $R_{BM}(i)$ models the mass of this basilar membrane segment.

4.4.7 Parameter values

As mentioned in paragraph 4.3.4, the values of the parameters can be adjusted so that the model exhibits the required behaviour. If the model faithfully represents the biological original, the values of the parameters (provided they have a physical meaning) should correspond to the one measured on its biological counterpart. In a less restrictive way, if two different models represent the same reality, their corresponding parameters should be in accordance.

In [26], the parameters used (and that are used also in the model described here) are shown to be approximatively in accordance with a collection of other models. However the corresponding parameters used in the model [24] and [47] are different by several orders of magnitude. More specifically, the basilar membrane mass per unit area of $2.47 \cdot 10^{-2} \text{kg/m}^2$ ([47], p. 2253) is 60 times lower than that used in [26]. With the same

liquid density, the transfer function using this basilar membrane mass per unit area would have the shape of the curves for $r = 0.01 \div 0.1$ in figure 4.12 which is not in accordance with the biological measurements. However, the resulting transfer functions shown in [24] are very similar to the one presented here, obtained with the parameters [26].

The difference between the model presented here and the model [24, 47] lies in the computation of the hydrodynamics in the liquid. Instead of approximating the Laplace equation by finite difference equations, the effect of the liquid is computed using a *Green's function* $G(x'_1, x'_2)$ which gives the force per unit length at a relative position $x'_1 = x_1/L$ on the basilar membrane caused by the acceleration of a basilar membrane segment at a relative position $x'_2 = x_2/L$, provided that all the other segments are immobile. This function, derived from the 3-D geometry of the cochlear duct, can be related to the equivalent resistance $R_G(i_1, i_2)$ given by the ratio of the voltage V_{i_1} at the node $(i_1, 0)$ of the resistive network corresponding to the relative position $x'_1 = i_1/M$ and the current $I(i_2)$ yielding V_{i_1} when injected at the node corresponding to the relative position $x'_2 = i_2/M$. As detailed in appendix A.3, the correspondence is given by:

$$\begin{aligned} R_G(i_1, i_2) &= \frac{F_v}{F_j} G(i_1/M, i_2/M) \\ &= \frac{F_v}{F_j} \frac{w(i_1 \Delta_x)^2}{4} \rho g(i_1/M, i_2/M) \end{aligned} \quad (4.47)$$

where $g(x'_1, x'_2)$, which depends only on the geometry of the cochlear duct, is given analytically in [47].

Figure 4.13 compares values of $R_G(i_1, i_2)$ derived from the Green's function of [24, 47] with those derived from simulating the resistive network whose resistances are given according to table 4.3 with a constant basilar membrane width $w(i) = 10^{-4}$ m, a liquid density $\rho = 1 \cdot 10^3$ kg/m³ and scaling factors $F_v = F_j = 1$.

Except for the little peak before the fall of R_G which is absent from the curves derived from the Green's functions (and which are actually also taken into account in [24, 47]), the general aspect of both curves is similar (within less than 10% relative error). However, their values show that the resistances of the network are overestimated by a factor 28. Therefore the basilar membrane mass per unit area of 1.5 kg/m² given in [26] is overestimated by the same factor, bringing the value it should have using

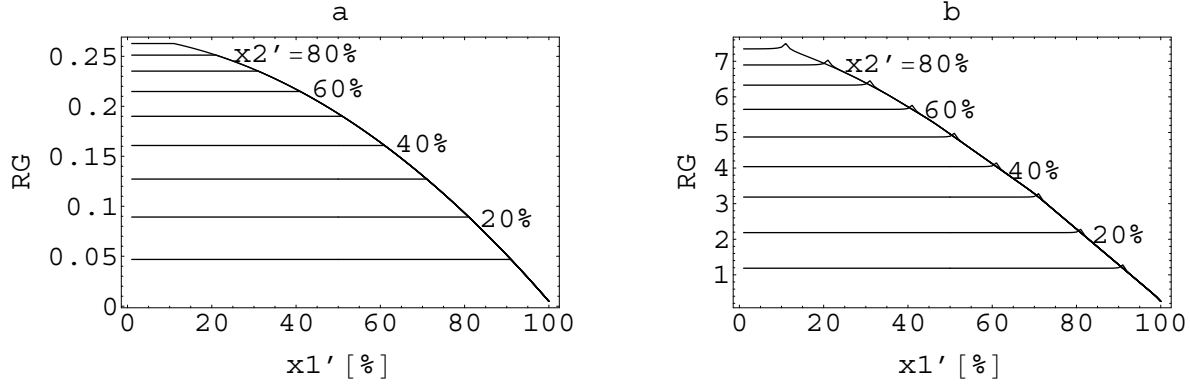


Figure 4.13: Resistive network equivalent resistances $R_G(x'_1, x'_2)$: a) derived from Green's function given in [24, 47], b) measured on a trumpet-like shape quantised with $M = 100$ points $\times N_{min} = 5$ points.

the Green's functions of [24, 47] to $5.36 \cdot 10^{-2}$ kg/m², which is only twice the value given in [24, 47].

The mass per unit area of the basilar membrane given in [26] seems actually too large, despite the fact that it includes the mass of the organ of Corti: assuming it to have an homogeneous density in the order of magnitude of the liquid density, the cochlear partition (basilar membrane and organ of Corti) would have a thickness of $1.5 \text{ kgm}^{-2} / 10^3 \text{ kgm}^{-3} = 1.5 \text{ mm}$, which is larger than the height of the cochlear duct! Since this value still yields appropriate transfer functions, this means that the hydrodynamics of the liquid is not modeled accurately enough by the 2-D description. This is due to the fact that the equipressure surfaces in the liquid are made proportional to equipressure contour in the 2-D model by the basilar membrane width; this means that the liquid is assumed to move uniformly over the full width of each basilar membrane segment, which is not the case in reality. Therefore the value of the basilar membrane width w used to calculate the sheet conductivity σ in equation (4.24) must be much lower than the geometric width of the basilar membrane. Equation 4.44 shows that to keep the same characteristic height, the effective width of the basilar membrane, which would displace the liquid uniformly above and below it must be 28 times lower than its geometrical width. Therefore, according to the Green's function computed in [24, 47], the 2-D reduction of the 3-D geometry of the cochlear duct presented here is valid, *provided that the width of the cochlear duct is taken about 30 times smaller than the width of*

the basilar membrane. The resulting reduction of the effective liquid load models thus its lateral movements, that do not interact with neighbouring basilar membrane segments.

The values of the viscosity and the stiffness per unit area are difficult to measure directly on live cochleae. Moreover it is probable that their effective value is different from their passive value due to the control by the outer hair cells. Actually, the effective basilar membrane mass might also be affected by the same feedback mechanism in order to tune accurately the shape of the frequency response. The most reliable parameter available from the biological cochlea is the liquid load, which may be calculated from the geometry of the cochlear duct. It is given in the present model by the effective duct width w to be used in equation (4.24). The optimal basilar membrane mass per unit length is obtained using the characteristic height H_c of equation (4.44) yielding the required shape of the frequency response. The basilar membrane stiffness is then adjusted to obtain the required tonotopy, i.e. the required repartition of the characteristic frequencies along the cochlea. Finally the viscosity term, which is modulated by the undamping u performed by the outer hair cell feedback, is continuously adjusted in an automatic gain control scheme around an operating point yielding the required frequency selectivity at maximal sensitivity.

4.5 Summary

A realistic 2-D model of the cochlea is proposed, whose most interesting feature is its ability to reproduce the very sharp frequency cutoff of 300dB per octave measured in the real cochlea. This requires relatively high quality factors for the basilar membrane resonators but it also results from the coupling of adjacent sections of the elastic basilar membrane through the liquid.

The 2-D movements in the liquid are emulated by a resistive network quantising the Laplace equations to which the liquid obeys. By symmetry only half of the cochlear duct is modeled, the one merging the scala media and the scala vestibuli. The basilar membrane boundary of the resulting cavity is modeled by a bank of second-order serial resonators. These resonators macro-model the micro-mechanics performed in the organ of Corti overlying the basilar membrane. The feedback effect of the outer hair cells is taken into account as an undamping variable which modulates the effective viscosity of the organ of Corti. Except for the coupling by the

liquid, no lateral interactions such as shearing resistance or longitudinal stiffness are taken into account in the resonator bank, as in most of the computational models found in the literature.

The longitudinal resolution of this discrete model must be large enough to sample without aliasing the sharp cutoffs at given frequency in the spatial responses along the basilar membrane. On the contrary, the resolution in the vertical axis has been shown to be less crucial, since the behaviour of the cochlea is practically unaltered when quantised down to 2 points per minimal cochlear duct height. The shape itself of the duct's cross-section appears not to be a relevant factor for the frequency response of the cochlea.

Although the 2-D model is based on an unrealistic assumption of the movements of the liquid in the dimension dropped by the dimension reduction, the adequate parameter's compensation such that it models accurately the 3-D hydrodynamics in the cochlear duct has been identified as the effective width of the cochlear duct.

Chapter 5

Analogue VLSI implementation in the log-domain of a 2-D model of the cochlea

5.1 Introduction

In order to achieve a compact VLSI implementation of the dense resistive network modeling the 2-D model of the cochlea, the use of resistors implemented with a single MOS transistor is envisaged. Such a use of the transistor as a *pseudo-conductance* [49] has proven to be very efficient in several signal processing systems (see [50] for a review), because in addition to its potential for very compact implementation, its current-mode operation permits a linear range much larger than those obtained in voltage mode implementations. However, the concept of pseudo-conductance is suited for spatial processing only. In order to include temporal processing, reactive components compatible with pseudo-conductances are needed, yielding filters which are closely related to log-domain filters [51].

Section 5.2 recalls the concept of pseudo-voltage and pseudo-conductances used in the log-domain and introduces the concept of *pseudo-capacitance*. In section 5.3 a compact implementation of a *pseudo-transcapacitor* is proposed, which integrates its differential input current into an output pseudo-voltage. It is designed to be fully compatible with the pseudo-conductances. Using a few additional transistors, the pseudo-transcapacitor can be used as a building block to implement grounded *pseudo-capacitors*, current-mode integrators and *pseudo-transinductors*. In section 5.4 the implementation in the log-domain of the resistive network and its bank of resonators modeling the 2-D hydrodynamics of the cochlea is proposed and analysed.

5.2 Spatio-temporal processing in the log-domain

5.2.1 Pseudo-conductance and pseudo-voltage in weak inversion

In weak inversion the channel current in a MOS transistor, defined positively when flowing from the terminal A to the terminal B (figure 5.1), is given by:

$$i_{AB} = \pm I_s e^{(v_G - V_{T0})/nU_T} \left(e^{-v_A/U_T} - e^{-v_B/U_T} \right), \quad (5.1)$$

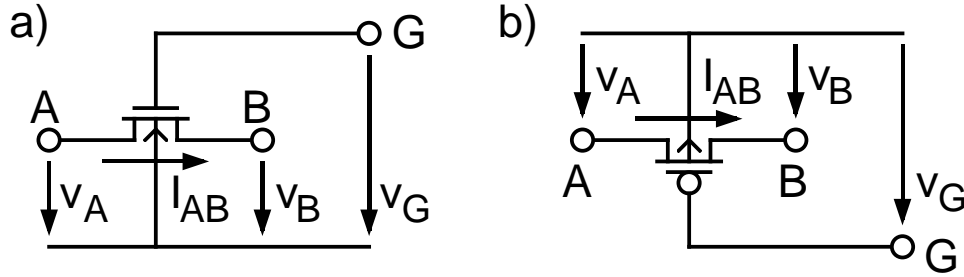


Figure 5.1: voltage and current definition for a) NMOS and b) PMOS transistor.

where n is the slope factor and $U_T = k_B T/q$ is the thermodynamic voltage [52]. The specific current I_S and the threshold voltage V_{T0} are positive values for both PMOS and NMOS transistors. The sign “+” applies for PMOS and the sign “-” for NMOS transistors. The variables v_G , v_A and v_B are the voltages at the gate G and at the channel terminals A and B, respectively, referred to the bulk voltage. They are defined positively from G, A and B to bulk for NMOS transistors (figure 5.1a) and inversely for PMOS transistors (figure 5.1b). Defining the *pseudo-voltage* by

$$v^* = \pm V_0 e^{-v/U_T} \text{ (+ for PMOS, - for NMOS)}, \quad (5.2)$$

where V_0 is an arbitrary positive scaling constant, transistors T_1 and T_2 in figure 5.2 implement a *pseudo-Ohm's law*

$$i = G^*(v_A^* - v_B^*), \quad (5.3)$$

with a pseudo-conductance $G^* = I_G/V_0$, if T_1 and T_2 are identical. Note that for $|v_A - v_B|$ larger than a few U_T , the pseudo-voltage at one terminal becomes negligible with respect to the pseudo-voltage at the other terminal. A saturated transistor corresponds thus to a pseudo-resistor connected to the *pseudo-ground* ($v^* = 0$, noted 0^*). This property is very convenient to extract the current of such pseudo-grounded pseudo-resistor using complementary transistors.

5.2.2 Current to pseudo-voltage conversion

The conversion from a pseudo-voltage to a current is performed by a single pseudo-grounded pseudo-conductance (figure 5.3a). The reverse conversion, i.e. from a current to a pseudo-voltage can be obtained with the

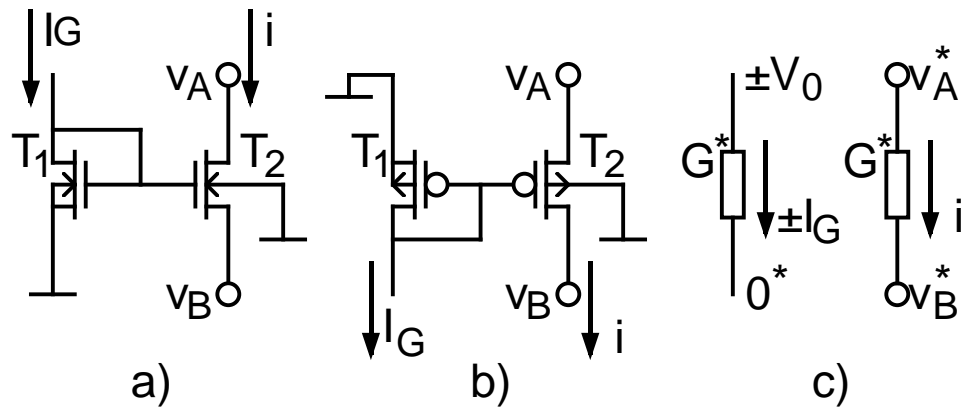


Figure 5.2: a) NMOS and b) PMOS implementation of a pseudo-conductance and its bias (c), where the signs “+” on V_0 and I_G applies for PMOS and the sign “-” for NMOS.

circuit of figure 5.3b. This structure can be seen as a diode-connected transistor in which the conversion transistor implementing the pseudo-conductance G^* is embedded: a feedback loop adjusts the gate voltage of the control transistor T_F such that it sinks/sources the imposed input current i_{in} , as well as the current i_{load} loading the pseudo-voltage output. Doing so, the drain voltage v_{out} of the control transistor T_F , which corresponds to the output pseudo-voltage v_{out}^* , adjusts so that the pseudo-conductance G^* allows the input current i_{in} to flow through it.

The diagram of figure 5.4 illustrates the behaviour of an NMOS current-to-pseudo-voltage converter. The input current i_{in} is expressed as a func-

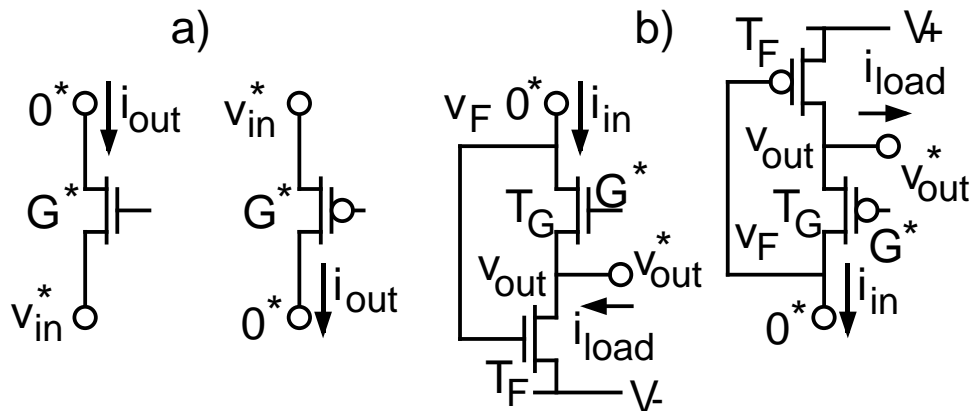


Figure 5.3: a) pseudo-voltage to current, b) current to pseudo-voltage conversion.

although the diagram assumes it saturated, T_F can work in both saturation and conduction regions, as long as v_{out} is larger than V_- (NMOS) or smaller than V_+ (PMOS). Therefore i_{inmax} , at which T_F desaturates (arrow e), corresponds to the limit of the validity of the diagram rather than the limit of the circuit itself.

5.2.3 Principle of the pseudo-capacitance

A linear capacitance imposes a voltage variation rate proportional to a current. In the log-domain, the corresponding pseudo-voltage should be defined by a voltage whose exponential has a variation rate proportional to the same current. Such a requirement can be fulfilled by charging a linear capacitor through a current mirror that modulates the input current with a gain controlled exponentially by the voltage across the linear capacitor, as shown in figure 5.5. Both transistors T_1 and T_2 of such a current mirror have the same gate voltage: assuming they are identical and saturated, they can be considered as pseudo-grounded pseudo-resistors having the same pseudo-conductance $G^* = \pm i/v_A^*$ (“+” for PMOS, “-” for NMOS) imposed by T_1 and imposing $i_c = V_0 G^*$ by T_2 . The voltage v_C follows the linear capacitance law $-dv_C/dt = i_c/C$. The voltage shift V_{sh} between v_A and v_C is constant, thus $dv_A/dt = dv_C/dt$ and, using the definition (5.2) of the pseudo-voltage,

$$\pm \frac{dv_A^*}{dt} = \pm \frac{dv_A^*}{dv_A} \frac{dv_A}{dt} = \frac{dv_A^*}{dv_A} \frac{V_0}{v_A^*} \frac{-i}{C} = \frac{V_0}{CU_T} i = \frac{i}{C^*} \quad (5.5)$$

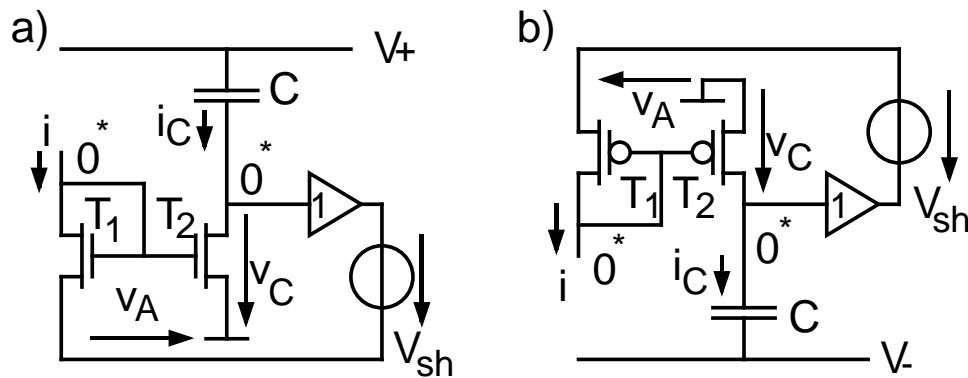


Figure 5.5: a) NMOS and b) PMOS single current input pseudo-transcapacitor; the bulks are connected to $V_- < 0$ in a) and $V_+ > 0$ in b).

describes the pseudo-capacitance law in terms of current and pseudo-voltage, using the pseudo-transcapacitance $C^* = CU_T/V_0$. The sign “+” in the two leftmost terms of the equation applies to PMOS transistors, whereas the sign “-” in the same terms applies to NMOS transistors. This means that the absolute value of v_A^* (which is negative for NMOS) increases with a positive input current i in both cases.

In order to prevent v_A to forward-bias the bulk-source junction of transistor T_1 , the common bulk voltage of the transistors is set lower/higher than ground (for NMOS/PMOS, respectively). The transistor voltages are thus referred to ground instead of bulk voltage, so that $v^* = \pm V_0$ when $v = 0$.

The voltage shift V_{sh} adjusts v_A close to the ground ($v_A^* \approx \pm V_0$) in order to maximise the dynamic range of the input current i by keeping the capacitor current i_C within the same order of magnitude as the input current i . Moreover, if the pseudo-voltage v_C^* is considered as the pseudo-transcapacitor’s output instead of v_A^* , the value of the pseudo-transcapacitance is multiplied by a factor $\exp(V_{sh}/U_T)$, which can be adjusted by V_{sh} .

5.3 Pseudo-transcapacitor circuit

5.3.1 Implementation of a pseudo-transcapacitor

The circuits of figure 5.5 can only charge the capacitor C . The pseudo-transcapacitor of figure 5.6 solves this problem using a differential current input. Only the PMOS version of the pseudo-transcapacitor is described here, which can be implemented in an N-well technology. An NMOS implementation would be functionally symmetrical.

The input i_1 charges the capacitor C according to equation (5.5) implemented by the transistors T_1 and T_2 , whereas the input i_2 , through T_3 and T_4 , discharges it similarly using the mirror T_5 - T_6 . The output pseudo-voltage is the capacitor voltage shifted by V_{shC} using the follower T_9 - T_{10} , whereas the voltage v_A at the source of transistors T_1 and T_3 was shifted by V_{shA} using T_7 - T_8 , resulting in

$$v_C^* = v_A^* e^{-V_{sh}/U_T}, \quad (5.6)$$

where $V_{sh} = V_{shA} - V_{shC}$. The circuit implements therefore

$$\frac{dv_C^*}{dt} = \frac{i_1 - i_2}{C^*}, \quad (5.7)$$

with a pseudo-transcapacitance

$$C^* = C \frac{U_T}{V_0} e^{V_{sh}/U_T}. \quad (5.8)$$

With $T_7 \equiv T_8$ and $T_9 \equiv T_{10}$, the voltage shifts V_{shA} and V_{shC} can be imposed at the gate of transistors T_8 and T_{10} , respectively. These voltages must impose a bias current across T_7 - T_8 and T_9 - T_{10} large enough so that the output current of the followers-shifter they implement is comparatively negligible not to affect v_A^* and v_C^* . In practice, V_{shA} and V_{shC} should set T_7 - T_8 and T_9 - T_{10} in strong inversion. This solution results in a very compact implementation of a pseudo-transcapacitor, but the price to pay is the large current biasing the follower-shifters. If power consumption is an important issue, the bias current flowing through transistors T_7 - T_8 can be reduced provided that copies of the input currents i_1 and i_2 , which is also the output current of the follower-shifter T_7 - T_8 , are sourced on the node v_A . The follower-shifter T_9 - T_{10} could be similarly unloaded by sourcing on its output node v_C a copy of the pseudo-transcapacitor output current, if available (see paragraph 5.4.3).

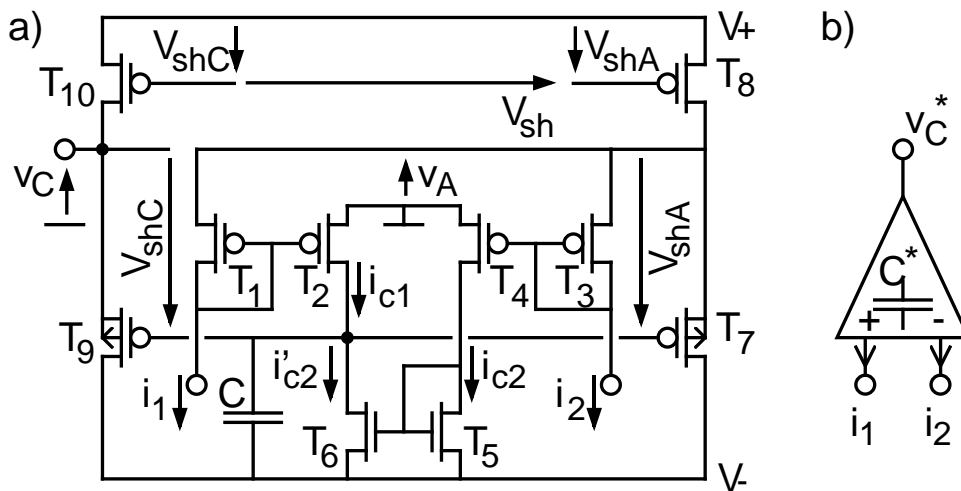


Figure 5.6: a) Diagram, b) symbol of a differential current input pseudo-transcapacitor.

5.3.2 Range of operation

The upper limit of the range of operation of the pseudo-transcapacitor circuit is determined by the weak inversion range of the transistors T_1 , T_2 , T_3 and T_4 , outside which equation (5.5) is not valid. The lower limit is imposed by the level of current required to exceed junction leakage and internal noise. According to figure 5.6, at given input currents $i_{1,2}$, the currents $i_{c1,2}$ charging the capacitor are imposed by the gain of the mirrors T_1 - T_2 and T_3 - T_4 ,

$$\frac{i_{c1,2}}{i_{1,2}} = e^{v_A/U_T} = \frac{V_0}{v_A^*}, \quad (5.9)$$

which is controlled by the pseudo-voltage v_A^* .

For a given common mode input current $i_1 = i_2 = I_0$, the excursion of pseudo-voltage v_A^* should control the mirror's gain so that the currents $i_{c1,2}$ stay within the limits I_{min} and I_{max} of the current range. The common mode input current I_0 is set at midway between I_{min} and I_{max} to have the largest excursion of the differential signal. With $I_{max} \gg I_{min}$, I_0 is thus set at about half the maximal current I_{max} : the pseudo-voltage v_A^* must therefore lie within the range

$$\frac{1}{2} \approx \frac{I_0}{I_{max}} \leq \frac{v_A^*}{V_0} \leq \frac{I_0}{I_{min}} \approx \frac{1}{2} \frac{I_{max}}{I_{min}}. \quad (5.10)$$

Outside the lower limit, the capacitor currents $i_{c1,2}$ become larger than I_{max} . The upper limit is given by the minimal capacitor currents having an influence on its charging. A small I_{min} permits thus a very large maximal value of pseudo-voltage v_A^* , but its corresponding voltage $v_A = -U_T \ln(v_A^*/V_0)$ still has a reasonable order of magnitude since it is logarithmically compressed.

The pseudo-transcapacitor functions as an integrator in the pseudo-voltage domain. With a dc input signal, it will always reach its upper or lower limits. For harmonic signals, it is however possible to determine the maximal amplitude of the differential input that keeps the circuit within its operating range. Equations (5.6), (5.7) and (5.8) result in

$$\frac{dv_A^*}{dt} = \frac{i_1 - i_2}{CU_T/V_0}, \quad (5.11)$$

which permits to express $v_A^*(t)/V_0$ when the differential input $i_1 - i_2$ is a

cosine wave at angular frequency ω having an amplitude I_{AC} :

$$\frac{v_A^*(t)}{V_0} = \frac{V_{A0}^*}{V_0} + \frac{I_{AC}}{C\omega U_T} \sin(\omega t), \quad (5.12)$$

where V_{A0}^*/V_0 is an arbitrary value resulting from the initial conditions of the pseudo-transcapacitor. With a constant common-mode current $I_0 = I_{max}/2$ at input i_2 , and for a capacitor current i_{c2} lying within $[I_{min}, I_{max}]$, the maximal amplitude of v_A^*/V_0 variations can be found by imposing the maximal and minimal value of equation (5.12), i.e. for $\sin(\omega t) = +1$ and -1 , equal to the upper and lower limits of equation (5.10), respectively, which yields

$$I_{ACmax} = \frac{C\omega U_T}{4} \left(\frac{I_{max}}{I_{min}} - 1 \right), \quad (5.13)$$

with a dc value of the pseudo-voltage at

$$V_{A0}^* = \frac{V_0}{4} \left(\frac{I_{max}}{I_{min}} + 1 \right). \quad (5.14)$$

The differential input is imposed by varying i_1 with an amplitude I_{AC} around the common mode input $I_0 = I_{max}/2$. The variation of the capacitor current i_{c1} is thus given, using equation (5.9), (5.12), (5.13) and (5.14), by

$$\frac{i_{c1}}{I_{max}} = 2 \frac{1 + i_{AC} \cos \alpha}{(I_{max}/I_{min} - 1)(1 + \sin \alpha) + 2}, \quad (5.15)$$

where $\alpha = \omega t$ is the electrical angle of the input signal and $i_{AC} = I_{AC}/I_0 = 2I_{AC}/I_{max}$ is the differential input relative to the common mode. The extrema of the right hand-side of equation (5.15) bound the range of the capacitor current i_{c1} , and these must lie within $[I_{min}, I_{max}]$. The analytical calculation of these extrema leads to a transcendental equation. The plot of i_{c1}/I_{max} as a function of the electrical angle α in figure 5.7 shows that, for dynamic ranges $I_{max}/I_{min} \geq 20$, the maximum is always reached at $\alpha = 3\pi/2$ which corresponds to the minimum of the denominator. For this angle, the pseudo-voltage v_A^* is minimal, the differential input equals 0 and the maximum of i_{c1}/I_{max} equals unity: the maximal value of i_{c1} is therefore ensured not to be larger than the maximal current I_{max} . At the other extreme, the electrical angle for which the minimum of i_{c1}/I_{max} is obtained shifts from $\pi/2$ for $i_{AC} = 0$ toward $\alpha = \pi$ for $i_{AC} = 1$ (where $i_{c1} = 0$ since $i_1 = 0$ in this case). Assuming as an initial guess that i_{AC}

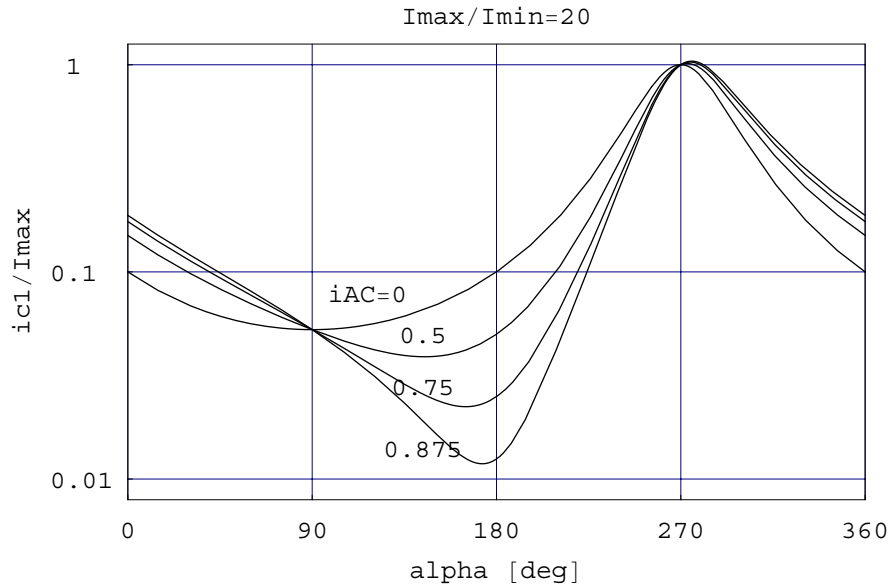


Figure 5.7: Plot of the function $i_{c1}/I_{max}(\alpha)$ with a current dynamic range imposed at $I_{max}/I_{min} = 20$ for several values of differential input amplitude i_{AC} .

is large enough so that the minimum occurs at $\alpha \approx \pi$, allows to obtain for $i_{c1} = I_{min}$, using equation (5.15), a maximal relative differential input amplitude

$$i_{ACmax} = \frac{2I_{ACmax}}{I_{max}} = \frac{1}{2} \left(1 + \frac{I_{min}}{I_{max}} \right) \approx \frac{1}{2}. \quad (5.16)$$

The maximal amplitude of the differential input must be half the common mode $I_{max}/2$ to ensure the capacitor current i_{c1} not to become lower than the minimal current I_{min} .

The minimal frequency ω_{min} of the differential input signal ensuring the largest output pseudo-voltage variations with the largest differential input range is finally given using equations (5.13) and (5.16):

$$\omega_{min} = \frac{I_{min}}{CU_T}. \quad (5.17)$$

Figure 5.8 shows the simulation results of the pseudo-transcapacitor of figure 5.6 (without its output follower-shifter T_9 - T_{10}), with an excitation $i_1(t) = I_1 + I_{AC} \cos(\omega t)$ at input i_1 and a constant value I_2 at input i_2 . The dc value I_1 , ideally equal to I_2 for a zero differential input, has been

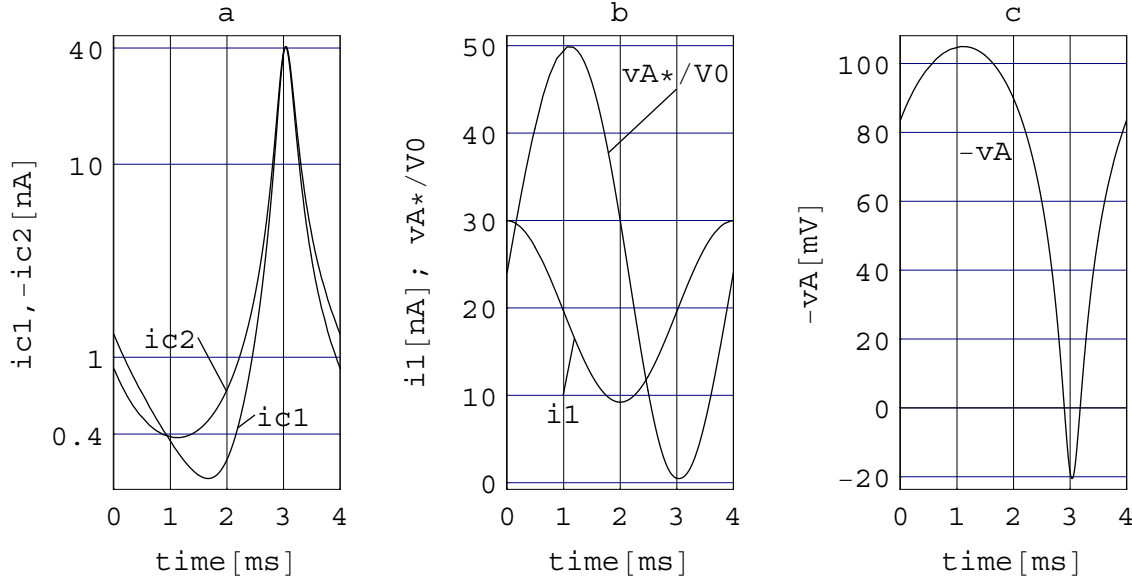


Figure 5.8: a) Capacitor currents $i_{c1,2}$, b) pseudo-voltage output v_A^*/V_0 and c) output voltage $-v_A$ in response to a cosine differential input with i_1 as in b) and i_2 constant (simulation results).

adjusted to compensate the effect of the circuit imperfections (i.e. the non-zero output conductances of the transistors), avoiding a drift of the dc pseudo-voltage V_{A0}^* . The aspect ratio of T_1 , T_2 , T_3 and T_4 was set to $W/L = 20\mu\text{m}/5\mu\text{m}$, which gives, with the technology simulated (ES2 0.7μ), a specific current $I_S = 2n\beta U_T^2 = 310$ nA with $n = 1.5$. Ensuring a maximal inversion coefficient $I_{max}/I_S = 1/8$ imposes a maximal current $I_{max} \approx 40$ nA. In order to minimise its current gain error, the transistors of the mirror T_5 - T_6 are set into moderate inversion using an aspect ratio $W/L = 2\mu\text{m}/20\mu\text{m}$; these longer transistors have also a reduced output conductance. (Note that using the equivalent circuit in a P-well technology would allow larger current with the same inversion factor and a mirror T_5 - T_6 set into stronger inversion because the specific current is usually 2 to 3 times higher for NMOS than for PMOS transistors.)

The simulation conditions were set to limit the current within a 40 dB dynamic range of currents, between $I_{min} = 400$ pA to $I_{max} = 40$ nA, by tuning the appropriate parameters V_{A0} , I_{AC} and I_1 while imposing $I_2 = 20$ nA and $\omega = 2\pi \cdot 250$ Hz with a capacitor $C = 10$ pF; The follower-shifter is implemented with transistors $T_{7,8}$ having an aspect ra-

parameter	theoretical	simulation
$-V_{A0} = -U_T \ln(V_{A0}^*/V_0)$	83.4mV	100.7mV
$I_1 = I_{max}/2$	20nA	19.592nA
$I_{AC} = I_{ACmax} 2\pi 250\text{Hz}/\omega_{min}$	10.31nA	10.38nA
$v_{Amin}^*/V_0 = 1/2$	0.5	see Fig 5.8b
$v_{Amax}^*/V_0 = I_{max}/2I_{min}$	50	see Fig 5.8b
$-v_{Amin} = -U_T \ln(v_{Amin}^*/V_0)$	-18.0mV	see Fig 5.8c
$-v_{Amax} = -U_T \ln(v_{Amax}^*/V_0)$	101.7mV	see Fig 5.8c

Table 5.1: Theoretical and adjusted values of parameters producing the behaviour of figure 5.8

tio $W/L = 20\mu\text{m}/5\mu\text{m}$, and it is sets for a voltage shift $V_{shA} = 1\text{V}$. Table 5.1 compares the adjusted parameters with their theoretical prediction, whereas figure 5.8 confirms the expected behaviour of the circuit, except for the value of the capacitor current i_{c1} which undershoots the minimal current I_{min} ; this undershoot is due to the overestimation in setting $\alpha = \pi$ to get the minimum of equation (5.15). The pseudo-voltage v_A^*/V_0 was actually measured as the current in a pseudo-grounded pseudo-conductance $G^* = 1\text{nA}/V_0$ connected to the pseudo-transcapacitor's node v_A .

5.3.3 Second-order effects

Second-order effects that affect the required relationship between electrical variables such as currents and voltages are analysed to estimate to what extent they affect the relationship between the currents and the pseudo-voltages.

The output conductances of transistors T_1 to T_6 will affect the gains of mirrors T_1 - T_2 , T_3 - T_4 and T_5 - T_6 . The unity current gain of a mirrors T_i - T_j (at $v_A = 0$ for the pairs T_3 - T_4 and T_5 - T_6) is affected by a constant error ϵ_{Eij} :

$$\frac{i_{Dj}}{i_{Di}} = \frac{V_{Dj} + V_E}{V_{Di} + V_E} \approx 1 + \frac{V_{Dj} - V_{Di}}{V_E} = 1 + \epsilon_{Eij}, \quad (5.18)$$

where i_{Di} , V_{Di} and V_E are the drain current, drain voltage and the voltage representing the current dependent output conductance $g_{DS} = I_D/V_E$ (V_E is equivalent to the *Early* voltage of bipolar transistors) of transistor T_i ,

respectively [52]. The drain currents are defined positively when entering the drain for NMOS and inversely for PMOS transistor, the drain voltages are defined positively from drain to local substrate for NMOS and inversely for PMOS transistors, and the voltage V_E is positive for both types of transistors. Equation (5.18) is valid when both transistors T_i and T_j are identical, i.e. they have the same threshold voltage and the same size.

The mismatch of the threshold voltage V_{T0} and the transconductance factor $\beta = \mu C_{ox} W/L$ between the transistors T_i and T_j results in another unity gain error ϵ_{Mij} . Assuming these errors small enough, they are additive, yielding a current gain $(1 + \epsilon_{Eij})(1 + \epsilon_{Mij}) \approx 1 + \epsilon_{ij}$, thus affected by an error $\epsilon_{ij} = \epsilon_{Eij} + \epsilon_{Mij}$.

A further imperfection to take into account is the current leaking from the capacitor's node. This leakage current I_L may be assumed constant since the voltage v_C has very small variations in the normal range of operation. Therefore the net current i_c charging the capacitor C is given by

$$i_c = [i_1(1 + \epsilon_1) - i_2(1 + \epsilon_2)] \frac{V_0}{v_A^*} - I_L, \quad (5.19)$$

where $\epsilon_1 = \epsilon_{12}$ is the gain error of the mirror T_1 - T_2 and $\epsilon_2 = \epsilon_{34} + \epsilon_{56} + \epsilon_{34}\epsilon_{56} \approx \epsilon_{34} + \epsilon_{56}$ is the one of the mirrors T_3 - T_4 and T_5 - T_6 ; the current gains of mirrors T_1 - T_2 and T_3 - T_4 are controlled by the sources of T_1 and T_3 according to equation (5.9). Differentiating the pseudo-voltage v_A^* with respect to time similarly to equation (5.5) and using the capacitor current i_c described by equation (5.19),

$$\frac{dv_A^*}{dt} = \frac{i_c v_A^*}{C U_T} = \frac{1}{C^*} [i_1(1 + \epsilon_1) - i_2(1 + \epsilon_2)] - v_A^* I_L / V_0, \quad (5.20)$$

shows that a constant leakage current I_L acts as a parasitic pseudo-conductance $g_L^* = I_L / V_0$ in parallel with the pseudo-capacitance $C^* = C U_T / V_0$ of the circuit. Note that with a negative leakage current I_L (charging the capacitor) the pseudo-conductance g_L^* is negative, making the circuit unstable instead of stabilising it in presence of an input dc offset (see paragraph 5.3.4).

The equivalent circuit for a constant common mode current $i_2 = I_0$ imposed at the negative input and the differential input signal i varying around this common mode at the positive input is shown in figure 5.9: the value of the pseudo-capacitance is modified by a factor $C'^* / C^* = 1 / (1 + \epsilon_1)$

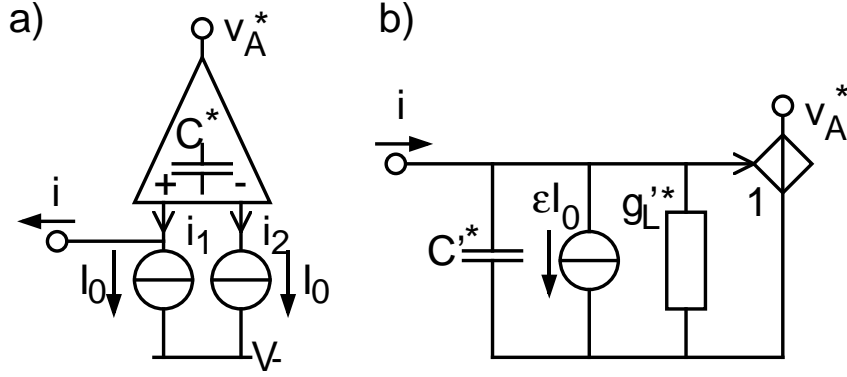


Figure 5.9: a) Pseudo-transcapacitor with its bias and input signal and b) its equivalent circuit in the log-domain.

and it has a constant current source $\epsilon I_0 = I_0(\epsilon_2 - \epsilon_1)/(1 + \epsilon_1)$ and a linear pseudo-conductance $g_L'^* = g_L^*/(1 + \epsilon_1)$ in parallel with it.

The gain errors ϵ_{E12} , ϵ_{E34} and ϵ_{E56} due to the output conductances of the transistors depend on their drain voltages, which are not constant. Assuming all transistors in weak inversion (although T_5 and T_6 are in moderate inversion) and neglecting the second-order error terms, these drain voltages are given by:

$$V_{D1} = n_1 V_+ + V_{T01} + n_1 U_T \ln \left[\frac{i_1}{I_{S1}} \frac{V_0}{v_A^*} \right], \quad (5.21)$$

$$\begin{aligned} V_{D2} &= V_+ + V_{shA} + v_A \\ &= V_+ + V_{shA} + U_T \ln \left[\frac{V_0}{v_A^*} \right], \end{aligned} \quad (5.22)$$

$$V_{D3} = n_3 V_+ + V_{T03} + n_3 U_T \ln \left[\frac{i_2}{I_{S3}} \frac{V_0}{v_A^*} \right], \quad (5.23)$$

$$\begin{aligned} V_{D4} &= V_+ - V_- - V_{D5} \\ &= V_+ - V_- - V_{T05} - n_5 U_T \ln \left[\frac{i_2}{I_{S5}} \frac{V_0}{v_A^*} \right], \end{aligned} \quad (5.24)$$

$$V_{D5} = V_{T05} + n_5 U_T \ln \left[\frac{i_2}{I_{S5}} \frac{V_0}{v_A^*} \right], \quad (5.25)$$

$$\begin{aligned} V_{D6} &= -V_- - V_{shA} - v_A \\ &= -V_- - V_{shA} + U_T \ln \left[\frac{V_0}{v_A^*} \right]. \end{aligned} \quad (5.26)$$

Using these expressions for the drain voltages in equation (5.18), the gain errors $\epsilon_{Eij} = \epsilon_{Eij0} + \tilde{\epsilon}_{Eij}$ have thus a constant term ϵ_{Eij0} which depends on supply voltages $V_{+,-}$, threshold voltages V_{T0} and “Early” voltages V_E , and a term $\tilde{\epsilon}_{Eij}$ which depends on the input currents $i_{1,2}$ and the output pseudo-voltage v_A^* ; this dependent term is given by:

$$\tilde{\epsilon}_{E12} = \frac{U_T}{V_{Ep}} \left[(n_p - 1) \ln \left(\frac{v_A^*}{V_0} \right) - n_p \ln \left(\frac{i_1}{I_{Sp}} \right) \right], \quad (5.27)$$

$$\tilde{\epsilon}_{E34} = \frac{U_T}{V_{Ep}} \left[2n_p \ln \left(\frac{v_A^*}{V_0} \right) - 2n_p \ln \left(\frac{i_2}{I_{Sp}} \right) \right], \quad (5.28)$$

$$\tilde{\epsilon}_{E56} = \frac{U_T}{V_{En}} \left[(n_n - 1) \ln \left(\frac{v_A^*}{V_0} \right) - n_n \ln \left(\frac{i_2}{I_{Sn}} \right) \right], \quad (5.29)$$

where the indices p and n apply for the PMOS transistors $T_{1,2,3,4}$ and for the NMOS transistors $T_{5,6}$, respectively. In parallel to the leakage pseudo-conductance g_L^* an additional nonlinear pseudo-admittance function $y_E^*(v_A^*)$ must therefore be added, which generates the current

$$i_E = y_E^*(v_A^*) = i_1 \tilde{\epsilon}_{E12} + i_2 (\tilde{\epsilon}_{E34} + \tilde{\epsilon}_{E56}). \quad (5.30)$$

The pseudo-admittance y_E^* depends actually on v_A^* and its time derivative dv_A^*/dt because the input currents $i_{1,2}$ that appear in equation (5.30) as well as in the expressions (5.27)-(5.29) of $\tilde{\epsilon}_{Eij}$ depend on the output pseudo-voltage through the pseudo-transcapacitance law $i_1 - i_2 = C^* dv_A^*/dt$. Since the full range signal is almost as large as the range of operation of the circuit, linearisation of y_E^* around its operating point for a small signal analysis is useless and the analysis of its dynamics is therefore not straightforward. Nevertheless, the effect of this nonlinear term might be small in a reasonable range of operation and it will be neglected at first approximation in further usage of the pseudo-transcapacitor circuit.

Interestingly, the above analysis shows that a constant current I_L on the capacitor C acts in the log-domain as a linear pseudo-conductance g_L^* in parallel with the pseudo-capacitance C^* : *constant variations* of the capacitor voltage due to constant current becomes in the log-domain *exponential variations* of the pseudo-voltage due to a parallel pseudo-conductance. Similarly, constant *multiplicative* error on the mirror gains results in constant current source *added* to the input current in the log-domain.

5.3.4 Stability

The stability analysis of a single capacitor seems a nonsense since it has an infinite number of stable points when its current is zero and it is unstable when charged by a current, even a very small one. However, the pseudo-transcapacitor circuit must be designed such that it does not reach a stable point for which the input current cannot anymore control the evolution of the output pseudo-voltage. This condition is of particular interest at the power-on of the circuit, when the operating point is not yet established.

The state of the pseudo-transcapacitor is determined by the voltage on the capacitor C , which imposes the output pseudo-voltage. Two situations resulting in the loss of control are possible:

1. The desaturation of the transistors sinking the input currents $i_{1,2}$.
2. A too small current gain V_0/v_A^* of the mirrors T_1 - T_2 and T_3 - T_4 .

When used within a larger circuit, the two input currents i_1 and i_2 of the pseudo-transcapacitor will generally be sunk by saturated complementary transistors T_{i1} and T_{i2} (see figure 5.10). The drain voltage $-v_{1,2} - V_-$ of $T_{i1,2}$ depends on the drain voltage on transistors $T_{1,3}$, given using equation (5.1) by

$$v_{1,2} = nv_A + (n - 1)V_+ + V_{T0} + nU_T \ln(i_{1,2}/I_S), \quad (5.31)$$

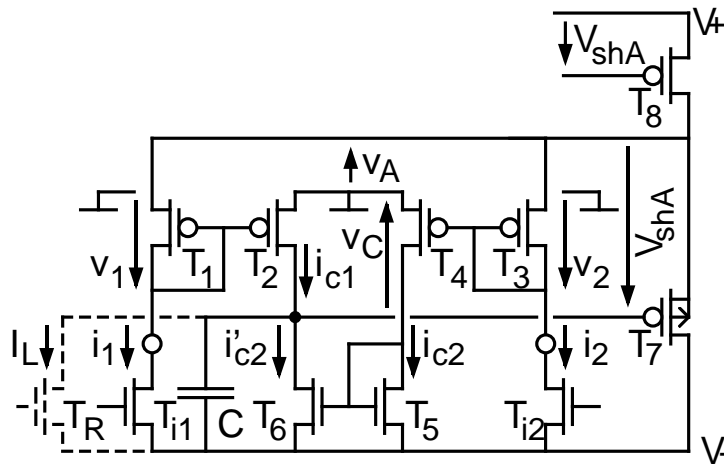


Figure 5.10: Pseudo-transcapacitor with its inputs controlled by complementary transistor.

where n , V_{T0} and I_S are the slope factor, the threshold voltage and the specific currents of transistors $T_{1,3}$, respectively; similarly to v_A , $v_{1,2}$ are defined positively from ground to the corresponding drain of $T_{1,3}$. The increase of $v_{1,2}$ to the point where the transistors $T_{i1,2}$ desaturates is therefore imposed by the increase of v_A , and thus the fall of the internal pseudo-voltage $v_A^* = V_0 \exp(-v_A/U_T)$. As illustrated by the simulation results of figure 5.11 (performed on the same circuit as in paragraph 5.3.2 with $T_{i1,2}$ having an aspect ratio $W/L = 5\mu\text{m}/5\mu\text{m}$), when the pseudo-voltage v_A^* falls linearly, $-v_A$ decreases logarithmically. This means that it is compressed as long as $d(-v_A/U_T)/d(v_A^*/V_0) = V_0/v_A^*$ is smaller than 1, thus when $-v_A > 0$. The limit $-v_A = 0$ corresponds to the unity gain of the mirrors T_1 - T_2 and T_3 - T_4 (occurring at 0.725ms and 1.055ms in the simulation, marked by vertical lines in figure 5.11), below and above which this gain increases and decreases, respectively. Therefore, if the output pseudo-voltage v_A^* falls linearly due to the constant differential input current $i_1 - i_2 < 0$ while $-v_A < 0$, v_A and thus $v_{1,2}$ will increase faster and faster. If $v_{1,2}$ become too large, practically $v_{1,2} = -V_{Dsat} + V_-$, transistors $T_{i1,2}$ desaturate. But in this case the drain of transistors $T_{1,3}$ as well as the gates of transistor $T_{2,4}$ would be close to V_- , and since $-V_-$ must be at least as large as two threshold voltages, transistors $T_{2,4}$ would fall into strong inversion, imposing currents $i_{c1,2}$ much larger than their nominal values. Transistor T_6 would therefore have already desaturated, at a relatively high drain voltage ($v_C - V_- \approx 30U_T$ in the simulation) and consequently stopped further increase of the voltage v_C , because the discharging current i'_{c2} is not anymore applied on the capacitor C , whereas the charging current i_{c1} is still imposed by T_2 . The voltage $-v_A = v_C + V_{shA}$ reaches thus a minimal value that will maintain transistors $T_{i1,2}$ saturated (with a drain voltage $-v_{1,2} - V_-$ of almost $20U_T$ in the simulation) and thus keep the pseudo-transcapacitor controllable by its input current.

At the other extreme, if the capacitor C is charged at a highest voltage V_+ , the feedback cannot work as long as v_C is not pulled down to a value that would bring the follower-shifter into its normal mode of operation, i.e. with T_7 and T_8 saturated. Before this point, T_7 is blocked and T_8 is in the conduction mode, imposing $-v_A = V_+$. Anyway, in this case the transistors $T_{i1,2}$ are ensured to be saturated, thus theoretically capable to control the charging of the capacitor. However, the gain of the mirrors T_1 - T_2 and T_3 - T_4 reaches in this case its minimal value $V_0/v_A^* = \exp(-V_+/U_T)$ which may yield currents $i_{c1,2}$ that are dominated by uncontrolled leakage

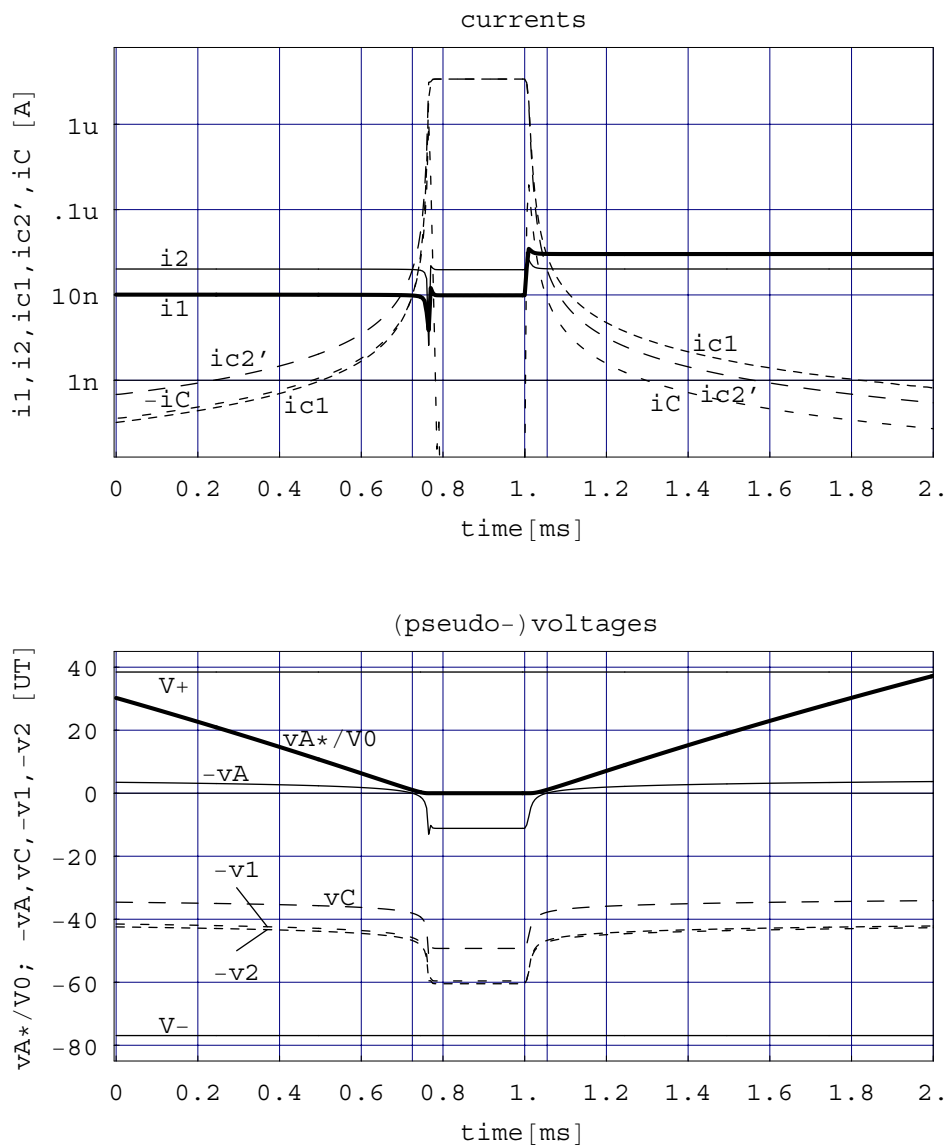


Figure 5.11: Behaviour of the pseudo-transcapacitor with a step-varying differential input signal, driving the circuit beyond the lower limit of output pseudo-voltage; voltages relative to U_T are plotted to illustrate the identical slope of v_A^*/V_0 and $-v_A/U_T$ at unity gain $i_{c1,2}/i_{1,2}$ (simulation results).

currents through the bulk-drain junction of T_2 and T_6 .

Simulations showed that the circuit was unable to reach a controllable operating point at startup with a supply voltage $V_+ = 1V$. However, reducing it down to $V_+ = 0.5V$, the circuit could be brought to a controllable

mode of operation from any initial capacitor voltage between the power supply rails. For higher values of initial capacitor voltage, a reset transistor T_R might be necessary to discharge the capacitor after startup. This transistor might also be used to control the leakage current I_L such that it sets a positive parallel pseudo-conductance G_L^* ensuring the stability of the circuit (see paragraph 5.3.3).

As a conclusion, the pseudo-transcapacitor circuit is controllable by its inputs for any initial capacitor voltage $V_- \leq V_{C0} \leq V_+$, provided that the transistor T_6 desaturates before the transistors sinking the input currents and that the positive supply voltage V_+ ensures a minimal possible gain of the mirrors T_1 - T_2 and T_3 - T_4 allowing them to source currents into the capacitor that are large enough to control its discharge.

5.3.5 Noise

The noise generated by the pseudo-transcapacitor circuit is modeled as additional equivalent noise sources in order to estimate its effect in larger circuits. An input equivalent current noise source will take into account all internal noise sources yielding the noise current entering the capacitor C . An additional output voltage noise source is then required to model the effect of the internal noise generated by the follower-shifter, since this noise is not integrated by the capacitor.

Each transistor T_i generates a noise current i_{Ni} having a power spectral density s_{Ii} . The noise level is usually small enough to linearise the circuit around its operating point, according to figure 5.12. With $g_{m6} = g_{m5}$, $g_{m2}/g_{m1} = I_{C1}/I_0 = g_{m4}/g_{m3} = I_{C2}/I_0 = V_0/V_A^*$ and $g_{s1} = I_{C1}/U_T = g_{s3} = I_{C2}/U_T = I_0 V_0/V_A^*$, the noise current i_{NC} charging the capacitor is given by:

$$\begin{aligned}
 i_{NC} &= \left[\frac{g_{m4} g_{m6}}{g_{m3} g_{m5}} g_{s3} - \frac{g_{m2}}{g_{m1}} g_{s1} \right] v_A \\
 &+ \frac{g_{m4} g_{m6}}{g_{m3} g_{m5}} i_{N3} - \frac{g_{m2}}{g_{m1}} i_{N1} + i_{N4} + i_{N2} - i_{N5} - i_{N6} \\
 &= (i_{N3} - i_{N1}) \frac{V_0}{V_A^*} + i_{N4} + i_{N2} - i_{N5} - i_{N6}. \quad (5.32)
 \end{aligned}$$

The thermal noise generated by each transistor T_i , when all transistors are saturated and assumed in the weak inversion region, has a power spectral density $s_{Ii} = 2n_i k_B T g_{mi}$, where k_B is the Boltzmann constant and T is

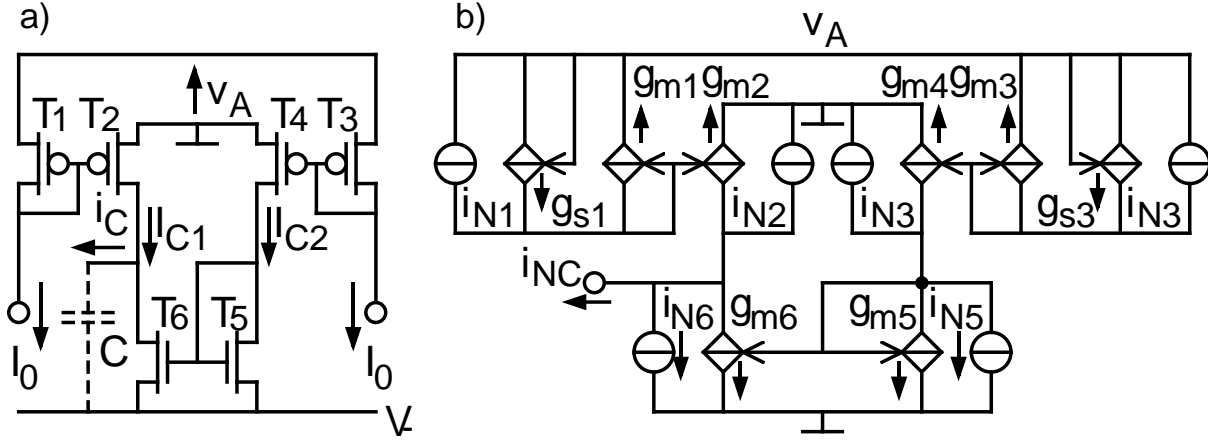


Figure 5.12: a) Pseudo-transcapacitor input circuit at its operating point and b) its linearised version with internal noise sources.

the temperature in Kelvin [52]. Since these noise sources are not correlated, their power spectral density add. The power spectral density s_{IC} of the capacitor current i_{NC} due to thermal noise is given by replacing the current $\pm i_{Ni}$ by their power spectral density $+s_{Ii}$ and squaring all gains in equation (5.32):

$$\begin{aligned} s_{IC} &= (s_{I3} + s_{I1}) \left(\frac{V_0}{V_A^*} \right)^2 + s_{I4} + s_{I2} + s_{I5} + s_{I6} \\ &= \frac{4k_B T}{U_T} I_0 \left(\frac{V_0}{V_A^*} \right)^2 \left(1 + 2 \frac{V_A^*}{V_0} \right). \end{aligned} \quad (5.33)$$

This power spectral density must be equal to that obtained when injecting an equivalent noise current i_{Nin} at input i_1 in the noiseless circuit. The power spectral density s_{Iin} of this input noise current i_{Nin} must be such that $s_{Iin} (V_0/V_A^*)^2 = s_{IC}$, thus:

$$s_{Iin} = \frac{4k_B T}{U_T} I_0 \left(1 + 2 \frac{V_A^*}{V_0} \right), \quad (5.34)$$

where V_A^*/V_0 is determined by the dc output of the pseudo-transcapacitor circuit. The input noise is injected at input i_1 only, but it can equivalently be injected at input i_2 . It can also be injected on both input i_1 and i_2 , provided its power spectral density is half the value given by equation (5.34).

The noise current i_{NC} is integrated by the capacitor C , yielding an output noise voltage having a power spectral density $s_{VC} = s_{IC}/(2\pi fC)^2$.

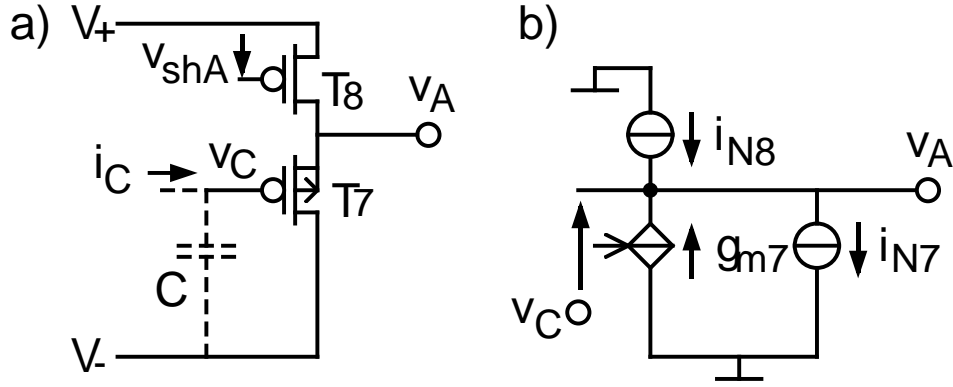


Figure 5.13: a) Output follower-shifter circuit of pseudo-transcapacitor at its operating point and b) its linearised version with internal noise sources.

However, additional noise is created at this output by the follower-shifter circuit, which can also be linearised around its operating point, according to figure 5.13. Since transistor T_7 has its substrate connected to v_A , g_{m7} is controlled by the voltage difference $v_C - v_A$, yielding an output voltage $v_A = v_C + (i_{N8} - i_{N7})/g_{m7}$. The power spectral density of the output noise voltage is thus given by $s_{VA} = s_{VC} + (s_{I8} + s_{I7})/g_{m7}^2$, whose second term represents the noise contribution of the follower-shifter stage alone. Since both transistors T_7 and T_8 are identical and have the same drain current, they have the same transconductance $g_{m7} = g_{m8}$; the same slope factor $n_7 = n_8$ is also assumed. These transistors being set in strong inversion, their current noise power spectral density is given by $s_{Ii} = (8/3)k_B T n_i g_{mi}$ [52], resulting in a noise contribution v_{Nout} of the output follower-shifter having a power spectral density:

$$s_{Vout} = \frac{16n_7}{3} \frac{k_B T}{g_{m7}}, \quad (5.35)$$

where g_{m7} is also the output conductance of the follower-shifter circuit: it can be considered as generating alone the output noise voltage of power spectral density $\gamma_{out} 4k_B T / g_{m7}$ with a noise factor $\gamma_{out} = 4n_7/3$. The transconductance $g_{m7} = g_{m8}$ is imposed by the shift voltage V_{shA} according to $g_{m8} = \beta_8 (V_{shA} - V_{T08})/n_8$, where β_8 , V_{T08} and n_8 are the transconductance factor, the threshold voltage and the slope factor of the transistors T_8 (and T_7), respectively.

The pseudo-transcapacitor circuit including the equivalent noise source is shown in figure 5.14: an input noise current source i_{Nin} with power

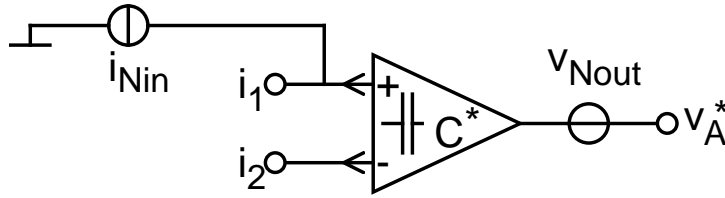


Figure 5.14: Pseudo-transcapacitor with its input and output equivalent noise sources

spectral density s_{Iin} is added at the input i_1 and the output noise voltage source v_{Nout} with power spectral density s_{Vout} is inserted at the output.

The output noise power v_{AN}^2 of the circuit is estimated by integrating over frequency the power spectral density of each source multiplied by the squared transfer function between the source and the output, thus

$$v_{AN}^2 = \int_0^{\infty} s_{Iin} \left(\frac{V_0}{V_A^*} \right)^2 \frac{df}{(2\pi fC)^2} + \int_0^{\infty} s_{Vout} df, \quad (5.36)$$

where the first term is due to the input noise source and the second to the output noise source. Both integrals yield an infinite value: the first one for the lower limit $f = 0$, which is an intrinsic feature of a pure integrator with a non-zero dc input noise, and the second for the limits $f = \infty$, because the output is not frequency limited. In practice, however, the low frequency gain is limited by the pseudo-conductance g_{L*} due to leakage current I_L (paragraph 5.3.3), and the output is high-frequency limited by the output conductance g_{m7} together with the parasitic capacitance at the output node. Furthermore, as the pseudo-transcapacitor is to be used as a building block for larger circuits, the effect of its input and output noise sources i_{Nin} and v_{Nout} is to be taken into account in the noise calculation of the whole circuit, as will be shown in the next section (paragraph 5.4.6).

5.3.6 Circuits based on pseudo-transcapacitors

Log-domain grounded capacitor

The pseudo-transcapacitor of figure 5.6 is transformed into a pseudo-grounded pseudo-capacitor by imposing its output pseudo-voltage on its input with a current conveyor, as shown on figure 5.15a. With a constant

current I_0 added to the pseudo-capacitor current i_C as well as imposed on the pseudo-transcapacitance input i_2 , this circuit implements:

$$C^* \frac{dv_C^*}{dt} = i_1 - i_2 = (i_C + I_0) - I_0 = i_C. \quad (5.37)$$

The mismatch between the two current sources I_0 , together with the internal offset source due to the imperfection pseudo-transcapacitor's mirrors (see paragraph 5.3.3), results in an offset current source in parallel with the pseudo-capacitor, which will just cause a dc pseudo-voltage offset when the terminal v_C^* is loaded by a pseudo-conductance.

Comanding integrator

Pseudo-transcapacitors are closely related to comanding integrators [51], which are based on a compression of the input current, an integration of the compressed current by a linear capacitor and an expansion of the resulting capacitor voltage. The pseudo-transcapacitor compresses and integrates, but the expansion is not needed since an output pseudo-voltage is required. Nevertheless, as shown in figure 5.15b, the expansion into a linear current is performed with a pseudo-grounded pseudo-conductance G^* (see paragraph 5.2.2), resulting in:

$$i_{out} = \frac{C^*}{G^*} \int_{-\infty}^t (i_1 - i_2) dx. \quad (5.38)$$

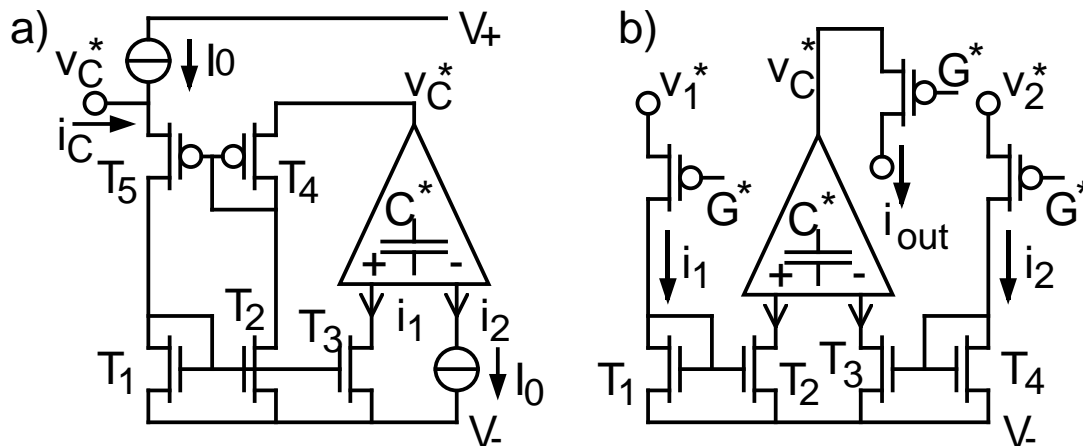


Figure 5.15: a) Log-domain grounded capacitor, b) comanding integrator/pseudo-transinductor.

Pseudo-transinductor

Using identical pseudo-conductances G^* , the input currents $i_{1,2}$ of a companding integrator can be controlled by pseudo-voltage $v_{1,2}^* = i_{1,2}/G^*$. The resulting pseudo-transinductor of figure 5.15b implements:

$$L^* \frac{di_{out}}{dt} = v_1^* - v_2^*, \quad (5.39)$$

where a gyrator made from the three transistors implementing the pseudo-conductances G^* transforms the pseudo-capacitance C^* into a pseudo-inductance $L^* = C^*/G^{*2}$.

5.4 Log-domain implementation of the 2-D cochlea

5.4.1 Basilar membrane resonator

The electrical equivalent of a basilar membrane section is a serial resonator made from a resistor, a capacitor and a *super-capacitor*. The super-capacitor is a dipole whose second derivative of the voltage difference v between its terminals is proportional to the current i flowing through it, i.e. in the frequency domain, $v \propto i/(j\omega)^2 = -i/(2\pi f)^2$. For this reason, this device is usually called *Frequency Dependant Negative Resistor* (FDNR). The term super-capacitor is preferred here, because it illustrates the fact that a serial RCS resonator is equivalent to a LRC resonator: the inductance L becomes a resistance R' , the resistance R a capacitor C' and the capacitor C a “super”-capacitor S' , provided that the current $i'(t)$ flowing through these elements corresponds to the time derivative $di(t)/dt$ of the current flowing through the LRC resonator:

$$\begin{aligned} v(t) &= L \frac{di(t)}{dt} + Ri(t) + \frac{1}{C} \int_{-\infty}^t i(x) dx \\ &= R' i'(t) + \frac{1}{C'} \int_{-\infty}^t i'(x) + \frac{1}{S'} \int_{-\infty}^t \int_{-\infty}^y i'(x) dx dy, \quad (5.40) \end{aligned}$$

where $R' = L/\tau_0$, $C' = \tau_0/R$, $S' = \tau_0 C$ and $i' = \tau_0 di/dt$, τ_0 being an arbitrary scaling time constant. Rewriting the equation of the serial RCS

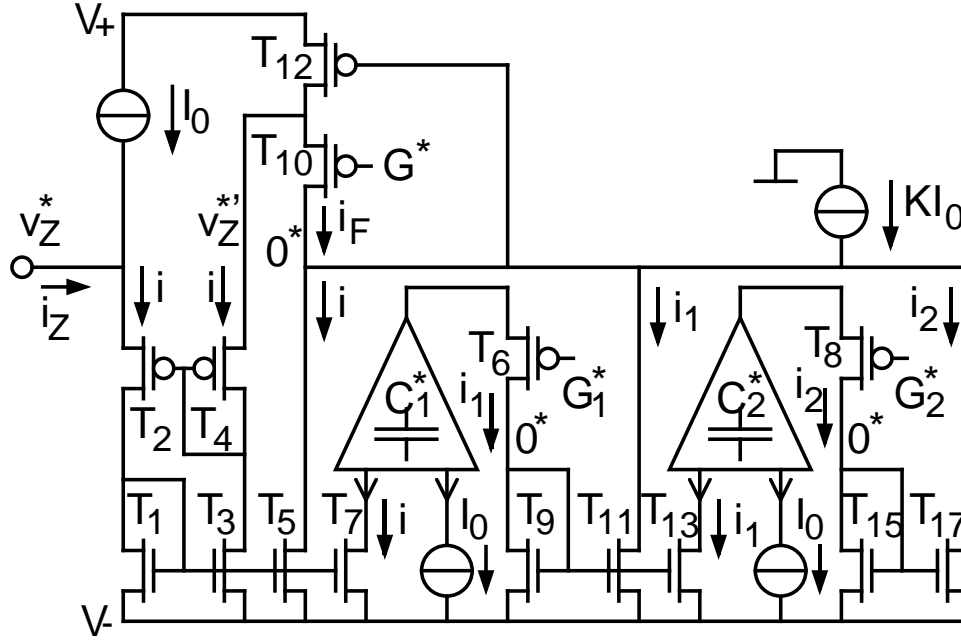


Figure 5.16: Log-domain implementation of the basilar membrane resonator.

resonator

$$v(t) = R' \left[i'(t) + \frac{1}{C'R'} \int_{-\infty}^t \left(i'(y) + \frac{C'}{S'} \int_{-\infty}^y i'(x) dx \right) dy \right], \quad (5.41)$$

indicates that the RCS resonator can be implemented using two companding integrators (paragraph 5.3.6), a current-to-pseudo-voltage converter (paragraph 5.2.2) and a current conveyor used similarly as for the log-domain grounded capacitor (paragraph 5.3.6), as shown in figure 5.16. The pseudo-voltage across the capacitor and the super-capacitor are converted into currents i_1 and i_2 by the pseudo-conductances G_1^* and G_2^* , respectively, whereas the pseudo-voltage across the resistor is already available as the current i . These currents are summed into the current i_F , which is converted back into the resonator pseudo-voltage $v_Z^{*'} = i_F/G^*$ using the pseudo-conductance G^* and finally fed back at the input through the current conveyor T_1 - T_3 - T_2 - T_4 that imposes $v_Z^* = v_Z^{*'}$.

Expressing the transfer function (5.38) of the companding integrator in the Laplace domain allows one to use

$$I_1(s) = \frac{1}{s\tau_1}(I(s) - I_0), \quad (5.42)$$

$$I_2(s) = \frac{1}{s\tau_2}(I_1(s) - I_0) = \frac{1}{s^2\tau_1\tau_2}(I(s) - I_0) - \frac{1}{s\tau_2}I_0 \quad (5.43)$$

in writing the sum of the currents converted into the resonator's pseudo-voltage $V_Z^*(s)$:

$$\begin{aligned} G^*V_Z^*(s) &= I(s) + I_1(s) + I_2(s) - KI_0 \quad (5.44) \\ &= I(s) \left[1 + \frac{1}{s\tau_1} + \frac{1}{s^2\tau_1\tau_2} \right] - I_0 \left[K + \frac{1}{s\tau_1} + \frac{1}{s\tau_2} + \frac{1}{s^2\tau_1\tau_2} \right], \end{aligned}$$

where $\tau_1 = C_1^*/G_1^*$ and $\tau_2 = C_2^*/G_2^*$. The current $I(s)$ is expressed from equation (5.44) and used to rewrite equations (5.42) and (5.43), with $v_Z^{*'} = v_Z^*$ ensured by the input current conveyor:

$$I(s) = V_Z^*(s)G^* \frac{s^2\tau_1\tau_2}{s^2\tau_1\tau_2 + s\tau_2 + 1} + I_0 \frac{Ks^2\tau_1\tau_2 + s\tau_1 + s\tau_2 + 1}{s^2\tau_1\tau_2 + s\tau_2 + 1}, \quad (5.45)$$

$$I_1(s) = V_Z^*(s)G^* \frac{s\tau_2}{s^2\tau_1\tau_2 + s\tau_2 + 1} + I_0 \frac{(K-1)s\tau_2 + 1}{s^2\tau_1\tau_2 + s\tau_2 + 1}, \quad (5.46)$$

$$I_2(s) = V_Z^*(s)G^* \frac{1}{s^2\tau_1\tau_2 + s\tau_2 + 1} + I_0 \frac{(K-2) - s\tau_1}{s^2\tau_1\tau_2 + s\tau_2 + 1}. \quad (5.47)$$

Since the bias current I_0 is dc ($s = j\omega = 0$), the second term of the three above equations simplifies into I_0 , I_0 and $(K-2)I_0$, respectively, resulting in

$$\frac{V_Z^*(s)}{I(s) - I_0} = \frac{V_Z^*(s)}{I_Z(s)} = \frac{1}{G^*} \left[1 + \frac{1}{s\tau_1} + \frac{1}{s^2\tau_1\tau_2} \right] = Z^*(s), \quad (5.48)$$

$$\frac{V_Z^*(s)}{I_1(s) - I_0} = \frac{s\tau_1}{G^*} \left[1 + \frac{1}{s\tau_1} + \frac{1}{s^2\tau_1\tau_2} \right] = s\tau_1 Z^*(s), \quad (5.49)$$

$$\frac{V_Z^*(s)}{I_2(s) - (K-2)I_0} = \frac{s^2\tau_1\tau_2}{G^*} \left[1 + \frac{1}{s\tau_1} + \frac{1}{s^2\tau_1\tau_2} \right] = s^2\tau_1\tau_2 Z^*(s), \quad (5.50)$$

where $Z^*(s) = V_Z^*(s)/I_Z(s)$ is the pseudo-impedance of the log-domain resonator. Expressing equation (5.48) in terms of the resonator input currents $I_Z(s) = I(s) - I_0$ and comparing it with equation (4.32) (p. 86), results in the correspondences between the electrical model of the basilar

electrical	log-domain
conductance G_{BM}	G^*
capacitance C_{BM}	$\tau_1 G^* = C_1^* \frac{G^*}{G_1^*}$
super-capacitance S_{BM}	$\tau_1 \tau_2 G^* = \frac{C_1^* C_2^* G^*}{G_1^* G_2^*}$

Table 5.2: Correspondences between the electrical model of the basilar membrane resonator and its log-domain implementation

membrane resonator and its log-domain implementation listed in table 5.2.

Using the time constant τ and quality factor Q defined by

$$\tau^2 = \tau_1 \tau_2 = \frac{C_1^* C_2^*}{G_1^* G_2^*}, \quad (5.51)$$

$$Q^2 = \tau_1 / \tau_2 = \frac{C_1^* G_2^*}{C_2^* G_1^*}, \quad (5.52)$$

the resonator impedance Z^* is expressed by:

$$Z^*(s) = \frac{1}{G^*} \frac{s^2 \tau^2 + s\tau/Q + 1}{s^2 \tau^2}. \quad (5.53)$$

The dc value of the currents i and i_1 when no ac excitation is present at the input v_Z equals I_0 since they correspond to the inputs of the pseudo-transcapacitors C_1^* and C_2^* which stabilise at a zero differential input. Therefore, at dc the current i_2 stabilises at a value $I_2 = I_F + (K - 2)I_0$, where $I_F = V_Z^* G^*$ is determined by the dc pseudo-voltage V_Z^* “across” the resonator. The dc value I_2 must be large enough to permit the maximal variation of i_2 ensuring $i_2 > 0$. On the other hand, the current-to-pseudo-voltage converter T_{10} - T_{12} needs a minimal input current I_{Fmin} flowing through G^* to function correctly (see paragraph 5.2.2). Therefore, the input pseudo-voltage v_Z^* must vary around a dc value V_Z^* which permits the maximal variation of v_Z^* to maintain $v_Z^* G^* > I_{Fmin}$. The current i_2 has thus two dc components, $I_2 = (K - 2)I_0 + V_Z^* G^*$. Setting $K = 3$, the first one equals to the common mode I_0 of the pseudo-transcapacitors, and the second corresponds to the dc value V_Z^* of the pseudo-voltage across the resonator, represented by the current $I_2 - I_0 = V_Z^* G^*$.

5.4.2 Parameter mapping

According to table 4.3 (p. 89), the conductance $G_{BM}(i)$ modeling the basilar membrane mass is the same for each resonator in the bank. The same applies to the capacitance $C_{BM}(i)$, but its value is modulated by the undamping term u , which can be local to a position i if an automatic gain control mechanism is implemented. Finally, the super-capacitance $S_{BM}(i)$ modeling the basilar membrane compliance increases exponentially with position i in the resonator bank. The correspondences of table 5.2 suggest therefore to map the super-capacitance $S_{BM}(i)$ with the pseudo-capacitance $C_2^*(i)$, and the unmodulated capacitance $C_{BM}(u = 0)$ with the pseudo-capacitance C_1^* . Since the pseudo-conductance G^* corresponds to the conductance G_{BM} that is constant, the pseudo-conductance G_1^* is imposed by the undamping term u according to $1 - u \propto G_1^*$, whereas the need of a constant product $G_0^{*2} = G_1^* G_2^*$ is imposed for each super-capacitor $S_{BM}(i)$. This choice of constraints is summarised in table 5.3.

5.4.3 Implementation of the log-domain resonator

The full diagram of the log-domain resonator is shown in figure 5.17. The pseudo-transcapacitors $C_{1,2}^*$ have their pseudo-capacitance controlled by a voltage imposed on their control input V_{shA} , while their second control input V_{shC} is kept constant (see figure 5.6, p. 112). Since $C_2^*(i)$ increases

mechanical	electrical	log-domain
mass $m'(i)$	$G_{BM} = \frac{F_j \Delta_x}{F_v m'}$	$G^*(i) = \frac{F_j \Delta_x}{F_v m'}$
viscosity $h'(i)$	$C_{BM}(i) = \frac{F_j \Delta_x}{F_v h'} \frac{1}{1 - u(i)}$	$C_1^*(i) = G_0^* \frac{m'}{h'}$ $G_1^* = G_0^*[1 - u(i)]$
stiffness $k'(i)$	$S_{BM}(i) = \frac{F_j \Delta_x}{F_v k'(0)} 2^{i/2b}$	$C_2^*(i) = G_0^* \frac{h'}{k'(0)} 2^{i/2b}$ $G_2^* = \frac{G_0^{*2}}{G_1^*}$

Table 5.3: Mapping of the parameters between the mechanical and electrical model of the basilar membrane resonator and its log-domain implementation

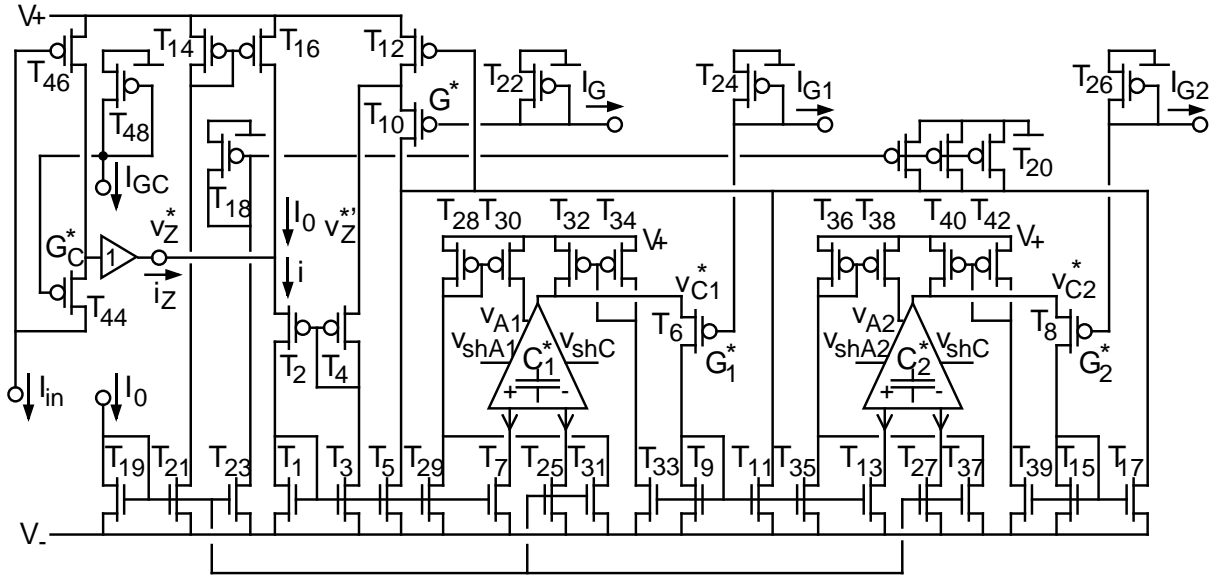


Figure 5.17: Log-domain implementation of the basilar membrane resonator.

exponentially with the position i of the resonator in the bank, the value of V_{shA2}/U_T , to which the logarithm of C_2^* is proportional must increase linearly, resulting in follower-shifter's bias currents that vary quadratically if the follower-shifter are in strong inversion or exponentially if they are in weak inversion.

However, these follower-shifters must source an output current, which will unbalance the current biasing their two transistors, resulting in a modulation of their output voltage. To prevent this effect, both follower-shifters of both pseudo-transcapacitors are unloaded by sourcing on their output a copy of their output current. The output current of the follower-shifter controlled by V_{shA} (at the internal node v_A of the pseudo-transcapacitor, see figure 5.6) corresponds to the sum of the pseudo-transcapacitor input currents, available by copying the current in the transistors that sink them (transistors T_{29} , T_{31} , T_{28} and T_{30} for C_1^* and T_{35} , T_{37} , T_{36} and T_{38} for C_2^* in figure 5.17); similarly, the output current of the follower-shifter controlled by V_{shC} (at the pseudo-transcapacitor output v_C) corresponds to the output current of the integrators $C_{1,2}^*G_{1,2}^*$, available by copying the current in transistors T_9 and T_{15} using T_{33} , T_{32} , T_{34} and T_{39} , T_{40} , T_{42} , respectively. At the expense of 7 additional transistors for each pseudo-transcapacitor, the power consumption mostly needed to bias the $2 \times 2 \times M$ fully loaded follower-shifters will be largely reduced.

The current sources KI_0 ($K = 3$) is implemented by a PMOS mirror

T_{18} - T_{20} having the source of its transistors connected to the ground instead of the voltage supply V_+ . This ensures the transistor T_{10} implementing the pseudo-conductance G^* to be saturated as long as the current KI_0 is correctly imposed by T_{20} saturated. Without this, the case may happen that the voltage v_Z^* at the source of T_{10} rises transitorily up to a value for which the input pseudo-voltage source imposing v_Z^* suddenly absorbs the totality of the input current source I_0 (transistor T_{16}), setting the conveyor T_1 - T_2 - T_3 - T_4 in an undesirable stable operating point that do not anymore impose $v_Z^* = v_Z^*$. The input current source I_0 , however is imposed by a PMOS mirror T_{14} - T_{16} having the source of its transistors connected at V_+ . Setting V_+ at a lower value than in the simulations of paragraphs 5.3.2 and 5.3.4 (0.5V instead of 1V), prevents also the internal pseudo-voltage v_A^* of the pseudo-transcapacitors to rise to a value making it uncontrollable due to the resulting very small gain of its compressing mirrors (see paragraph 5.3.4).

NMOS transistors			PMOS transistors		
name	W/L	I_S	name	W/L	I_S
M_1 - M_{39}	$2\mu\text{m}/20\mu\text{m}$	26nA	$M_2, M_4,$ M_{14} - $M_{20},$ M_{28} - $M_{42},$	$2\mu\text{m}/20\mu\text{m}$	7.7nA
			M_6 - $M_{12},$ M_{22} - $M_{26},$ M_{46} - M_{48}	$20\mu\text{m}/5\mu\text{m}$	308nA
pseudo-transcapacitors (according to diagram in fig. 5.6)					
M_5, M_6	$2\mu\text{m}/20\mu\text{m}$	26nA	M_1 - M_4	$20\mu\text{m}/5\mu\text{m}$	308nA
			M_7 - M_{10}	$5\mu\text{m}/5\mu\text{m}$	77nA
voltage sources			current sources		
name	value		name	value	
V_+	+0.5V		I_0	20nA	
V_-	-2.0V		I_G	20nA	
V_{shA1}	$-0.5\text{V} - U_T \ln(t)$		I_{G1}	$8\text{nA}/q$	
V_{shA2}	$-0.5\text{V} - U_T \ln(t)$		I_{G2}	$8\text{nA} \cdot q$	
V_{shC}	-0.5V		I_{GC}	20nA	

Table 5.4: Parameters values for simulation; note that all voltages are defined positively terminal from node to ground.

5.4.4 Transient simulation

The full circuit of figure 5.17 was simulated. The input pseudo-voltage v_Z^* was imposed through a follower by a current-to-pseudo-voltage converter T_{44}, T_{46}, T_{48} having a pseudo-transresistance $v_Z^*/I_{in} = 1/G_C^* = V_0/I_{GC}$. The size of the transistors and the value of the currents and voltages sources are summarised in table 5.4.

The input signal I_{in} is a current switching between 10nA and 30nA, which corresponds to an input pseudo-voltage $v_Z^*/V_0 = I_{in}/I_{GC}$ varying between 0.5 and 1.5. The time constant τ of the resonator is controlled by the voltage $V_{shA1,2}$ of both pseudo-transcapacitors C_1^* and C_2^* . In the simulation, these voltages are adjusted logarithmically by the parameter t , imposing $t^2 \propto C_1^*C_2^*$, thus $t \propto \tau$; the quality factor Q of the resonator is controlled by the currents I_{G1} and I_{G2} imposing the pseudo-conductances G_1^* and G_2^* . This modulation is performed to keep the product $G_1^*G_2^*$ constant to a value $G_0^* = 8\text{nA}/V_0$, while the ratio $G_2^*/G_1^* = q^2$ is adjusted by a parameter q , imposing thus $q \propto Q$. With identical capacitor $C = 5\text{pF}$ in both pseudo-transcapacitors and independently from the parameter q , the time constant τ at $t = 1$ theoretically equals $CU_T/(G_0^*V_0) = U_T5\text{pF}/8\text{nA} = 16.25\mu\text{s}$, corresponding to a 10 kHz characteristic frequency; similarly, for $q = 1$, the quality factor Q theoretically equals 1 independently from the parameter t .

Figure 5.18 shows the resonator input current i_Z and its internal currents i , i_1 and i_2 representing the voltage across the resistor G_{BM} , the capacitor C_{BM} and the super-capacitor S_{BM} , respectively, in response to the input pseudo-voltage steps v_Z^*/V_0 , for $t = 4$ and $q = 1$. The dc value at which these currents stabilise is different from their theoretical prediction ($I_Z = 0$, $I = I_1 = I_0 = 20\text{nA}$ and $i_2 = I_0 + V_Z^*/V_0 = 30 \div 50\text{nA}$), mainly because of the gain error in the mirrors copying I_0 , due to the output conductance of their transistors. This shift of dc current values is functionally not crucial, since the output variable of the equivalent serial resonator is its current (emulating the basilar membrane acceleration) integrated over time (basilar membrane velocity), thus a current proportional to i_1 , whose dc component is meaningless. Therefore the current offset must just be small enough not to move the current level outside of the operational range of the resonator circuit. For i , i_1 and i_2 this offset is thus not so important. However, the dc offset I_{Zoffs} of the input current i_Z of all resonator $Z^*(i)$ in the bank will create a dc pseudo-voltage offset V_{Zoffs}^* on the distributed load consisting of the pseudo-resistive network

emulating the cochlear liquid. The systematic offset due to the output conductances of the mirror would thus accumulate all along the resonator bank and lead to local value of $v_Z^*(i)$ that might bring the resonator out of its range of operation. However, the random offset due to component

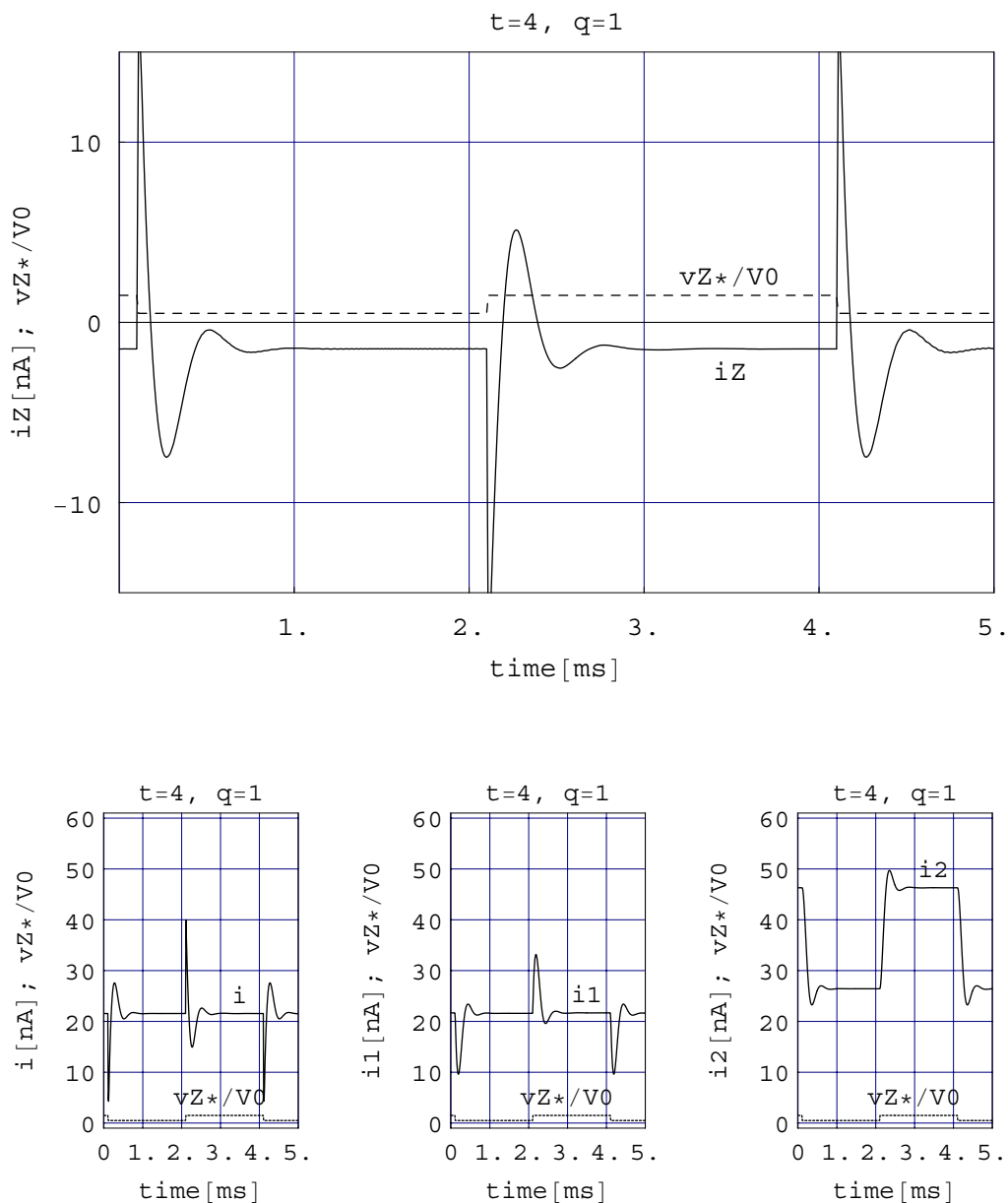


Figure 5.18: Step response currents i_Z (top), i , i_1 and i_2 (bottom, from left to right), for $t = 4$ and $q = 1$ (simulation results).

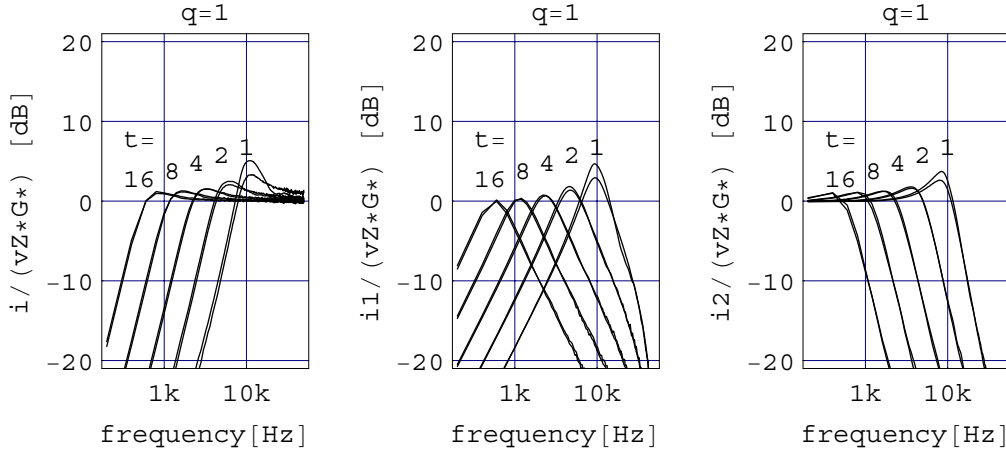


Figure 5.19: Frequency response of the resonator for several values of time constant $t\tau$, with a quality factor imposed with $q = 1$ (simulation results).

mismatch will accumulate to a lesser extent, since it is the variance of these offsets that accumulates (see paragraph 5.4.7).

The frequency response (5.48), (5.49) and (5.50) of the resonator was verified by taking the Fourier transform of the time derivative of the corresponding step response of figure 5.18 for several values of t and q . Figure 5.19 shows the frequency response for several values of time constant and a fixed quality factor set with $q = 1$. The response obtained from the positive step ($v_Z^*/V_0 = 0.5 \rightarrow 1.5$) and the negative step ($v_Z^*/V_0 = 1.5 \rightarrow 0.5$) are superimposed to show the low sensitivity to current level of the resonator time constant.

Figure 5.20 shows the same frequency response for several imposed quality factors and a fixed time constant set with $t = 8$; similarly to figure 5.19, the response to both positive and negative input steps are superimposed to illustrate the insensitivity to the input dc level for the relatively large time constant 8τ . For smaller time constants, however, the sensitivity of the quality factor to the amplitude of the input level increases, as illustrated in the curves $t = 1$ and $t = 2$ of figure 5.19.

Such a level sensitivity of the quality factor to the dc input pseudo-voltage V_Z^* at relatively high characteristic frequency ($> 5\text{kHz}$) prevents to implement large quality factors. Even with a fixed dc pseudo-voltage at the input of the full cochlear model (pseudo-resistive network and resonator bank), the local value of $V_Z^*(i)$ will vary with position i due to the dc offset

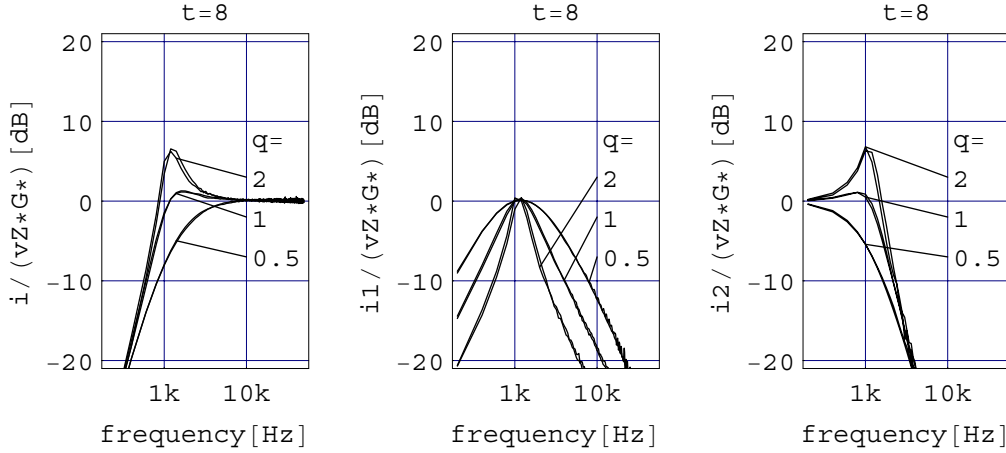


Figure 5.20: Frequency response of the resonator for several values of imposed quality factor and a time constant set to 8τ (simulation results).

$I_{Z_{offs}}(i)$ of the current $i_Z(i)$ on the loading pseudo-resistive network (see paragraph 5.4.7). The origin of this sensitivity must therefore be identified.

5.4.5 Stability

The cause of this sensitivity of the quality factor to dc input voltage resides in the feedback block of the resonator that may make it unstable. As shown in figure 5.21, the resonator is split into two parts. The *forward block*

$$A_f(s) = \frac{I(s) + I_1(s) + I_2(s)}{I(s)} = \frac{s^2\tau^2 + s\tau/Q + 1}{s^2\tau^2}, \quad (5.54)$$

is made from the integrators $C_1^*G_1^*$ and $C_2^*G_2^*$ and the transistor T_5 of figures 5.16 and 5.17. It injects the current $i_f = i + i_1 + i_2$ into the *feedback block* $A_b(s)$, which consists of the current-to-pseudo-voltage converter T_{10} - T_{12} and the current conveyor T_1 - T_2 - T_3 - T_4 . The feedback block outputs in turn the current i_b into the forward block. The forward block does not need to be linearised since its current mode implementation makes it linear on the full operational current range. In the log-domain, the feedback block consists ideally of the single pseudo-conductance G^* . However, the imperfections of the feedback block that can make the resonator unstable, i.e. the parasitic gate capacitances and output conductances of its transistors are not linear in the log-domain. The feedback block must therefore

be linearised around its operating point, which is signal dependent. The input voltage v_Z may be converted into an equivalent input current $g_C v_Z$, but the stability is analysed using the open loop gain $A_f(s)A_b(s)$ with a dc input voltage V_Z , cancelling its small signal variations.

The linearised transfer function $A_b(s)$ of the feedback block was estimated by an AC simulation of the current-to-pseudo-voltage block and the current conveyor alone. The input pseudo-voltage was set to a constant value V_Z^* , the ac input current i_f was sunk from the input of the current-to-pseudo-voltage converter and the resulting ac output current i_b was measured at the drain of transistor T_5 . In order to set the appropriate operating point, a DC simulation was performed with the drain of T_5 looped on the input of the current-to-pseudo-voltage converter ($I_f = I_b$ at dc) before the AC analysis.

This process was performed for three dc input pseudo-voltages V_Z^* corresponding to a current input $I_{in} = G_C^* V_Z^*$ set at 10nA, 20nA and 30nA, according to the transient simulation performed in paragraph 5.4.4. This simulation shows that in the frequency range of operation, the feedback

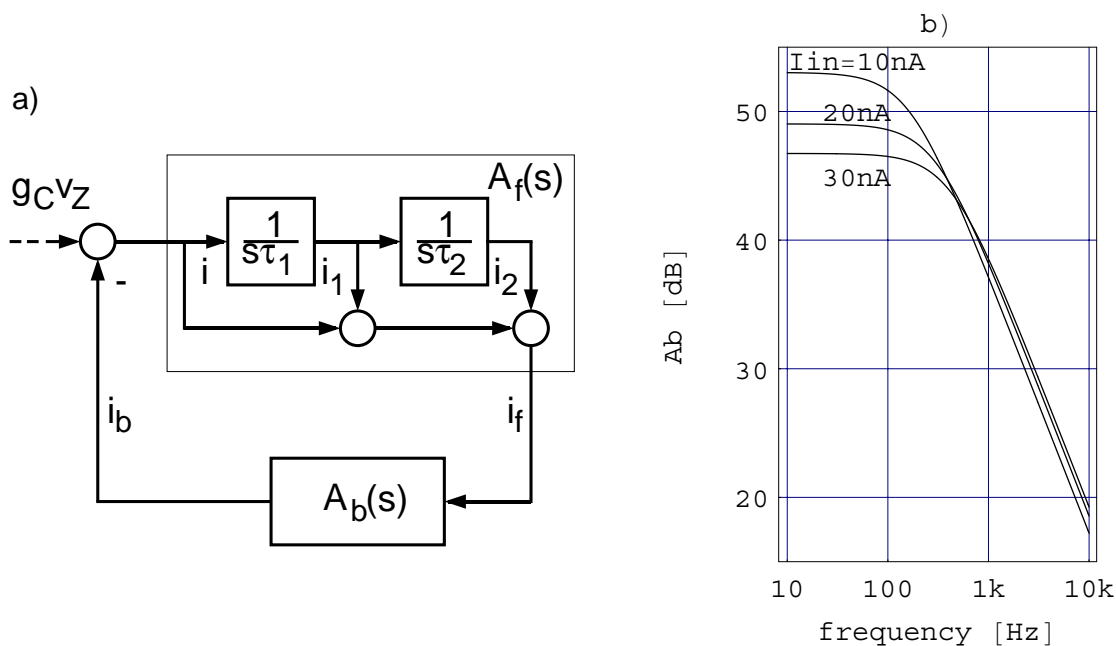


Figure 5.21: Linearised resonator for stability analysis.

block presents a first-order low-pass transfer function

$$A_b(s) = \frac{I_b(s)}{I_f(s)} = \frac{A}{s\tau_b + 1}, \quad (5.55)$$

whose dc gain A and cutoff frequency $1/2\pi\tau_b$ vary between 53dB and 47dB and between 100Hz and 200Hz, respectively, for a dc input pseudo-voltage V_Z^* set by I_{in} varying between 10nA and 30nA (figure 5.21b).

The Nyquist diagrams of the open loop gain $A_b(j\omega)A_f(j\omega)$ shown in figure 5.22 are drawn for varying resonator's characteristic frequency $1/2\pi\tau$ and quality factors Q , with a feedback block having a 200Hz cutoff frequency and a 47dB dc gain; they confirm that the quality factor of a resonator having a 10kHz characteristic frequency must be limited to a maximal value of 4, and vice versa, to ensure its stability (recall that the Nyquist stability criterion states that the point $(-1, j0)$ must be left on the left when following a complex locus for increasing frequencies, i.e. toward the point $(0, j0)$ in the present diagram, since the open loop gain has a low pass characteristic).

This analysis shows that the maximal quality factor of the resonator will be limited by the frequency response of its feedback block. Increasing its dc gain or its cutoff frequency would allow higher quality factor at

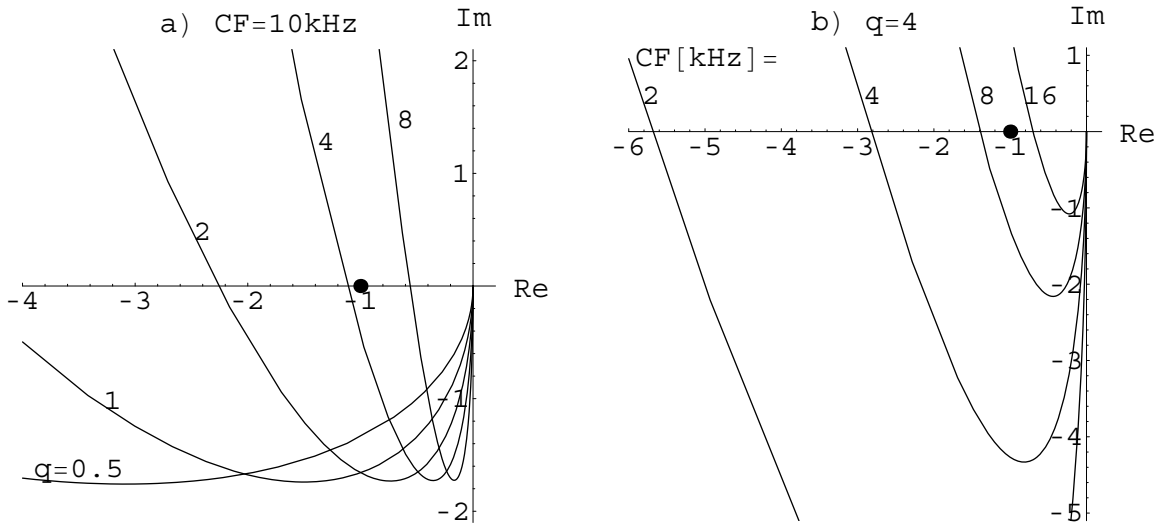


Figure 5.22: Nyquist diagram of the resonator open loop gain $A_bA_f(j\omega)$, for a) varying resonators' quality factor and b) characteristic frequency (CF); the frequency parameter ω increases toward the point $(0, j0)$.

higher characteristic frequency. This result, obtained from an AC analysis of the linearised feedback circuit is in accordance with the one obtained from the transient analysis.

5.4.6 Noise

Basilar membrane resonator

The effect of internal noise is analysed on the resonator circuit linearised around its operating point. The operating point is set for a dc input pseudo-voltage V_Z^* and a zero ac input signal. The linearised circuit is therefore valid for small signal variations, which is assumed to be the case of noise. As detailed in appendix A.4, the noisy small-signal equivalent of the basilar membrane resonator is a serial RCS resonator in which each dipole

$$G_{BM} = G, \quad (5.56)$$

$$C_{BM} = \frac{G}{G_1} C'_1, \quad (5.57)$$

$$S_{BM} = \frac{G}{G_2} \frac{C'_1 C'_2}{G_1} \quad (5.58)$$

features a parallel noise current source i_{NG} , i_{NC} and i_{NS} having power spectral densities

$$s_{IG} = \gamma_G 4k_B T G, \quad (5.59)$$

$$s_{IC} = \gamma_C 4k_B T G_1, \quad (5.60)$$

$$s_{IS} = \gamma_S 4k_B T G_2, \quad (5.61)$$

respectively (figure 5.23). The values of the noise factors γ_G , γ_C and γ_S depends on the dc values I , I_1 and I_2 of the currents i , i_1 and i_2 at the operating point where the circuit is linearised, and on its bias currents and voltages, according to equations (A.104) to (A.107) given in appendix A.4. The values of the linearised conductances G , G_1 and G_2 as well as the linearised input-referred capacitance C'_1 and C'_2 of the pseudo-transcapacitors, are recalled in table 5.5, together with their log-domain equivalents.

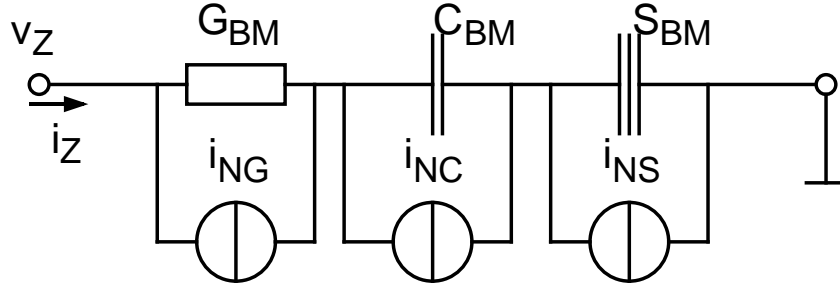


Figure 5.23: noisy equivalent of the basilar membrane RCS resonator

Replacing the linearised conductances and capacitances by their log-domain equivalents in the expression of the output noise voltage

$$v_Z = \frac{i_Z + i_{NG}}{G_{BM}} + \frac{i_Z + i_{NC}}{sC_{BM}} + \frac{i_Z + i_{NS}}{s^2S_{BM}} \quad (5.62)$$

yields

$$\frac{V_Z^*}{U_T} v_Z = v_Z^* = \frac{i_Z + i_{NG}}{G_{BM}^*} + \frac{i_Z + i_{NC}}{sC_{BM}^*} + \frac{i_Z + i_{NS}}{s^2S_{BM}^*}, \quad (5.63)$$

where $V_Z^* v_Z / U_T$ expresses the small-signal pseudo-voltage v_Z^* around a dc pseudo-voltage V_Z^* as a function of the small-signal voltage v_Z linearised around a dc value V_Z :

$$V_Z^* + v_Z^* = V_0 e^{(V_Z + v_Z)/U_T} = V_0 e^{V_Z/U_T} e^{v_Z/U_T}$$

linearised	log-domain
$G = \frac{I_F}{U_T}$	$G^* = \frac{I_F}{V_Z^*} = \frac{I_G}{V_0}$
$G_1 = \frac{I_1}{U_T}$	$G_1^* = \frac{I_{G1}}{V_0}$
$G_2 = \frac{I_2}{U_T}$	$G_2^* = \frac{I_{G2}}{V_0}$
$C_1' = \frac{I_1}{I_{G1}} C e^{V_{sh1}/U_T}$	$C_1^* = \frac{C U_T}{V_0} e^{V_{sh1}/U_T}$
$C_2' = \frac{I_2}{I_{G2}} C e^{V_{sh2}/U_T}$	$C_2^* = \frac{C U_T}{V_0} e^{V_{sh2}/U_T}$

Table 5.5: Linearised and log-domain conductances and capacitances

$$\approx V_Z^* \left(1 + \frac{v_Z}{U_T} \right) = V_Z^* + V_Z^* \frac{v_Z}{U_T}. \quad (5.64)$$

(Note that for this equivalence, the voltages are defined positively from the node to a reference, inversely to the definition (5.2) of the pseudo-voltage in PMOS transistors; this is required to be compatible with the voltage definitions used for linearising the circuit around its operating point.)

The output quantity of the resonator is the integral of the current flowing through it, which models the integral of the basilar membrane acceleration, thus the basilar membrane velocity. This quantity is available as the (pseudo-)voltage $v_C^{(*)}$ across the (pseudo-)capacitor $C_{BM}^{(*)}$. The (pseudo-)voltage noise $v_{NC}^{(*)}$ that affects this output may be estimated in a single RCS resonator having a dc (pseudo-)voltage $V_Z^{(*)}$ using the equivalent diagram of figure 5.23 with both end connected together (small-signal analysis):

$$v_{NC}^{(*)} = \frac{1}{sC_{BM}^{(*)}} \frac{s^2\tau^2 i_{NG} + (1 + s^2\tau^2)i_{NC} + i_{NS}}{s^2\tau^2 + s\tau/Q + 1}, \quad (5.65)$$

where

$$\tau^2 = \frac{S_{BM}^{(*)}}{G_{BM}^{(*)}}, \quad (5.66)$$

$$Q^2 = \frac{C_{BM}^{2(*)}}{G_{BM}^{(*)}S_{BM}^{(*)}} \quad (5.67)$$

are the same as defined by equations (5.51) and (5.52), respectively.

Using equations (5.59) to (5.61), the corresponding (pseudo-)voltage noise power spectral density is thus given by

$$s_{VC}^{(*)} = \frac{4k_B T}{C_{BM}^{2(*)}} \tau^2 \left[(\gamma_G G + \gamma_C G_1) \left\| \frac{j\Omega}{1 - \Omega^2 + j\Omega/Q} \right\|^2 + (\gamma_C G_1 + \gamma_S G_2) \left\| \frac{1/j\Omega}{1 - \Omega^2 + j\Omega/Q} \right\|^2 \right], \quad (5.68)$$

where $\Omega = 2\pi f\tau$ is the frequency normalised on the characteristic frequency of the resonator. The corresponding voltage noise power is calcu-

lated by integrating equation (5.68) over frequency f , using $x = \Omega^2$:

$$v_{NC}^{2(*)} = \frac{k_B T}{C_{BM}^{2(*)}} \frac{\tau}{\pi} \left[(\gamma_G G + \gamma_C G_1) \int_0^\infty \frac{x^{1/2} dx}{x^2 + \left(\frac{1}{Q^2} - 2\right)x + 1} + (\gamma_C G_1 + \gamma_S G_2) \int_0^\infty \frac{x^{-1/2} dx}{x^2 + \left(\frac{1}{Q^2} - 2\right)x + 1} \right], \quad (5.69)$$

where both integrals converge to πQ . Hence, since equations (5.66) and (5.67) yields $\tau Q = C_{BM}^{(*)}/G_{BM}^{(*)}$ and since $G_{BM}^{(*)} = G^{(*)}$, the (pseudo-)voltage noise power on the (pseudo-)capacitor $C_{BM}^{(*)}$ becomes simply

$$v_{NC}^{2(*)} = \frac{k_B T}{C_{BM}^{(*)}} \left[\gamma_G \frac{G}{G^{(*)}} + 2\gamma_C \frac{G_1}{G^{(*)}} + \gamma_S \frac{G_2}{G^{(*)}} \right]. \quad (5.70)$$

Dynamic range of a single resonator

The output dynamic range of a single resonator may be estimated by expressing the variation Δi_1 of the current i_1 around its dc value I_0 . This variation corresponds to the pseudo-voltage v_C^* across the pseudo-capacitor C_{BM}^* :

$$\Delta i_1 = i_1 - I_0 = G^* v_C^*. \quad (5.71)$$

The minimal amplitude ΔI_{1min} of this variation Δi_1 , assumed to be a sine wave, must yield a pseudo-voltage power v_C^{*2} that equals the pseudo-voltage noise power v_{NC}^{2*} (unity signal/noise ratio). Therefore, using equation (5.70) and the log-domain equivalent of equation (5.57), this condition imposes

$$\frac{\Delta I_{1min}^2}{2G^{*2}} = v_{NC}^{*2} = \frac{k_B T}{C_1^*} \frac{G_1^* G}{G^{*2}} \gamma, \quad (5.72)$$

where

$$\gamma = \gamma_G + 2\gamma_C \frac{G_1}{G} + \gamma_S \frac{G_2}{G} = \gamma_G + 2\gamma_C \frac{I_1}{I_F} + \gamma_S \frac{I_2}{I_F}. \quad (5.73)$$

The maximal current variation ΔI_{max} at the input of a pseudo-transcapacitor was shown in paragraph 5.3.2 to have an amplitude half its dc

value. Since the current i_1 is copied at the input of the second pseudo-transcapacitor C_2^* , a maximal amplitude $\Delta I_{1max} = I_0/2$ is used to calculate the dynamic range of the output current i_1 , which becomes, using the equivalences listed in table 5.5:

$$\frac{\Delta I_{1max}^2}{\Delta I_{1min}^2} = \frac{\frac{I_0}{I_{G1}} e^{V_{sh1}/U_T}}{8\gamma} \frac{I_0}{I_F} \frac{CU_T}{q_e}, \quad (5.74)$$

where $q_e = k_B T / U_T$ is the charge of an electron ($0.16 \cdot 10^{-18}$ As).

In order to estimate its order of magnitude, this dynamic range is calculated using equations (5.73) and (A.104) to (A.107) in which $I = I_1 = I_F = I_2/2 = I_{shC1}/4 = I_{shC2}/4 = I_0$, $I_{G1} = I_{G2}$, $V_{sh1} = V_{sh2}$, and $n = 1.5$, yielding:

$$\frac{\Delta I_{1max}^2}{\Delta I_{1min}^2} = \frac{\frac{I_0}{I_{G1}} e^{V_{sh1}/U_T}}{232 + 112 \frac{I_0}{I_{G1}} e^{V_{sh1}/U_T}} \frac{CU_T}{q_e}. \quad (5.75)$$

The term $(I_{G1}/I_0) \exp(V_{sh1}/U_T)$ corresponds to the internal dc pseudo-voltage V_A^*/V_0 of the pseudo-transcapacitor C_1^* , as shown by equation (A.89) in appendix A.4. This term also corresponds to the inverse of the pseudo-transcapacitor's mirror gain. Its optimal value depends on the current range over which the transcapacitor performs correctly. For a current range spanning 2 decades, an internal pseudo-voltage V_A^*/V_0 set to 25 at dc ensures an optimal range of operation (paragraph 5.3.2). Therefore, with a capacitor $C = 6.4$ pF ($CU_T/q_e = 10^6$ at room temperature) a dynamic range of nearly 40dB can be obtained. This value is 12dB lower than the theoretical input dynamic range of the voltage-mode second-order stage cascade described in chapter 3 (paragraph 3.4.7, p. 58). However within this range the resonator is theoretically perfectly linear. Accepting some distortion, the maximal amplitude of the signal variation can be increased by up to a factor 2 ($\Delta I_{max} = I_0$, corresponding to 100% modulation of the signal around its dc value), increasing the dynamic range by 6dB.

The bandwidth and the power consumption of the resonator are related to its dynamic range through the factor CU_T/q_e . The dynamic range is increased with an increasing capacitance C , but in order to maintain the same frequency response, the current level must be increased proportionally, increasing thus power consumption proportionally to the dynamic range.

Resistive network

The noise is analysed similarly in the single transistors implementing the pseudo-conductances in the resistive network. Since a zero-dc current flows through each resonator, the same apply in any pseudo-resistor of the network. The transistors implementing them are thus in the conduction mode instead of being saturated, and they are still in weak inversion.

The conduction mode can be seen as the superposition of a forward and a reverse saturation mode (similarly to the Ebers and Moll model of the bipolar transistor). The channel current I is the difference between the forward saturation current I_F and the reverse saturation current I_R . For a PMOS transistor, it is expressed by

$$I = I_F - I_R = I_G e^{V_1/U_T} - I_G e^{V_2/U_T}, \quad (5.76)$$

where the voltage at the channel terminal V_1 and V_2 are defined positively from terminal to a reference, and I_G is the forward saturation current when $V_1 = 0$ and $-V_2 \gg 4U_T$. The value of I_G is controlled by the gate voltage and it can be imposed using a diode-connected identical transistor (figure 5.24a). Linearising equation (5.76) around $V_1 = V_2 = 0$, thus for $I_R = I_F = I_G$, yields a small-signal channel current

$$i = g_{cF}v_1 - g_{cR}v_2 = g_c(v_1 - v_2), \quad (5.77)$$

where $g_c = g_{cF} = g_{cR} = I_G/U_T$ is the linearised conductance of the transistor (figure 5.24b).

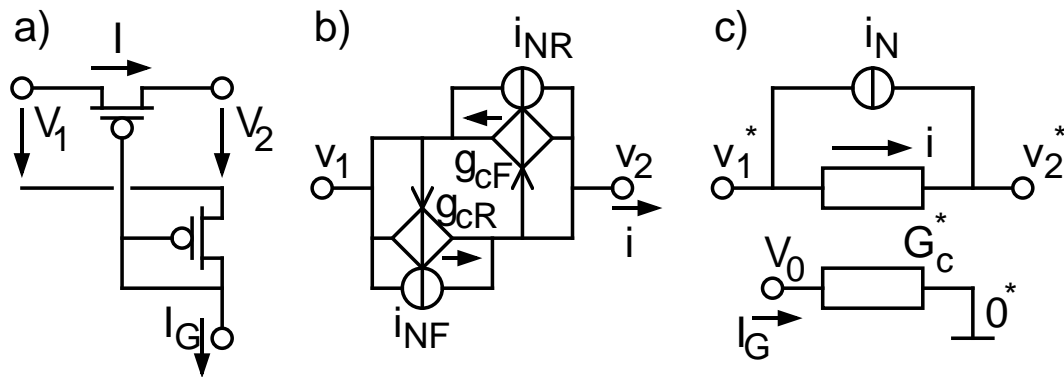


Figure 5.24: a) Transistor in the conduction mode with its biasing transistor, b) its small-signal and c) log-domain noisy equivalents.

The current noise source in parallel with a transistor in the conduction mode is thus given by summing the noise current sources $i_{NF,R}$ due to its forward and reverse saturation current $I_{F,R}$ [53]. Since the forward and reverse noise are not correlated, their power spectral densities $s_{IF,R}$ add, resulting in a single current noise source i_N having a power spectral density

$$s_I = s_{IF} + s_{IR} = 2q_e I_F + 2q_e I_R = 4q_e I_G = 4k_B T g_c. \quad (5.78)$$

When interpreted as pseudo-conductances (figure 5.24c), the biasing transistor defines a pseudo-conductance

$$G_c^* = \frac{I_G}{V_0} = \frac{i}{v_1^* - v_2^*}. \quad (5.79)$$

Expressing the voltage difference $\Delta v = v_1 - v_2$ across the linearised transistor as a function of its currents,

$$\Delta v = \frac{i + i_N}{g_c} = \frac{i + i_N}{I_G} U_T = \frac{i + i_N}{G_c^*} \frac{U_T}{V_0}, \quad (5.80)$$

is thus equivalent to express the small-signal pseudo-voltage $\Delta v^* = v_1^* - v_2^*$ around its pseudo-voltage V_0 at the operating point, according to equation (5.64):

$$\Delta v^* = \frac{V_0}{U_T} \Delta v = \frac{i + i_N}{G_c^*}. \quad (5.81)$$

The equivalence between linearised quantities and their log-domain correspondent yields a simple model of linear noisy resonator and network resistors. This model is very convenient to analyse and/or simulate the full cochlear model using only passive devices having a noise current source in parallel.

5.4.7 Implementation of the full cochlea

Linear model

The major difficulty in analysing the full cochlear model resides in the interactions between the basilar membrane resonators through the resistive network modeling the liquid which surround them. Nevertheless, such analysis might be facilitated thanks to the linear behaviour of the circuit

in the log-domain. Moreover, the effect of the noise can reasonably be assumed to be also linear, as shown in paragraph 5.4.6. This assumption is valid provided that the noise current variation are small with respect to the dc currents, which is the case in the class-A implementation of the pseudo-transcapacitors. It was shown to be true also for the network pseudo-resistors, despite the fact that a 0-dc current flows through them.

As a consequence, the analogue VLSI implementation in the log-domain of the full cochlear model amounts to the analysis of the electrical model of figure 4.7 (p. 88). The difference with the linear electrical model analysed in section 4.4 and its electronic implementation resides in the imperfections of the electronic circuitry. The imperfections at the level of a single resonator were analysed in the previous paragraphs, whereas this one focuses on their effect on the full bank of resonator loaded by the resistive network. Since the effects of the major imperfections, i.e, noise and dc current offset are linear, their analysis may be carried out using the rich battery of tools applying to linear systems.

Canonic resistance matrix

The resistive network can be transformed into a canonic matrix of conductances $G_{k,l}$, each of them connecting a pair (k, l) of nodes, restricted to the cochlea input and the M resonator inputs. The *admittance matrix* relative to these input nodes is obtained by injecting a current I_k at each of these nodes and leaving the other ones floating. The linear system describing the entire network is arranged such that

$$\begin{bmatrix} \mathbf{I}_A \\ 0 \end{bmatrix} = \begin{bmatrix} G_{AA} & G_{AB} \\ G_{BA} & G_{BB} \end{bmatrix} \begin{bmatrix} \mathbf{V}_A \\ \mathbf{V}_B \end{bmatrix}, \quad (5.82)$$

where $\mathbf{I}_A = [I_{in}, I_1 \cdots I_M]^T$ and $\mathbf{V}_A = [V_{in}, V_1 \cdots V_M]^T$ are the current injected at the input nodes and their voltage, respectively; the vector \mathbf{V}_B gather the voltages at the internal nodes of the resistive network. All currents are defined positively when entering the network. The admittance matrix expressing $\mathbf{I}_A = G_A \mathbf{V}_A$ is thus given by:

$$G_A = G_{AA} - G_{AB} G_{BB}^{-1} G_{BA}. \quad (5.83)$$

The conductance $G_{k,l}$ linking a node pair (k, l) is determined by imposing a voltage $V_k = V$ at node k , while grounding the other nodes ($V_{i \neq k} = 0$), and determining the current I_l getting out from node l . Since in

such configuration $I_l = -g_{Ak,l}V$, the conductance $G_{k,l}$ corresponds to the element $-g_{Ak,l}$ at column k and row l of the admittance matrix $-G_A$.

$$G_{k,l} = -g_{Ak,l}. \quad (5.84)$$

Doing so, the element g_{Akk} corresponds to the input admittance at node k of the network with all other node grounded.

The matrices G_{AA} , G_{AB} , G_{BA} and G_{BB} needed to produce the matrix G_A can be generated automatically for a rectangular resistive network similar to the one presented in figure 4.6 (p. 85). Figure 5.25 shows that on such a $L \times H$ rectangular network quantised to $M \times N$ points, $G_{k,l}$ decreases exponentially with the distance between node k and node l (at a rate of about half a decade per millimetre on a network quantising a $20 \text{ mm} \times 1 \text{ mm}$ rectangular, homogeneous resistive sheet). This means that the resonators are only locally coupled by the resistive network. The conductances $G_{k,l}$ also decrease with increasing longitudinal resolution M , due to the fact that more of them are set in parallel to quantise a given current path in the continuous resistive sheet.

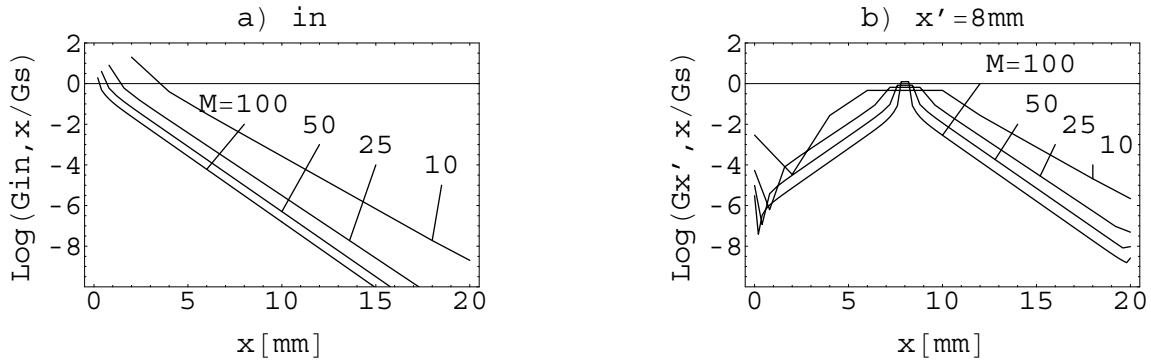


Figure 5.25: Equivalent network conductances $G_{k,l}$ that links a) the input node or b) the node $k = (x'/\Delta x, 0)$ on the basilar membrane to nodes $l = (x/\Delta x, 0)$; calculated from a $M \times N$ resistive network that quantises a $20 \text{ mm} \times 1 \text{ mm}$ rectangular resistive sheet having an homogeneous sheet conductance G_s ; the nodes $k \in (i = 1 \dots M, j = 0)$ are located on the bottom edge of the resistive sheet; $N = 10$ in all cases and the input voltage is applied on nodes $(i = 0, j = 3 \dots 7)$ on the left edge of the resistive sheet, similarly to figure 4.6.

Effect of resonator current offset

The admittance matrix G_A may be used advantageously to estimate the effect at any node k of the offset current generated by every resonators. A constant input voltage V_{in} is imposed at the input node, whereas a dc offset current source I_k is injected at each node k connected to the resonators. The system of equation describing such a setting is expressed by:

$$\begin{bmatrix} I_{in} \\ \mathbf{I}_{bm} \end{bmatrix} = G_A \begin{bmatrix} V_{in} \\ \mathbf{V}_{bm} \end{bmatrix} = \begin{bmatrix} g_{in} & \mathbf{g}_{in,bm}^T \\ \mathbf{g}_{bm,in} & G_{bm} \end{bmatrix} \begin{bmatrix} V_{in} \\ \mathbf{V}_{bm} \end{bmatrix}, \quad (5.85)$$

where the $M \times M$ sub-matrix G_{bm} relates the voltages $\mathbf{V}_{bm} = [V_1 \cdots V_M]^T$ and currents $\mathbf{I}_{bm} = [I_1 \cdots I_M]^T$ at the M resonator nodes when $V_{in} = 0$. This notation permits to express the voltages \mathbf{V}_{bm} at the resonator nodes as a function of the resonator currents \mathbf{I}_{bm} and the input voltage V_{in} :

$$\mathbf{V}_{bm} = G_{bm}^{-1} \mathbf{I}_{bm} - G_{bm}^{-1} \mathbf{g}_{bm,in} V_{in}. \quad (5.86)$$

The mean voltage offset μ_{V_k} at each resonator node k can be estimated using equation (5.86) in which the currents I_k are replaced by their mean value μ_{I_k} . Figure 5.26a shows this mean offset voltage distribution along the resonator bank with a constant $\mu_{I_k} = \mu_I \forall k$. It is represented as an equivalent resistance $R_{\mu k} = \mu_{V_k} / \mu_I$, normalised to the sheet conductance G_s of the resistive sheet. The effect of the horizontal quantisation is clearly visible: if the current injected by each resonator is independent from the spatial resolution of the bank, it corresponds to a local current density in the continuous case. Therefore, increasing the resolution results in increasing proportionally the total current injected along a given section of the basilar membrane edge of the resistive sheet, increasing thus the local current density. Since the resistive sheet has a sheet conductivity G_s independent from spatial resolution, an increasing current density augments proportionally the voltage offset along the basilar membrane edge.

This effect is similar for the standard deviation σ_{V_k} of this voltage offset as a function of the standard deviation σ_{I_k} of the resonator offset current, assumed uncorrelated. However, in this case the elements of the matrix G_{bm}^{-1} must be individually squared before replacing the voltages V_k by $\sigma_{V_k}^2$ and the currents I_k by $\sigma_{I_k}^2$ in using equation (5.86), whose second term of its right hand-side is cancelled due to the zero standard deviation of the imposed input voltage V_{in} . The equivalent resistance $R_{\sigma k} = \sigma_{V_k} / \sigma_I$

normalised on the sheet conductance G_s is shown in figure 5.26b, where an identical standard deviation $\sigma_{Ik} = \sigma_I \forall k$ was assumed for all resonators. As expected, the random component σ_I of the resonator offset currents has less effect than its systematic component μ_I on the resonator input voltage.

Figure 5.26b shows that the maximal voltage offset is reached at the apex of the cochlea ($x = L$). Simulations showed also that R_μ scales proportionally with the aspect ratio L/H of the resistive sheet; however it was shown to be independent from the size of the input contact and from the vertical resolution N . The resistance $R_{\mu max}$ expressing the maximal mean voltage offset (at $x = L$) normalised on mean current offset injected in the resistive network can thus be expressed by

$$R_{\mu max} = \frac{\mu_{Vmax}}{\mu_I} \approx 0.4 \frac{L}{H} \frac{M}{G_s}, \quad (5.87)$$

The parameter (in-) dependence was tested for values around $L = 20$ mm, $H = 1$ mm, $M = 50$ and $N = 10$ on a rectangular 2-D duct whose input contacted from 30% to 70% of its left edge ($x = 0, y = 0.3H \div 0.7H$): it might become invalid for parameters too far from these values. Note that a cochlear duct modeled by a single row of M serial horizontal resistances $R_x = L/HG_sM$ and having a constant offset current μ_I injected between each of them, results in a parabolic distribution of the offset voltages $\mu_{V_k} \approx \mu_I R_x [M^2 - (k - M)^2]/2$ (for $M \gg 1$), in accordance with the one

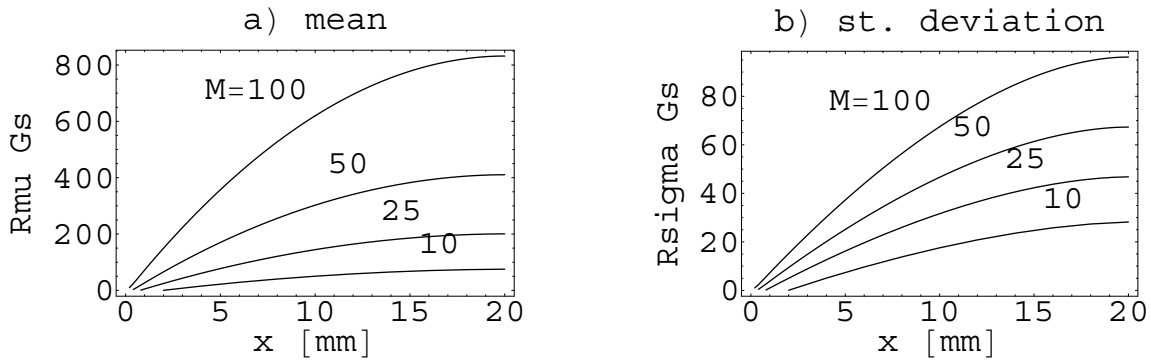


Figure 5.26: a) Mean and b) standard deviation of the voltage along the basilar membrane due to current offset generated by the resonators, for different longitudinal resolution M ; the offset voltage are normalised on the offset currents, assumed having a constant mean and standard deviation for all resonator.

shown in figure 5.26a. Its maximal value μ_{Vmax} at $k = M$ yields $R_{\mu max} = M^2 R_x / 2 = LM / 2HG_s$, which corresponds closely to equation (5.87).

Similarly, the resistance $R_{\sigma max}$ expressing the standard deviation of this maximal voltage offset normalised on the standard deviation of the offset currents may be approximated within the same range of parameters by

$$R_{\sigma max} = \frac{\sigma_{Vmax}}{\sigma_I} \approx 0.5 \frac{L}{H} \frac{\sqrt{M}}{G_s}. \quad (5.88)$$

The dependence from longitudinal resolution is due to the fact that the current injected by each resonator is independent from resolution, and so is the sheet resistance of the network. However, it was shown in chapter 4 (paragraph 4.4.6, p. 98) that the density of the liquid (modeled by the sheet conductance G_s) is related to the basilar membrane mass (modeled by the resonator's resistance G_{BM}) such that the characteristic height H_c defined by equation (4.44) should equal 0.75 mm. Using the definitions of the network resistance listed in tables 4.3 (p. 89) and 4.2 (p. 86), the sheet conductance G_s , or equivalently the horizontal and vertical conductances $G_x = G_s \Delta_y / \Delta_x$ and $G_y = G_s \Delta_x / \Delta_y$, can be expressed as a function of the resonator conductance G_{BM} :

$$G_s = G_x \frac{L}{H} \frac{N}{M} = G_y \frac{H}{L} \frac{M}{N} = \frac{H_c G_{BM}}{\Delta x} = \frac{H_c}{L} M G_{BM}, \quad (5.89)$$

yielding together with equation (5.87) and (5.88):

$$R_{\mu max} = 0.4 \frac{L^2}{H^2} \frac{H}{H_c} \frac{1}{G_{BM}}, \quad (5.90)$$

$$R_{\sigma max} = 0.5 \frac{L^2}{H^2} \frac{H}{H_c} \frac{1}{\sqrt{M} G_{BM}}, \quad (5.91)$$

which equals $213/G_{BM}$ and $267/\sqrt{M}G_{BM}$, respectively, for the ideal characteristic height $H_c = 0.75$ mm on a rectangular 20 mm \times 1 mm cochlear duct. Quantising such a cochlear duct by $M = 100$ horizontal points and $N = 10$ vertical point, the vertical and horizontal conductances of the network become, using equation (5.89), $G_x = 1.875 \cdot G_{BM}$ and $G_y = 7.5 \cdot G_{BM}$. Their corresponding pseudo-conductances G_x^* and G_y^* are advantageously implemented using transistor controlled by the same gate voltage as the pseudo-conductances G_{BM} , thus by the control current I_G defining $G_{BM}^* = G^* = I_G/V_0$ (see paragraph 5.4.3). Since the ratios

between these conductances is imposed by the parameters L , H , M , and N that are determined by the layout of the circuit, they can be imposed by the aspect ratio of the corresponding transistors without loosing functional flexibility. Doing so, the maximal systematic and random pseudo-voltage offsets are imposed by

$$\frac{\mu_{V_{max}}^*}{V_0} = 0.4 \frac{L^2}{H^2} \frac{H}{H_c} \frac{\mu_I}{I_G}, \quad (5.92)$$

$$\frac{\sigma_{V_{max}}^*}{V_0} = 0.5 \frac{L^2}{H^2} \frac{H}{H_c} \frac{1}{\sqrt{M}} \frac{\sigma_I}{I_G}. \quad (5.93)$$

Considering the 20 mm \times 1 mm cochlear duct quantised by $M = 100$ horizontal point, a characteristic height $H_c = 0.75$ mm, a systematic current offset $\mu_I = -5\%I_0$ (as shown by simulation of paragraph 5.4.4) and a random offset $\sigma_I = 30\%I_0$, the maximal systematic and random pseudo-voltage offset become $\mu_{V_{max}}^*/V_0 = -10I_0/I_G$ and $\sigma_{V_{max}}^*/V_0 = 8I_0/I_G$.

Interestingly, the effect of the systematic current offsets generated by the resonators on their input pseudo-voltage when loaded by the pseudo-resistive network does not depend on the horizontal resolution. Moreover, the effect of random current offsets decreases with the square root of the horizontal resolution. It should be noted however that increasing the number of resonator toward infinity would not reduce the random pseudo-voltage offset to zero, because it would also require resonator areas that tend to zero in order to implement the circuit in a finite area. In this case, the random current pseudo-voltage σ_I cannot anymore be assumed independent from the longitudinal resolution.

Both systematic and random pseudo-voltage offsets are proportional to the square aspect ratio L^2/H^2 of a rectangular cochlear duct and to its absolute height H . Increasing H reduces quadratically the voltage offset, and since a minor effect of the cochlear duct height was shown by simulation (paragraph 4.4.5, p. 96), one can expect to use this parameter for reducing the offset voltage. However, the effect of the duct height on the voltage offset as well as on the frequency behaviour of the cochlea was shown for duct heigh varying by 0.5 to 2 times its nominal value. Major improvement using this parameter should thus be considered with caution.

The last option resides of course in a careful design of the resonator that minimises its dc current offset and/or that is tolerant to large variations of its dc input pseudo-voltage. The latter is however mainly determined by the implementation of the exponential decrease of the characteristic

frequency along the resonator bank.

Range of operation

The variation of the resonator input pseudo-voltage is constrained by the variation range of the internal pseudo-voltage v_A^*/V_0 of its pseudo-transcapacitors. This internal pseudo-voltage was shown by equation (5.10) (p. 113) to be limited between 0.5 and half the current ratio I_{max}/I_{min} between strong inversion and leakage limits. The dc pseudo-voltage V_Z^* at the input of the resonator being imposed at the output of its second pseudo-transcapacitor (modeling the super-capacitor), it results on an internal dc pseudo-voltage $V_{A2}^* = V_Z^* \exp[V_{sh2}/U_T]$, where the exponential factor determines the pseudo-capacitance C_2^* , according to equations (5.6) and (5.8), respectively (p. 111). This pseudo-capacitance C_2^* models the basilar membrane compliance, that increases exponentially toward the apex of the cochlea. The variation of C_2^* must thus span twice the frequency range of the cochlea, both being expressed logarithmically in decades as shown in figure 5.27a. As a consequence, the ratio V_{Amax}^*/V_{Amin}^* of pseudo-transcapacitor's internal pseudo-voltage limits must be larger than the square ratio $f_c(0)^2/f_c(L)^2$ of the highest and lowest characteristic frequency of the resonators along the cochlea. An additional lower limits V_{Zmin}^* is directly imposed on the resonators' pseudo-voltage input, that must ensure a feedback current $i_{Fmin} = v_{Zmin}^* G^*$ large enough to maintain saturated the transistor implementing G^* (see paragraph 5.4.1).

The dc input pseudo-voltage V_{in}^* modeling the input pressure applied

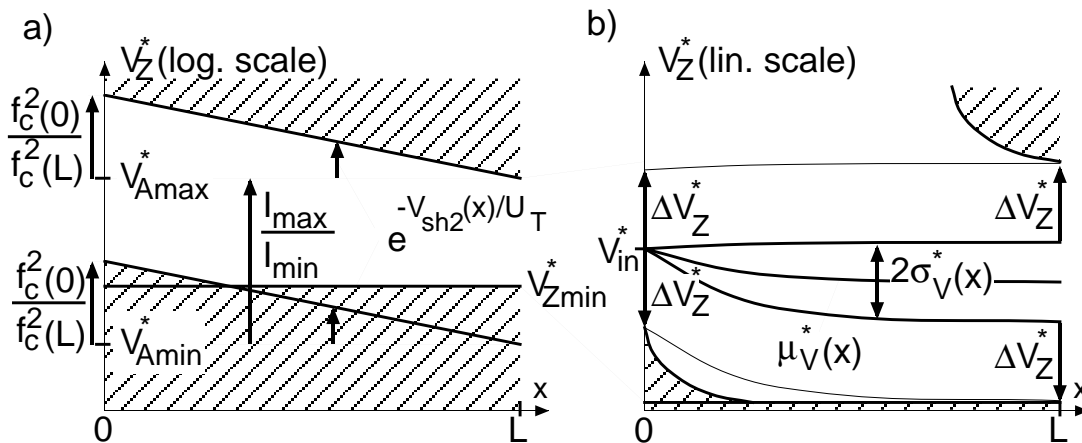


Figure 5.27: Operating range on the entire cochlea.

on the cochlea must therefore be adjusted such that it ensures the maximal variation ΔV_Z^* of the resonator input pseudo-voltage to not trespass the limits $V_{Z_{max}}^*(x)$ and $V_{Z_{min}}^*(x)$ all along the cochlea, taking into account the effect of the systematic and random offset voltage as illustrated in figure 5.27b. It appears clearly that the range of operation will be imposed mainly by the characteristic frequency range of the cochlea that is to be modeled and by the current range available between leakage and strong inversion limits of the pseudo-transcapacitors.

5.5 Summary

Linear spatio-temporal systems can be emulated by VLSI electronic circuits working in the log-domain. The linear relationship between voltages and currents of linear electrical circuits remains unaltered as long as logarithmically compressed voltages, called pseudo-voltages, are considered instead of voltages. In this scheme, a pseudo-conductance can be implemented using a single MOS transistor, whereas a basic circuit, the pseudo-transcapacitor permits to implement various reactive components working linearly in the log-domain.

The pseudo-capacitance of the pseudo-transcapacitor circuit can be controlled exponentially by a voltage that might theoretically set it to very large values. In practice it will however be limited by leakage currents, whose effect is similar to a parasitic parallel pseudo-conductance. According to the polarity of the leakage, this pseudo-conductance may even be negative. Nevertheless, provided that the leakage currents are small, large time constants can be implemented without the need of using just-above-leakage currents to carry the signal in the entire circuit.

The pseudo-transcapacitor circuit has a differential input current but a single pseudo-voltage output. Differential pseudo-voltage output might be possible using two pseudo-transcapacitors. Alternatively, a single pseudo-voltage might control pseudo-conductances of opposite type to generate differential output current in larger systems. In order to build compact circuits, however, a class-A implementation was proposed, in which the signal vary around a dc current set at mid-operating range. In this scheme, the pseudo-transcapacitor circuit was shown to be perfectly linear for signal varying by $\pm 50\%$ of the dc carrier. The output pseudo-voltage dynamic range was shown to equal the current dynamic range between leakage and strong inversion limit.

The 2-D cochlear model is advantageously emulated in the log-domain because each pseudo-conductance of the large network modeling the liquid can be implemented using a single transistor, whereas the basilar membrane is implemented by a 1-D bank of serial resonators, each of them made from 2 pseudo-transcapacitors. In addition to its compact implementation, the advantage of the circuit is that it performs linearly within a large current swing and under low supply voltage.

Each resonator is made equivalent to a serial resistor-capacitor-“super-capacitor” circuit. Since the log-domain equivalent of these dipoles are pseudo-grounded, the sum of the pseudo-voltages across them is performed by converting these voltages into currents, summing them and transforming them back into a pseudo-voltage that is fed back at the input of the resonator. This feedback loop is susceptible to bring the circuit into instability if the resonator dipoles have values that implement large quality factors or high characteristic frequencies. The feedback block must be designed such that the open loop gain including the resonator dipoles ensures a sufficient gain margin on the full range of characteristic frequency and quality factor required to faithfully model the cochlea. Moreover, this requirement must be fulfilled within the full variation range of operating point, that vary along the cochlea due to resonators offset currents injected in the pseudo-resistive network.

For a given network sheet pseudo-resistance, the offset pseudo-voltage at the resonator input normalised to its offset current was shown to be proportional to the spatial resolution of the resonator bank modeling the continuous basilar membrane and to the equivalent longitudinal pseudo-resistance of the network (between base and apex). However, for a given resonator pseudo-resistance (that scales with its offset current), the model requires a network sheet pseudo-resistance that is inversely proportional to this longitudinal resolution, resulting in a pseudo-voltage offset that depends only on the longitudinal pseudo-resistance of the network, independently from its spatial quantisation. Moreover, the pseudo-voltage offset due to random variations of the resonator current offset even decreases with the square root of the longitudinal resolution.

The noise generated by the log-domain components was analysed in order to estimate the dynamic range that may be expected from the electronic implementation of the 2-D cochlear model. At the level of a single pseudo-transcapacitor, the output noise power cannot be integrated on the full frequency range due to the pure integration performed by the circuit

and to the noise source in its output follower. As for the resonator, a simple linear noise model was proposed that consists of a white noise current source in parallel with each of its log-domain components. The output dynamic range of the pseudo-voltage across the resonator's pseudo-capacitor was estimated to about 40dB on a single resonator.

Each network pseudo-conductance is itself noisy. The effect of all noise sources in the resistive network and the resonator bank is not straightforward to estimate analytically. Thanks to the linearity of the system, this analysis might be simplified using an equivalent network of pseudo-resistance, each of them linking a pair of resonators or a resonator with the network input node. This pseudo-resistance was shown to present a fast exponential increase with the distance between resonators. This means that a reduced number of resonators are effectively coupled, facilitating so the estimation of their performance.

Finally it must be pointed out that the cochlear model to be emulated has characteristic frequencies that spans several decades. This parameter is supported by the exponentially varying stiffness of the basilar membrane, that must span twice this range, expressed logarithmically. Its electronic implementation should therefore be able to support such a variation, which is determined by the available current range within which the pseudo-transcapacitors function correctly (if the integrated capacitor are identical for all resonators). Such current range is restricted between the level of leakage current and the limit of strong inversion of the transistors beyond which the log-domain is left.

Chapter 6

Conclusions

6.1 Original results

Two analogue VLSI cochlear models were investigated in this thesis. The first one focuses on an efferent gain control system added to an existing analogue VLSI cochlear model. The original contribution of the present work resides in the proposed architecture rather than in its physical implementation, except for the circuits developed for the gain control block. A working chip proved the validity of the gain control mechanism proposed in this thesis.

As for the second model, an original low-power analogue VLSI circuit was proposed to efficiently emulate the 2-D hydrodynamics of the cochlea. The novelty brought by this work thus mainly concerns implementation aspects. Specifically, a framework was proposed to implement linear spatio-temporal processing in the log-domain. Such implementations exploit the exponential relationship between the voltage at the channel terminals of the transistor in weak inversion and its channel current.

This chapter summarises and discusses the results obtained from this research and suggests further exploration as well as potential applications.

6.2 Cochlear models

6.2.1 Active cochlea

The active cochlea proposed in chapter 3 is based on the well-known filter cascade proposed by Lyon and Mead [34]. The novelty proposed in the present work resides in a simple scheme for controlling the transduction gain of the cochlea between acoustical pressure and its neural representation on the auditory nerve.

This control loop postulates efferences originating from higher levels of neural processing in the biological cochlea. The simplest form of such a processing is hypothesised to yield a spatial distribution of mean spiking rate coding tonotopically the envelopes of the input signal in the different frequency band filtered by the cochlea. This simple “high-level neural processing” already permits to reproduce the sound level compression, transient enhancement and two-tone suppression measured in live cochleae.

This gain control is performed by modulating the quality factor of the individual filters, modeling the effect of the cochlea’s outer hair cells. It is frequency-selective, as a consequence of its local action on a tonotopic

architecture that maps the frequency components of the signal and the position along the cascade. The tonotopic gain distribution along the cochlear filter cascade is opportunistically exploited to efficiently distribute the gain control signal back to its filters, so that a single low-pass filter and quality factor control block is required per stage. Such a control mechanism also reproduces the increased frequency selectivity at low input level.

However, the model's frequency selectivity is far from that achieved by real cochleae. This is an unfortunate intrinsic side-effect of the pseudo-resonance implemented by the cascade model, that permits high accumulated gains despite the low individual quality factor of its stages. Another drawback of the cascade structure is that the delay and the accumulated gain for a given individual quality factor increase with spatial resolution; similarly, the frequency selectivity for a given accumulated gain diminishes with resolution. A minimum resolution is however imposed by the need of overlapping the bumps of the individual filter's frequency response.

Nevertheless, computer simulations of the model showed that a frequency selective level compression from an 80 dB input dynamic range to a 30 dB output dynamic range featuring efficient transient enhancement, could be achieved using this simple and biologically plausible efferent gain control mechanism.

6.2.2 2-D hydrodynamic model

The second cochlear model analysed in chapter 4 was inspired by the model proposed by Watts in 1993 [27]. In this approach the hydrodynamics of a 2-D description of the cochlea are emulated by a network of linear electrical dipoles. Although not analysed in this approach, the quality factor control loop developed for the cascade model is likely to apply similarly to this model.

The performance of the model was thoroughly analysed using electrical simulations of the network of linear dipoles. These simulations showed that the steep frequency cutoff of about 300 dB per octave measured in the live cochlea could be reproduced, but that basilar membrane resonators having a quality factor of about 60 are required. Implementing such a high quality factor into an analogue VLSI circuit is however somewhat challenging.

Much effort was devoted to mapping the electrical parameters of the model with realistic physical quantities of the biological cochlea. This anal-

ysis showed that simplification of the 3-D hydrodynamics of the cochlea can be properly mapped onto a 2-D description if the equivalent width of the cochlea (dropped in the dimension reduction) is made smaller than the physical basilar membrane width, in order to take into account fluid movement in the missing dimension.

6.3 VLSI implementations

6.3.1 Filter cascade with automatic gain control

The implementation of the filter cascade itself is almost identical to the voltage-mode implementation proposed in previous work [34, 35]. An improvement was brought in an early model by biasing the filters using compatible bipolar transistors [37]. The novelty of the design proposed in this thesis consists of embedding these bipolar transistors within a translinear loop to control the filter quality factors. In this way, the quality factor control block can be implemented using just two additional bipolar transistors per filter.

A careful analysis of the effect of internal noise showed that the noise accumulates along the cascade at the same rate as the gain, cancelling the advantage of high accumulated gains. Moreover, in the automatic gain control scheme the accumulated noise reduces the gain of the cascade even in absence of input signal, when the gain must be maximal.

Chip measurements confirmed the feasibility of the proposed automatic gain control mechanism, but the resulting level compression was less impressive than the one theoretically expected and obtained from the computer model. This is mainly due to the accumulated noise and to the need for setting reduced individual quality factors. The nominal quality factor must be reduced in order to prevent its variations due to component mismatch along the cascade to cause local ringing. Efficient transient enhancement of speech signals was also difficult to obtain from the chip. The reason for this is the difficulty in creating time constants large enough to filter the slow variations of the speech signal envelope using limited-size integrated capacitors and above-leakage currents.

The fundamental handicap of the cascade model, as of any cascade structure, is that the performance of the entire system is very sensitive to the weakness of its individual components. If a single stage is defective, the rest of the cascade does not work anymore.

6.3.2 Log-domain spatio-temporal processing

To avoid the shortcomings inherent to the VLSI implementation of a cascade structure, the 2-D model approach was proposed to emulate the cochlear hydrodynamics in a more collective fashion, thus with a reduced sensitivity to the imperfections of individual components.

The large resistor network that emulates the cochlear liquid is implemented using pseudo-conductances, each of which consists of a single transistor. Pseudo-conductances are equivalent to a linear dissipative component in the log-domain. The reactive components needed to model the basilar membrane are based on an original circuit, the pseudo-transcapacitor, which is linear in the log-domain and fully compatible with the pseudo-conductances.

The pseudo-transcapacitor circuit, as well as the pseudo-conductance on which it is based, exploits the exponential control of the transistor current by its source/drain instead of its gate/bulk. This permits to express logarithmically compressed voltages as pseudo-voltages that are linear with respect to currents. The consequence is that the exponential relationship between voltage and pseudo-voltage is neither affected by the slope factor nor by the threshold voltage of the transistor, making it compatible with bipolar log-domain implementations. However, this eliminates one of the most interesting advantage of current mode implementation, i.e. the absence of noise at zero-signal. This property does not apply to pseudo-conductance crossed by a zero-current, because it is even twice as noisy as it would be if crossed by a current that saturates the transistor used to implement it.

In the proposed design, the pseudo-transcapacitors work in class A. The signal is carried by current variations around a non-zero dc value. The noise at zero-signal can be estimated by linearising the circuit around its dc operating point. The internal noise of the basilar membrane resonators can be modeled by adding a white-noise current source in parallel with each of its log-domain components. Since the same apply to the pseudo-conductances of the pseudo-resistive network, the noise performance of the entire circuit can be analysed or simulated within the framework of linear systems. The dynamic range of a single basilar membrane resonator output (between noise floor and full operating range) was shown to reach about 40dB for resonator input pseudo-voltages within its appropriate operation range.

Interestingly, the pseudo-voltage offset resulting from the dc offset cur-

rent injected by the resonators into the pseudo-resistive network does not depend on the number of resonators. This is due to the required scaling between the resonator pseudo-conductance per unit basilar membrane length and the sheet pseudo-conductance of the pseudo-resistive network: increasing the number of resonators having a given pseudo-conductance increases the total current offset, but it also requires to proportionally decrease the network sheet resistance. The effect of random offset variations (that can be important in weak inversion implementations) even diminishes with spatial resolution. This illustrates the positive effect of the collective behaviour of a large number of processing units.

Theoretically, the pseudo-capacitances can be set to very large values to implement large time constants, but in practice their performance will be limited by leakage currents. However, the current carrying the signal can be much larger than the leakage current. A circuit implementing large time constants need to be designed only very locally for very low signal current.

The resonator quality factor is limited by the performance of its feedback loop, which must ensure a gain margin large enough over the full range of characteristic frequencies and quality factors (up to 60!) required for the ideal resonators. It is expected, however, that the risk that an individual resonator becomes unstable due to random performance variation of its feedback loop is likely to be reduced by the coupling with neighbouring resonators through the resistive network.

The design of the electronic model is facilitated if spatially varying characteristics depend on few parameters, preferably electrical rather than geometrical for the sake of flexibility. In the proposed log-domain implementation, the characteristic frequency (which spans nearly three decades in the biological cochlea), is controlled by a single pseudo-capacitance, which should therefore span 6 decades to cover the same range. Although this pseudo-capacitance can be controlled exponentially by a linear voltage tilt, it was shown that the dynamic pseudo-voltage range at the output of the pseudo-capacitor is equal to the dynamic range of the pseudo-capacitance it implements. However, the pseudo-voltage dynamic range corresponds to the available current dynamic range between leakage and strong inversion limits, which hardly spans more than 3 decades.

6.3.3 Analogue VLSI vs. biology

The drawback of both implementations, which is common to all analogue continuous-time VLSI circuit, resides in the difficulty of implementing very-large time constant, high quality factors, and parameters that vary over several decades while allowing large signal dynamic range within the full range of parameters. How does the biological cochlea do it so well...?

As for the large time constants and quality factors, the reason lies in inherent differences between the substrates. Physiological and biomechanical processing are much slower than their electronic counterpart due to the large mechanical and electrochemical time constants. Biomechanical passive spring-mass resonators can have high quality factors at low losses: they are sure to be stable since the losses stay positive. In analogue VLSI, the necessity to use active feedback circuitry to implement resonators excludes large quality factors: the inherent mismatches that deteriorate this feedback loop might bring the system into instability. In fact, it has been shown that in the biological cochlea active feedback brings it occasionally into instability. It is surmised that the components of its active feedback loop are finely tuned during the morphogenesis.

The design of an electronic circuit having spatially varying characteristics is simplified if it can be implemented on a regular structure, whose local characteristics are controlled by a small number of electrical parameters. On the contrary, the morphogenesis of a live system allows it to locally tune many of its parameters in order to make it function properly on a wide range of characteristics.

As for the very large signal dynamic range, mechanical processes are submitted to the same constraint of thermal noise as electronic circuits. It is probable that higher levels of neural processing deal with signals drowned out by noise, which would extend the effective dynamic range by tolerating signal/noise ratios lower than unity.

It is often argued that since both biological structure and analogue electronics share the same imperfections (low precision, nonlinearity and noise), the latter is an ideal medium to emulate the former. Several objections to this belief emerged during this research. First, biological elements are not imprecise, because they are tuned by morphogenesis, learning and short-time adaptation to ideally fulfill their task. As for nonlinearities, the nonlinear behaviour of perceptive sensors is not necessarily caused by the nonlinearities of its processing elements. This is true for the cochlea, whose compressive nonlinearity is mainly performed by controlling the damping

of linear filters.

The design of a faithful model of the cochlea therefore requires building blocks that are linear over a large signal range, which is still challenging for low-power continuous-time analogue VLSI circuits. The log-domain design proposed in this thesis is a promising attempt to reach this goal.

Analogue VLSI is perhaps not the ideal medium to faithfully model the cochlea. However, trying to understand the cochlea using analogue VLSI implementations appears to be a rich source of inspiration for developing novel engineering techniques for low power analogue VLSI circuits. As an example drawn from this work, the frequency behaviour of the cochlea was shown to rely on two-dimensional movements of the cochlear liquids. This suggests novel temporal filtering techniques that exploits both temporal *and spatial* processing, and are performed collectively by a large number of elements.

On the other hand, in applications where an efficient, continuous- and real-time, low-power and low-voltage emulation of the cochlea is needed, analogue VLSI is still the ideal candidate.

6.4 Future work and applications

Modeling an active cochlea was prompted by problems encountered in developing a system that exploits cochlear delay to perform continuous-time predictive filtering of speech signal for recognition [4, 5]. It was expected that an active cochlea that could perform enhancement of transients could segment the speech signal efficiently into relevant stationary portions of speech. This approach, left on standby in order to develop the cochlear models, remains to be pursued.

The development of the log-domain implementation was undertaken too late in this research to integrate and measure a chip. Instead, a careful analysis of the proposed design has shown its feasibility, while relentlessly tracking its potential problems and limitations. The next immediate step is therefore to integrate a pseudo-transcapacitor in order to measure its performance. The same applies to the log-domain 2-D model of the cochlea or at least a reduced part of it. The possibility to improve the log-domain 2-D cochlea with an efferent gain control mechanism may be envisaged in a next version.

More elaborate spatial processing can be performed in the feedback loop that models higher levels of neural processing in the efferent control

mechanism. As an example, lateral inhibition performed in the feedback block might yield improved spectral selectivity. Such structure would be similar to the neural “second filter” postulated to explain the sharp tuning measured on the auditory nerve before the discovery of the role of the outer hair cells. The effect of such neural filtering would be measurable at the level of basilar membrane vibrations, since it is included in the gain control loop.

Similarly, the potential of spatio-temporal processing for temporal filtering, as performed by the cochlear hydrodynamics, can be analysed further, in a more general approach. Such spatio-temporal processing is a good application for analogue VLSI log-domain implementation, in which the concepts of pseudo-conductances in weak inversion and log-domain filters are unified in a common “pseudo-linear” framework.

As for applications, the main advantages of analogue VLSI cochlear models, mentioned all along this thesis, makes them the ideal candidates for any auditory-like processing system that requires real-time, low power consumption and small volume. Applications that come directly to mind are single-chip models of larger portions of the auditory pathway, sound/speech preprocessing for portable systems dedicated to classification/recognition, hearing aids and cochlear implants.

Appendices

Appendix A

Mathematical derivations

A.1 Noise accumulated in the cochlear filter cascade

According to the diagram of a noisy filter stage in figure A.1, the transfer functions between the voltages $v_{N\tau 1}$, $v_{N\tau 2}$ and v_{NQ} generated by the input noise resistances $R_{N\tau}$ and R_{NQ} of the OTAs $g_{m\tau}$ and g_{mQ} , and the voltages v_y and v_Q are given by:

$$\left. \frac{v_y}{v_{N\tau 1}} \right|_{\substack{v_{N\tau 2} = 0 \\ v_{NQ} = 0}} = H(s), \quad (\text{A.1})$$

$$\left. \frac{v_Q}{v_{N\tau 1}} \right|_{\substack{v_{N\tau 2} = 0 \\ v_{NQ} = 0}} = (1 + s\tau) H(s), \quad (\text{A.2})$$

$$\left. \frac{v_y}{v_{N\tau 2}} \right|_{\substack{v_{N\tau 1} = 0 \\ v_{NQ} = 0}} = \left(\frac{1}{Q} - 1 + s\tau \right) H(s), \quad (\text{A.3})$$

$$\left. \frac{v_Q}{v_{N\tau 2}} \right|_{\substack{v_{N\tau 1} = 0 \\ v_{NQ} = 0}} = \left(\frac{1}{Q} - 2 \right) H(s), \quad (\text{A.4})$$

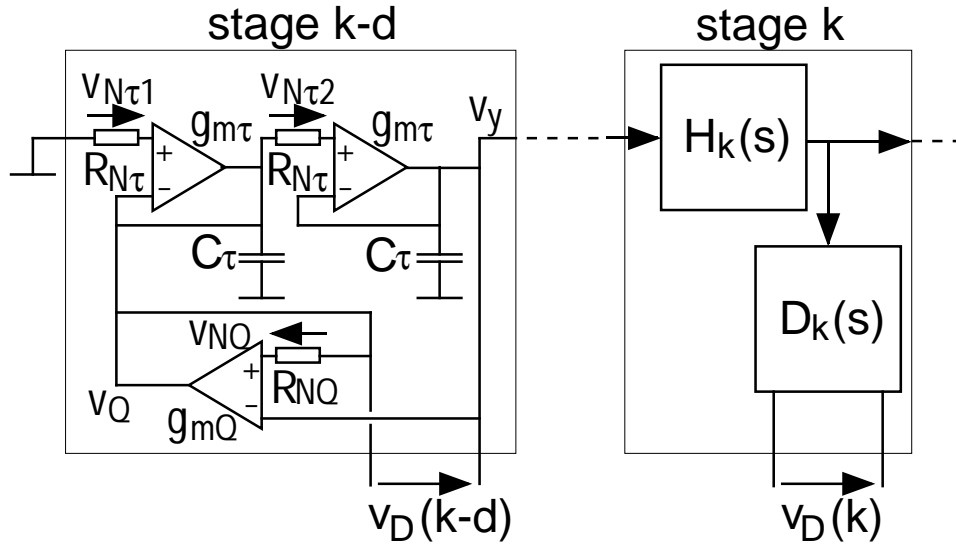


Figure A.1: Noisy cochlear filter cascade

$$\left. \frac{v_y}{v_{NQ}} \right|_{\substack{v_{N\tau_1}=0 \\ v_{N\tau_2}=0}} = \left(2 - \frac{1}{Q}\right) H(s), \quad (\text{A.5})$$

$$\left. \frac{v_Q}{v_{NQ}} \right|_{\substack{v_{N\tau_1}=0 \\ v_{N\tau_2}=0}} = (1 + s\tau) \left(2 - \frac{1}{Q}\right) H(s), \quad (\text{A.6})$$

where $H(s) = 1/(s^2\tau^2 + s\tau/Q + 1)$ is the transfer function of the cochlear filter having a time constant $\tau = C_\tau/g_{m\tau}$ and a quality factor $Q = 2 - g_{mQ}/g_{m\tau}$.

The power spectral density (psd) s_y of the noise at the output v_y of a single stage is given by the sum of the noise psd $s_N = 4k_B T R_N$ generated by each of its noise resistance R_N and multiplied by the power transfer function between the noise resistance and this output, which results in

$$s_y = \|H(s)\|^2 \left[s_{N\tau_1} + s_{N\tau_2} \|1/Q - 1 + s\tau\|^2 + s_{NQ} \|2 - 1/Q\|^2 \right]. \quad (\text{A.7})$$

Using the noise resistances as defined in section 3.4.7, the noise psd they generate is split into a thermal component

$$s_{T\tau_1} = s_{T\tau_2} = 4k_B T R_{T\tau} = \frac{k_B T}{C_\tau} \frac{2}{\pi} \frac{\gamma_{T\tau}}{f_c}, \quad (\text{A.8})$$

$$s_{TQ} = 4k_B T R_{TQ} = \frac{k_B T}{C_\tau} \frac{2}{\pi} \frac{\gamma_{T\tau}}{f_c} \frac{1}{2 - \frac{1}{Q}}, \quad (\text{A.9})$$

where $f_c = 1/2\pi\tau$ is the cutoff frequency of the filter, and a flicker component

$$s_{F\tau_1} = s_{F\tau_2} = 4k_B T R_{F\tau} = \frac{k_B T}{C_F} \frac{2}{\pi} \frac{\gamma_{F\tau}}{f}, \quad (\text{A.10})$$

$$s_{FQ} = 4k_B T R_{FQ} = \frac{k_B T}{C_F} \frac{2}{\pi} \frac{\gamma_{FQ}}{f}. \quad (\text{A.11})$$

Since $s\tau = j\omega\tau = jf/f_c$, introducing equations (A.8) to (A.11) into equation (A.7) yields $s_y = s_{Ty} + s_{Fy}$, where

$$\frac{s_{Ty}}{k_B T/C_\tau} = \Gamma_T(Q) \frac{2}{\pi} \frac{1}{f_c} \|H(jf/f_c)\|^2$$

$$+ \gamma_{T\tau} \frac{2}{\pi} \frac{1}{f_c} \left(\frac{f}{f_c} \right)^2 \|H(jf/f_c)\|^2 \quad (\text{A.12})$$

is the thermal component normalised to $k_B T/C$ and

$$\begin{aligned} \frac{s_{Fy}}{k_B T/C_F} &= \Gamma_F(Q) \frac{2}{\pi} \frac{1}{f} \|H(jf/f_c)\|^2 \\ &+ \gamma_{F\tau} \frac{2}{\pi} \frac{1}{f} \left(\frac{f}{f_c} \right)^2 \|H(jf/f_c)\|^2 \end{aligned} \quad (\text{A.13})$$

is the flicker component normalised to $k_B T/C_F$. The factors

$$\begin{aligned} \Gamma_T(Q) &= \gamma_{T\tau} \left[1 + (1/Q - 1)^2 \right] \\ &+ \gamma_{TQ} (2 - 1/Q), \end{aligned} \quad (\text{A.14})$$

$$\begin{aligned} \Gamma_F(Q) &= \gamma_{F\tau} \left[1 + (1/Q - 1)^2 \right] \\ &+ \gamma_{FQ} (2 - 1/Q)^2 \end{aligned} \quad (\text{A.15})$$

group the noise factors of the OTAs and depend on the quality factor of the filter.

The thermal component $s_T(k, d)$ and the flicker component $s_F(k, d)$ of the noise psd at the differentiated output $v_D(k)$ of a stage k due to the internal noise of a stage $k - d$ is obtained by multiplying the output noise psd s_y of the stage $k - d$ by the power transfer function $\prod_{l=k-d+1}^k \|H_l(s)\|^2$ of the stages $k - d + 1$ to k and the power transfer function $\|D_k(s)\|^2 = (2\pi f\tau_k)^2 = (f/f_c(k))^2$ of the differentiator of the stage k . Normalising the frequency f to the cutoff frequency $f_c(k)$ of the stage k with $\Omega = f/f_c(k)$, and exploiting the exponential decrease of the cutoff frequencies along the cascade expressed by $f_c(k)/f_c(k - d) = 2^{-d/b}$ yields:

$$\begin{aligned} \frac{s_T(k, d)}{k_B T/C_\tau} &= \Gamma_T(Q) \frac{2^{-d/b}}{f_c(k)} \frac{2}{\pi} \prod_{l=k-d}^k \|H_l(\Omega)\|^2 \Omega^2 \\ &+ \gamma_{T\tau} \frac{2^{-3d/b}}{f_c(k)} \frac{2}{\pi} \prod_{l=k-d}^k \|H_l(\Omega)\|^2 \Omega^4, \end{aligned} \quad (\text{A.16})$$

$$\frac{s_F(k, d)}{k_B T/C_F} = \Gamma_F(Q) \frac{1}{f_c(k)} \frac{2}{\pi} \prod_{l=k-d}^k \|H_l(\Omega)\|^2 \Omega$$

$$+ \gamma_{F\tau} \frac{2^{-2d/b}}{f_c(k)} \frac{2}{\pi} \prod_{l=k-d}^k \|H_l(\Omega)\|^2 \Omega^3, \quad (\text{A.17})$$

where $H_l(\Omega)$ is defined by equation (3.16) in section 3.2.5. The corresponding thermal and flicker noise powers $V_T^2(k, d)$ and $V_F^2(k, d)$ are calculated by integrating equations (A.16) and (A.17) over frequency $f = f_c(k)\Omega$:

$$\begin{aligned} \frac{V_T^2(k, d)}{k_B T / C_\tau} &= \Gamma_T(Q) 2^{-d/b} \frac{2}{\pi} \int_0^\infty \prod_{l=k-d}^k \Omega^2 \|H_l(\Omega)\|^2 d\Omega \\ &+ \gamma_{T\tau} 2^{-3d/b} \frac{2}{\pi} \int_0^\infty \prod_{l=k-d}^k \Omega^4 \|H_l(\Omega)\|^2 d\Omega, \end{aligned} \quad (\text{A.18})$$

$$\begin{aligned} \frac{V_F^2(k, d)}{k_B T / C_F} &= \Gamma_F(Q) \frac{2}{\pi} \int_0^\infty \prod_{l=k-d}^k \Omega \|H_l(\Omega)\|^2 d\Omega \\ &+ \gamma_{F\tau} 2^{-2d/b} \frac{2}{\pi} \int_0^\infty \prod_{l=k-d}^k \Omega^3 \|H_l(\Omega)\|^2 d\Omega. \end{aligned} \quad (\text{A.19})$$

Equations (A.18) and (A.19) do not apply for $d = 0$ because the differentiator $D_k(s)$ is embedded in the filter of the stage k . The noise power at the differentiated output v_D of a stage caused by its own internal noise must be calculated separately, starting from equations (A.1) to (A.6) to calculate the noise psd at the output $v_D = v_Q - v_y$. Since the internal noise sources are not correlated, the output noise psds s_y and s_Q add. With s_y given by equation (A.7) and s_Q calculated similarly,

$$\begin{aligned} s_Q &= \|H(s)\|^2 \left[s_{N\tau 1} \|1 + s\tau\|^2 + s_{N\tau 2} \|1/Q - 2\|^2 \right. \\ &\quad \left. + s_{NQ} \|(1 + s\tau)(2 - 1/Q)\|^2 \right], \end{aligned} \quad (\text{A.20})$$

the noise psd at the differentiated output v_D becomes

$$\begin{aligned} s_D &= \|H(s)\|^2 \left[s_{N\tau 1} (1 + \|1 + s\tau\|^2) \right. \\ &\quad \left. + s_{N\tau 2} (\|1/Q - 1 + s\tau\|^2 + \|1/Q - 2\|^2) \right. \\ &\quad \left. + s_{NQ} (1 + \|1 + s\tau\|^2) \|2 - 1/Q\|^2 \right]. \end{aligned}$$

(A.21)

Separating again s_D into a thermal component s_{TD} and a flicker components s_{FD} using equation (A.8) to (A.11) and using the normalised frequency $\Omega = f/f_c(k)$ results in

$$\begin{aligned} \frac{s_{TD}}{k_B T / C_\tau} &= \Gamma_{TD1}(Q) \frac{2}{\pi} \frac{1}{f_c(k)} \|H(\Omega)\|^2 \\ &+ \Gamma_{TD2}(Q) \frac{2}{\pi} \frac{1}{f_c(k)} \Omega^2 \|H(\Omega)\|^2, \end{aligned} \quad (\text{A.22})$$

$$\begin{aligned} \frac{s_{FD}}{k_B T / C_F} &= \Gamma_{FD1}(Q) \frac{2}{\pi} \frac{1}{\Omega f_c(k)} \|H(\Omega)\|^2 \\ &+ \Gamma_{FD2}(Q) \frac{2}{\pi} \frac{\Omega}{f_c(k)} \|H(\Omega)\|^2, \end{aligned} \quad (\text{A.23})$$

where

$$\begin{aligned} \Gamma_{TD1}(Q) &= \gamma_{T\tau} \left[2 + (1/Q - 1)^2 + (1/Q - 2)^2 \right] \\ &+ 2\gamma_{TQ} (2 - 1/Q), \end{aligned} \quad (\text{A.24})$$

$$\Gamma_{TD2}(Q) = 2\gamma_{T\tau} + \gamma_{TQ} (2 - 1/Q), \quad (\text{A.25})$$

$$\begin{aligned} \Gamma_{FD1}(Q) &= \gamma_{T\tau} \left[2 + (1/Q - 1)^2 + (1/Q - 2)^2 \right] \\ &+ 2\gamma_{TQ} (2 - 1/Q)^2, \end{aligned} \quad (\text{A.26})$$

$$\Gamma_{FD2}(Q) = 2\gamma_{T\tau} + \gamma_{TQ} (2 - 1/Q)^2. \quad (\text{A.27})$$

Finally, the thermal and flicker noise power V_{TD}^2 and V_{FD}^2 at the differentiated output v_D of each stage due to its own internal noise sources is obtained by integrating s_{TD} and s_{FD} over frequency $f = \Omega f_c$:

$$\begin{aligned} \frac{V_{TD}^2}{k_B T / C_\tau} &= \Gamma_{TD1}(Q) \frac{2}{\pi} \int_0^\infty \|H(\Omega)\|^2 d\Omega \\ &+ \Gamma_{TD2}(Q) \frac{2}{\pi} \int_0^\infty \Omega^2 \|H(\Omega)\|^2 d\Omega, \end{aligned} \quad (\text{A.28})$$

$$\begin{aligned} \frac{V_{FD}^2}{k_B T / C_F} &= \Gamma_{FD1}(Q) \frac{2}{\pi} \int_0^\infty \frac{\|H(\Omega)\|^2}{\Omega} d\Omega \\ &+ \Gamma_{FD2}(Q) \frac{2}{\pi} \int_0^\infty \Omega \|H(\Omega)\|^2 d\Omega. \end{aligned} \quad (\text{A.29})$$

Because $\|H(\Omega)\|^2$ is a second-order low-pass function, both integrals in equations (A.18), (A.19) and (A.28), as well as the integral of the second term of equation (A.29) converge. However, due to its $1/\Omega$ factor, the integral of the first term of equation (A.29) diverges if integrated from $\Omega = 0$. This integral can be approximated by replacing its lower limit by Ω_1 . With Ω_1 small enough to assume $\|H(\Omega_1)\|^2 = 1$, this approximation can be compensated by adding $\int_{\Omega_0}^{\Omega_1} d\Omega/\Omega = \ln(\Omega_1/\Omega_0)$, where Ω_0 can be as small as required by the accuracy of the approximation, which is practically determined by the observation window used for measuring the noise.

A.2 Finite difference approximation of the Laplace equation implemented with a resistive network

The two-dimensional Laplacian of a function $V(x, y)$ is given by

$$\Delta V(x, y) = \frac{\partial^2 V(x, y)}{\partial x^2} + \frac{\partial^2 V(x, y)}{\partial y^2}. \quad (\text{A.30})$$

The finite difference approximation of the Laplacian is obtained by locally approximating the function $V(x, y)$ with a second-order function $\tilde{V}(x, y)$:

$$\tilde{V}(x, y) = a_x x^2 + a_y y^2 + a_{xy} xy + b_x x + b_y y + c. \quad (\text{A.31})$$

The function \tilde{V} is sampled spatially at coordinate $x = i\Delta_x$ and $y = j\Delta_y$, which yields the values $V_{i,j}$, $V_{i-1,j}$, $V_{i+1,j}$, $V_{i,j-1}$, and $V_{i,j+1}$ at the sampled position $(i\Delta_x, j\Delta_y)$ and its four neighbours. Expressing these five values using equation (A.31) allows one to extract

$$2a_x = \frac{V_{i-1,j} + V_{i+1,j} - 2V_{i,j}}{\Delta_x^2}, \quad (\text{A.32})$$

$$2a_y = \frac{V_{i,j-1} + V_{i,j+1} - 2V_{i,j}}{\Delta_y^2}. \quad (\text{A.33})$$

The Laplacian of \tilde{V} is thus approximated by

$$\begin{aligned} \Delta \tilde{V}(i\Delta_x, j\Delta_y) &= 2a_x + 2a_y = \\ &= \frac{V_{i-1,j} + V_{i+1,j} - 2V_{i,j}}{\Delta_x^2} + \frac{V_{i,j-1} + V_{i,j+1} - 2V_{i,j}}{\Delta_y^2}. \end{aligned} \quad (\text{A.34})$$

Similarly, the gradient of the function $V(x, y)$ is approximated by

$$\mathbf{grad} \tilde{V}(i\Delta_x, j\Delta_y) = \begin{bmatrix} \frac{\partial \tilde{V}(x, y)}{\partial x} \\ \frac{\partial \tilde{V}(x, y)}{\partial y} \end{bmatrix} = \begin{bmatrix} 2a_x i\Delta_x + a_{xy} j\Delta_y + b_x \\ 2a_y j\Delta_y + a_{xy} i\Delta_x + b_y \end{bmatrix}, \quad (\text{A.35})$$

where both components may also be expressed using the values of \tilde{V} at position $(i\Delta_x, j\Delta_y)$ and its neighbours:

$$2a_x i\Delta_x + a_{xy} j\Delta_y + b_x = \frac{V_{i,j} - V_{i-1,j} + a_x \Delta_x^2}{\Delta_x}, \quad (\text{A.36})$$

$$2a_y j\Delta_y + a_{xy} i\Delta_x + b_y = \frac{V_{i,j} - V_{i,j-1} + a_y \Delta_y^2}{\Delta_y}, \quad (\text{A.37})$$

thus yielding, using equations (A.32) and (A.33)

$$\mathbf{grad} \tilde{V}(i\Delta_x, j\Delta_y) = \begin{bmatrix} \frac{V_{i+1,j} - V_{i-1,j}}{2\Delta_x} \\ \frac{V_{i,j+1} - V_{i,j-1}}{2\Delta_y} \end{bmatrix}. \quad (\text{A.38})$$

To solve the Laplace equation $\Delta \tilde{V} = 0$, boundary conditions are required. For simplification we will consider only boundaries (x_b, y_b) superimposed on the grid, i.e. defined by $(x_b = i\Delta_x, y_b = N\Delta_y)$ for a boundary parallel to the x -axis at $y_b = N\Delta_y$ and by $(x_b = M\Delta_x, y_b = j\Delta_y)$ for a boundary parallel to the y -axis at $x_b = M\Delta_x$. The boundary conditions may be expressed by imposing the value V_{i_b, j_b} of the function \tilde{V} at positions $(i_b\Delta_x, j_b\Delta_y)$ sampled on the boundary (x_b, y_b) . Alternatively, the gradient of the function \tilde{V} perpendicular to the boundary may be imposed. The component $\partial_x V_{M,j} \mathbf{e}_x$ of $\mathbf{grad} \tilde{V}$ is imposed at position $(M\Delta_x, j\Delta_y)$ on a boundary parallel to the y -axis. Similarly, the component $\partial_y V_{i,N} \mathbf{e}_y$ of $\mathbf{grad} \tilde{V}$ is imposed at position $(\Delta_x, N\Delta_y)$ on a boundary parallel to the x -axis. The unit vectors \mathbf{e}_y and \mathbf{e}_x are defined positively when pointing outside the boundary and the notations $\partial_{x,y}$ represent the partial differentiation operators $\partial/\partial x, y$. The gradient expressed by equations (A.35), (A.36) and (A.37) allows one to calculate the parameters a_x at a boundary position $(M\Delta_x, j\Delta_y)$:

$$a_x = \frac{\partial_x V_{M,j} \Delta_x + V_{M-1,j} - V_{M,j}}{\Delta_x^2}, \quad (\text{A.39})$$

and a_y at a boundary position $(i\Delta_x, N\Delta_y)$:

$$a_y = \frac{\partial_y V_{i,N} \Delta_y + V_{i,N-1} - V_{i,N}}{\Delta_y^2}. \quad (\text{A.40})$$

The approximation of the Laplacian $\Delta\tilde{V}(x, y) = 2a_x + 2b_y$ also applies at the boundaries, with a_x given by equation (A.39) and a_y by equation (A.33) at the boundary position $(M\Delta_x, j\Delta_y)$:

$$\begin{aligned} \Delta\tilde{V}(M\Delta_x, j\Delta_y) &= 2 \frac{V_{M-1,j} - V_{M,j} + \partial_x V_{M,j} \Delta_x}{\Delta_x^2} \\ &+ \frac{V_{M,j-1} + V_{M,j+1} - 2V_{M,j}}{\Delta_y^2}, \end{aligned} \quad (\text{A.41})$$

and inversely with a_x given by equation (A.32) and a_y by equation (A.40) at the boundary position $(i\Delta_x, N\Delta_y)$:

$$\begin{aligned} \Delta\tilde{V}(i\Delta_x, N\Delta_y) &= \frac{V_{i-1,N} + V_{i+1,N} - 2V_{i,N}}{\Delta_x^2} \\ &+ 2 \frac{V_{i,N-1} - V_{i,N} + \partial_y V_{i,N} \Delta_y}{\Delta_y^2}. \end{aligned} \quad (\text{A.42})$$

In a resistive sheet, the potential $V(x, y)$ obeys the Laplace equation $\Delta V(x, y) = 0$. The surface current density $\mathbf{J}(x, y)$ is given by the conduction equation

$$\mathbf{J}(x, y) = -\sigma(x, y) \mathbf{grad} V(x, y), \quad (\text{A.43})$$

where $\sigma(x, y)$ is the sheet conductivity of the resistive sheet. Modeling the resistive sheet by a network of resistors arranged on a rectangular grid is equivalent to performing a finite-difference approximation of the Laplace equation of the resistive sheet. Each node (i, j) sampled at position $(i\Delta_x, j\Delta_y)$ on the resistive sheet is connected to its neighbouring nodes $(i-1, j)$ and $(i, j-1)$ by resistors $R_x(i, j)$ and $R_y(i, j)$, respectively.

Kirchoff law states that currents flowing into any nodes (i, j) sum to zero, thus, for a node within the resistive sheet:

$$\frac{V_{i-1,j} - V_{i,j}}{R_x(i, j)} + \frac{V_{i+1,j} - V_{i,j}}{R_x(i+1, j)} + \frac{V_{i,j-1} - V_{i,j}}{R_y(i, j)} + \frac{V_{i,j+1} - V_{i,j}}{R_y(i, j+1)} = 0. \quad (\text{A.44})$$

If $R_x(i, j) = R_x(i + 1, j)$ and $R_y(i, j) = R_y(i, j + 1)$ may be assumed, equation (A.44) corresponds to the finite difference of the Laplace equation $\Delta\tilde{V}(x, y) = 0$ where $\Delta\tilde{V}(x, y)$ is given by equation (A.38), provided that

$$R_x(i, j) \frac{\Delta y}{\Delta x} = R_y(i, j) \frac{\Delta x}{\Delta y} = R(i, j). \quad (\text{A.45})$$

The current flowing in the four resistors $R_x(i, j)$, $R_x(i + 1, j)$, $R_y(i, j)$ and $R_y(i, j + 1)$ connecting the node (i, j) corresponds to the current density $\mathbf{J}(x, y) = [J_x(x, y), J_y(x, y)]^T$ in the resistive sheet. Both components of $\mathbf{J}(x = i\Delta_x, y = j\Delta_y)$ are estimated by averaging the current flowing in the resistors neighbouring the node (i, j) , i.e. in $R_x(i, j)$ and $R_x(i + 1, j)$ for the component J_x and in $R_y(i, j)$ and $R_y(i, j + 1)$ for the component J_y . This average current at node (i, j) is thus expressed by a current vector

$$\begin{bmatrix} I_x(i, j) \\ I_y(i, j) \end{bmatrix} = \frac{1}{2} \begin{bmatrix} \frac{V_{i-1,j} - V_{i,j}}{R_x(i, j)} + \frac{V_{i,j} - V_{i+1,j}}{R_x(i+1, j)} \\ \frac{V_{i,j-1} - V_{i,j}}{R_y(i, j)} + \frac{V_{i,j} - V_{i,j+1}}{R_y(i, j+1)} \end{bmatrix}, \quad (\text{A.46})$$

where the current components $I_x(i, j)$ and $I_y(i, j)$ are defined to be positive in the direction of growing i and j . Assuming again $R_x(i, j) = R_x(i + 1, j)$ and $R_y(i, j) = R_y(i, j + 1)$, equation (A.46) can be rewritten, using equation (A.45):

$$-R(i, j) \begin{bmatrix} \frac{I_x(i, j)}{\Delta y} \\ \frac{I_y(i, j)}{\Delta x} \end{bmatrix} = \begin{bmatrix} \frac{V_{i+1,j} - V_{i-1,j}}{2\Delta_x} \\ \frac{V_{i,j+1} - V_{i,j-1}}{2\Delta_y} \end{bmatrix}, \quad (\text{A.47})$$

The right-hand side of equation (A.47) corresponds to the finite difference approximation of the potential gradient $\mathbf{grad} \tilde{V}(x, y)$ given in equation (A.38). Therefore, the conduction equation A.43 may be implemented by the resistor network using the following correspondences:

$$R_x(i, j) = \frac{1}{\sigma(x, y)} \frac{\Delta x}{\Delta y}, \quad (\text{A.48})$$

$$R_y(i, j) = \frac{1}{\sigma(x, y)} \frac{\Delta y}{\Delta x}, \quad (\text{A.49})$$

$$I_x(i, j) = \Delta_y J_x(i\Delta_x, j\Delta_y), \quad (\text{A.50})$$

$$I_y(i, j) = \Delta_x J_y(i\Delta_x, j\Delta_y). \quad (\text{A.51})$$

These correspondences are valid inside the resistive sheet. They must now be determined at the boundaries of the resistive sheet, which depends on the nature of the boundary conditions. These can either consist of an imposed voltage $V(x_b, y_b)$, or a voltage gradient $\mathbf{grad} V(x_b, y_b)$ imposed by a current density $\mathbf{J}(x_b, y_b)$.

Each node (i, N) following a boundary $(x_b = i\Delta_x, y_b = N\Delta_y)$ is connected to three resistors, namely $R_x(i, N)$, $R_x(i + 1, N)$ and $R_y(i, N)$. Similarly, each node (M, j) following a boundary $(x_b = M\Delta_x, y_b = j\Delta_y)$ is connected to the resistors $R_y(M, j)$, $R_y(M, j + 1)$ and $R_x(M, j)$. If voltages $V_{i,N}$ and $V_{i-1,N}$ (or $V_{M,j}$ and $V_{M,j-1}$) are imposed as a boundary condition on two successive nodes, the resistor $R_x(i, N)$ (or $R_y(M, j)$) between these nodes is irrelevant, because it only affects the current flowing through it. This current is provided by the voltage source imposing $V_{i,N} - V_{i-1,N}$ (or $V_{M,j} - V_{M,j-1}$) and does not affect the voltages and currents elsewhere in the network. A constant voltage is usually imposed on a portion of the boundary by connecting the corresponding edge of the resistive sheet using a metallic contact. In the corresponding resistive network, this is equivalent to shorting out all the resistors following the boundary on which such condition apply, as shown in figure A.2b at the boundary $(x_b = 0, y_b = j\Delta_y)$.

The current density $J_x(x_b, y_b)$ or $J_y(x_b, y_b)$ flowing out the resistive sheet perpendicular to a boundary $(x_b = M\Delta_x, y_b = j\Delta_y)$ or $(x_b = i\Delta_x, y_b = N\Delta_y)$ is modeled in the resistive sheet by the current $I_x(M, j)$ or $I_y(i, N)$ flowing out of the boundary node (M, j) or (i, N) . Assuming again $R_y(M, j) = R_y(M, j + 1)$ and $R_x(i, N) = R_x(i + 1, N)$, Kirchoff's law yields

$$0 = \frac{V_{M-1,j} - V_{M,j} - R_x(M, j)I_x(M, j)}{R_x(M, j)} + \frac{V_{M,j-1} + V_{M,j+1} - 2V_{M,j}}{R_y(M, j)}, \quad (\text{A.52})$$

$$0 = \frac{V_{i-1,N} + V_{i+1,N} - 2V_{i,N}}{R_x(i, N)} + \frac{V_{i,N-1} - V_{i,N} - R_y(i, N)I_y(i, N)}{R_y(i, N)}. \quad (\text{A.53})$$

Comparing equations (A.52) and (A.53) with equations (A.41) and (A.42), in which the left-hand side $\Delta\tilde{V}(x, y)$ equals zero because the Laplace equa-

tion is valid at the boundary and where the conduction equation imposes

$$\partial_x V_{M,j} = -\frac{J_x(M\Delta_x, j\Delta_y)}{\sigma(x, y)}, \quad (\text{A.54})$$

$$\partial_y V_{i,N} = -\frac{J_y(i\Delta_x, N\Delta_y)}{\sigma(x, y)}, \quad (\text{A.55})$$

results in the following correspondences:

$$R_x(M, j) = \frac{1}{\sigma(x, y)} \frac{\Delta_x}{\Delta_y}, \quad (\text{A.56})$$

$$R_y(M, j) = \frac{2}{\sigma(x, y)} \frac{\Delta_y}{\Delta_x}, \quad (\text{A.57})$$

$$I_x(M, j) = \Delta_y J_x(M\Delta_x, j\Delta_y), \quad (\text{A.58})$$

$$R_x(i, N) = \frac{2}{\sigma(x, y)} \frac{\Delta_x}{\Delta_y}, \quad (\text{A.59})$$

$$R_y(i, N) = \frac{1}{\sigma(x, y)} \frac{\Delta_y}{\Delta_x}, \quad (\text{A.60})$$

$$I_y(i, N) = \Delta_x J_y(i\Delta_x, N\Delta_y). \quad (\text{A.61})$$

Comparing equations (A.57) and (A.59) with equations (A.49) and (A.48), it appears that the resistors following the boundaries are twice large as they would be if they were within the network. This is explained by the fact that the resistive path from two positions well inside the resistive sheet spreads symmetrically around the median line joining these two points. On the edge of the resistive sheet, however, the resistive path can only spread inside the sheet, reducing the width of the path by a factor of two and thus increasing its resistance by the same ratio (see figure A.2a).

Another case of boundary conditions is possible, which consists of a boundary connected to a grounded admittance per unit length $Y'(x_b, y_b)$. This admittance imposes a current density $J(x_b, y_b) = Y'(x_b, y_b)V(x_b, y_b)$ normal to the boundary. The effect of such an admittance following the boundary ($x = i\Delta_x, 0$) is presented here. The current density $J_y(i\Delta_x, 0)$ flowing out of the resistive sheet perpendicular to this boundary imposes a voltage gradient

$$\partial_y V(i, 0) = -\frac{J_y(i\Delta_x, 0)}{\sigma(x, y)} = -\frac{Y'(i\Delta_x, 0)}{\sigma(x, y)} V_{i,0}. \quad (\text{A.62})$$

In the resistor network, the admittance per unit length $Y'(i\Delta_x, 0)$ is quantised to an admittance $Y(i, 0)$ connecting the node $(i, 0)$ to ground. The other resistors connecting the node $(i, 0)$ to the nodes $(i - 1, 0)$, $(i + 1, 0)$ and $(i, 1)$ are named following the usual notation $R_x(i, 0)$, $R_x(i + 1, 0)$ and $R_y(i, 1)$, respectively. Again, $R_x(i, 0) = R_x(i + 1, 0)$ is assumed. Kirchoff's law applied at node $(i, 0)$ gives

$$\begin{aligned} 0 &= \frac{V_{i-1,0} + V_{i+1,0} - 2V_{i,0}}{R_x(i, 0)} \\ &+ \frac{V_{i,1} - [1 + R_y(i, 0)Y(i, 0)]V_{i,0}}{R_y(i, 1)}. \end{aligned} \quad (\text{A.63})$$

Comparing the right-hand sides of equation (A.63) and equation (A.42), in which the indices N and $N - 1$ corresponding to the boundary $(i\Delta_x, N\Delta_y)$ are replaced by their equivalent indices 0 and 1 of the boundary $(i\Delta_x, 0)$, and using equation (A.62) yields the correspondences

$$R_x(i, 0) = \frac{2}{\sigma(x, y)} \frac{\Delta_x}{\Delta_y}, \quad (\text{A.64})$$

$$R_y(i, 1) = \frac{1}{\sigma(x, y)} \frac{\Delta_y}{\Delta_x}, \quad (\text{A.65})$$

$$Y(i, 0) = \Delta_x Y'(i\Delta_x, 0). \quad (\text{A.66})$$

It is important to note that in order to establish the exact correspondence between the resistive network and the resistive sheet we had to assume $R_x(i, j) = R_x(i + 1, j)$ and $R_y(i, j) = R_y(i, j + 1)$, which can only be respected using a resistive sheet having a homogeneous conductivity $\sigma(x, y) = \sigma$. However the error made by using an inhomogeneous conductivity will depend on the differences between neighbouring resistances, which may be made as small as required by decreasing the grid size. At a given grid size, this error is minimised if each resistor $R_x(i, j)$ and $R_y(i, j)$ which connect the node pairs $(i - 1, j) - (i, j)$ and $(i, j - 1) - (i, j)$ corresponds to the local conductivities between the positions of the node pairs, i.e. $\sigma(x = (i - 0.5)\Delta_x, y = j\Delta_y)$ and $\sigma(x = i\Delta_x, y = (j - 0.5)\Delta_y)$.

The values of the dipoles and boundary currents of the network of figure A.2b which quantise the inhomogeneous resistive sheet with the boundary conditions shown in figure A.2a are summarised in table A.1.

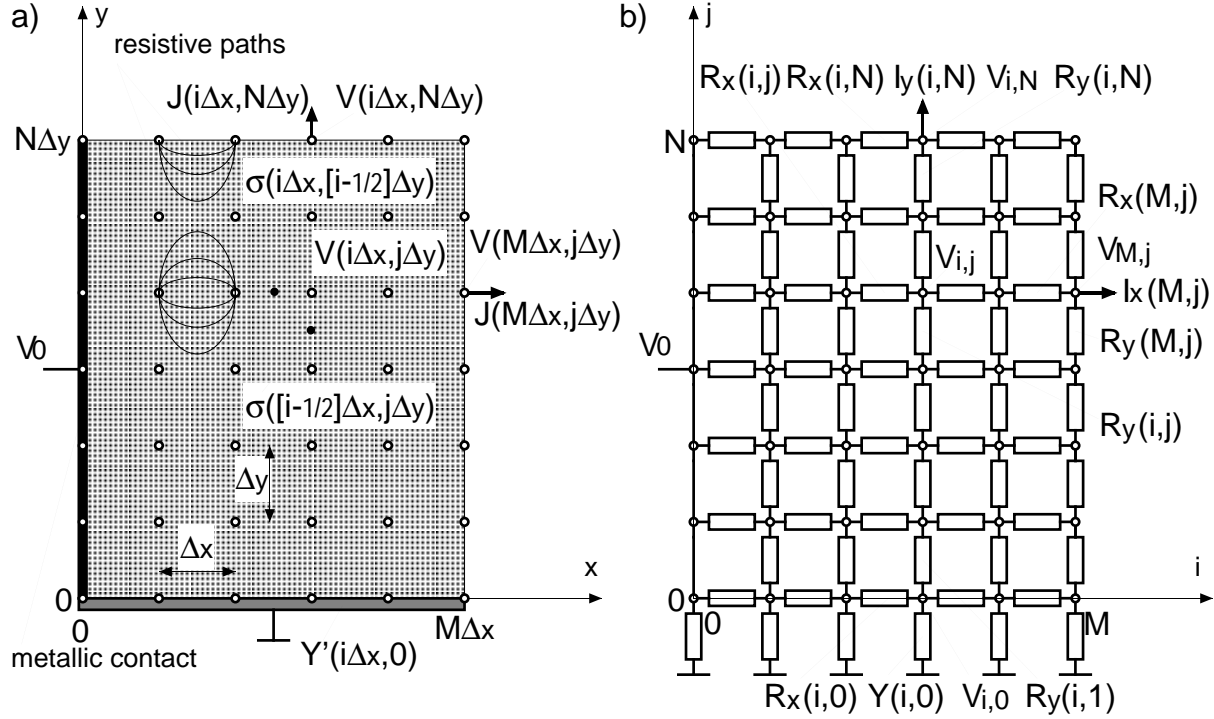


Figure A.2: a) resistive sheet and its boundary conditions; spatial quantisation by a network of resistors.

A.3 Green's function in a 2-D resistive sheet

The Green's function $G(x_1, x_2)$ used in [24] establishes the relationship between the infinitesimal force per unit length $dF'(x_1)$ applied on the basilar membrane at position x_1 due to the acceleration $a(x_2)$ of an infinitesimal basilar membrane segment of length dx_2 at position x_2 , provided it moves alone:

$$dF(x_1) = a(x_2)G(x_1, x_2) dx_2. \quad (\text{A.67})$$

The infinitesimal force per unit length $dF(x_1)$ is given by the difference of the infinitesimal pressures $dP_{SM}(x_1)$ in the scala media and $dP_{ST}(x_1)$ in the scala tympani multiplied by the width $w(x_1)$ of the basilar membrane segment, thus

$$[dP_{SM}(x_1) - dP_{ST}(x_1)]w(x_1) = a(x_2)G(x_1, x_2) dx_2. \quad (\text{A.68})$$

The Laplace equation and its boundary conditions states that the pressure difference between two positions x_a and x_b along the basilar membrane and caused by the acceleration of the basilar membrane at position x_2 , can

$R_x(i, j) = \frac{1}{\sigma([i - \frac{1}{2}]\Delta_x, j\Delta_y)} \frac{\Delta_x}{\Delta_y}$ $R_y(i, j) = \frac{1}{\sigma(i\Delta_x, [j - \frac{1}{2}]\Delta_y)} \frac{\Delta_y}{\Delta_x}$
$R_x(M, j) = \frac{1}{\sigma([M - \frac{1}{2}]\Delta_x, j\Delta_y)} \frac{\Delta_x}{\Delta_y}$ $R_y(M, j) = \frac{1}{\sigma(M\Delta_x, [j - \frac{1}{2}]\Delta_y)} \frac{\Delta_y}{\Delta_x}$ $I_x(M, j) = \Delta_y J_x(M\Delta_x, j\Delta_y)$
$R_x(i, N) = \frac{2}{\sigma([i - \frac{1}{2}]\Delta_x, N\Delta_y)} \frac{\Delta_x}{\Delta_y}$ $R_y(i, N) = \frac{1}{\sigma(i\Delta_x, [N - \frac{1}{2}]\Delta_y)} \frac{\Delta_y}{\Delta_x}$ $I_y(i, N) = \Delta_x J_y(i\Delta_x, N\Delta_y)$
$R_x(i, 0) = \frac{2}{\sigma([i - \frac{1}{2}]\Delta_x, 0)} \frac{\Delta_x}{\Delta_y}$ $R_y(i, 1) = \frac{1}{\sigma(i\Delta_x, \frac{1}{2}\Delta_y)} \frac{\Delta_y}{\Delta_x}$ $Y(i, 0) = \Delta_x Y'(i\Delta_x, 0)$

Table A.1: Correspondences between resistive sheet parameters and resistive network parameters.

be calculated by integrating the acceleration along the curvilinear axis $l(x, x_2)$ following any acceleration flow line in the liquid resulting from the acceleration imposed at x_2 :

$$P(x_a) - P(x_b) = \int_{x=x_a}^{x=x_b} \rho a(x) dl(x, x_2). \quad (\text{A.69})$$

The curvilinear axis $l(x, x_2)$ is always orthogonal to equipressure surfaces $S(x, x_2)$ in the liquid, and the acceleration flow integrated over these surfaces is constant all along $l(x, x_2)$, in particular at coordinate x_2 where the basilar membrane segment of area $dx_2 w(x_2)$ imposes the acceleration

$a(x_2)$:

$$a(x)S(x, x_2) = a(x_2)w(x_2) dx_2. \quad (\text{A.70})$$

Equation (A.69) can thus be rewritten

$$dP(x_a) - dP(x_b) = a(x_2)w(x_2) dx_2 \int_{x=x_a}^{x=x_b} \rho \frac{dl(x, x_2)}{S(x, x_2)}. \quad (\text{A.71})$$

The infinitesimal pressure difference across the basilar membrane at position x_1 becomes thus:

$$dP_{SM}(x_1) - dP_{ST}(x_1) = a(x_2)w(x_2)\rho g(x_1, x_2) dx_2, \quad (\text{A.72})$$

where

$$g(x_1, x_2) = \int_{x=x_1}^{x=x_h} \frac{dl_{SM}(x, x_2)}{S_{SM}(x, x_2)} + \int_{x=x_h}^{x=x_1} \frac{dl_{ST}(x, x_2)}{S_{SM}(x, x_2)} \quad (\text{A.73})$$

integrates the inverse of the equipressure surfaces $S_{BM}(x, x_2)$ from x_1 to the helicotrema at x_h along the curvilinear coordinate $dl_{SM}(x, x_2)$ in the scala media, and then integrates similarly $dl_{ST}(x, x_2)/S_{ST}(x, x_2)$ in the scala tympani, back from x_h to x_1 . If the cochlea has a longitudinal symmetry, $S_{SM}(x, x_2) = S_{ST}(x, x_2) = S(x, x_2)$ and $dl_{SM}(x, x_2) = -dl_{ST}(x, x_2) = dl(x, x_2)$ simplifies equation (A.73) into

$$g(x_1, x_2) = 2 \int_{x=x_1}^{x=x_h} \frac{dl(x, x_2)}{S(x, x_2)}. \quad (\text{A.74})$$

Comparing equations (A.68) and (A.72) allows one to express the Green's function by:

$$G(x_1, x_2) = w(x_1)w(x_2)\rho g(x_1, x_2). \quad (\text{A.75})$$

The function $g(x_1, x_2)$ is obtained from the 3-D geometry of the cochlear duct. In order to map it on a 2-D resistive sheet, equation (A.74) is rewritten:

$$\rho g(x_1, x_2) = \int_{x=x_1}^{x=x_h} 2\rho w(x) \frac{dl(x, x_2)}{L(x, x_2)} \frac{1}{w(x)^2}, \quad (\text{A.76})$$

where the 2-D projection of the equipressure surfaces $S(x, x_2)$ become equipressure contour $L(x, x_2) = S(x, x_2)/w(x)$, assuming that the width of the duct is equal to the basilar membrane width and that the liquid moves uniformly all along this width. Assuming in addition that the width does not change enough from x_1 to x_h to use $w(x) = w(x_1)$ allow to remove the term $1/w(x)^2$ from the integral, thus:

$$\rho w(x_1)^2 g(x_1, x_2) = \int_{x=x_1}^{x=x_h} 2\rho w(x) \frac{dl(x, x_2)}{L(x, x_2)}. \quad (\text{A.77})$$

Using the analogy between the liquid density ρ and the sheet conductance σ of the resistive sheet given by equation (4.24) yields

$$\frac{F_v}{F_j} \rho w(x_1)^2 g(x_1, x_2) = \int_{x=x_1}^{x=x_h} \frac{1}{\sigma} \frac{dl(x, x_2)}{L(x, x_2)}, \quad (\text{A.78})$$

whose right-hand side corresponds to the equivalent resistance $R_G(x_1, x_2)$ of the resistive sheet which relates the current $I(x_2) = J(x_2)dx_2$ injected at position x_2 along the basilar membrane edge and the voltage $V(x_1)$ measured at position x_1 .

The Green's function used in [24, 47] are computed from the function $g(x'_1, x'_2)$ where the positions are given relative to the cochlea length. The nodes i_1 and i_2 at which the voltage is measured and the current injected corresponds thus to relative positions $x'_1 = i_1/M$ and $x'_2 = i_2/M$, respectively. Moreover, it is important to note that the effective basilar membrane widths used in [24, 47] to compute the Green's function have half their geometric values in order to take into account the bending of the basilar membrane along its width. The equivalent resistances $R_G(i_1, i_2)$ that should be measured on the network to yield the Green's function used in [24, 47] is finally expressed by:

$$R_G(i_1, i_2) = \frac{F_v}{F_j} \frac{w(i_1 \Delta_x)^2}{4} \rho g(i_1/M, i_2/M), \quad (\text{A.79})$$

where

$$g(x'_1, x'_2) = \begin{cases} (1.08 - 0.2x'_2 - 0.88x'_2{}^2) \cdot 10^5 \text{m}^{-1} & : x'_2 > x'_1 \\ (1.08 - 0.2x'_1 - 0.88x'_1{}^2) \cdot 10^5 \text{m}^{-1} & : x'_2 \leq x'_1 \end{cases}, \quad (\text{A.80})$$

according to [47], p. 2254.

A.4 Basilar membrane resonator noise

A.4.1 Integrator

The equivalent noise sources of the log-domain basilar membrane resonator are estimated using the diagram of figure 5.17. The log-domain integrators $C_{1,2}^* - G_{1,2}^*$ with their input current sinking transistors $T_{7,13}$ and output unloading mirrors $T_{9,15}-T_{33,39}-T_{34,42}-T_{32,40}$ are replaced by their linearised noisy equivalents. The output v_{Gout} is determined from the resulting linearised diagram of figure A.3:

$$v_{Gout} = \frac{g_{m0}}{(g_{m3} - g_{m4}) + g_{m0}g_{m3}/g_{s2}} v_C \quad (\text{A.81})$$

$$+ \frac{1}{(g_{m3} - g_{m4}) + g_{m0}g_{m3}/g_{s2}} \left[\frac{g_{m4}}{g_{m6}} (i_{N5} - i_{N6}) + \frac{g_{m0}}{g_{s2}} i_{N2} - \left(1 + \frac{g_{m0}}{g_{s2}} \right) i_{N3} + i_{N4} + i_{No} \right].$$

Transistors T_2 to T_6 are all in weak inversion and they are crossed by the same dc current I ; their corresponding transconductances are thus all equal, $g_{m2} = g_{m3} = g_{m4} = g_{m5} = g_{m6} = I/nU_T$ and $g_{s2} = ng_{m2}$, simplifying equation (A.81) into

$$v_{Gout} = n v_C \quad (\text{A.82})$$

$$+ \frac{n}{g_{m0}} \left[i_{N5} - i_{N6} + \frac{g_{m0}}{ng_{m3}} i_{N2} - \left(1 + \frac{g_{m0}}{ng_{m3}} \right) i_{N3} + i_{N4} + i_{No} \right],$$

where n is the slope factor, assumed identical for all transistors.

The output noise power spectral density (psd) is calculated by replacing the uncorrelated noise currents $\pm i_{Ni}$ by their psd $+s_{Ii}$ and squaring all gains between them and the output. Since all transistors are saturated and in weak inversion, their noise current psd is given by $s_{Ii} = 2q_e I = 2k_B T n g_{mi}$. The psd s_{Io} of the noise source i_{No} is twice this value since it corresponds to the output follower-shifter of the pseudo-transcapacitor, made from the two transistors crossed by the same bias current I_{shC} . Both are also assumed here in weak inversion, thus $s_{Io} = 2q_e I_{shC} = 4k_B T n g_{mo}$. The output noise psd becomes

$$s_{VGout} = n^2 s_{VC} + \gamma_{out} \frac{4k_B T}{g_{s2}}, \quad (\text{A.83})$$

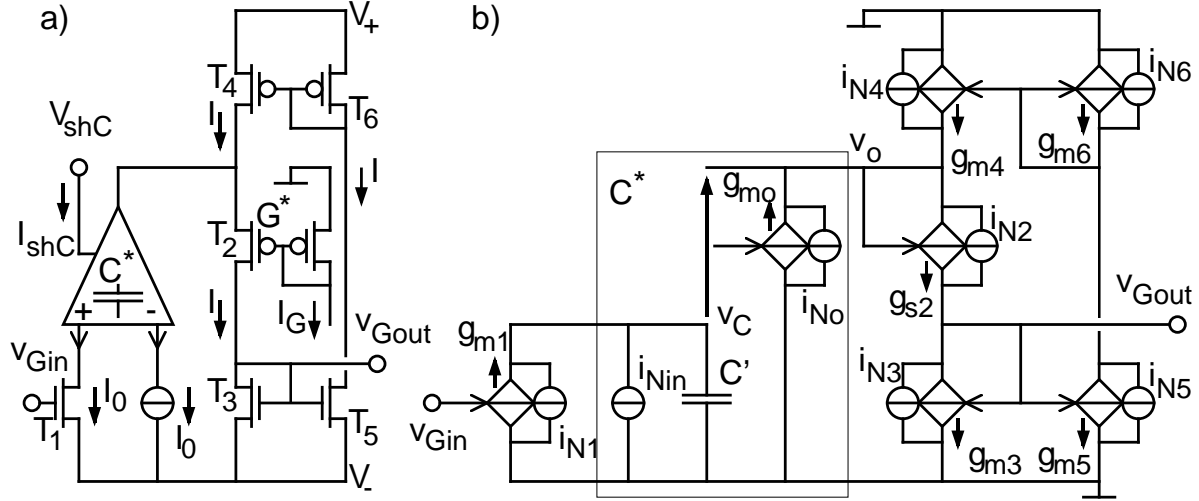


Figure A.3: a) Log-domain integrator and b) its noisy small signal equivalent

where the noise factor

$$\gamma_{out} = n^2 \left[2 \left(\frac{g_{s2}}{g_{m0}} \right)^2 + (1+n) \frac{g_{s2}}{g_{m0}} + 1 \right] \quad (\text{A.84})$$

depends on the ratio between the dc output current I and the follower-shifter bias current I_{shC} since $g_{s2}/g_{m0} = nI/I_{shC}$.

Without the output unloading transistors T_4 - T_5 - T_6 , the follower-shifter requires a bias current $I_{shC} \gg I$ ensuring its output conductance g_{m0} to be larger than its loading conductance, thus $g_{m0} \gg g_{s2}$. In such a configuration, $g_{m4} = g_{m5} = g_{m6} = 0$, $I_{N4} = I_{N5} = I_{N6} = 0$ and the output noise factor can be calculated similarly:

$$\gamma_{outL} = n^2 \left[\frac{1}{2} \left(\frac{g_{s2}}{g_{m0}} \right)^2 + (1+n) \frac{g_{s2}}{g_{m0}} + 1 \right] \approx n^2. \quad (\text{A.85})$$

The noise psd s_{vC} of the capacitor voltage v_C is determined by the noise psd s_{iC} of the total current crossing it:

$$s_{vC} = \frac{V_0}{V_A^*} \frac{s_{iC}}{(2\pi fC)^2} = \frac{s_{Iin} + s_{I1} + g_{m1}^2 s_{vGin}}{(2\pi fC')^2}, \quad (\text{A.86})$$

where $s_{I1} = 2k_B T n g_{m1}$ is the current noise psd generated by transistor T_1 and s_{vGin} is the voltage noise psd at the input v_{Gin} of the circuit.

The current gain V_0/V_A^* of the pseudo-transcapacitor circuit (see paragraph 5.3.5) is lumped into an input-referred capacitance $C' = CV_A^*/V_0$. The input-referred current noise psd of the pseudo-transcapacitor circuit is given by equation (5.34)

$$s_{Iin} = 4k_B T n g_{m1} \left(1 + 2 \frac{V_A^*}{V_0} \right), \quad (\text{A.87})$$

where $g_{m1} = I_0/nU_T$ is given by the dc input current I_0 of the pseudo-transcapacitor at equilibrium. The internal dc pseudo-voltage V_A^* is related to the output dc pseudo-voltage V_C^* by the voltage shift V_{sh} introduced by the follower-shifter according to equation (5.6):

$$v_A^* = v_C^* e^{V_{sh}/U_T}, \quad (\text{A.88})$$

where V_C^* is determined by the pseudo-conductance G^* implemented by T_2 , biased using a current $I_G = V_0/G^*$ and crossed by the dc output current I , resulting in:

$$\frac{V_A^*}{V_0} = \frac{I}{G^* V_0} e^{V_{sh}/U_T} = \frac{I}{I_G} e^{V_{sh}/U_T}, \quad (\text{A.89})$$

thus

$$s_{VC} = \left[s_{VGin} + \gamma_{in} \frac{4k_B T}{g_{m1}} \right] \frac{g_{m1}^2}{(2\pi f C')^2}, \quad (\text{A.90})$$

where

$$\gamma_{in} = n \left[\frac{3}{2} + \frac{2I}{I_G} e^{V_{sh}/U_T} \right] \quad (\text{A.91})$$

and

$$C' = C \frac{V_A^*}{V_0} = \frac{I}{I_G} C e^{V_{sh}/U_T}. \quad (\text{A.92})$$

The output noise voltage psd of the integrator at the gate of transistor T_3 is finally given by

$$s_{VGout} = \left(\frac{n g_{m1}}{2\pi f C'} \right)^2 \left[s_{VGin} + \gamma_{in} \frac{4k_B T}{g_{m1}} \right] + \gamma_{out} \frac{4k_B T}{g_{s2}}, \quad (\text{A.93})$$

with the noise factors

$$\gamma_{in}(I, I_G) = n \left[\frac{3}{2} + \frac{2I}{I_G} e^{V_{sh}/U_T} \right], \quad (\text{A.94})$$

$$\gamma_{out}(I, I_{shC}) = n^2 \left[2 \left(\frac{nI}{I_{shC}} \right)^2 + (1+n) \frac{nI}{I_{shC}} + 1 \right]. \quad (\text{A.95})$$

A.4.2 Feedback block

The same analysis is now performed with the current-to-pseudo-voltage converter together with the current conveyor of figure A.4a, using its noisy small signal equivalent of figure A.4b. The input current i_{in} is converted into a (pseudo-) voltage by transistor T_6 (pseudo-conductance G^*) and fed back at the output node v_Z . At this output node a dc current I_0 is injected; this current corresponds to the bias currents of the integrators, at which the current entering v_Z stabilises in the full resonator circuit. Assuming equal transconductances $g_{m1} = g_{m2} = g_{s2}/n = g_{m3} = g_{m4} = I_0/nU_T$, an output conductance g_{ds6} much smaller than $g_{s6} = I/U_T$ and $g_{m8} = (I + I_0)/nU_T$, the output voltage v_Z as a function of the input current i_{in} and the internal noise sources i_{Ni} is given by

$$v_Z = \frac{i_{in}}{g_{s6}} + \frac{i_{N1} + i_{N2} - i_{N3} - i_{N4}}{g_{s2}} - \frac{i_{N6} - i_{N10}}{g_{s6}} - \frac{g_{ds6}}{g_{s6}} \frac{i_Z + i_{N8}}{g_{m8}}, \quad (\text{A.96})$$

where the last term may be neglected due to the small value of g_{ds6} .

With the current noise psd s_{Ii} of the transistors given as in the integrator's noise calculation, the output voltage noise psd becomes

$$s_{VZ} = \frac{s_{Iin}}{g_{s6}^2} + \gamma f \frac{4k_B T}{g_{s6}}, \quad (\text{A.97})$$

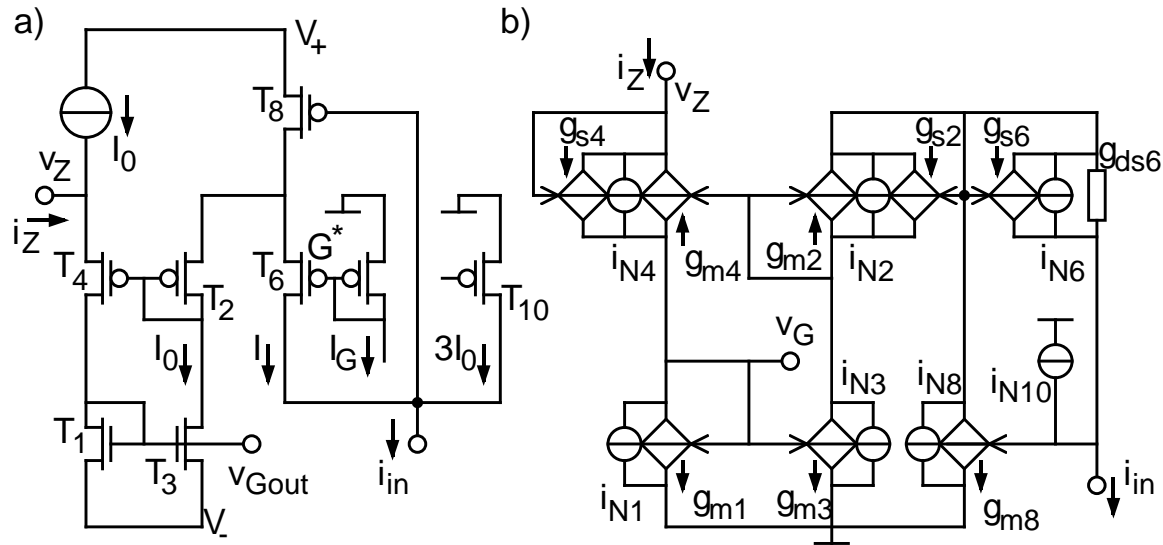


Figure A.4: a) current-to-pseudo-voltage converter and current conveyor; b) its noisy small signal equivalent

where s_{Iin} is the current noise psd of the input current i_{in} and the noise factor weighting the equivalent noisy conductance g_{s6} is given by

$$\gamma_f(I, I_0) = \frac{2I}{I_0} + \frac{3I_0}{2I} + \frac{1}{2}. \quad (\text{A.98})$$

As for the gate voltage v_{Gout} , it is simply given by

$$v_{Gout} = \frac{i_Z - i_{N1}}{g_{m1}}, \quad (\text{A.99})$$

having thus a voltage noise psd

$$s_{V_{Gout}} = \frac{s_{IZ}}{g_{m1}^2} + \frac{2k_B T n}{g_{m1}} = \frac{1}{2n} \frac{4k_B T}{g_{m1}}, \quad (\text{A.100})$$

where s_{IZ} is the current noise psd injected at node v_Z .

A.4.3 Full resonator

Interpreting equations (A.93), (A.97) and (A.100), the noisy small signal equivalent in figure A.5 of the full basilar membrane resonator of figure 5.16 is used to calculate the voltage noise on its node v_Z as a function of its input current i_Z and its internal noise sources

$$v_Z = v_{NG} + \frac{1}{G} (g_{mf} v + g_{mf1} v_1 + g_{mf2} v_2 + i_{Nf} + i_{Nf1} + i_{Nf2})$$

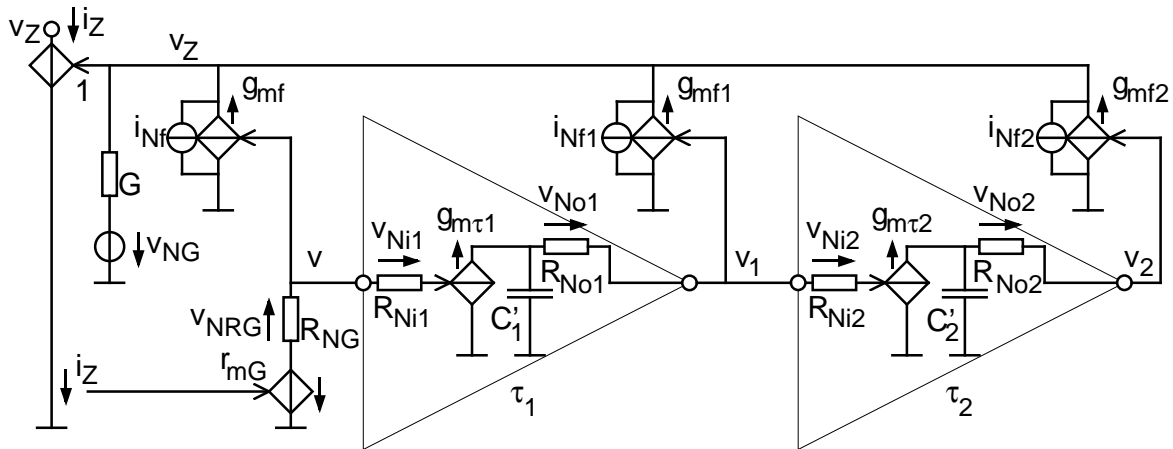


Figure A.5: noisy small signal equivalent of the basilar membrane resonator

$g_{m\tau 1} = \frac{I}{U_T}$ $C'_1 = \frac{I_1}{I_{G1}} C e^{-V_{sh1}/U_T}$	$g_{m\tau 2} = \frac{I_1}{U_T}$ $C'_2 = \frac{I_2}{I_{G2}} C e^{-V_{sh2}/U_T}$
$R_{Ni1} = \gamma_{in}(I_1, I_{G1}) \frac{nU_T}{I}$ $s_{Vi1} = 4k_B T R_{Ni1}$	$R_{Ni2} = \gamma_{in}(I_2, I_{G2}) \frac{nU_T}{I_1}$ $s_{Vi2} = 4k_B T R_{Ni2}$
$R_{No1} = \gamma_{out}(I_1, I_{shC1}) \frac{U_T}{I_1}$ $s_{Vo1} = 4k_B T R_{No1}$	$R_{No2} = \gamma_{out}(I_2, I_{shC2}) \frac{U_T}{I_2}$ $s_{Vo2} = 4k_B T R_{No2}$
$g_{mf1} = \frac{I_1}{nU_T}$ $s_{If1} = 2k_B T n g_{mf1} = 2k_B T \frac{I_1}{U_T}$	$g_{mf2} = \frac{I_2}{nU_T}$ $s_{If2} = 2k_B T n g_{mf2} = 2k_B T \frac{I_2}{U_T}$
$g_{mf} = \frac{I}{nU_T}$ $s_{If} = 2k_B T n g_{mf} = 2k_B T \frac{I}{U_T}$	$r_{mG} = \frac{nU_T}{I}$
$R_{NG} = \frac{r_{mG}}{2n} = \frac{U_T}{2I}$ $s_{VRG} = \frac{4k_B T}{R_{NG}} = k_B T U_T / I$	$G = \frac{I_F}{U_T}$ $s_{VG} = \gamma_f(I_F, I_0) \frac{4k_B T}{G}$

Table A.2: Parameters of the small signal noisy resonator.

$$\begin{aligned}
&= r_{mG} \frac{g_{mf}}{G} i_Z + \frac{g_{mf1}}{G} v_{No1} + \frac{g_{mf2}}{G} v_{No2} \\
&+ \frac{g_{fm}}{G} v_{NRG} + v_{NG} + \frac{i_{Nf} + i_{Nf1} + i_{Nf2}}{G} \\
&+ \frac{g_{m\tau 1}}{\omega C'_1} \frac{g_{mf1}}{G} (r_{mG} i_Z + v_{NRG} + v_{Ni1}) \\
&+ \frac{g_{m\tau 2}}{\omega C'_2} \frac{g_{mf2}}{G} (v_{No1} + v_{Ni2}) \\
&+ \frac{g_{m\tau 1} g_{m\tau 2}}{\omega^2 C'_1 C'_2} \frac{g_{mf2}}{G} (r_{mG} i_Z + v_{Ni1} + v_{NRG}), \tag{A.101}
\end{aligned}$$

where the values of the elements are listed in table A.2 as a function of the currents I , I_1 , I_2 , I_0 and $I_F = I + I_1 + I_2 - 3I_0$. The currents I , I_1 and I_2 correspond to the currents i , i_1 and i_2 , respectively, in figure 5.16 at the operating point used for linearisation. Using these values, the voltage

noise psd at the node v_Z becomes:

$$\begin{aligned}
s_{vZ} &= \frac{U_T^2}{I_F^2} \left(S_{IZ} + \frac{I_1^2}{U_T^2} \frac{S_{Vo1}}{n^2} + \frac{I_2^2}{U_T^2} \frac{S_{Vo2}}{n^2} \right. \\
&\quad \left. + \frac{I^2}{U_T^2} \frac{S_{VRG}}{n^2} + \frac{I_F^2}{U_T^2} S_{VG} + s_{If} + s_{If1} + s_{If2} \right) \\
&+ \frac{I_1^2}{I_F^2} \frac{1}{\omega^2 C_1'^2} \left(S_{IZ} + \frac{I^2}{U_T^2} \frac{s_{VRG} + s_{Vi1}}{n^2} + \frac{C_1'^2}{C_2'^2} \frac{I_2^2}{U_T^2} \frac{s_{Vo1} + s_{Vi2}}{n^2} \right) \\
&+ \frac{I_2^2}{I_F^2} \frac{I_1^2}{U_T^2} \frac{1}{\omega^4 C_1'^2 C_2'^2} \left(s_{IZ} + \frac{I^2}{U_T^2} \frac{s_{Vi1} + s_{VRG}}{n^2} \right), \tag{A.102}
\end{aligned}$$

which may be expressed by

$$\begin{aligned}
s_{vZ} &= \frac{1}{G^2} (s_{IZ} + 4k_B T G \gamma_G) \\
&+ \frac{G_1^2}{G^2 \omega^2 C_1'^2} (s_{IZ} + 4k_B T G_1 \gamma_C) \\
&+ \frac{G_1^2 G_2^2}{G^2 \omega^4 C_1'^2 C_2'^2} (s_{IZ} + 4k_B T G_2 \gamma_S), \tag{A.103}
\end{aligned}$$

where $G = I_F/U_T$, $G_1 = I_1/U_T$, $G_2 = I_2/U_T$ and using the noise factors

$$\gamma_G = \frac{I^2}{I_1 I_F} \gamma_{o1} + \frac{I_2}{I_F} \gamma_{o2} + \gamma_f + \frac{I}{I_F} \frac{1}{2n^2} + \frac{I + I_1 + I_2}{2I_F}, \tag{A.104}$$

$$\gamma_C = \frac{I}{I_1} \left[\frac{1}{2n^2} + \gamma_{i1} \right] + \frac{(C_1'/G_1)^2}{(C_2'/G_2)^2} (\gamma_{o1} + \gamma_{i2}), \tag{A.105}$$

$$\gamma_S = \frac{I}{I_2} \left[\frac{1}{2n^2} + \gamma_{i1} \right], \tag{A.106}$$

and

$$\begin{aligned}
\gamma_{i1} &= \frac{3}{2} + \frac{2I_1}{I_{G1}} e^{V_{sh1}/U_T}, \\
\gamma_{i2} &= \frac{3}{2} + \frac{2I_2}{I_{G2}} e^{V_{sh2}/U_T}, \\
\gamma_{o1} &= 2 \left(\frac{nI_1}{I_{shC1}} \right)^2 + (1+n) \frac{nI_1}{I_{shC1}} + 1,
\end{aligned}$$

$$\gamma_{o2} = 2 \left(\frac{nI_2}{I_{sh}C_2} \right)^2 + (1+n) \frac{nI_2}{I_{sh}C_2} + 1,$$

$$\gamma_f = \frac{2I_F}{I_0} + \frac{3I_0}{2I} + \frac{1}{2},$$

derived from equations (A.94), (A.95) and (A.98).

According to equation (A.103), the noisy basilar membrane resonator is thus equivalent to the serial RCS resonator of figure A.6, in which each dipole

$$G_{BM} = G, \quad (\text{A.107})$$

$$C_{BM} = \frac{G}{G_1} C'_1, \quad (\text{A.108})$$

$$S_{BM} = \frac{G}{G_2} \frac{C'_1 C'_2}{G_1}, \quad (\text{A.109})$$

features a parallel noise current source i_{NG} , i_{NC} and i_{NS} having power spectral densities

$$s_{IG} = \gamma_G 4k_B T G, \quad (\text{A.110})$$

$$s_{IC} = \gamma_C 4k_B T G_1, \quad (\text{A.111})$$

$$s_{IS} = \gamma_S 4k_B T G_2, \quad (\text{A.112})$$

respectively.

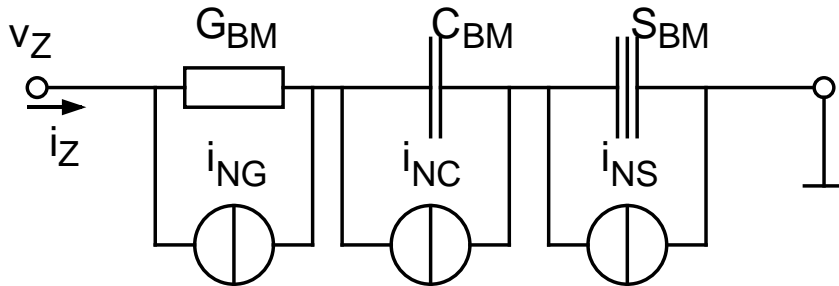


Figure A.6: noisy equivalent of the basilar membrane RCS resonator

Bibliography

- [1] Carver A. Mead. *Analog VLSI and Neural Systems*, chapter 11, pages 179–192. Addison-Wesley, 1989.
- [2] Eric A. Vittoz. Analog VLSI signal processing: why, where and how? *Analog Integrated Circuit and Signal Processing and Journal of VLSI Signal Processing*, 8:27–44, July 1994. Published jointly.
- [3] Carver A. Mead, Xavier Arreguit, and John Lazzaro. Analog VLSI model of binaural hearing. *IEEE transactions on Neural Networks*, 2(2):230–236, March 1991.
- [4] Eric Fragnière, André van Schaik, and Eric A. Vittoz. Linear predictive coding of the speech using an analogue cochlear model. In *Proceedings Eurospeech '95*, volume 1, pages 119–123, Madrid, Spain, September 1995.
- [5] Eric Fragnière. Cochlear linear predictive coding: Interfacing an analogue cochlear model with a conventional speech recognition system. In *MANTRA Centre for Neuromimetic Systems 1992-1995 Activity Report*, pages 105–116. Swiss Federal Institute of Technology, Lausanne, January 1996.
- [6] André van Schaik. *Analogue VLSI Building Blocks for an Electronic Auditory Pathway*. PhD. thesis no. 1764, Swiss Federal Institute of Technology (EPFL), Lausanne, Switzerland, December 1997.
- [7] André van Schaik, Eric Fragnière, and Eric A. Vittoz. An analogue electronic model of ventral cochlear nucleus neurons. In *Proceedings of MicroNeuro '96*, pages 52–59, Lausanne, Switzerland, February 1996.

- [8] John J. Rosowski. Models of external- and middle-ear function. In L. Hawkins, Harold, A. McMullen, Teresa, N. Popper, Arthur, and R. Fay, Richard, editors, *Auditory Computation*, volume 6, chapter 2, pages 15–61. Springer, 1996.
- [9] Allyn E. Hubbard and David C. Mountain. Analysis and synthesis of cochlear mechanical function using models. In L. Hawkins, Harold, A. McMullen, Teresa, N. Popper, Arthur, and R. Fay, Richard, editors, *Auditory Computation*, volume 6, chapter 3, pages 62–120. Springer, 1996.
- [10] David C. Mountain and Allyn E. Hubbard. Computational analysis of hair cell and auditory nerve processes. In L. Hawkins, Harold, A. McMullen, Teresa, N. Popper, Arthur, and R. Fay, Richard, editors, *Auditory Computation*, volume 6, chapter 4, pages 121–156. Springer, 1996.
- [11] James O. Pickles. *An Introduction to the Physiology of Hearing*. Academic Press, London, 2nd edition, 1988.
- [12] Jonathan E. Gale and Jonathan F. Ashmore. An intrinsic frequency limit to the cochlear amplifier. *Nature*, 389(4):63–66, September 1997.
- [13] Mario A. Ruggero. Response to sound of the basilar membrane of the mammalian cochlea. *Current Opinion in Neurobiology*, 2:449–456, 1992.
- [14] D. T. Kemp. Stimulated acoustic emission from within the human auditory system. *Journal of the Acoustical Society of America*, 64:1386–1391, 1978.
- [15] J. F. Ashmore. A fast motile response in guinea-pig outer hair cells: the cellular basis of the cochlear amplifier. *Journal of Physiology*, 388:323–347, 1987.
- [16] Shuwan Xue, David C. Mountain, and Allyn E. Hubbard. Electrically evoked basilar membrane motion. *Journal of the Acoustical Society of America*, 97(5):3030–3041, May 1995.
- [17] Nigel P. Cooper. Two-tone suppression in cochlear mechanics. *Journal of the Acoustical Society of America*, 99(5):3087–3098, May 1996.

- [18] D. O. Kim. Active and nonlinear cochlear biomechanics and the role of outer-hair-cell subsystem in the mammalian auditory system. *Hearing Research*, 22:105–114, 1986.
- [19] I. J. Russel and P. M. Sellick. Low-frequency characteristics of intracellularly recorded receptor potential in guinea-pig cochlear hair cells. *Journal of Physiology*, 338:179–206, 1983.
- [20] Ray Meddis. Simulation of mechanical to neural transduction in the auditory receptor. *Journal of the Acoustical Society of America*, 79(3):702–711, March 1986.
- [21] Stephen T. Neely and D. O. Kim. An active cochlear model showing sharp tuning and high sensitivity. *Hearing Research*, 9:123–130, 1983.
- [22] Daniel C. Geisler and Xueshan Shan. A model for cochlear vibrations based on feedback from motile outer hair cells. In P. Dallos, C. D. Geisler, J. M. Matthews, M. A. Ruggero, and C. R. Steele, editors, *The Mechanics and Biophysics of Hearing*, pages 86–95, Berlin, 1990. Springer Verlag.
- [23] Georges Zweig. Finding the impedance of the organ of Corti. *Journal of the Acoustical Society of America*, 89:1221–1254, 1991.
- [24] F. Mammano and R. Nobili. Biophysics of the cochlea: Linear approximation. *Journal of the Acoustical Society of America*, 93(6):3320–3332, June 1993.
- [25] S. T. Neely and D. O. Kim. A model for active elements in cochlear biomechanics. *Journal of the Acoustical Society of America*, 79(5):1472–1480, May 1986.
- [26] Stephen T. Neely. Finite difference solution of a two-dimensional mathematical model of the cochlea. *Journal of the Acoustical Society of America*, 69(5):1386–1393, May 1981.
- [27] Lloyd Watts. *Cochlear Mechanics: Analysis and Analog VLSI*. PhD thesis, California Institute of Technology, 1993.
- [28] H. W. Strube. A computationally efficient basilar-membrane model. *Acustica*, 58:207–214, 1985.

- [29] A. Aertsen and P. Johannesma. Spectro-temporal receptive fields of auditory neuron in the grass frog. I. characterization of tonal and natural stimuli. *Biology and Cybernetics*, 38:223–234, 1980.
- [30] Roy D. Patterson, John Holdsworth, and Michael Allerhand. Auditory models as preprocessors for speech recognition. In M. E. H Schouten, editor, *The Auditory Processing of Speech: from Auditory Periphery to Words*, pages 67–89. Mouton de Gruyler, Berlin, 1992.
- [31] Stephanie Seneff. A joint synchrony/mean rate model of auditory speech processing. *Journal of Phonetics*, 16(1):55–76, 1988.
- [32] Richard F. Lyon. Filter cascades as analogs of the cochlea. *Analog Integrated Circuits and Signal Processing: Special Issue on Neuromorphic Engineering*, 13(1/2):9–17, June 1997.
- [33] Neal Bhadkamkar. A variable resolution, nonlinear silicon cochlea. Technical Report CSL-TR-93-558, Stanford University, 1993.
- [34] Richard F. Lyon and Carver A. Mead. An analog electronic cochlea. *IEEE transactions on Acoustics, Speech and Signal Processing*, 36(7):1119–1134, July 1988.
- [35] Lloyd Watts, Douglas A. Kerns, Richard F. Lyon, and Carver A. Mead. Improved implementation of the silicon cochlea. *IEEE journal of Solid-State Circuits*, 27(5):692–700, May 1992.
- [36] Rahul Sarpeshkar, Richard F. Lyon, and Carver A. Mead. An analog VLSI cochlea with new transconductance amplifiers and nonlinear gain control. In *Proceedings of the IEEE Symposium on Circuits and Systems*, volume 3, pages 292–295, Atlanta, May 1996.
- [37] André van Schaik, Eric Fragnière, and Eric A. Vittoz. Improved silicon cochlea using compatible lateral bipolar transistors. In D. S. Touretzky, M. C. Mozer, and Hasselmo M. E., editors, *Advances in Neural Information Processing Systems*, 8, pages 671–677. MIT Press, 1996.
- [38] Eric Fragnière, André van Schaik, and Eric Vittoz. Design of an analogue VLSI model of an active cochlea. *Analog Integrated Circuit and Signal Processing: Special Issue on Neuromorphic Engineering*, 13(1):19–35, June 1997.

- [39] Dan Haronian and Noel C. MacDonald. A microelectromechanics based artificial cochlea (MEMBAC). In *Proceedings of the 8th International Conference on Solid-State Sensors and Actuators, and Eurosensors IX*, pages 708–711, Stockholm, Sweden, June 1995.
- [40] John Lazzaro, John Wawrzyneck, and Alan Kramer. Systems technologies for silicon auditory models. *IEEE Micro*, pages 7–15, June 1994.
- [41] Richard F. Lyon and Carver A. Mead. Cochlear hydrodynamics demystified. Technical Report Caltech-CS-TR-88-4, California Institute of Technology, 1988.
- [42] Kim D. O., S. Ghoshal, and Y. Ye. Integration of ascending and descending signals representing stimulus intensity in the marginal shell of the anteroventral cochlear nucleus. In R. Palmer, A., A. Rees, Q. Summerfield, A., and R. Meddis, editors, *Proceedings of 11th International Symposium on Hearing*, pages 171–177, Grantham, U.K., August 1997.
- [43] M. P. Sellick, R. Patuzzi, and B. M. Johnstone. Measurement of basilar membrane motion using the Moessbauer technique. *Journal of the Acoustical Society of America*, 72:131–141, 1982.
- [44] Eric A. Vittoz. MOS transistors operated in in the lateral bipolar mode and their application in CMOS. *IEEE Journal of Solid-State Circuits*, SC-18(3), June 1983.
- [45] Xavier Arreguit. *Compatible Lateral Bipolar Transistors in CMOS Technology: Model and Applications*. PhD. thesis no. 817, Swiss Federal Institute of Technology (EPFL), Lausanne, Switzerland, 1989.
- [46] J. F. Ashmore and D. G. Housley. Ionic currents of outer hair cells isolated from the guinea-pig cochlea. *Journal of Physiology*, 448:73–98, 1992.
- [47] R Nobili and F Mammano. Biophysics of the cochlea II: Stationary nonlinear phenomenology. *Journal of the Acoustical Society of America*, 99(4):2244–2255, April 1996.

- [48] Mario A. Ruggero. Physiology and coding of sound in the auditory nerve. In Arthur N. Popper and Richard R. Fay, editors, *The Mammalian Auditory Pathway: Neurophysiology*, Springer Handbook of Auditory Research, chapter 3, pages 34–93. Springer-Verlag, New York, 1992.
- [49] Eric A. Vittoz and Xavier Arreguit. Linear networks using transistors. *Electronics Letters*, 29:297–299, February 1993.
- [50] Eric A. Vittoz. Pseudo-resistive networks and their application to analog collective computation. In *Proceedings of MicroNeuro'97*, pages 163–172, Dresden, Germany, September 1997.
- [51] E. Seevink. Companding current-mode integrator: a new circuit principle for continuous-time monolithic filters. *Electronics Letters*, 26(24):2046–2047, November 1990.
- [52] Eric Vittoz. Intensive summer course on CMOS VLSI design, analog & digital. Lecture notes, Electronics Laboratories, EPFL, Lausanne, Switzerland, September 1988.
- [53] Rahul Sarpeshkar, Tobias Delbrück, and Carver A. Mead. White noise in MOS transistors and resistors. *IEEE Circuits and Devices*, pages 23–29, November 1993.

Biographical data

Publications

- [A1] Eric Fragnière, André van Schaik, Eric Vittoz. Linear Predictive Coding of Speech using an Analogue Cochlear Model. In *Proceedings of EuroSpeech'95*, vol. 1, pp. 119–122, Madrid, Spain, September 18–21, 1995.
- [A2] Eric Fragnière, André van Schaik, Eric Vittoz. Cochlear Linear Predictive Coding: Interfacing an Analogue with a Conventional Speech Recognition System. In *MANTRA Centre for Neuro-Mimetic Systems, 1992-1996 Activity Report*, pp. 105–116, Swiss Federal Institute of Technology (EPFL), Lausanne, Switzerland, 1996.
- [A3] Eric Fragnière, André van Schaik, Eric Vittoz. Design of an Analogue VLSI Model of an Active Cochlea. In *Analog Integrated Circuits and Signal Processing, Special Issue on Neuromorphic Engineering*, vol. 13, no. 1/2, pp. 19–36, May/June 1997.
- [A4] Eric Fragnière, André van Schaik, Eric Vittoz. Experiments with a Model of the Active Cochlea Designed for an Analogue VLSI Implementation. In *Proceedings of MicroNeuro'97*, pp. 154–161, Dresden, Germany, September 24–26, 1997.
- [A5] Eric Fragnière, André van Schaik, Eric Vittoz. *Reactive Components for Pseudo-Resistive Networks*. *Electronics Letters*, vol. 33, No. 23, pp. 1913–1914, November 1997.

Curriculum Vitae

Surname:	Fragnière	First name:	Eric
Birtdate:	23 February 1964	Nationality:	Swiss
Citizenship:	Fribourg	Civil Status:	Married, one child
Adresses:	home:	work:	
	ch. des cèdres 13	MANTRA-DI-EPFL	
	1004 Lausanne	1015 Lausanne	
	Switzerland	Switzerland	
telephone:	(021) 647 69 48	(021) 693 66 19	
E-mail:		Eric.Fragniere@epfl.ch	

languages: French (mother tongue), English (fluent), German, Spanish, Japanese.

Experience:

1993-1998 Research assistant at the MANTRA center for neuro-mimetic systems and at the Electronic Laboratory, EPFL.

1992-1993 R&D engineer at the “Institut für flexible Automation”, Technische Universität, Vienna, Austria.

1991-1992 R&D engineer at Nitto-Kohki, Ltd,. Koosai-choo, Japan.

1990-1991 Post-graduate traineeship at Fujitsu Laboratories, Ltd,. Kawasaki, Japan.

1987-1989 Part-time teaching (electrical engineering, mathematics) at the “Ecole d’Ingénieur”, Fribourg.

1987 Temporary workshop management (electricity and computer sciences) at the “Ecole des Métiers”, Fribourg.

1987 Under-graduate traineeship (6 weeks) at the Danish Acoustical Institute, Lyngby, Denmark.

Studies:

1985-1990 Ecole polytechnique fédérale de Lausanne (EPFL), “Diplôme d’Ingénieur Electricien EPF” (“Jean Landry” award).

1982-1985 Ecole d’Ingénieur de Fribourg, “Diplôme d’Ingénieur ETS en Electrotechnique” (“Sodeco-Saia” award).

1979-1982 Ecole des Métier de Fribourg, “Certificat Fédéral de Capacité de mécanicien-électronicien”.